UNIVERSITÀ DEGLI STUDI DI MILANO

FACOLTÀ DI SCIENZE MATEMATICHE, FISICHE E NATURALI

DOTTORATO DI RICERCA IN
FISICA, ASTROFISICA E FISICA APPLICATA

STUDY OF CHARMONIUM RESONANCES IN THE $\gamma\gamma\to K_S^0K^\pm\pi^\mp$ AND $\gamma\gamma\to K^+K^-\pi^+\pi^-\pi^0$ PROCESSES

Settore Scientifico Disciplinare FIS/04

Coordinatore: Prof. Marco Bersanelli

Tutore: Prof. Fernando Palombo

Tesi di Dottorato di:
Pietro Biassoni
SLAC-R-983
Ciclo XXIV

Anno Accademico 2010-2011

Den kloke navigatören är den som
gör en cirkel större och större,
som förstår att osäkerheten
är den enda visshet som finns att tillgå

The wise navigator is one who
makes his circle wider and wider,
who knows that uncertainty
is the only certainty there is.

Long John Silver, Björne Larsson

Contents

Introduction

The discovery of the J/ψ resonance in 1974 by Ritcher and Ting was a real breakthrough in the history of modern particle physics. The existence of a fourth quark named *charm* had already been supposed, and the spectacular discovery of the first bound $c\bar{c}$ state confirmed that the quark model was following the right path. Bound particle-antiparticle states, such as e^+e^- positronium, $c\bar{c}$ charmonium and $b\bar{b}$ bottomonium are considered as ideal laboratories to test fundamental properties of the forces binding such systems. In particular, the charmonium system is suitable to study the dynamics of the strong interaction that binds the quarks inside the hadronic matter. Furthermore, this system is challenging on the theoretical side because it lies in a mass region where the strong force shows up with both perturbative and non-perturbative effects. The first are easy to compute, while the latter are non trivial and not completely understood, yet. Phenomenological models able to describe the charmonium mass spectrum and transitions accurately were available in the 80's. In the 90's major theoretical efforts to link such phenomenological models to first principles were undertaken. Issues that remained still open were the existence of states predicted but not-yet discovered, and some inconsistencies between experimental measurement and theoretical predictions. However, the charmonium model was considered to be quite successful in describing data.

The *BABAR* and Belle experiments, operated at the high-luminosity B-factories PEP-II and KEKB, were built in the late 90's with a physics program only marginally devoted to charmonium spectroscopy. Their main goal was the measurement of the elements of the Cabibbo-Kobayashi-Maskawa (CKM) matrix, that describes the CP-violation in the Standard Model. Furthermore, they were expected to search for phenomena beyond the Standard Model in CP-violation. The precise determination of the CP-violation parameters in the B-meson sector provided by *BABAR* and Belle confirms the validity of the CKM picture and strongly constraints the flavor sector of many new physics scenarios. The results obtained at the B-factories contributed to the awarding of the 2008 Nobel prize in Phsyics to Kobayashi and Maskawa "*for the discovery of the origin of the broken symmetry which predicts the existence of at least three families of quarks in nature*". The large dataset available at B-factories also allowed to first observe $c\bar{c}$ and $b\bar{b}$ particles that were still escaping detection.

In 2003 an unexpected discovery was reported by Belle. A charmonium-like state with unusual properties that cannot fit in the charmonium model was observed. This state, dubbed $X(3872)$, was subsequently confirmed by *BABAR* and many other experiments. Despite the large number of available measurements, its interpretation on the theoretical side is still ambiguous. The great excitement due to such a discovery brought to a renaissance of the charmonium spectroscopy, that is actually one of the most active fields in the B-factories research. Up to date more than ten new unconventional states have been reported.

In 2008, Belle reported the observation of highly unconventional states carrying non-zero electric charge. Two more states with this highly non-conventional property were observed by Belle in the same year. These discoveries have been strongly debated on the experimental ground. *BABAR* did not confirm, but was neither able to refute them. If the existence of such states were confirmed, they could not be interpreted as simple $q\bar{q}$ states. Models that predict the existence of exotic hadronic states, such as tetraquarks or meson molecules, have been proposed since long time. During the last thirty years, some states have been claimed to have unconventional nature, but no definitive answer are available. If observation of electric-charged states by Belle were confirmed, this would finally establish the existence of such exotic hadronic states. At present, an improvement of the charmonium model is needed in order to solve the open inconsistencies and to be able to clearly determine the exotic nature of the newly observed states. Thus, precise measurements of conventional charmonium state properties are highly welcome, in order to tune and test theoretical models.

This thesis reports the analysis of the $e^+e^-\to e^+e^-K^0_SK^\pm\pi^\mp$ and $e^+e^-\to e^+e^-K^+K^-\pi^+\pi^-\pi^0$ processes using the final dataset of the *BABAR* experiment located at the SLAC National Accelerator Laboratory. From previous measurements, the $K^0_SK^\pm\pi^\mp$ final state is known to show a clear signal from the $\eta_c(2S)$ particle. This $c\bar{c}$ state escaped detection for almost twenty years and its properties are still not well established on the experimental ground, while accurate predictions exist on the theoretical side. The $e^+e^-\to e^+e^-K^+K^-\pi^+\pi^-\pi^0$ process is first studied in this thesis. An accurate determination of the $\eta_c(2S)$ properties is obtained in the $K^0_SK^\pm\pi^\mp$ decay mode. We also report the first observation of $\eta_c(2S)$ and other charmonium states to the $K^+K^-\pi^+\pi^-\pi^0$ final state. The results of this thesis have been published in *Physical Review D*, and will be useful to test theoretical models describing the charmonium system.

The thesis is organized in four chapters. The first one gives a brief introduction of the theoretical models used to describe the charmonium system. The second one discuss the current status of conventional and exotic charmonium spectroscopy, reporting recent experimental results and their interpretation. The third Chapter is devoted to describe the *B*A*B*AR experiment. The analysis technique and results are described in Chapter 4. Finally, conclusions from this analysis are drawn.

Chapter 1

Theoretical overview

1.1 Introduction

In this chapter we outline the theoretical tools used to describe the charmonium system. We cover the theory that predicts both the mass spectrum and transition rates. In sight of the new unexpected results for unconventional states above the $D\overline{D}$ threshold, we also review the main features of some possible exotic states predicted by quantum-chromodynamics (QCD). The discussion presented here is not intended to be exhaustive. Comprehensive reviews reporting an up to date state of the understanding of the charmonium system on both theoretical and experimental grounds can be found in Refs. [1, 2].

1.2 Charmonium quantum numbers

Since the discovery of the J/ψ meson [3, 4], the so-called *charmonium* states have been considered as an ideal system to test the QCD theory in a region where both perturbative and non-perturbative effects are manifest. The charmonium is a bound state of a c and $\overline{c}$ quark. Using the spectroscopic notation $n^{2S+1}[L]_J$, each state is identified by four quantum numbers. The radial quantum number n labels the radial excitation of the state. The spin S is obtained from the combination of the spin-1/2 constituent quarks, thus the $c\overline{c}$ system can be in a spin-singlet $S = 0$ or spin-triplet $S = 1$ configuration. The quantum number L is the orbital momentum between the c and $\overline{c}$ quark. The common notation for $[L]$ is S for $L = 0$, P for $L = 1$ and D for $L = 2$. No state with $L > 2$ has been observed to date. According to quantum mechanics rules for the sum of angular momenta, $J = S + L$ ranges from $|S - L|$ to $S + L$.

Historically, the n^1S_0 states are named $\eta_c(nS)$. The ${}^3S_1$ state is the J/ψ, while its radial excitations are named $\psi(nS)$. The n^3P_J, n^1D_2, and n^3D_J states are named $\chi_{cJ}(nP)$, $\eta_{c2}(nD)$, and $\psi_J(nD)$, respectively.

A $c\overline{c}$ state is both a parity P and charge conjugation C eigenstate. The parity operator transforms a wavefunction $\phi(\vec{p})$ in $\phi(-\vec{p})$. The angular part of the $c\overline{c}$ bound state wavefunction can be described by spherical harmonics that have the property $P = (-1)^L$. Since $\overline{c}$ is the c antiparticle, the product of their intrinsic parity is -1. Thus, the $c\overline{c}$ state has parity $P = (-1)^{L+1}$. The C operator transform a particle in its antiparticle. As for the P operator, the angular part of the $c\overline{c}$ wavefunction has $C = (-1)^L$. The spin part of the $c\overline{c}$ wavefunction is symmetric for $S = 1$ and antisymmetric for $S = 0$, thus $C = (-1)^{S+1}$. The product of the spin part with the angular part and the inclusion of a -1 factor from c and $\overline{c}$ intrinsic parity leads to $C = (-1)^{L+S}$, for a $c\overline{c}$ state.

1.3 The charmonium spectrum

1.3.1 Energy scales

The charmonium system is characterized by three energy scales: the charm quark mass m_c, the relative momentum between charm quarks $p \sim m_c v \sim 1/r_c$, and the charmonium binding energy $E \sim m_c v^2$, where v is the quark bound state velocity and r_c the $c\overline{c}$ state radius. Since m_c is heavy (~ 1.5 GeV$/c^2$), the velocity is believed to be small $v \ll 1$. Using a simple potential model (see Eq. (1.2) below), the average kinetic energy $\langle T \rangle$ of the heavy quarks is found to be 0.37 GeV [5]. Since $\langle T \rangle = 2 \cdot (1/2) m_c \langle v^2 \rangle$, using $m_c \sim 1.5$ GeV$/c^2$ one gets $\langle v^2 \rangle \sim 0.24$. Thus, the following relations hold

$$m_c \gg m_c v \gg m_c v^2. \tag{1.1}$$

Using the value of $\langle v^2 \rangle$ obtained above, we get $m_c v^2 \sim 0.5$ GeV. The estimate $m_c v \sim 0.9$ GeV is obtained as the geometric mean between m_c and $m_c v^2$.

Another important scale in QCD is the confinement scale Λ_{QCD}, where the value of the coupling constant $\alpha_s(m)$ becomes large. The constant $\alpha_S(m_c)$ at mass m_c is much smaller than one. Thus, phenomena occurring at the m_c mass scale are successfully treated in a perturbative approach. To ensure that a perturbative approach is valid, also $\alpha_S(m_c v)$ and $\alpha_S(m_c v^2)$ should be much smaller than one. This condition is likely to be true only for the low-lying $c\overline{c}$ states, while it is probably violated for excited states. Due to the absence of a direct experimental probe of the size of r_c (and so of $m_c v$) the range where the perturbative approach is valid is debated [2].

1.3.2 Potential models

Early attempts to describe the charmonium spectrum were performed by using potential models. An *ad hoc* potential is chosen to describe the $c\bar{c}$ interaction and it is used to solve the Schrödinger equation.

A simple potential named the "*Cornell Model*" [6, 7] was first used:

$$V(r) = V_V(r) + V_S(r) = -\frac{4}{3}\frac{\alpha_S}{r} + br. \tag{1.2}$$

The first term is a one-gluon-exchange short-range Coulomb-like interaction, the second one is linear in r and describes the quark confinement effect. To obtain a realistic description of the charmonium spectrum, one should account for spin-spin (SS), Thomas precession (LS), and tensor (T) interactions terms in the potential. Such terms are [1]

$$\begin{aligned} V_{SS}(r) &= \frac{\sigma_c\sigma_{\bar{c}}}{6m_c^2}\nabla^2 V_V(r), && (1.3)\\ V_{LS}(r) &= \frac{L\cdot S}{2m_c^2 r}\left(3\frac{dV_V}{\mathrm{d}r} - \frac{dV_S}{\mathrm{d}r}\right), && (1.4)\\ V_T(r) &= \frac{S_T}{12m_c^2}\left(\frac{1}{r}\frac{dV_V}{\mathrm{d}r} - \frac{d^2V_V}{\mathrm{d}r^2}\right), && (1.5) \end{aligned}$$

where σ_c is the Pauli matrix acting on the spin of the c quark, and $S_T \equiv 2[3(S\cdot\hat{r})(S\cdot\hat{r} - S^2)]$, with $\hat{r}$ being the unit vector in the $\vec{r}$ direction. The expectation value of S_T is non-zero only for $L > 0$ spin-triplet state and is equal to

$$\langle {}^3L_J|S_T|{}^3L_J\rangle = \begin{cases} -\frac{2L}{(2L+3)} & J = L+1 \\ +2 & J = L \\ -\frac{2(L+1)}{(2L-1)} & J = L-1 \end{cases} \tag{1.6}$$

The form of the terms in Eq. (1.3)–(1.5) is determined by the Lorentz nature of the potential of Eq. (1.2), that is the sum of a vector and a scalar part. The confining part of the potential does not contribute to any term in $V_{SS}(r)$ and $V_T(r)$, due to its scalar nature. The $\nabla^2 V_V(r)$ term in $V_{SS}(r)$ is proportional to $\delta^3(r)$, thus the $V_{SS}(r)$ term is non-zero only for S-wave. However, the running of the coupling constant α_S leads to small effects also for $L > 0$ states.

Studies aiming at systematically including relativistic and running coupling constant effects in this model started in 1985 [8]. This modification allowed to describe different $q\bar{q}$ systems ($c\bar{c}$, $b\bar{b}$, ...) in the framework of a unified model. To date, full relativistic calculations, and the inclusion of the effect of non-leading order effects provide an accurate description of the charmonium spectrum [9–14], which is shown in Fig. 1.1. In order

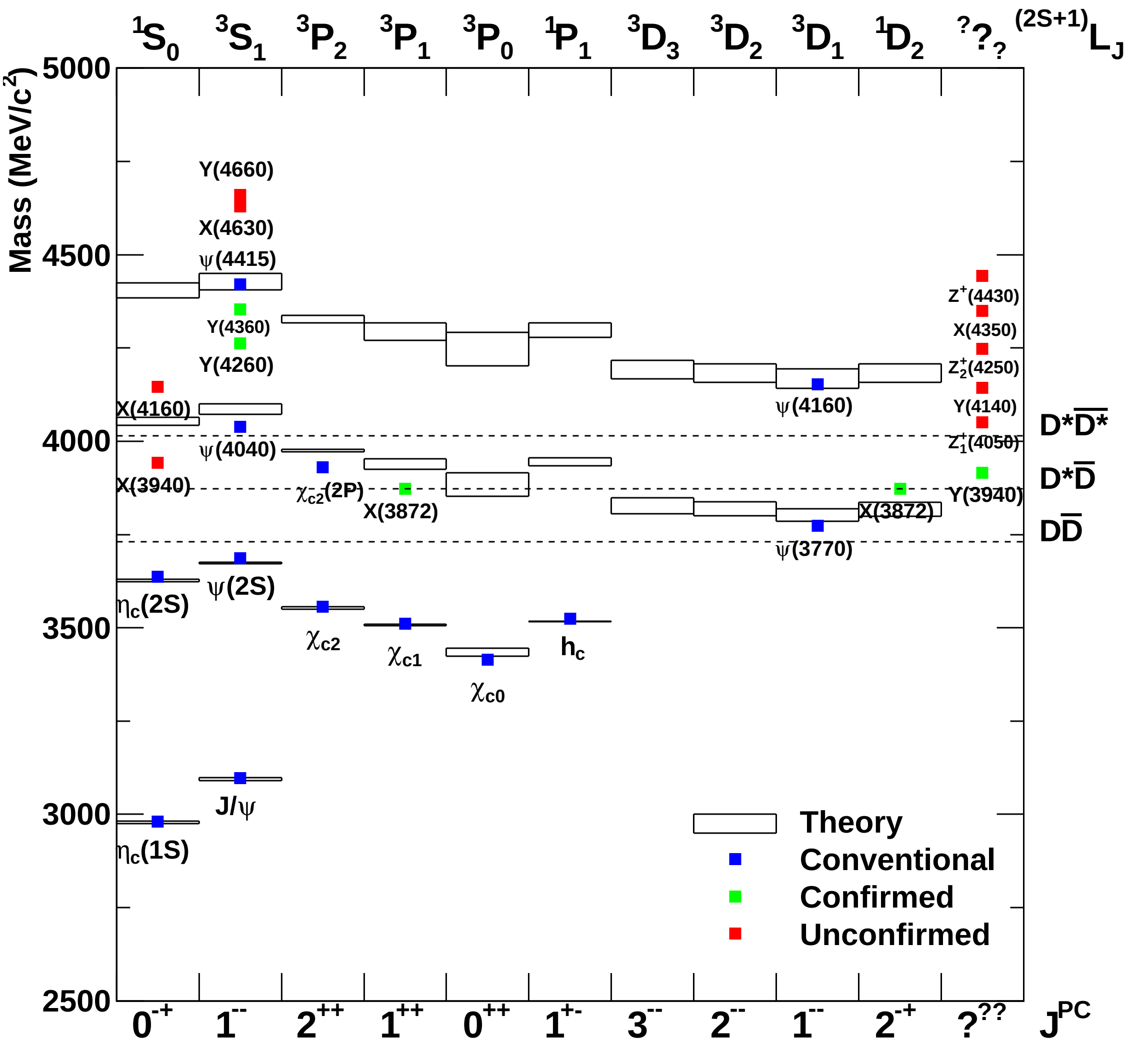

Figure 1.1: Spectrum of the charmonium system. Black boxes are mass predictions from potential models [14], blue squares are the measured mass for conventional states, green squares are the measured mass of confirmed exotic states, and red squares are the measured masses for unconfirmed exotic states.

to improve the description of the charmonium system above the open-charm threshold, the inclusion of a screening term in the potential has been proposed [15–17] The $V_S(r)$ term of Eq. (1.2) is replaced by $b\left(\frac{1-e^{-\mu r}}{\mu}\right)$, where μ is a screening factor. This allows to stop the linear growth of the confining term at r values where vacuum polarization effects become dominant. Results obtained with this method show a fairly good agreement with experimental results [17].

1.3.3 Non-Relativistic QCD

Despite the great success of the potential models in terms of accuracy of their predictions, they suffer some problems. First of all the connection with the underlying QCD theory is hidden, second the energy scale at which they are defined is not clear, and finally there is no systematic procedure to improve them. To address such problems an intense theoretical effort is being made to relate the potential models to the QCD principles.

The QCD lagrangian is

$$\mathcal{L}_{QCD} = \mathcal{L}_{light} + \overline{\Psi}(i\gamma^{\mu} D_{\mu} - m_c)\Psi, \tag{1.7}$$

where $\mathcal{L}_{light}$ describes gluons and light quarks, and the second term describes the charm quark.

In the non-relativistic limit $v \ll 1$, the QCD lagrangian can be simplified by integrating out the modes with a momentum larger than a certain cutoff Λ_{hard} that satisfies the condition $m_c v \ll \Lambda_{hard} \ll m_c$[1]. The resulting effective theory is named Non Relativistic QCD (NRQCD), since the charm quarks are considered as non-relativistic fields [19, 20]. If we take a virtual $c\bar{c}$ state with a quark with momentum of order m_c, such state is off-shell by $\mathcal{O}(m_c)$. The propagation length of such state is $\mathcal{O}(1/m_c)$ that is pointlike on the distance $\mathcal{O}(1/m_c v)$, where the dynamic of the $c\bar{c}$ state takes place. Thus, phenomena occurring at scale m_c or higher can be described by local operators in the effective lagrangian. The coefficients of such operators are calculated by matching the full QCD theory and the effective theory at scale m_c, where QCD becomes perturbative. The creation and annihilation of charm quarks is strongly suppressed by the fact that charm quark fields are separated from light quarks and gluons in the NRQCD lagrangian. However, the total annihilation rate of the charmonium states can be described accurately by using the optical theorem and adding appropriate local operators to the NRQCD lagrangian [18]. The NRQCD lagrangian is

$$\mathcal{L}_{NRQCD} = \mathcal{L}_{light} + \mathcal{L}_0 + \delta\mathcal{L}, \tag{1.8}$$

$\mathcal{L}_0$ is the leading order NRQCD contribution

$$\mathcal{L}_0 = \psi^{\dagger}\left(iD_0 + \frac{\mathbf{D}}{2m_c}\right)\psi + \chi^{\dagger}\left(iD_0 + \frac{\mathbf{D}}{2m_c}\right)\chi, \tag{1.9}$$

where ψ and χ are the Pauli spinor fields of the charm quark and antiquark, respectively.

---

[1] In principle to obtain the effective lagrangian, one can take Eq. (1.7) and perform the transformation needed to remove modes with momenta larger than Λ_{hard}. Actually, an effective field theory approach is commonly used. For details see Ref. [18].

D_0 and $\mathbf{D}$ are defined by $D^\mu = \partial^\mu + igA^{\mu a}T^a = (D_0, -\mathbf{D})$, and g, A and T are the usual coupling, gluon field, and color matrix of QCD. This term can reproduce the splittings between radial and orbital-angular-momentum excitations up to errors of relative order v^2 [18]. However, it is unable to reproduce spin-spin splittings due to the symmetry under the transformation $\psi \to U\psi$ and $\chi \to V\chi$, with U and V being $SU(2)$ matrices (*heavy quark spin symmetry*).

The $\delta\mathcal{L}$ term includes v^2 correction terms for $\mathcal{L}_0$ and is equal to

$$\begin{aligned}\delta\mathcal{L} = \quad & \frac{c_1}{8m_c^3}\psi^\dagger(\mathbf{D}^2)^2\psi + \frac{c_2}{8m_c^2}\psi^\dagger g(\mathbf{D}\cdot\mathbf{E} - \mathbf{E}\cdot\mathbf{D})\psi + \frac{c_3}{2m_c}\psi^\dagger g\sigma\cdot\mathbf{B}\psi \\ & + i\frac{c_4}{8m_c^2}\psi^\dagger g\sigma\cdot(\mathbf{D}\times\mathbf{E} - \mathbf{E}\times\mathbf{D})\psi + \text{charge conjugate,} \end{aligned} \tag{1.10}$$

where σ are the Pauli matrices. $\mathbf{E}$ and $\mathbf{B}$ are the chromoelectric and chromomagnetic fields, defined by $[D_0, D_i] = igE_i$ and $[D_i, D_j] = ig\varepsilon_{ijk}B_k$, with $i, j = 1, 2, 3$, and ε_{ijk} is the Levi-Civita tensor. The coefficients c_1, c_2, c_3, c_4 should be matched in order to insure that NRQCD correctly reproduces the QCD behavior at low energy. The presence of the Pauli matrices breaks the heavy quark spin symmetry and reproduces spin-spin splittings up to errors of relative order v^2 [18]. The radial and orbital-angular-momentum excitations are reproduced up to errors of relative order v^4 [18].

1.3.4 Potential Non-Relativistic QCD

A second effective field theory, named potential NRQCD (pNRQCD), is obtained by NRQCD by integrating out the $m_c v$ scale [21–23]. The integration of soft gluon in the $m_c v$ scale causes the appearance of potential terms in the lagrangian. Thus, pNRQCD offers a method to compute potentials by matching pNRQCD to NRQCD, and addresses the problem of linking potential models to the underlying theory. We should distinguish two situations: weakly coupled pNRQCD when $\Lambda_{QCD} \ll m_c v$ and strongly coupled pNRQCD when $\Lambda_{QCD} \sim m_c v$.

The weakly coupled case is of prominent interest for $b\bar{b}$ and $t\bar{t}$ physics, but the description of the $c\bar{c}$ spectrum in such a framework is not likely to hold, even for the $^1S_0$ and $^3S_1$ ground states $\eta_c(1S)$ and J/ψ [24].

In the strongly coupled scenario with $\Lambda_{QCD} \sim m_c v$, the $m_c v$ scale is non-perturbative and the matching between pNRQCD and NRQCD cannot rely on perturbation theory. The matching would require calculations on the lattice or in QCD vacuum models.

1.3.5 Lattice QCD

Recently, calculations of the charmonium properties using lattice NRQCD methods have been performed [20, 21, 25–33]. In this approach, the QCD phenomenology is studied on a discrete lattice with spacing a, thus providing a cut-off on the available momentum and curing the divergences. Calculations are performed for different values of the lattice spacing $a \ll \Lambda_{QCD}^{-1}$, and results are obtained by extrapolating the results for $a \to 0$. This approach is valid as far as no important physics effect takes place at a momentum scale $\approx a^{-1}$. Lattice QCD is a promising tool to investigate non-perturbative effects in the charmonium system and significant improvements of its results have been obtained recently [34].

1.4 Charmonium decay

In this section we briefly review the theory of electromagnetic (EM) and hadronic decays of charmonia. We do not suppose to give a detailed and updated status of the theoretical understanding of these aspects, but to point out some facts that are important to the interpretation of the experimental results. In particular, the properties of EM transitions where recently used to explain some inconsistencies in the $\eta_c(1S)$ width measurements [35], while the pattern of the hadronic decay width is useful to understand some basic and fundamental properties of the resonances studied in this thesis.

1.4.1 Hadronic transitions

Hadronic transitions play a prominent role in charmonium decays.

For states lying over the $D\overline{D}$ threshold, the decay is mediated by OZI-favored diagrams [36–38] (Fig. 1.2). Such states decay into $D^{(*)}\bar{D}^{(*)}$ final states with a decay width of tens of MeV. The decay into $D^{(*)}\bar{D}^{(*)}$ is expected to be dominant, unless some suppression rule is involved in the transition (such as for $\eta_{c2}(1D)$). In 2003, the Belle Collaboration reported the observation of a resonance, the $X(3872)$, at a mass higher than the $D\bar{D}^{*}$ threshold, but with a decay width of few MeV [39]. To date many states with unusual properties have been observed [40–48]. The interpretation of such states is still ambiguous (see sec. 2.4).

Below the $D\overline{D}$ threshold, hadronic decays of charmonium proceed via multi-gluon transitions (Fig. 1.3). In particular $\eta_c(1S)$, $\eta_c(2S)$, and $\chi_{cJ}(1P)$ states decay via double-gluon emission, while J/ψ decays via three-gluon transitions, since double-gluon is for-

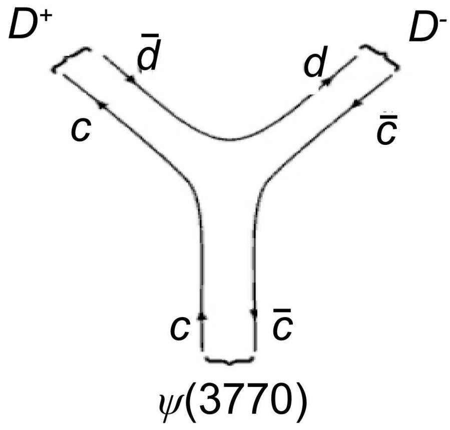

Figure 1.2: Feynman diagram of the OZI-allowed transition $\psi(3770)\to D^+D^-$.

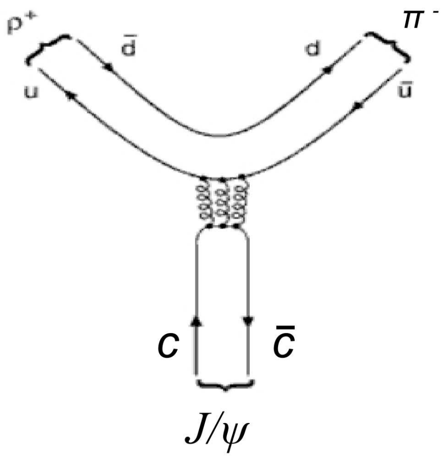

Figure 1.3: Feynman diagram of the OZI-forbidden transition $J/\psi\to\rho^+\pi^-$.

bidden due to C-parity conservation. Expressions for the multi-gluon decay width are [8]:

$$\begin{aligned}
\Gamma(^1S_o\to 2g) &= \frac{8\pi\alpha_S^2}{3m_c^2}|S_0(\Psi)|^2 && (1.11)\\
\Gamma(^1S_1\to 3g) &= \frac{40(\pi^2-9)\alpha_S^3}{81m_c^2}|S_0(\Psi)|^2 && (1.12)\\
\Gamma(^3P_2\to 2g) &= \frac{32\pi\alpha_S^2}{45m_c^2}|S_1(\Psi)|^2 && (1.13)\\
\Gamma(^3P_0\to 2g) &= \frac{8\pi\alpha_S^2}{3m_c^2}|S_1(\Psi)|^2, && (1.14)
\end{aligned}$$

where α_S is evaluated at the meson mass, and $S_L(\Psi)$ is given by

$$S_L(\Psi) \equiv \frac{1}{(2\pi)^{3/2}}\int d^3p\frac{1}{\sqrt{4\pi}}\Phi(p)\left[\frac{p}{E}\right]^L\frac{m}{E} \qquad (1.15)$$

with $\phi(\vec{p}) = \Phi(p)Y_{LM}(\theta_p,\phi_p)$ being the normalized Fourier transform of the wavefunction $\Psi(\vec{r})$. Corresponding numerical predictions are: $\Gamma(\eta_c(1S)) = 22$ MeV, $\Gamma(J/\psi) = 176$ keV , and $\Gamma(\eta_c(2S)) = 7.3$ MeV [8]. Even if such predictions are not fully consistent with currently measured values [49], the overall pattern describes the charmonium system with a rather good accuracy. The predicted J/ψ to $\eta_c(1S)$ decay width ratio is 0.008 to be compared with the experimental value 0.0029 ± 0.0002 [49], thus the qualitative behavior is good. Furthermore, the predicted $\eta_c(2S)$ to $\eta_c(1S)$ decay width ratio 0.33 is consistent with the experimental value 0.42 ± 0.18 obtained in this thesis. The large difference between the $\eta_c(1S)$ and $\eta_c(2S)$ width originates from the differences in the wavefunctions of such states that enter in Eq. (1.11). More recent derivations of the hadronic decay widths of charmonium states also including next-to-leading order (NLO) corrections, can be found in Refs. [50, 51].

1.4.2 Electromagnetic transitions

Electromagnetic transitions are sizable in the charmonium system below the threshold, due to the OZI-rule that suppresses strong decays. Typical branching fractions of radiative transitions are of 1-10%. In the potential model approach, the spatial dependence of the EM transition amplitudes reduces to functions of quark momentum and position between the initial and final state wave functions. Using multipole expansion, the main contributions to electromagnetic transitions are the electric dipole (E1) and electric monopole (M1) amplitudes. Higher multipole contributions such as magnetic quadrupole (M2) are not discussed here.

Magnetic dipole transitions

Magnetic dipole transitions flip the spin quark. For S-wave states, the wave function orthogonality ensures that the spatial overlap is one for states with the same radial quantum number and zero otherwise. Relativistic corrections introduce a small overlap between states not sharing the same radial quantum number, making the transition possible. The transition rates are [6, 7, 52, 53]:

$$\left\{ \begin{array}{l} \Gamma(n^3S_1 \to n'^1S_0 + \gamma) \\ \Gamma(n^1S_0 \to n'^3S_1 + \gamma) \end{array} \right\} = \frac{16}{27m_c^2}\alpha E_\gamma^3 (2J_f + 1)|\langle f|j_0(E_\gamma r/2)|i\rangle|^2 \tag{1.16}$$

where α is the electromagnetic coupling, E_γ is the photon energy, $f(i)$ indicates the final(initial) state, and $j_0(x) = \sin x/x$. If the photon energy is small, the matrix element $j_0(E_\gamma r/2) \approx 1$, thus transitions between states with the same radial quantum number, that are close in mass, are favored. The inclusion of fully relativistic correction to describe M1 transitions has been studied by several authors [8, 12, 54–58]. A calculation performed in pNRQCD approach [59] shows that the matrix element for the $(n+1)^3S_1 \to n^1S_0 + \gamma$ transition is proportional to E_γ^7, after including all the corrections.

Electric dipole transitions

Electric dipole transitions cannot change the quark spin, but do change the orbital angular momentum L. The partial widths of such transitions between two S-wave and P-wave states are [6, 7, 52, 53]:

$$\Gamma(n^{2S+1}L_{iJ_i}\rightarrow n'^{2S+1}L_{fJ_f}+\gamma)=\frac{16\alpha E_\gamma^3}{27}(2J_f+1)\mathcal{S}_{if}|\langle f|r|i\rangle|^2 \tag{1.17}$$

with $S_{ij}=1/9$. Expressions for transitions between P and D-wave states are given in Ref. [60]. There are many corrections to the leading behavior of these transitions accounting for relativistic modification of the wave functions and of the transition operator, and finite-size corrections. Details for the interested reader can be found in Ref. [1] and references therein.

1.5 Exotic charmonium

The spectrum of newly observed charmonium-like states is reported in Fig. 1.1. Exotic $c\bar{c}$ configurations, other than conventional ones, can be accommodated by the QCD interaction. In this section, we list such states and briefly discuss their characteristics. A more comprehensive review can be found in Ref. [2]. An illustrative picture of such states is shown in Fig. 1.4.

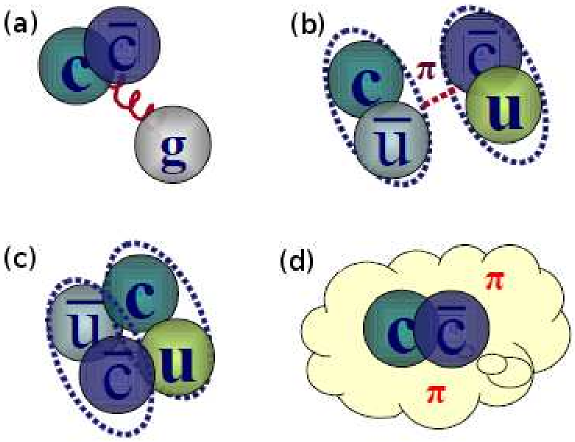

Figure 1.4: Illustrative picture of exotic quark configurations: (a) hybrid, (b) molecular state, (c) compact tetraquark, and (d) hadrocharmonium.

Hybrids

The presence of the gluon field in the QCD lagrangian allows for the existence of more states than $q\bar{q}$: glueballs and hybrids. Hybrids are conventional $c\bar{c}$ states, with excited gluonic degree of freedom [61–66]. Lattice calculations of the lightest hybrid mass lead to a value of about $4.4\ \mathrm{GeV}/c^2$ [2]. It has been shown [67–69] that the decay of a hybrid in open-charm channels is suppressed. This implies a small width for such states, even above the $D\overline{D}$ threshold.

Molecular states

A molecular state is constituted by a pair of $D^{(*)}$ meson bound by the exchange of soft pions [70–78]. The molecule is characterized by an extremely small binding energy $\mathcal{O}(100\ \mathrm{keV}\ )$. Such small binding energy implies that the $D^{(*)}$ mesons should be in S-wave state, since it is unlikely that pion exchange can bind P-wave states [79]. It was shown that the existence of a $D^{*0}\bar{D}^0$ molecule does not imply the existence of $D^{*0}\bar{D}^{*0}$ or $D^0\bar{D}^0$ states [80]. The molecular states can mix with ordinary $c\overline{c}$ states. Methods addressing the problem of determining the composition of such admixture have been proposed [81–86]. Molecular states can accommodate large isospin-violating effects [75].

Tetraquarks

Color-neutral configurations in the meson system can be achieved with quark combinations other than $q\bar{q}$. The existence of tightly bound four-quark (tetraquark) $[cq][\overline{cq}']$ states have been proposed [87–93]. The main feature, that may be a drawback of this picture, is the relevant number of predicted states [87, 94]. Furthermore the existence of states with non-zero net electric charge is predicted. Models with even more exotic five-quark (pentaquarks) [95, 96] and six-quarks (exaquarks) [97] configurations have been studied.

Hadrocharmonium

The hadrocharmonium picture [98–100] is motivated by the observation that some exotic $c\overline{c}$ states decay to a specific conventional $c\overline{c}$ resonance plus light mesons, but decays to other $c\overline{c}$ resonances or open charm appear to be suppressed [40–42, 45, 46, 101, 102]. The hadrocharmonium is constituted by a $c\overline{c}$ resonance embedded in a shell of light-quark and gluon matter. The de-excitation of the hadronic matter into light meson causes the decay. This picture implies that baryocharmonium states, decaying for example to $J/\psi\, p^+$, should also exist [99].

Artifacts

Some of the unconventional observed states have been questioned to be artifacts due to threshold or coupled channel effect [103–108]. Furthermore, many states are classified as exotics because their measured mass does not match theory predictions for yet-unobserved states. Some authors argue that prediction obtained by using potential models may be not completely reliable above the open charm threshold [109], or that coupling effects may shift the actual mass of the resonances [110–114].

Chapter 2

Experimental status of charmonium spectroscopy

2.1 Introduction

In this chapter we give an overview of the status of charmonium spectroscopy. In sec. 2.2 we review experimental techniques used to study charmonium at B-factories. We outline both the advantages and drawbacks of each technique on both the experimental and theoretical grounds. In sec. 2.3 we discuss the status of the conventional charmonium spectroscopy, giving a particular emphasis to the states studied in this analysis. In sec. 2.4 we report recent results on new charmonium-like states observed above the $D\overline{D}$ threshold. We discuss the experimental status of the measurement of their properties and theoretical interpretations on their nature. A comprehensive review of the status of charmonium spectroscopy can be found in Ref. [2].

2.2 Experimental techniques at B-factories

The charmonium states can be created via several production mechanism at e^+e^- colliders. We briefly review the experimental techniques used to study charmonium resonances by exploiting the characteristic of each production mechanism.

2.2.1 B decays

Charmonium is produced via Cabibbo-favored $B{\rightarrow}c\overline{c}X$ decays (Fig. 2.1(a)). Usually $B{\rightarrow}XK^{(*)}$ decays are used in experimental searches, where X can be both an exclusive or inclusive final state. The dominant contributions to this process come from the decay of the b quark into a color-singlet $c\overline{c}$ state plus a s quark. In the factorization approach [115,

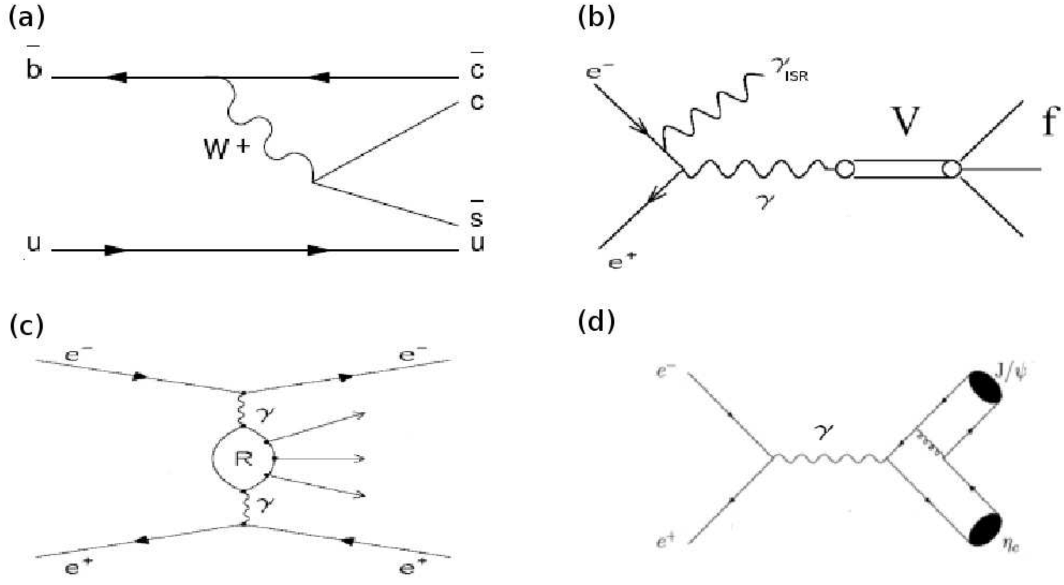

Figure 2.1: Representative Feynman diagrams for charmonium production modes at B-factories: (a) B-meson decay, (b) Initial State Radiation (ISR), (c) two-photon fusion, and (d) double charmonium.

116], the effective lagrangian describing this process is [117] $[\bar{c}\gamma^\mu(1-\gamma_5)c][\bar{b}\gamma^\mu(1-\gamma_5)s]$. This current can describe the production of J/ψ, $\eta_c(1S)$, $\chi_{c1}(1P)$, and $\psi(2S)$. On the contrary, decays involving $\chi_{c0}(1P)$, $\chi_{c2}(1P)$, and $h_c(1P)$ are not allowed at leading order in α_S, since a $V-A$ current cannot produce $J^{PC}=0^{++},1^{+-}$, or 2^{++} [117, 118]. Such P-wave states can be produced by the decay of the b quark into a color-octet S-wave $c\bar{c}$ state that radiates a soft gluon and forms a color-singlet P-wave state [119, 120]. Such process is described by $[\bar{c}(\lambda_a/2)\gamma^\mu(1-\gamma_5)c][\bar{b}(\lambda_a/2)\gamma^\mu(1-\gamma_5)s]$, where λ_a are color SU(3) matrices. The effect of long-distance interactions that mix the $c\bar{c}K$ final state with channels like $D^{(*)}D_s^{(*)}$ may also be sizable [121,122]. The decay $B\to\chi_{c0}(1P)K$ has been observed with an unexpected large branching fraction [49]. The non-observation of the $B\to\chi_{c2}(1P)K$ decay [49] seems to indicate that the color-octet mechanism is suppressed with respect to the color-singlet one.

At the B-factory experiments *BABAR* and Belle, the B mesons are produced via the decay of the $\Upsilon(4S)$ resonance, produced in e^+e^- interaction, into a pair of $B\overline{B}$ mesons. Events containing a pair of $B\overline{B}$ mesons can be discriminated against continuum $q\bar{q}$ ($q = u,\ d,\ s,\ c$) background by means of event-shape variables, since $B\overline{B}$ events are more spherical with respect to back-to-back jet-like $q\bar{q}$ events (Fig. 2.2). Well-reconstructed B mesons can be identified by means of kinematic variables that exploit the closed kinematic information, such as $\Delta E \equiv E_B - \frac{1}{2}\sqrt{s}$ and $m_{\rm ES} \equiv \sqrt{s/4 - |\vec{p}_B|^2}$, where $(E_B, \vec{p}_B)$ is the B four-momentum vector expressed in the $\Upsilon(4S)$ rest frame. The ΔE distribution shows

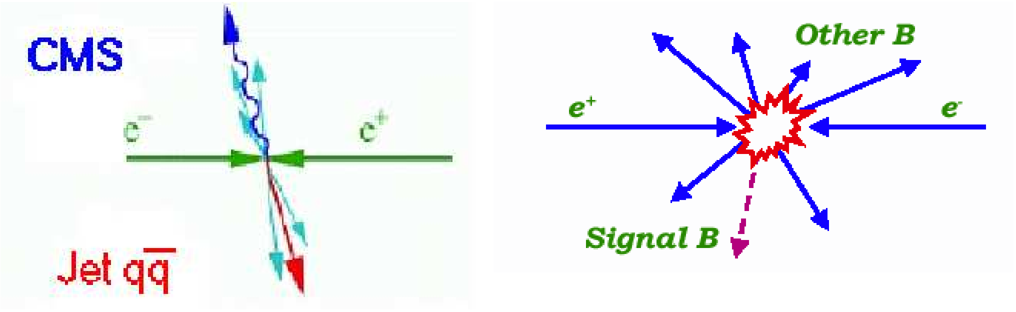

Figure 2.2: Schematic topological representations of (left) $e^+e^-\to q\bar{q}$ and (right) $e^+e^-\to\Upsilon(4S)\to B\overline{B}$ events.

a peak at $\sim$ 0 MeV for well-reconstructed signal events, while for $q\bar{q}$ background a smooth shape is expected (Fig. 2.3(a)). The $m_{\rm ES}$ distribution is peaked at $m_{\rm ES} \sim \mathrm{m}_B$ for signal events, while it is described by an ARGUS function [123] for combinatorial $q\bar{q}$ background (Fig. 2.3(b)). The relevant background-subtracted X invariant mass m_X is

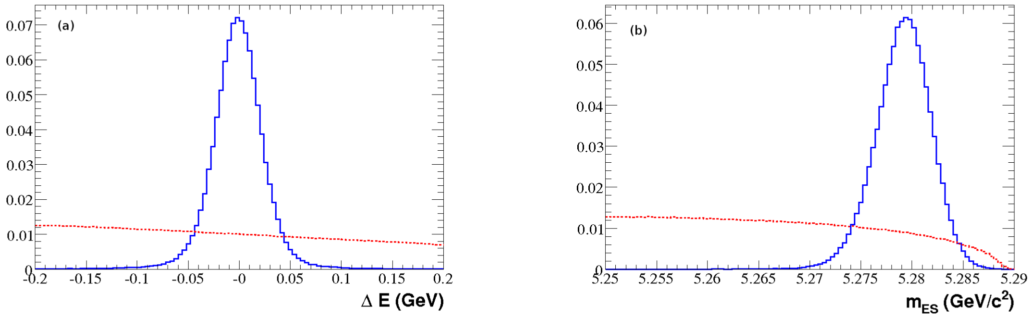

Figure 2.3: Distributions of (a) ΔE and (b) $m_{\rm ES}$ for well-reconstructed signal B events (solid blue line) and combinatorial background (red dotted line).

usually obtained by fitting the $m_{\rm ES}$ (or ΔE) distribution in intervals of m_X.

2.2.2 Initial State Radiation (ISR)

Charmonium states with $J^{PC} = 1^{--}$ can directly couple to virtual photons originating from e^+e^- collisions. In charm-factories, such as BESIII [124] and CLEO-c [125], the e^+e^- center-of-mass (CM) energy corresponds to J/ψ or $\psi(nS)$ mass, in order to maximize the production of such resonances. The B-factories experiments *BABAR* and Belle, are located at the PEP-II and KEKB accelerators that are mainly operated at the $\Upsilon(4S)$ energy. Charmonium states with $J^{PC} = 1^{--}$ can be produced by e^+e^- annihilation after

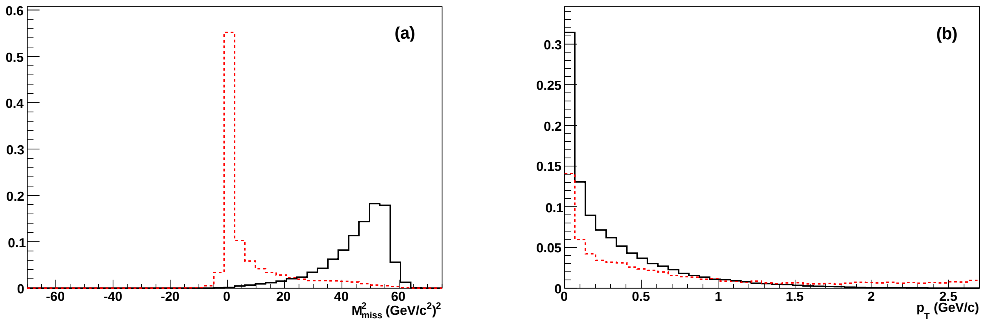

Figure 2.4: Distributions of (a) M^2_{miss} and (b) p_T for simulated $\gamma\gamma \to K^+K^-\pi^+\pi^-\pi^0$ (solid black) and $e^+e^- \to \gamma_{ISR}K^+K^-\pi^+\pi^-\pi^0$ (red dashed) events.

one of the incoming electrons[1] radiates an energetic (initial state) photon, thus lowering the CM energy to the $c\bar{c}$ resonance mass (Fig. 2.1(b)).

The kinematics of the $e^+e^- \to \gamma_{ISR} f$ process, with f being an exclusive final state, is closed. Thus we expect that the squared missing mass $M^2_{\mathrm{miss}} \equiv (p_{beams} - p_{reco})^2$ is $\sim 0\ (\mathrm{GeV}/c^2)^2$ for well-reconstructed events, where p_{beams} and p_{reco} are the four-momenta of the beams and reconstructed final state, respectively. Since the cross-section for radiating the ISR photon has a maximum in the forward direction [126], the transverse momentum p_T of the final state products with respect to the beam axis is expected to be small. Usually, the ISR photon detection is not required in order to increase the reconstruction efficiency. The M^2_{miss} and p_T shapes for simulated ISR events are shown in Fig. 2.4. The presence of a small number of tracks in the event is a further advantage of this production mechanism, since it provides a clean environment and allows for the rejection of high-multiplicity background from $e^+e^- \to q\bar{q}$ $(q = u,\, d,\, s,\, c)$ and $B\overline{B}$ events.

2.2.3 Two-photon fusion

Charmonium resonances can be produced via the interaction of two virtual photons emitted by the incoming electrons (Fig. 2.1(c)). The scattering angle of the outgoing electrons is related to the momentum transfer $q^2 = (p'_e - p_e)^2$, where p'_e and p_e are the momenta of the electron in the final and initial state, respectively. Events resulting by two-photon collisions are usually classified into three categories:

- *no-tag* events, where both the outgoing electrons are scattered at small angle along the beam pipe and thus escape detection;

---

[1] Here and in the following, we use the word “*electron*” to refer to both e^+ or e^-, unless otherwise specified.

- *single-tag* events, where one of the outgoing electrons is scattered at large angle and might be detected;

- *double-tag* events, where both the outgoing electrons are scattered at large angle and might be detected.

In *single-tag* events the scattering angle of the detected electron is related to the momentum transfer q^2. Thus such kind of events are useful in order to measure the cross-section dependence on q^2, allowing for the extraction of the resonance form factor [127].

In *no-tag* events the momentum transfer $q^2 \sim 0\ (\mathrm{GeV}/c)^2$, so the interacting photons are quasi-real. This implies a selection rule on the allowed quantum numbers of the produced resonance [128]: $J^P = 0^{\pm}, 2^{\pm}, 3^{+}, 4^{\pm}, \ldots$. Values of $J > 2$ are usually suppressed by phase-space availability. Furthermore the coupling of the resonance to the two-photon initial state implies $C = +1$. Hybrids and glueballs are expected to have small coupling to the two-photon initial state and it is not likely that they can be produced by this mechanism. There are two characteristic signatures for *no-tag* events. First, the low momentum transfer $q^2 \sim 0$ implies that the two quasi-real photons collide head-on, so $p_T \sim 0\ \mathrm{GeV}/c$. Second, since the outgoing electrons are scattered at small angle, they are not detected and are lost in the beampipe, carrying away a large portion of the beam energy, thus resulting in a large value for M^2_{miss} in the event. The M^2_{miss} and p_T shapes for simulated two-photon *no tag* events are shown in Fig. 2.4.

2.2.4 Double charmonium production

The production of a $c\overline{c}$ resonance recoiling against a J/ψ in the processes $e^+e^- \to J/\psi\,(c\overline{c})$ was first observed at B-factories [129, 130] (Fig. 2.1(d)). The measured $e^+e^- \to J/\psi\, c\overline{c}$ cross-section was surprising larger, by about one order of magnitude, than available NRQCD expectations at leading order [131–138]. Relativistic corrections [139–141] and NLO perturbative effects [142–144] are shown to enhance the production cross-section. Taking both these effects into account, theoretical predictions can be reconciled with experimental results. So far only $J = 0$ resonances have been observed in this production mechanism. Speculations aimed at explaining the χ_{c1} and χ_{c2} suppression have been proposed [145].

Background from quantum-elctrodynamics (QED), two-photon and $\tau^+\tau^-$ processes are rejected by requiring a minimum number of tracks in the event. The J/ψ is reconstructed in its clean leptonic e^+e^- and $\mu^+\mu^-$ decay modes. The mass recoiling against it is obtained as $M^2_{\mathrm{recoil}} = [(\sqrt{s} - E^*_{J/\psi})^2 - p^{*2}_{J/\psi}]^2$, where $\sqrt{s}$ is the CM energy, and $(E^*_{J/\psi}, \vec{p}^{\,*}_{J/\psi})$ is the J/ψ four-momentum vector expressed in the CM rest frame.

2.3 Conventional charmonium

In this section we review the status of conventional charmonium spectroscopy below the $D\overline{D}$ threshold, with a particular attention for the $\eta_c(1S)$ and $\eta_c(2S)$ resonances.

2.3.1 $\eta_c(1S)$

The charmonium ground state $\eta_c(1S)$ was observed in 1980 by Mark-II experiment in the $\psi(2S)\to\gamma\eta_c(1S)$ decay [146]. To date the $\eta_c(1S)$ has been observed in several production mechanism, including J/ψ and $\psi(2S)$ decays, two-photon fusion, $p\overline{p}$ collision, double charmonium production, and B-decays [49].

Measurements of the $\eta_c(1S)$ mass and width taken from Ref. [49] are reported in Fig. 2.5. With several available measurements, a large spread is observed.

In the width measurements a quite peculiar pattern seems to emerge: experiments that produce the $\eta_c(1S)$ via J/ψ and $\psi(2S)$ radiative decays tend to report a value of the width of about 15 MeV, while measurements performed by using other production mechanisms report values centered at about 30 MeV. The $\eta_c(1S)$ production in J/ψ and $\psi(2S)$ radiative decay has been investigated by several experiments [146–154], by studying both the inclusive photon spectrum, or reconstructing exclusive final states. A recent paper by CLEO [154] has pointed out that the use of a simple Breit-Wigner shape gives a poor description of the $\eta_c(1S)$ peak in the photon energy spectrum from the $J/\psi\to\eta_c(1S)$ decay. The observed spectrum should actually take into account that the M1 transition matrix element is not uniform as a function of the photon energy (sec. 1.4.2). Taking into account a factor E_γ^3 in the fit improves the data description, but gives unsatisfactory results on the high-energy tail. The introduction of a damping factor $exp(-E_\gamma^2/\beta^2)$, where β is a fit parameter, inspired by the overlap of two ground-state function, gives a good agreement with data. A similar approach is used to fit the $\psi(2S)\to\gamma\eta_c(1S)$ transition, where a factor E_γ^7 [59] is taken into account. The fitted $\eta_c(1S)$ width is (31.5 ± 1.5) MeV, which is consistent with results obtained in other production processes. The BESIII collaboration presented a preliminary measurement of the $\eta_c(1S)$ parameters in the $\psi(2S)\to\gamma\eta_c(1S)$ decay, with $\eta_c(1S)$ reconstructed in several exclusive hadronic decays [155]. In order to obtain a good description of the mass spectrum, both the energy dependence of the transition amplitude and the interference effects with non-resonant background are taken into account. The measured $\eta_c(1S)$ mass and width are $(2984.4\pm0.5(stat)\pm0.6(syst))\ \mathrm{MeV}/c^2$ and $(30.5\pm1.0(stat)\pm0.9(syst))\ \mathrm{MeV}$. The KEDR collaboration uses a similar analysis technique [156] with a modified dumping factor and obtains results consistent with the BESIII ones, but with a larger uncertainty. In the light of these new results, it is likely that neglecting the energy dependence of the M1 transition may have biased previous $\eta_c(1S)$

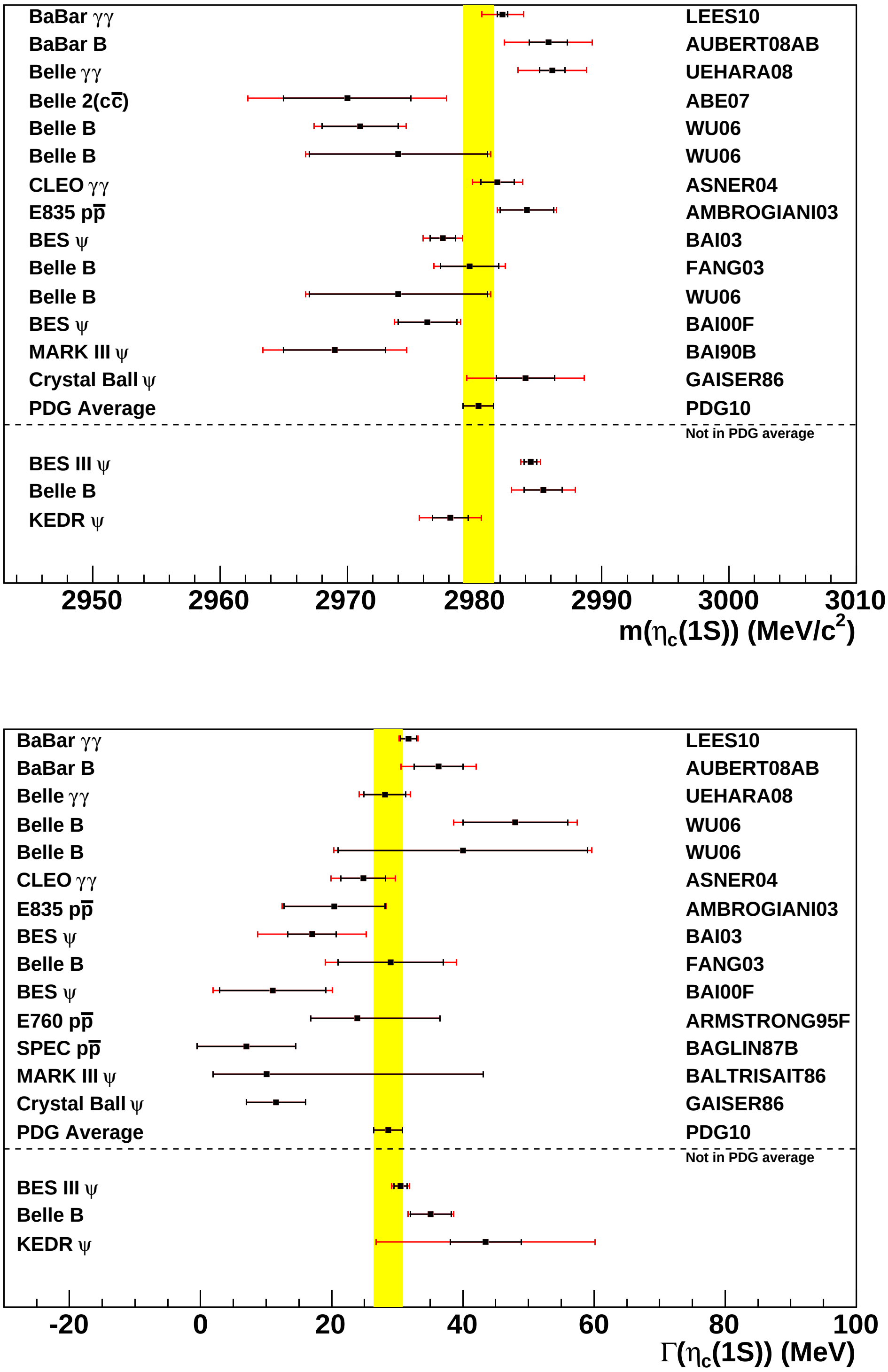

Figure 2.5: Measured values of the $\eta_c(1S)$ mass and width used to obtain world-average values [49]. The squares are the measured values with black bars for statistic uncertainty and red bars for the sum in quadrature of statistic and systematic uncertainties. If the red bars are missing, the black bars are the sum in quadrature of the statistical and systematic errors. For each measure we report the experiment that performed it and the production mechanism exploited: two-photon fusion ($\gamma\gamma$), B-meson decay (B), double charmonium ($2(c\bar{c})$), J/ψ or $\psi(2S)$ radiative decay (ψ), and $p\bar{p}$ annihilation ($p\bar{p}$). Below the dashed line we report new measurements not included in the world average. The yellow box is the $\pm 1\sigma$ region with respect to world-average values. The last column reports the PDG [49] reference to the paper where the measure is reported.

parameters measurement in the J/ψ and $\psi(2S)$ radiative decays.

The $\eta_c(1S)$ is studied also in B-meson decays and two-photon fusion. The most accurate results from these production modes are obtained by Belle [157] and *BABAR* [158], respectively. The Belle analysis reconstructs the $B^{\pm}\to K_S^0 K^{\pm}\pi^{\mp}K^{\pm}$ decay mode and measures the $\eta_c(1S)$ parameters by a two-dimensional fit to the the $K_S^0 K^{\pm}\pi^{\mp}$ mass distribution and the K_S^0 helicity angle. This angle is defined as the angle between the K_S^0 and the B-meson recoil direction, in the $K_S^0 K^{\pm}\pi^{\mp}$ rest frame. Interference between the $\eta_c(1S)$ signal and non-resonant background contribution is taken into account. The effect of such interference is to produce a mass shift of $+0.6\ \mathrm{MeV}/c^2$ in the measured $\eta_c(1S)$ mass value. The change in the value of the $\eta_c(1S)$ width is $+0.3\ \mathrm{MeV}$. Taking into account interference effects, the measured $\eta_c(1S)$ mass and width are $(2985.4 \pm 1.5(stat)^{+0.5}_{-2.0}(syst))\ \mathrm{MeV}/c^2$ and $(35.1 \pm 3.1(stat)^{+1.0}_{-1.6}(syst))\ \mathrm{MeV}$ [157]. The *BABAR* analysis studies the $\gamma\gamma\to K_S^0 K^{\pm}\pi^{\mp}$ process in *no-tag* mode and measure the $\eta_c(1S)$ parameters [158]. The $\eta_c(1S)$ mass is obtained by measuring the $J/\psi - \eta_c(1S)$ mass difference and using the nominal J/ψ mass [49]. The measured $\eta_c(1S)$ mass and width are $(2982.2 \pm 0.4(stat) \pm 1.6(syst))\ \mathrm{MeV}/c^2$ and $(31.7 \pm 1.2(stat) \pm 0.8(syst))\ \mathrm{MeV}$. The inclusion of the interference with non-resonant background causes a change of up to. $1.5\ \mathrm{MeV}/c^2$ in the mass value and is taken into account in the systematic uncertainty. The $\eta_c(1S)$ study in two-photon production is also reported in a preliminary, unpublished result by Belle [159]. In this analysis, the inclusion of the interference of the signal with non-resonant background in the fit leads to a shift of $+2.2\ \mathrm{MeV}/c^2$ for the mass and $+0.6\ \mathrm{MeV}$ for the width value.

The $\eta_c(1S)$ is also observed by Belle in double charmonium production in the inclusive mass spectrum recoiling against a J/ψ [129, 160]. The fitted value of the $\eta_c(1S)$ mass is $2970 \pm 5(stat) \pm 7(syst)$ [160]. The measured mass of all the charmonium states observed are shifted of about $10\ \mathrm{MeV}/c^2$ towards lower values. The origin of this shift is identified in the mismodeling of high-energy tails of the resonances. The magnitude of this effect is estimated by MC simulation and is equal to $6\ \mathrm{MeV}/c^2$, that is taken as systematic uncertainty The $\eta_c(1S)$ is observed in double charmonium production also by *BABAR* [130].

2.3.2 The vector J/ψ and $\psi(2S)$ states

The J/ψ and $\psi(2S)$ states have $J^{PC} = 1^{--}$ and have thus been studied via $e^+e^-\to\gamma^*\to J/\psi\,(\psi(2S))$ since the J/ψ discovery [3, 4, 161]. The parameters of such states are known with a great precision and many decay modes have been observed [49].

The study of the M1 transition from J/ψ and $\psi(2S)$ to $\eta_c(1S)$ and $\eta_c(2S)$ provides important check of the ability of the theory to describe the charmonium system. The most precise determinations of radiative decay rates to $\eta_c(1S)$ are provided by CLEO [35]

$$\begin{aligned}\mathcal{B}(J/\psi\to\gamma\eta_c(1S)) &= (1.98\pm 0.09(stat)\pm 0.30(syst))\% &(2.1)\\ \mathcal{B}(\psi(2S)\to\gamma\eta_c(2S)) &= (0.432\pm 0.016(stat)\pm 0.060(syst))\% &(2.2)\end{aligned}$$

A prediction of the $\mathcal{B}(J/\psi\to\gamma\eta_c(1S))$ from potential models [1] gives $(3.05\pm 0.07)\%$, which is larger than the experimental value. A calculation performed in pNRQCD approach [59] gives $(1.6\pm 1.1)\%$, where the uncertainty comes from expected contributions from higher-order corrections. The transition $\psi(2S)\to\gamma\eta_c(2S)$ has been recently observed by BESIII [155] with a branching fraction of $(4.7\pm 0.9(stat)\pm 3.0(syst))\times 10^{-4}$. The measured value is in a good agreement with the phenomenological estimate $(3.9\pm 1.1.)\times 10^{-4}$ [162] obtained by assuming that the matrix element is the same for the $J/\psi\to\gamma\eta_c(1S)$ transition and accounting for the ratio of the J/ψ and $\psi(2S)$ widths and changes in the available phase space.

Hadronic decays of the J/ψ and $\psi(2S)$ are not completely understood yet, a long-standing problem known as "*$\rho\pi$ puzzle*". Perturbative QCD predicts that the decay rate of $\psi(2S)$ and J/ψ into a given hadronic final state or into a lepton pair should be proportional to the square of the wave functions at the origin [163, 164], the so-called "*12% rule*"

$$Q_h=\frac{\mathcal{B}(\psi(2S)\to hadrons)}{\mathcal{B}(J/\psi\to hadrons)}=\frac{\mathcal{B}(\psi(2S)\to e^+e^-)}{\mathcal{B}(J/\psi\to e^+e^-)}\approx 12\% \qquad (2.3)$$

A large violation of this rule was observed in the $\rho\pi$ and $K^{*+}K^-$ decays by Mark-II [165]. Many hadronic decay modes that violate the *12% rule* have been measured to date, for both J/ψ and $\psi(2S)$. The study of the decay to $\rho\pi$ is sensible to the procedure used to extract the $\rho\pi$ contribution from the $\pi^-\pi^+\pi^0$ final state. For the $\psi(2S)\to\rho\pi$ decay, results from CLEO [166] and BESII [167] are based on a mass cut and a partial wave analysis, respectively, and disagree at 2σ level. Using a weighted average of the two results, the world-average value for $\mathcal{B}(J/\psi\to\rho\pi)$ [49], and information given in Ref. [168], one obtains $Q_{\rho\pi}=(0.13\pm 0.05)\%$ which is suppressed by two order of magnitude with respect to the 12% expectation. The values of Q_h for decays into pseudoscalar-vector and vector-tensor final states are generally suppressed with respect to the expectation, while transitions to pseudoscalar-pseudoscalar final states appear to be enhanced. Decays to multihadron and baryonic final states do not exhibit a clear pattern. Although models that explain discrepancies into specific decay modes are available, no model can accomodate the *12% rule* violation into a general picture [2].

2.3.3 The $\chi_{cJ}(1P)$ triplet

The $\chi_{cJ}(1P)$ P-wave states are well known on the experimental ground, with their parameters measured with a good precision and many decay modes observed or searched for [49]. These states have been considered as an ideal laboratory to test charmonium models predictions on radiative and hadronic transistions.

The matrix element $|\langle 1P|r|2S\rangle|$ for the E1 transition of Eq. (1.17) can be extracted from the angular distributions of the $\psi(2S)\to\gamma\chi_{cJ}(1P)$ decays. They are equal to (2.51 ± 0.10) GeV^{-1}, (2.05 ± 0.08) GeV^{-1}, and (1.90 ± 0.06) GeV^{-1} [1], for $\chi_{c0}(1P)$, $\chi_{c1}(1P)$, and $\chi_{c2}(1P)$, respectively. Such values are in rather bad agreement with simple predictions from non-relativistic potential models, that are independent on the J value and range from 2.4 to 2.7 GeV^{-1} [5–7, 52, 53, 169, 170]. The inclusion of relativistic corrections [8, 12, 55, 58, 171, 172] allows to describe the observed $|\langle\chi_{c2}(1P)|r|\psi(2S)\rangle| > |\langle\chi_{c1}(1P)|r|\psi(2S)\rangle| > |\langle\chi_{c0}(1P)|r|\psi(2S)\rangle|$ pattern, even if the numerical agreement with experimental results is still unsatisfactory. Similarly the matrix element $|\langle 1S|r|1P\rangle|$ can be extracted form $\chi_{cJ}(1P)\to\gamma J/\psi$ measurements [1]. The predictions for such quantities from non-relativistic potential models [5–7,52,53,169,170] have a surprising better agreement with data than those obtained by including relativistic corrections [8,12,55,58, 171,172].

Simple calculations of the $\chi_{cJ}(1P)$ decay rates into hadronic final states taking into account only the color-singlet $c\bar{c}\to hadrons(\gamma\gamma)$ contributions give a poor agreement with experimental results [173–175]. The inclusion of color-octet $c\bar{c}g\to hadrons(\gamma\gamma)$ contributions in the calculation improves the agreement with experimental data [176,177]. The ratio between the two-photon decay width for $\chi_{c0}(1P)$ and $\chi_{c2}(1P)$[2] has been calculated in the color-singlet model [50,178]

$$R_{\gamma\gamma} \equiv \frac{\Gamma(\chi_{c2}(1P)\to\gamma\gamma)}{\Gamma(\chi_{c0}(1P)\to\gamma\gamma)} = \frac{4}{15}\cdot\frac{1-1.70\alpha_s}{1+0.06\alpha_s} = 0.128, \qquad (2.4)$$

where we used $\alpha_s(m_c^2) = 0.3$. The value obtained from experimental results is $R_{\gamma\gamma} = 0.22\pm 0.03$ [2], thus resulting in a poor agreement with theoretical expectations. Possible color-octet contributions may improve the theoretical expectations [179]. Recent calculations based on NRQCD approach give a value of $R_{\gamma\gamma}$ equal to 0.27 and 0.18 at LO and NLO, respectively.

Another peculiarity of the $\chi_{cJ}(1P)$ system was pointed out by a recent measurement of $\chi_{cJ}(1P)\to VV$ decays by BESIII [180], where V is ϕ or ω. Decays of $\chi_{c0}(1P)$ and $\chi_{c2}(1P)$ into these final states were previously measured at the 10^{-3} level [181, 182], well above predictions based on perturbative QCD [183]. The measured branching ratios

---

[2] $\chi_{c1}(1P)$ cannot couple to two-photon state, since $J^{PC} = 1^{++}$ [128].

for $\chi_{c1}{\to}VV$ final states are $(4.4 \pm 0.3(stat) \pm 0.5(syst)) \times 10^{-4}$, $(6.0 \pm 0.3(stat) \pm 0.7(syst)) \times 10^{-4}$, and $(0.22 \pm 0.06(stat) \pm 0.02(syst)) \times 10^{-4}$, for $\phi\phi$, $\omega\omega$, and $\phi\omega$, respectively. The decay $\chi_{c1}(1P){\to}VV$ is expected to be suppressed by the helicity selection rule [184]. The $\chi_c{\to}\phi\omega$ has a further suppression due to the OZI-rule. Mechanisms that allow to evade the helicity suppression rules via long-distance interaction have been proposed [185, 186], resulting in branching fractions of $\mathcal{O}(10^{-4})$. However, the expected branching fraction of the OZI-suppressed $\chi_{c1}(1P){\to}\phi\omega$ decay is more than an order of magnitude smaller than the experimental value. This points to the necessity of a deeper theoretical investigations of mechanisms allowing for the evasion of the OZI rule in $\chi_{c1}(1P)$ decays.

2.3.4 The $h_c(1P)$ singlet

Together with the $\eta_c(2S)$, the $h_c(1P)$ has been one of the most elusive particles of the charmonium spectrum. Its existence was predicted at the very beginning of the potential models, but it was actually observed only in 2005 by CLEO [187]. The $h_c(1P)$ state is of a particular relevance to test the charmonium model, since the hyperfine splittings for P-wave states is expected to be of few MeV/c^2, since the Coulomb-like potential contribution is proportional to $\delta^3(\vec{r})$ [1]. This naive expectation is confirmed by potential calculation including relativistic corrections [12], and lattice calculations [29, 188]. Thus one expect the $h_c(1P)$ mass to be about equal to the center of gravity of the $\chi_{cJ}(1P)$ triplet $\langle m(^3P_J)\rangle = (m(\chi_{c0}(1P)) + 3m(\chi_{c1}(1P)) + 5m(\chi_{c2}(1P)))/9 = (3525.30 \pm 0.07)\ \mathrm{MeV}/c^2$ [2].

The most precise measurement of the $h_c(1P)$ mass comes form CLEO [189] and BESIII [190], that study the $\psi(2S){\to}\pi^0 h_c(1P){\to}\pi^0\gamma\eta_c(1S)$ transition, and from E835 [191] that reports a 3σ evidence in the $p\overline{p}{\to}h_c(1P){\to}\gamma\eta_c(1S){\to}\gamma\gamma\gamma$ process. CLEO has also studied the angular distribution of the photon from the $h_c(1P){\to}\gamma\eta_c(1S)$ decay [189] that is consistent with a pure E1 transition. A preliminary result from BESIII [155] obtained by studying the $\psi(2S){\to}\pi^0 h_c(1P){\to}\pi^0\gamma\eta_c(1S)$ transition with the $\eta_c(1S)$ exclusively reconstructed in several exclusive final states, reports a measured value of the $h_c(1P)$ mass that agrees at 1σ level with that obtained by studying $\eta_c(1S)$ decay to an inclusive final state [190]. The $h_c(1P)$ is also observed by CLEO in $e^+e^-{\to}\pi^+\pi^- h_c(1P)$ process [192], but the measurement of the mass has a large ($\sim 2\ \mathrm{MeV}/c^2$) systematic uncertainty related to the determination of the beam energy.

The weighted average of the measurements reported in Refs. [189–191] gives $m(h_c(1P)) = (3525.45 \pm 0.15)\ \mathrm{MeV}/c^2$, where we sum the statistical and systematic uncertainties in quadrature. The hyperfine splitting is $(-0.15 \pm 0.17)\ \mathrm{MeV}/c^2$, compatible with 0 in agreement with predictions. However, the same potential model calculation used to determine $\langle m(^3P_J)\rangle$ predicts [2]

$$\frac{m(\chi_{c1}(1P)) - m(\chi_{c0}(1P))}{m(\chi_{c2}(1P)) - m(\chi_{c1}(1P))} = \frac{5}{2}, \tag{2.5}$$

while the experimental value is 20% smaller [49].

2.3.5 $\eta_c(2S)$

The first radial excitation $\eta_c(2S)$ of the charmonium ground state $\eta_c(1S)$ is predicted to lie below the $D\bar{D}$ threshold in the heavy quark potential model [7–14]. Calculations within this model predict a mass splitting $m_{\psi(2S)} - m_{\eta_c(2S)}$ in the range $[42, 103]$ MeV/c^2.

The $\eta_c(2S)$ escaped the detection for more than 20 years and its decay modes are almost unknown. The Crystal Ball experiment reported in 1982 an evidence of a signal attributed to the $\eta_c(2S)$ in $\psi(2S)$ radiative decay, with a mass of $(3594 \pm 5)\mathrm{MeV}/c^2$ [193], well below theoretical expectations. This claim remained unconfirmed and unrefuted for about 20 years until the observation of the $\eta_c(2S)$ at B Factories. The $\eta_c(2S)$ was first observed by Belle in the $B{\to}K^0_S K^\pm \pi^\mp K$ process [194] and confirmed by a subsequent analysis by *BABAR* by using $B^{+(0)}$ decays to $K\bar{K}\pi K^{+(*0)}$ final states [195]. In the *BABAR* analysis, the $K\bar{K}\pi$ system is reconstructed into $K^0_S K^\pm\pi^\mp$ and $K^+K^-\pi^0$ final states, but separate contributions from the different decay modes are not reported in the results. Belle recently has performed an update of the analysis [157] using a dataset about ten times larger than that used in the previous analysis [194]. The analysis technique is similar to that used to study the $\eta_c(1S)$ resonance, described in sec. 2.3.1. Including the effect of the interference between the $\eta_c(2S)$ and non-resonant background has a dramatic impact on the measured $\eta_c(2S)$ parameters. The mass value is $(3646.5 \pm 3.7(stat)^{+1.2}_{-2.9}(syst))$ MeV/c^2 in the fit without the interference, and $(3636.1^{+3.9}_{-4.2}(stat + model)^{+0.7}_{-2.0}(syst))$ MeV/c^2 when taking the effect into account. Similarly the width value is $(41.1 \pm 12.0(stat)^{+6.4}_{-10.9}(syst))$ MeV and $(6.6^{+8.4}_{-5.1}(stat + model)^{+2.6}_{-0.9}(syst))$ MeV when not considering or including the interference effect in the fit [157].

The $\eta_c(2S)$ decay into the $K^0_S K^\pm\pi^\mp$ final state is also studied by CLEO [196], and *BABAR* [197] in two-photon production process. A preliminary, unpublished result by Belle [159] is also available. The p_T shape of events is consistent with those expected in two-photon production. In Ref. [197] an analysis of the angular distribution of the decay products in the $\eta_c(2S)$ signal region has been performed. The results of the analysis have confirmed the consistency with the two-photon production mechanism and the inconsistency with ISR one. The preliminary Belle analysis [159] reports values of the $\eta_c(2S)$ parameters in good agreement with values reported by other experiments. A study of the effect of the interference of the $\eta_c(2S)$ with non-resonant background on the value of

$\eta_c(2S)$ parameters is performed. The change in the fitted mass and width value when including interference effect is $1.1\ \mathrm{MeV}/c^2$ and $4\ \mathrm{MeV}$, respectively. Recently, BESIII observed the $\eta_c(2S)$ decay into $K_S^0 K^{\pm}\pi^{\mp}$, with the $\eta_c(2S)$ produced in the $\psi(2S)\to\eta_c(2S)$ decay [155].

Hadronic decays branching fractions for $\eta_c(2S)$ are expected to be similar to those of $\eta_c(1S)$ [198]. However, the measured $\mathcal{B}(\eta_c(2S)\to K\bar{K}\pi) = (1.9 \pm 1.2)\%$ [195] is significantly smaller than the corresponding $\mathcal{B}(\eta_c(1S)\to K\bar{K}\pi) = (7.0 \pm 1.2)\%$ [49], where the error is the sum in quadrature of the statistical and systematic uncertainties. Furthermore, many other decay modes were searched for, but until 2011 all the searches has been insuccesfull. The $\eta_c(2S)$ was searched for in the decay to $(h^+h^-)(h'^+h'^-)$ (with $h^{(\prime)} = K, \pi$) final state with no significant results [199]. The branching fraction for the corresponding $\eta_c(1S)$ decay is $\sim 1\%$ [49]. The production mechanism $p\overline{p}$ was used to search for the $\eta_c(2S)$ in the $\gamma\gamma$ final state, but no significant signal was found [200]. A preliminary result by Belle reports the observation of $\eta_c(2S)$ decays to six-particle final states [201].

The $\eta_c(2S)$ is also observed in the inclusive mass distribution of the system recoiling against a J/ψ in e^+e^- annihilation by both Belle [129, 160, 202] and *BABAR* [130]. An evidence at 1.8σ level for $\eta_c(2S)$ decay into inclusive final state is also reported by *BABAR* in B-meson decays to $X_{c\bar{c}}K^{\pm}$ [203]. The analysis is performed by fully reconstructing one B-meson (B_{reco}), so the signal B-meson (B_{sig}) momentum is known from the B_{reco} and beam momenta. Events with one charged kaon not associated with B_{reco} are selected and the kaon momentum is calculated in the B_{sig} rest frame. The mass of $X_{c\bar{c}}$ is $m_X = \sqrt{m_B^2 + m_K^2 - E_K m_B}$, where m_B and m_K are the $B^{\pm}$ and $K^{\pm}$ mass and E_K is the $K^{\pm}$ energy.

The parameters of the $\eta_c(2S)$ are known with poor experimental precision, even if important step torward their determination have been done in last few years. We show in Fig. 2.6 the experimental status: the mass measurements obtained in different processes are consistent within experimental errors, and show a large spread ranging from $3626\ \mathrm{MeV}/c^2$ to $3645\ \mathrm{MeV}/c^2$. These measurements are inconsistent with the first result reported by the Crystal Ball Collaboration [193]), that may originate from a misidentification of the $\psi(2S)\to J/\psi X$ feeddown process, with $J/\psi\to\gamma\eta_c(1S)$. The measured photon energy $(91 \pm 5)\ \mathrm{MeV}$ [193] is comparable, although not fully consistent, with the $J/\psi - \eta_c(1S)$ mass difference $(117 \pm 1)\ \mathrm{MeV}/c^2$ [49]. Using the number of $\psi(2S)$ produced [193], the reported efficiency [193], and relevant branching ratios [49], the number of expected events from this background process is 8011 ± 2381 that is consistent with the 5582 ± 1270 signal events reported by the Crystal Ball Collaboration [193].

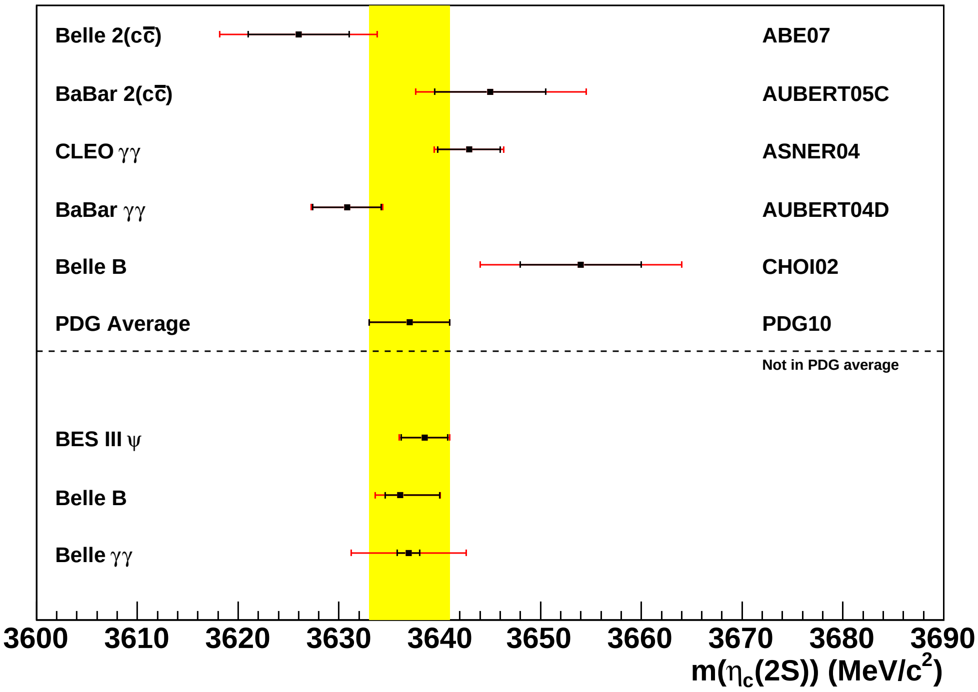

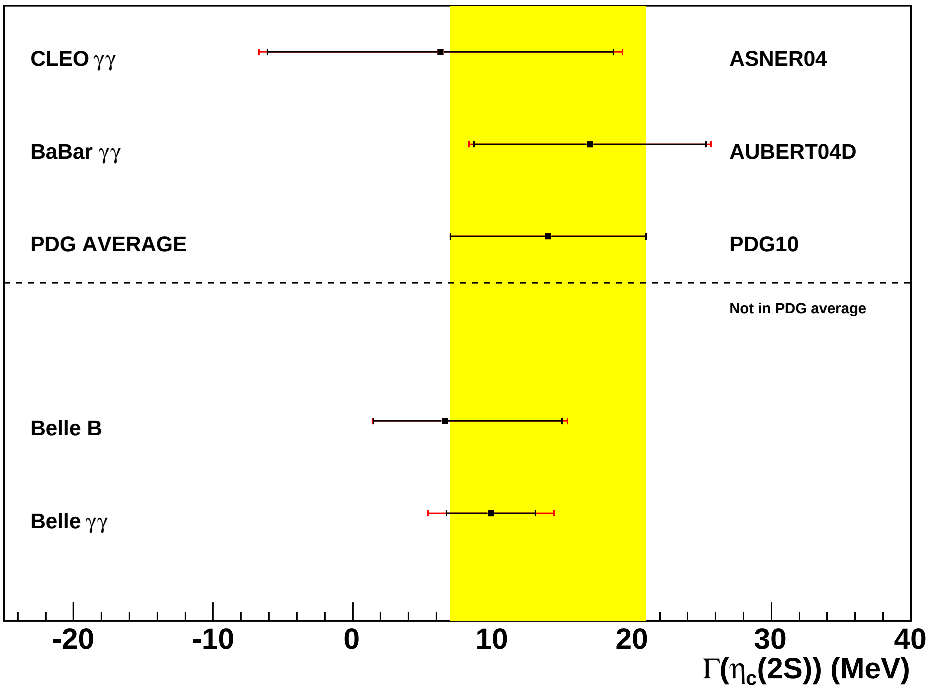

Figure 2.6: Measured values of the $\eta_c(2S)$ mass and width used to obtain world-average values [49]. The squares are the measured values with black bars for statistic uncertianty and red bars for the sum in quadrature of statistic and systematic uncertainties. If the red bars are missing, the black bars are the sum in quadrature of the statistical and systematic errors. For each measure we report the experiment that performed it and the production mechanism exploited: two-photon fusion ($\gamma\gamma$), B-meson decay (B), double charmonium ($2(c\bar{c})$), and J/ψ or $\psi(2S)$ radiative decay (ψ). Below the dashed line we report new measurements not included in the world average. The yellow box is the $\pm 1\sigma$ region with respect to world-average values. The last column reports the PDG [49] reference to the paper where the measure is reported.

2.3.6 $\chi_{c2}(2P)$

The $\chi_{c2}(2P)$ was the first observed conventional charmonium state above the threshold. First dubbed $Z(3930)$, it was observed by Belle [204] and confirmed by *BABAR* [205] in two-photon production process and $D\bar{D}$ final state. The measured mass and width are $(3929 \pm 5(stat) \pm 2(syst))\ \mathrm{MeV}/c^2$ and $(29 \pm 10(stat) \pm 2(syst))\ \mathrm{MeV}$ for Belle and $(3927 \pm 2(stat) \pm 1(syst))\ \mathrm{MeV}/c^2$ and $(21 \pm 7(stat) \pm 4(syst))\ \mathrm{MeV}$ for *BABAR*. The agreement between the two measurements is very good. The decay into spinless final state, combined with the fact that $C = +1$ due to the production mechanism, implies that $J = L$ is even and thus $P = +1$. The value of J is determined by studying the angular distribution of the decay products, in particular the angle between the directions of the $D\bar{D}$ system and the beam. Both experiments favor $J^{PC} = 2^{++}$ assignment. Belle provides a measurement of the branching fraction ratio $\mathcal{B}(Z(3930) \rightarrow D^+D^-)/\mathcal{B}(Z(3930) \rightarrow D^0\bar{D}^0) = 0.74 \pm 0.43(stat) \pm 0.16(syst)$ [204] which suggests isospin invariance, as expected for conventional $c\bar{c}$. The product of the two-photon width times the decay branching ratio $\Gamma_{\gamma\gamma}(Z(3930)) \times \mathcal{B}(Z(3930) \rightarrow D\bar{D})$ is found to be (0.18 ± 0.06) keV and (0.24 ± 0.05) keV, by Belle and *BABAR*, respectively, where the error is the sum in quadrature of the statistical and systematic uncertainties. There is a general agreement on the interpretation of this state, which is identified as χ'_{c2} [49]. The mass, two-photon width and decay angular distribution are consistent with theoretical expectation for this charmonium state [8,13,206].

2.4 Exotic charmonium

In this section we review the new states discovered since 2003 whose interpretation is still ambiguous. For each state we report experimental facts and the status of the theoretical understanding. We give particular emphasis to theoretical considerations about the compatibility of available measurements with the different proposed models.

2.4.1 $X(3872)$

The $X(3872)$ was discovered by Belle in 2003 [39], in the $B \rightarrow X(3872)K \rightarrow J/\psi\pi^+\pi^-K$ process, and subsequently confirmed by several experiments [207–211]. Quite a large number of experimental results are available for this state.

The $J/\psi\pi^+\pi^-$ decay mode, where this state was discovered [39], also provides insight on its nature. Belle precisely measures the mass in this decay mode and puts an upper limit of $1.2\ \mathrm{MeV}$ on its width [212]. The $\pi^-\pi^-$ mass distribution is consistent with subthreshold ρ production [213]. The CDF collaboration has performed a full angular analysis of the decay, excluding all the possible J^P numbers, but 1^+ and 2^- [214]. Belle has performed a spin-parity analysis using $711~\mathrm{fb}^{-1}$ [212] of data. A study of angular distributions suggested in Refs. [215, 216] favors a 1^{++} assignment, but does not exclude 2^{-+}. The study of the $\pi^+\pi^-$ mass distribution gives some insight on the state parity. In fact, the mass distribution near the kinematic endpoint is suppressed by a centrifugal barrier factor. Both CDF [213] and Belle [212] found that accounting for ρ-ω interference in the analysis, the information carried by the dipion mass distribution is insufficient to discriminate between the 1^{++} and 2^{-+} assignment.

Decay to $D^0\bar{D}^0\pi^0$ has been observed [217] and interpreted as $D^0\bar{D}^{*0}$. This interpretation has been confirmed in subsequent analyses [218, 219]. Both *BABAR* and Belle analyses constrain the D^{*0} mass to its nominal value, so the study of the $X(3872)$ line-shape in this decay mode is not feasible.

Belle reported preliminary unpublished evidence of the decay into $J/\psi\pi^+\pi^-\pi^0$ [220]. The three pion mass distribution is consistent with subthreshold ω production. The ratio of branching fractions $\mathcal{B}(X(3872)\to J/\psi\pi^+\pi^-\pi^0)/\mathcal{B}(X(3872)\to J/\psi\pi^-\pi^-)$ is $1.0 \pm 0.4(stat) \pm 0.3(syst)$. Recently, *BABAR* has reported evidence of decay into the $J/\psi\omega$ final state with a significance of 4 standard deviations (σ) [221]. The angular distribution of the three-pion system strongly supports their origin from an ω meson. The ratio $\mathcal{B}(X(3872)\to J/\psi\omega)/\mathcal{B}(X(3872)\to J/\psi\pi^-\pi^-)$ is equal to 0.7 ± 0.3 and 1.7 ± 1.3, for charged and neutral B decays, respectively, where the error is the sum in quadrature of the statistical and systematic uncertainties. An analysis of the three pions mass distribution is performed. The agreement with $P = -1$ (61.9%) is far better than with $P = +1$ (7.1%). Thus, $J^{PC} = 2^{-+}$ is favored, in contrast with Belle preliminary indication of $J^{PC} = 1^{++}$ [222].

Radiative $X(3872)$ decay into $J/\psi\gamma$ has been observed by *BABAR* [223] and Belle [224]. This observation implies that the $X(3872)$ has positive C-parity. *BABAR* reports an evidence of the decay into $\psi(2S)\gamma$ final state [223] at 3.5σ level , using a data sample of $424~\mathrm{fb}^{-1}$. The measured branching fraction ratio $\mathcal{B}(X(3872)\to\psi(2S)\gamma)/\mathcal{B}(X(3872)\to J/\psi\gamma) = 3.4 \pm 1.4$, where the error is the sum in quadrature of the statistical and systematic uncertainties, is unexpectedly large. Recently, Belle searched for the $\psi(2S)\gamma$ decay using $849~\mathrm{fb}^{-1}$ of data [224]. No significant signal is observed. The branching fraction upper limit at 90% confidence level is $\mathcal{B}(X(3872)\to\psi(2S)\gamma)/\mathcal{B}(X(3872)\to J/\psi\gamma) < 2.1$. This results challenge previous *BABAR* evidence [223].

A consensus concerning the interpretation of $X(3872)$ has not been reached. Possible conventional charmonium assignments are $\chi_{c1}(2P)$ or $\eta_{c2}(1D)$. The first is challenged by the fact that $\chi_{c2}(2P)$ has a mass of about $3930~\mathrm{MeV}/c^2$. This implies that the mass splitting in the $\chi_{cJ}(2P)$ triplet should be larger than expected. It was noticed that the effect of the coupling to $D\bar{D}^*$ channel may shift the 1^{++} state mass down to $D\bar{D}^*$ threshold, while the shift of the 2^{++} state is expected to be much smaller [110–114]. Radiative decay rates of the $\chi_{c1}(2P)$ to $\gamma J/\psi$ and $\gamma\psi(2S)$ are in agreement with the measured values [225]. The $\eta_{c2}(1D)$ interpretation is favored by *BABAR* assignment of $J^{PC} = 2^{-+}$. The measured $X(3872)$ mass is consistent with the 1^1D_2 state mass predicted in Ref. [8], but not consistent with the values reported in many recent papers [14, 226, 227]. Theoretical calculations [228, 229] show that the predicted decay rate of such a state to $\psi(2S)\gamma$ is inconsistent with the results reported by *BABAR* [223]. It should be noted that recent Belle result [224] for this decay mode disagrees with *BABAR* one [224], thus mitigating this inconsistence. Recently it has been noticed that also the decay rate to $D^0\bar{D}^{*0}$ cannot fit the 1^1D_2 assignment [229].

The interpretation of $X(3872)$ as a $D^0\bar{D}^{*0}$ molecule was suggested by many authors [73–75, 230, 231], and may accommodate the large observed isospin violation [75]. The decays into $J/\psi\gamma$ and $\psi(2S)\gamma$ imply that this molecular state should mix with χ'_{c1} [109, 232–235]. Such a mixing would not need to be as large as earlier proposed, in the light of the new Belle result on the $\psi(2S)\gamma$ decay [224]. Molecular interpretation is usually challenged by *BABAR* $J^{PC} = 2^{-+}$ assignment, but a molecular model with a $D\bar{D}^*$ molecule with this J^{PC} assignment was proposed [236]. The $X(3872)$ production rate in B meson decays in the molecular picture [237] is consistent with experimental results. Oppositely, the large cross-section for prompt production that can be derived from CDF results seems inconsistent with this model [238].

The interpretation of $X(3872)$ as a tetraquark [87] predicts a mass in good agreement with the experimental results. It was noticed [239] that mass measurement are likely not to be able to discriminate between tetraquark and molecular picture, while radiative decay rates should exhibit different patterns for the two hypotheses. The predicted radiative decay rate into $\gamma J/\psi$ for $X(3872)$ as a tetraquark [240] is consistent with the experimental results. The tetraquark picture predicts the presence of neutral and charged partners in the same mass region. Such states were searched for and not found by *BABAR* [241], CDF [242] and Belle [212]. Furthermore, calculations of the binding energy seem to favor the molecule picture with respect to the tetraquark one [243].

2.4.2 $Y(3940)$

The $Y(3940)$ was observed by Belle in the $B \to J/\psi\omega K$ process [47], and confirmed by *BABAR* [48]. The same structure is not observed in the $B \to D^0\bar{D}^{*0}K$ process [218, 219]. Belle measures the mass $(3943 \pm 11(stat) \pm 13(syst))$ MeV/c^2 and width $(87 \pm 22(stat) \pm 26(syst))$ MeV. A resonance in the the $J/\psi\omega$ final state, dubbed $X(3915)$, was observed by Belle in two-photon collisions [244]. The measured mass and width are $(3914 \pm$

$3(stat) \pm 2(syst))$ MeV/c^2 and $(17 \pm 10(stat) \pm 3(syst))$ MeV, respectively. A recent *BABAR* re-analysis of the $B \to J/\psi\,\omega$ decay [221] provides a Y(3940) mass and width of $(3919.1^{+3.8}_{-3.5}(stat) \pm 2.0(syst))$ MeV/c^2 and $(31^{+10}_{-8}(stat) \pm 5(syst))$ MeV, respectively. This latter measurement favors a $Y(3940)$ mass slightly lower than the one first reported by Belle [47]. This value is in agreement with the one measured by Belle for the $X(3915)$ in the two-photon process. Thus, it seems likely that the same particle, with a mass of about 3915 MeV/c^2, is observed in two distinct production processes. Belle reports a product of the two-photon width times the decay branching ratio $\Gamma_{\gamma\gamma}(Y(3940)) \times \mathcal{B}(Y(3940) \to J/\psi\,\omega)$ equal to $(61 \pm 17(stat) \pm 8(syst))$ eV and $(18 \pm 5(stat) \pm 2(syst))$ eV for $J^P = 0^+$ and 2^+ assignments, respectively [244]. Assuming $\Gamma_{\gamma\gamma}(Y(3940)) \sim 1$ keV, that is a typical value for excited charmonium, the branching ratio $\mathcal{B}(Y(3940) \to J/\psi\,\omega)$ is in the range [1,6]%, which is unexpectedly large, compared to other excited $c\bar{c}$ states [49].

The proposed interpretation of $Y(3940)$ as the $\chi_{c1}(2P)$ state, where the final state interaction enhances the $J/\psi\,\omega$ decay [1], is ruled out by the observation of this state in two-photon production. Interpretation as $\chi_{c0}(2P)$ was also suggested [245]. Interpretation as a charmonium hybrid is seriously challenged by lattice calculations that show that the expected mass for hybrid ground state should be approximatively 500 MeV/c^2 higher than the one of $Y(3940)$ [2]. Interpretation in the framework of molecular model has been proposed [246–248]. It was suggested that the search of the decay into the $D^*\bar{D}\gamma$ may give more insight on the nature of this state [248]. The $X(3915)$ was supposed to be the $\chi_{c2}(2P)$ state [249]. Since the $Z(3930)$ assignment as the $\chi_{c2}(2P)$ is commonly accepted [49], this interpretation is problematic, unless $Y(3940)$ and $\chi_{c2}(2P)$ are the same particle. However, if this were the case, it would be difficult to explain the large value of $\mathcal{B}(Y(3940) \to J/\psi\,\omega)$.

2.4.3 New states in double charmonium production

Belle has observed two charmonium-like resonances, dubbed $X(3940)$ and $X(4160)$, produced in association with a J/ψ meson in e^+e^- annihilation [160]. The measured mass and width of the two resonances are $m(X(3940)) = (3942^{+7}_{-6}(stat) \pm 6(syst))$ MeV/c^2 $m(X(4160)) = (4156^{+25}_{-20}(stat) \pm 15(syst))$ MeV/c^2, $\Gamma(X(3940)) = (37^{+26}_{-15}(stat) \pm 8(syst))$ MeV, and $\Gamma(X(4160)) = (139^{+111}_{-61}(stat) \pm 21(syst))$ MeV [250]. The $X(3940)$ is observed in the inclusive mass spectrum recoiling against a J/ψ meson [160]. An search for its decay to $D^{(*)}\bar{D}^{(*)}$ is performed by studying the $e^+e^- \to J/\psi\, D^{(*)}X$, where the J/ψ and the $D^{(*)}$ are exclusively reconstructed, and the invariant mass of the X system is consistent with D or D^* [160, 250]. A clear enhancement in the $D^*\bar{D}$ spectrum is observed, while a broad structure is observed in the $D\bar{D}$ spectrum. An exclusive search of the $X(3940)$ decay to the $J/\psi\omega$ final state is performed, but no significant signal is found [160]. The $X(4160)$ is observed in the $D^*\bar{D}^*$ mass spectrum. No results are available by experiments other than Belle.

Since large $\eta_c(1S)$ and $\eta_c(2S)$ signals are observed in double charmonium production, the $X(3640)$ may be identified as the $\eta_c(3S)$ state. The measured mass is lower than expectations for this state [14]. However, screened potential model provides a mass estimate only $50\ \mathrm{MeV}/c^2$ higher than the measured value for $X(3940)$ [109]. The measured width is consistent with theoretical estimates [251]. Another possible interpretation as the first radial excitation $\chi_{c1}(2P)$ of the $\chi_{c1}(1P)$ meson is favored by the expected large branching fraction of this state in the $D\bar{D}^*$ final state [1]. This interpretation is challenged by the fact that $J^{PC} = 1^{++}$ particle production seems to be suppressed in double charmonium process [129, 130, 145], and by an inconsistency with the expected $\chi_{c1}(2P)$ width [252]. The non-observation in the $J/\psi\omega$ final state [160] points to the fact that $X(3940)$ and $Y(3940)$ are distinct particles.

The $X(4160)$ was tentatively interpreted as the $\eta_c(4S)$ state [253]. The $\chi_{c0}(3P)$ interpretation was also proposed [253]. In this scenario the broad structure in the $D\bar{D}$ spectrum can be due to feed-down from the $\chi_{c0}(3P)\to D^*\bar{D}^*$ decay. The predicted mass in the screened potential model [109] favors the $\chi_{c0}(3P)$ assignment. These interpretations are disfavored by the $D^{(*)}\bar{D}^{(*)}$ decay width reported in Ref. [254], that suggests a $\eta_{c2}(2^1D_2)$ assignment. The interpretation as $\chi_{c0}(3P)$ state is also disfavored by the absence of any signal corresponding to the $\chi_{c0}(2P)$ in the same production process. It was suggested [109] that the broad bump observed in the $D\bar{D}$ spectrum can be the missing state. Interpretation as a $D_s^*\bar{D}_s^*$ molecule was also proposed [255].

2.4.4 The 1^{--} states

Several $J^{PC} = 1^{--}$ states have been observed in the last years. Such states are potential exotic candidates both for their unnatural properties, and for the excess of observed $J^{PC} = 1^{--}$ states with respect to conventional charmonium model expectations.

These states are observed in ISR production, thus their J^{PC} assignment is clearly established. *BABAR* first observed a state decaying to $J/\psi\ \pi^+\pi^-$, with a mass of $(4259 \pm 8(stat)^{+2}_{-6}(syst))\ \mathrm{MeV}/c^2$ and a width in the range $[50, 90]\ \mathrm{MeV}$ [40]. This observation is confirmed by both CLEO [41] and Belle [42]. CLEO also searched for the $J/\psi\ \pi^0\pi^0$ and $J/\psi K^+K^-$ final states and reports for a significant signal of the first decay, and evidence for the latter. Belle measures the $Y(4260)$ mass and width to be $(4247 \pm 12(stat)^{+12}_{-32}(syst))\ \mathrm{MeV}/c^2$, and $(108 \pm 19(stat) \pm 10(syst))\ \mathrm{MeV}$. Furthermore a second broad structure with mass and width of $(4008 \pm 40(stat)^{+114}_{-28}(syst))\ \mathrm{MeV}/c^2$ and $(226 \pm 44(stat) \pm 87(syst))\ \mathrm{MeV}$ is observed. A preliminary, unpublished updated analysis by *BABAR* [256] confirms the previous $Y(4260)$ observation and measures a width of $(105 \pm 18(stat)^{+4}_{-6}(syst))$ MeV. No evidence of any structure in the $4008~\mathrm{MeV}/c^2$ mass region is found. Possible $Y(4260)$ decay in open-charm channels was searched for by studying the $D^{(*)}\bar{D}^{(*)}$ cross-section in ISR events [257, 258]. No significant signal is found. Searches for decays into hadronic exclusive final states containing a $c\bar{c}$ meson other than the observed $J/\psi\pi^+\pi^-$, $J/\psi\pi^0\pi^0$, or $J/\psi K^+K^-$ modes, were unsuccessfully [41].

The study of the $\psi(2S)\pi^+\pi^-$ final state in ISR production was motivated by the search of new decay modes of the newly discovered $Y(4260)$. A first search performed by *BABAR* resulted in the observation of a peaking structure at a mass of $(4324 \pm 24)~\mathrm{MeV}/c^2$ with a width of (172 ± 33) MeV [43], where the error is the sum in quadrature of statistic and systematic uncertainties. While the mass that is not fully consistent with that of the $Y(4260)$ pointed to the presence of a new resonance, the limited statistics available prevented to clearly establish this. A subsequent analysis by Belle confirmed the existence of the peak observed by *BABAR*, and reported the presence of another resonance with mass of $(4664 \pm 11(stat) \pm 5(syst))~\mathrm{MeV}/c^2$ and with of $(48 \pm 15(stat) \pm 3(syst))$ MeV [44]. The larger statistic used in the Belle analysis allows to establish that the $Y(4360)$ and $Y(4660)$ are not the same state observed in the $J/\psi~\pi^+\pi^-$ decay.

The absence of any signal from $Y(4260)$ and $Y(4360)$ meson in open-charm decay modes motivated the study of the $e^+e^-\to\gamma_{ISR}\Lambda_c^+\Lambda_c^-$ [259]. While no signal is observed at an invariant $(\Lambda_c^+\Lambda_c^-)$ mass corresponding to the above mentioned resonances, a clear enhancement is visible close to the $\Lambda_c^+\Lambda_c^-$ threshold opening. Fitting the enhancement with a relativistic Breit-Wigner shape results in a mass of $(4634^{+8}_{-7}(stat)^{+5}_{-8}(syst))~\mathrm{MeV}/c^2$ and a width of $(92^{+40}_{-24}(stat)^{+10}_{-21}(syst))$ MeV [259]. The measured mass of the enhancement is consistent with the $Y(4660)$ mass and with predictions for the $\eta_c(5S)$ state [260]

Recently CLEO reported an analysis of the $e^+e^-\to\pi^+\pi^-h_c(1P)$ [192]. The measured cross-section at a CM energy of $4260~\mathrm{MeV}/c^2$ is larger than at $4170~\mathrm{MeV}/c^2$. Unfortunately, this excess is not statistically significant to determine if it originates from $Y(4260)$ resonant production [192].

The interpretation of these states as conventional charmonium states are disfavored by the fact that no $J^{PC} = 1^{--}$ state is predicted at a mass close to the observed one, and by the absence of any evidence of decay into open-charm. Screened potential models predict the mass for the $\psi(4S)$, $\psi(3D)$, and $\psi(6S)$ to be $4273~\mathrm{MeV}/c^2$, $4317~\mathrm{MeV}/c^2$, and $4608~\mathrm{MeV}/c^2$ [109]. Such results do not take into account complicated $S-D$ mixing effects, that can explain the actual discrepancies with the measured mass of the $Y(4260)$, $Y(4360)$, and $Y(4660)$ resonances. In any case, this assignment is far from being conclusive [109]. Interpretation as a hybrid [261] is supported by a general selection rule that forbids the decay of a P-wave hybrid into an S-wave $D^{(*)}\bar{D}^{(*)}$ final state [69].

Furthermore, a large branching fraction to the $D\bar{D}_1$ final state is expected [68]. While first lattice calculations of the lowest-lying charmonium hybrid mass predicted a value close to $4200\ \mathrm{MeV}/c^2$ [262], more recent calculations [263] find a value $\sim 200\ \mathrm{MeV}/c^2$ larger, that is only marginally compatible with the measured $Y(4260)$ mass. The same calculation favors models where the $Y(4260)$ is a D_1D or D^0D^{*0} molecule [264]. Similar results are obtained in Ref. [265]. The distribution of the dipion invariant mass in the $Y(4660)$ decay points to the presence of a large $f_0(980)$ contribution. Interpretation as a $\psi(2S)f_0(980)$ molecule was proposed [266, 267]. Due to isospin symmetry an $\eta_c(2S)f_0(980)$ molecule is expected at a mass of about $4615\ \mathrm{MeV}/c^2$, with dominant decay to $\eta_c(2S)\pi\pi$ [267, 268]. In this picture, the $X(4630)$ and the $Y(4660)$ can be interpreted as being the same particle [269] Possible identification of the $Y(4260)$ as a $cs\overline{cs}$ tetraquark in P-wave state was proposed [94, 270, 271]. Authors of Ref. [94] predict that the decay to $D_s\bar{D}_s$ should be dominant. Furthermore, an isospin partner of this tetraquark decaying to $J/\psi\pi^+\pi^-\pi^0$ is expected [261]. The calculation of the $cs\overline{cs}$ tetraquark mass performed in Ref. [265] is consistent with the value measured for the $Y(4360)$. Thus interpretation of the $Y(4260)$ as a $cs\overline{cs}$ tetraquark is problematic. Possible interpretation as P-wave $cq\overline{cq}$ tetraquark was proposed [265]. However, different calculations of the mass of this state give quite different results that can be either consistent [272] or inconsistent [265] with the measured value. The peculiar decay pattern of the $Y(4260)$ and $Y(4360)$, where each state has a prominent decay into J/ψ or $\psi(2S)$, with an apparent suppression of the decay into the other charmonium state, has triggered the idea of *hadrocharmonium* [98, 99]. In this picture, the exotic resonance is composed by a charmonium core, embedded into light quarks matter by residual strong interactions. The existence of the $Y(4260)$ state as real resonant state has been questioned by many authors that suggest that it may be an artifact originating from coupled channels effect [103], or interference between the $e^+e^-\to J/\psi\pi\pi$, $e^+e^-\to\psi(4160)\to J/\psi\pi\pi$, and $e^+e^-\to\psi(4415)\to J/\psi\pi\pi$ amplitudes [273]. Similarly, the $Y(4630)$ was suggested to be an artifact originating from the interference between the $e^+e^-\to\psi(2S)\pi\pi$, $e^+e^-\to\psi(4160)\to\psi(2S)\pi\pi$, and $e^+e^-\to\psi(4415)\to\psi(2S)\pi\pi$ amplitudes [274]. Concerning the $X(4360)$, it should be noted that near-threshold enhancements are a feature observed in several processes, like $e^+e^-\to\Lambda\Lambda$ [275]. However, they do not usually create peaking-like structures, but smooth shapes.

2.4.5 New $J/\psi\,\phi$ states

The search of structures in the $J/\psi\,\phi$ mass spectrum is motivated by the prediction that a $c\bar{c}s\bar{s}$ tetraquark is expected to have sizable branching ratio to this final state and a mass in the range [4270,4350] MeV/c^2 [276]. A first CDF measurement has reported an evidence of a resonance-like candidate, dubbed $Y(4140)$, with a significance of 3.8σ [277]. A subsequent analysis performed by using a two times larger statistics [278] has confirmed the previous evidence with a significance of more than 5σ, and has reported a 3.1σ evidence of another structure at a mass of about 4270 MeV/c^2. The $J/\psi\,\phi$ final state is studied in $B^+\to J/\psi\,\phi K^+$ decay. The measured $Y(4140)$ mass and width are $(4143.4^{+2.9}_{-3.0}(stat) \pm 0.6(syst))\ \mathrm{MeV}/c^2$ and $(15.3^{+10.4}_{-6.1}(stat){\pm}2.5(syst))\ \mathrm{MeV}$ [278]. The measured mass and width for the second structure are $(4274.4^{+8.4}_{-6.7}(stat) \pm 1.9(syst))\ \mathrm{MeV}/c^2$ and $(32.3^{+21.9}_{-15.3}(stat) \pm 7.6(syst))\ \mathrm{MeV}$. The measured branching fraction ratio $R_{Y(4140)} = \mathcal{B}(B^+\to Y(4140)K^+) \times \mathcal{B}(Y(4140)\to J/\psi\,\phi)/\mathcal{B}(B^+\to J/\psi\,\phi K^+)$ value is $0.149 \pm 0.039(stat) \pm 0.024(syst)$ [278].

Belle has searched for the $Y(4140)$ using the same production mechanism, and found no evidence of it [279]. Due to small detection efficiency near the $J/\psi\,\phi$ threshold, the upper limit on the branching ratio is $\mathcal{B}(B^+\to Y(4140)K^+) \times \mathcal{B}(Y(4140)\to J/\psi\,\phi) < 6 \times 10^{-6}$. Using the world-average value for $\mathcal{B}(B^+\to J/\psi\,\phi K^+) = (5.2 \pm 1.7) \times 10^{-5}$, one gets $R_{Y(4140)} < 0.115$, that is not in contradiction with CDF measurement, considering its large uncertainty. A recent search by LHCb [280], performed by using a data sample about three times larger that CDF one [278], has given negative results. The measured upper limits on $R_{Y(4140)}$ ranges between 0.04 and 0.07, depending on the shape used to parameterize the background. This measure seriously challenge previously reported CDF observation.

Several interpretations were proposed for the $Y(4140)$ and the $Y(4270)$, including a $D_s^{*+}D_s^{*-}$ molecule [247,255,281–289], an exotic 1^{-+} hybrid [287], a $c\bar{c}s\bar{s}$ tetraquark [290], and an effect of the $J/\psi\,\phi$ threshold opening [291]. Some arguments were raised against the interpretation as a standard $c\bar{c}$ state [292] and scalar $D_s^{*+}D_s^{*-}$ molecule [293, 294]. Authors of Ref. [247] predict, in the $D_s^{*+}D_s^{*-}$ molecule picture, the product of the two-photon width times the decay branching ratio $\Gamma_{\gamma\gamma}(Y(4140)) \times \mathcal{B}(Y(4140)\to J/\psi\,\phi)$ to be sizable, with large theoretical uncertainties.

Belle searched for the $Y(4140)$ in two-photon production and found no evidence of it [295]. Furthermore, Belle has reported evidence of a narrow structure with a mass equal to $(4350^{+4.6}_{-5.1}(stat) \pm 0.7(syst))\ \mathrm{MeV}/c^2$ and width $(13^{+18}_{-9}(stat) \pm 4(syst))\ \mathrm{MeV}$. The structure, dubbed $X(4350)$, has a significance of 3.2σ. The measured mass is inconsistent with that of the $Y(4140)$. Interpretation of the $X(4350)$ as χ''_{c2} was suggested [245]. Other interpretations as an exotic state are similar to the ones proposed for the $Y(4140)$ [285, 286, 290, 296, 297].

2.4.6 Charged states

Belle reported the evidence of the narrow $Z(4430)^-$ decaying into $\psi(2S)\pi^-$, with a significance of 5.4σ [298]. This state was studied in the decay $B^0\to\psi(2S)\pi^-K^+$. The Dalitz plot of this decay is dominated by the presence of the K^* resonances. In a previous analysis by Belle, a veto was applied to remove such contributions [299]. In a more recent analysis, a Dalitz plot analysis was performed [298]. Both analyses report the same value for the mass $(4433^{+15}_{-12}(stat)^{+19}_{-13}(syst))$ MeV$/c^2$ [298]. The measured widths are equal to $(45^{+18}_{-13}(stat)^{+30}_{-13}(syst))$ MeV and $(107^{+86}_{-43}(stat)^{+74}_{-56}(syst))$ MeV, in the first [299] and latter [298] analysis, respectively. These measurements are consistent within the large uncertainties of the latter. *BABAR* has searched for the $Z(4430)$ in both $J/\psi\,\pi^-$ and $\psi(2S)\pi^-$ final states, but no evidence of resonance-like structures has been found [300]. In this analysis, *BABAR* has performed a study of the reflections of the K^* system in the $J/\psi\,(\psi(2S))\pi^-$ mass spectrum, and found that such reflections reproduce data well, without the need of any additional resonant structures. The upper limit at 90% confidence level on the branching fraction product $\mathcal{B}(B^0\to Z(4430)^-K^+)\times\mathcal{B}(Z(4430)^-\to\psi(2S)\pi^-)$ reported by *BABAR* is 3.1×10^{-5}. This is not in contrast with the measured value $(3.2^{+1.8+5.3}_{-0.9-1.6})\times10^{-5}$ reported by Belle [298]. No analysis of the $J/\psi\ \pi^-$ final state has been reported by Belle so far.

Belle reported an evidence of two more states ($Z_1(4050)^-$ and $Z_2(4250)^-$) with non-zero electric charge in the final state $\chi_{c1}\pi^-$ [301]. These states were found in $B\to\chi_{c1}\pi^-K$, whose Dalitz plot is dominated by the K^* resonances. A Dalitz plot analysis is performed. The solution with two resonant structures is favored with respect to the one with no resonant contributions, with a significance of 5.7σ. The mass of these states are $(4051\pm14(stat)^{+20}_{-41}(syst))$ MeV$/c^2$ and $(4248^{+44}_{-28}(stat)^{+180}_{-35}(syst))$ MeV$/c^2$, respectively. Their widths are $(82^{+21}_{-17}(stat)^{+47}_{-22}(syst))$ MeV and $(177^{+54}_{-39}(stat)^{+316}_{-61}(syst))$ MeV, respectively. The reported branching fraction is $\mathcal{B}(\overline{B}^0\to Z_1^-K^+)\times\mathcal{B}(Z_1^-\to\chi_{c1}\pi^-) = (3^{+1.5}_{-0.8}(stat)^{+3.7}_{-1.6})\times10^{-5}$ and $\mathcal{B}(\overline{B}^0\to Z_2^-K^+)\times\mathcal{B}(Z_2^-\to\chi_{c1}\pi^-) = (4^{+2.3}_{-0.9}(stat)^{+19.7}_{-0.5})\times 10^{-5}$. *BABAR* has searched for the Z_1^- and Z_2^- in the same final state [302], with an analysis technique similar to that used for the Z^+ analysis [300]. No significant signal for an exotic resonance is found. The observed $\chi_{c1}\pi^-$ mass spectrum is well described by the reflections of the K^* meson. The upper limits at 90% confidence level on the resonance branching fractions are $\mathcal{B}(\overline{B}^0\to Z_1^+K^-)\times\mathcal{B}(Z_1^+\to\chi_{c1}\pi^-) < 1.8\times10^{-5}$ and $\mathcal{B}(\overline{B}^0\to Z_2^+K^-)\times\mathcal{B}(Z_2^+\to\chi_{c1}\pi^-) < 4.0\times10^{-5}$. These results disfavor the existence of the Z_1^+ and Z_2^+ resonances. However, the measured upper limits are not sufficiently stringent to refute Belle claims. More insight on these debated states will be provided in the near future by experiments at hadronic machines like Tevatron and LHC.

If future experiments confirm the observation of resonant states with non-zero net electric charge, this will be a striking evidence of a state with an unconventional nature, since it would be inconsistent with the electric neutral $q\bar{q}$ structure. Interpretation as a $D^{*-}\bar{D}_1^0$ molecule [92,303–306], $cu\overline{cd}$ tetraquark [307] or hadrocharmonium [98,99] have been proposed. Molecular models provide a natural suppression of the $Z(4430)$ decay to open-charm $D^{(*)-}\bar{D}^{(*)0}$ final states, while these modes are likely to be dominant in the tetraquark picture [308]. In the tetraquark picture, an approach based on the $SU(3)$ symmetry predicts the existence of strange partners of the $Z(4430)^-$ decaying to $J/\psi\,K^+$ and $J/\psi\,K_S^0$ [309]. Non exotic interpretations have also proposed: the $Z(4430)^-$ could be interpreted as a radial excitation of the D_s^- meson [310] or it could be an artifact due to $D_1\bar{D}^*$ rescattering [104, 105, 107, 108]

Chapter 3

The *BABAR* experiment

3.1 Introduction

In this Chapter, after a brief overview of the PEP-II B-factory, we describe the *BABAR* detector. Each *BABAR* subsystem is described, and we point out the solutions adopted to match the demanding performances required by the physics program.

3.2 B-factories overview

The experiments *BABAR* [311] and Belle [312] operated at the PEP-II and KEKB B-factories were designed to study the CP violation in the B system. The $\Upsilon(4S)$ resonance provides a very clean environment for B reconstruction, with a very favorable ratio of $b\overline{b}$ production from e^+ and e^- beams compared to lighter quark pairs ($\sigma(b\overline{b})/\sigma(q\bar{q}\ ) \simeq 0.28$). Asymmetric e^+ and e^- beams provide a boost to the produced B meson pair, allowing for reconstruction of B flavor as a function of time of flight through the separation of the B vertices in the lab frame. The concept of asymmetric B-factories was first proposed in 1987 by Pier Oddone [313]. He proposed that the best way to produce and study B particles would be to construct an asymmetric collider that could create a separation in space between the decay products of individual B and $\overline{B}$ mesons. In fact, unlike symmetric beams, the B particles are carried downstream in the direction of the higher energy beam and due to this forward boost the distances between their decay vertices is large enough to be measured. This configuration allows to study time-dependent CP asymmetries.

Thanks to the high cross-section for $c\overline{c}$ production, $\sigma(c\overline{c}) = 1.3$ nb, the B-factories are, in fact, also $charm$-factories becoming a very attractive environment to study open charm and charmonium spectroscopy. Furthermore, $c\overline{c}$ can also be produced by the ISR and two-photon fusion mechanisms.

BABAR and Belle operated in the last fifteen years and collected about 1.5 ab^{-1} of data. The *BABAR* and Belle experiments are very similar, with some important differences: the KEK-B/Belle B factory has a nonzero beam crossing angle (4.2 mr) at the interaction point (IP), whereas the PEP-II/*BABAR* B factory has a more traditional collinear IP. The particle identification method also differs between *BABAR* and Belle: as will be described in section 3.4.3, *BABAR* uses quartz bars to internally reflect Čerenkov light to a backward-mounted detector (the DIRC), whereas Belle uses an aerogel Čerenkov detector. In addition, *BABAR* has a 5-layer silicon vertex detector (SVT, see sec. 3.4.1) that can perform standalone tracking, whereas Belle uses a 3-layer silicon vertex detector. In Fig. 3.1 we show a sketch of the *BABAR* detector, where we indicate the location of each subdetector. The longitudinal section is shown in Fig. 3.2. The PEP-II accelerator ceased its operations on 7^{th} April 2008, having integrated $553.5\mathrm{fb}^{-1}$. KEK-B ceased its operations in 2010, having integrated more than 1 ab^{-1}. Both machines reached luminosity values far beyond the design ones.

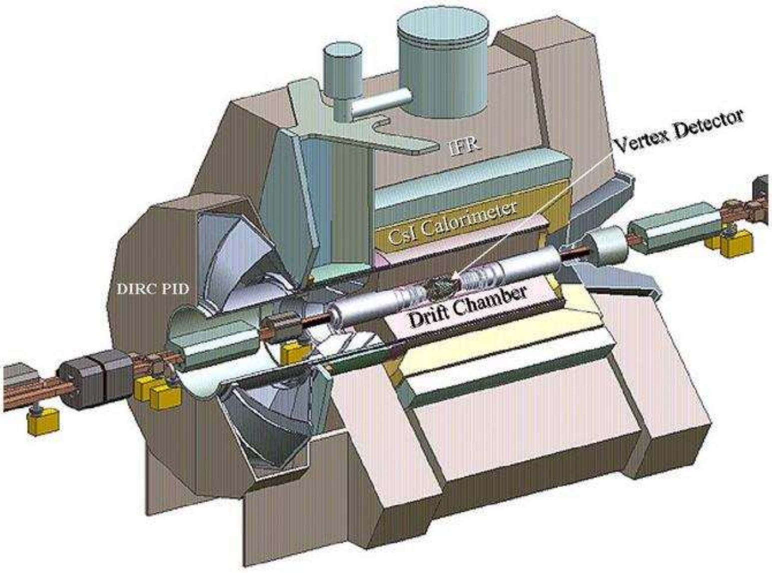

Figure 3.1: The *BABAR* detector, where each subdetector is indicated.

3.3 The PEP-II asymmetric collider

The design of PEP-II is shown in Fig. 3.3. The 9.0 GeV electrons and 3.1 GeV positrons are injected in PEP-II from the SLAC linac via bypass lines in the linac gallery. They collide in the single interaction point of PEP-II, where *BABAR* is situated. The collisions take place inside a beryllium beam-pipe, with a diameter of 2.5 cm. The beam parameters are listed in Table 3.1. PEP-II surpassed design goals both in instantaneous and in average integrated luminosity.

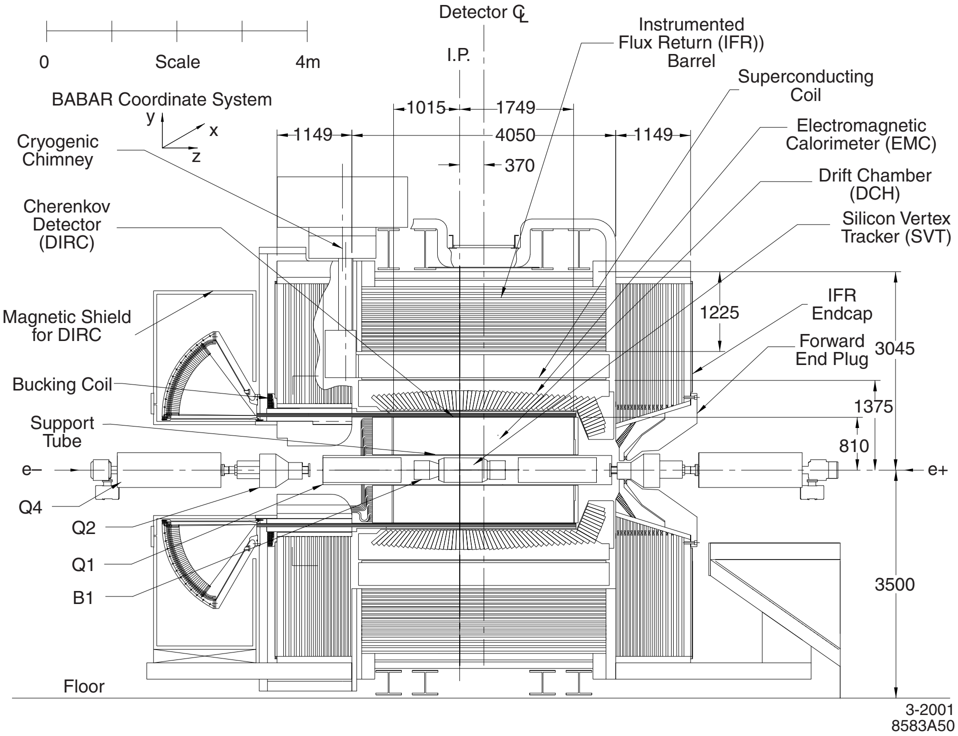

Figure 3.2: *BABAR* detector longitudinal section.

The energy in the center-of-mass system (CMS) is $\sqrt{s} = 10.58$ GeV, which corresponds to $\Upsilon(4S)$ resonance. With this configuration, the CMS moves in laboratory frame with a relativist boost of $\beta\gamma = 0.56$, which gives an average separation between the two B (coming from $\Upsilon(4S)$ decay) vertexes of $\beta\gamma c\tau = 270\,\mu$m. The cross-sections of production of fermionic pairs at CMS energy are shown in Table 3.2.

PEP-II data operations started in 1999 and ceased on 7^{th} April 2008. Most of the data were taken at the $\Upsilon(4S)$ resonance (on-peak). Approximately 10% were taken at 40 MeV below the resonance peak (off-peak), where there is no $\Upsilon(4S)$ resonance production, to provide a control sample of non-$B\overline{B}$ events in data (see Fig. 3.4). In the last period of operation PEP-II also ran at $\Upsilon(3S)$ and $\Upsilon(2S)$ resonance energies. A scan above the $\Upsilon(4S)$ region was also performed. The total integrated luminosity during the duration of the experiment was 432.89 fb^{-1} at $\Upsilon(4S)$ resonance, 30.23 fb^{-1} at $\Upsilon(3S)$ resonance, 14.45 fb^{-1} at $\Upsilon(2S)$ resonance and 53.85 fb^{-1} at off-peak energy. A plot of PEP-II integrated luminosity, *BABAR* recorded integrated luminosity as a function of time and integrated luminosity per day is shown in Fig. 3.5. During data taking, PEP-II integrated 553.48 fb^{-1}, while *BABAR* recorded 531.43 fb^{-1}(which corresponds to an efficiency of 96.0%).

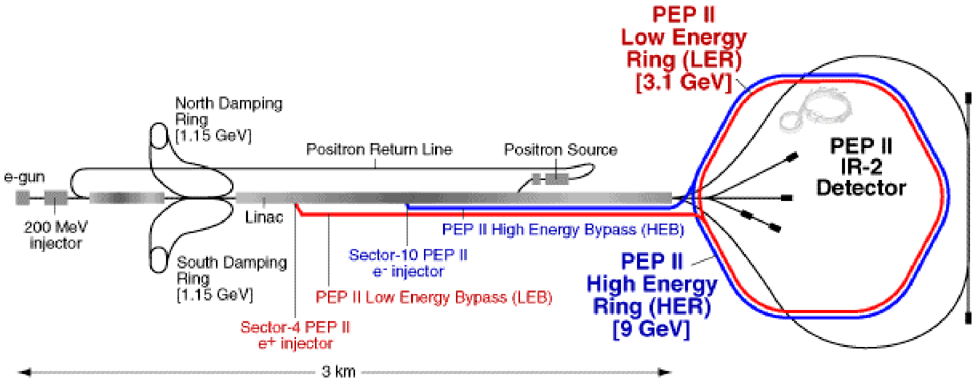

Figure 3.3: The PEP-II asymmetric storage ring and the SLAC linear accelerator. The SLAC linac is the injector for PEP-II. The single interaction point of PEP-II is at Interaction Region 2, where *BABAR* is situated.

Parameters	Design	Typical
Energy HER/LER (GeV)	9.0/3.1	9.0/3.1
Current HER/LER (A)	0.75/2.15	1.88/2.90
# of bunches	1658	1732
σ_{Lx} (μm)	110	120
σ_{Ly} (μm)	3.3	4.1
σ_{Lz} (mm)	9	1.75
Luminosity ($10^{33}\,\mathrm{cm}^{-2}\mathrm{s}^{-1}$)	3	11-12
Luminosity (pb^{-1}/d)	135	891

Table 3.1: PEP-II beam parameters. Values are given for the design and for typical colliding beam operations. HER and LER refer to the high energy e^- and low energy e^+ ring, respectively. σ_{Lx}, σ_{Ly}, and σ_{Lz} refer to the R.M.S. horizontal, vertical, and longitudinal bunch size at the IP.

$e^+e^- \rightarrow$	Cross-section (nb)
$b\bar{b}$ ($\sigma_{b\bar{b}}$)	1.05
$c\bar{c}$ ($\sigma_{c\bar{c}}$)	1.30
$s\bar{s}$ ($\sigma_{s\bar{s}}$)	0.35
$u\bar{u}$ ($\sigma_{u\bar{u}}$)	1.39
$d\bar{d}$ ($\sigma_{d\bar{d}}$)	0.35
$\tau^+\tau^-$ (σ_τ)	0.94
$\mu^+\mu^-$ (σ_μ)	1.16
e^+e^- (σ_e)	~40

Table 3.2: Cross-sections σ of production of fermionic pairs at the $\Upsilon(4S)$ mass energy in $\mathrm{nb} = 10^{-33}\mathrm{cm}^2$.

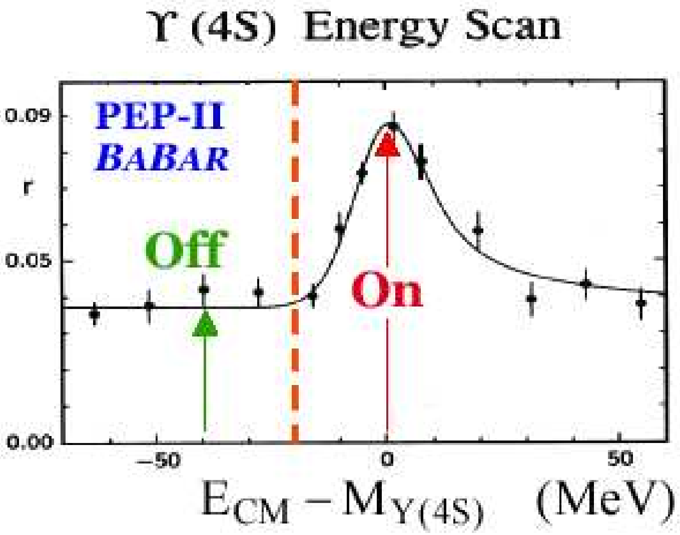

Figure 3.4: Plot of the cross-section as function of the $\Upsilon(4S)$ resonance mass and PEP-II CMS energy. We show the two regions corresponding to on-peak and off-peak energies.

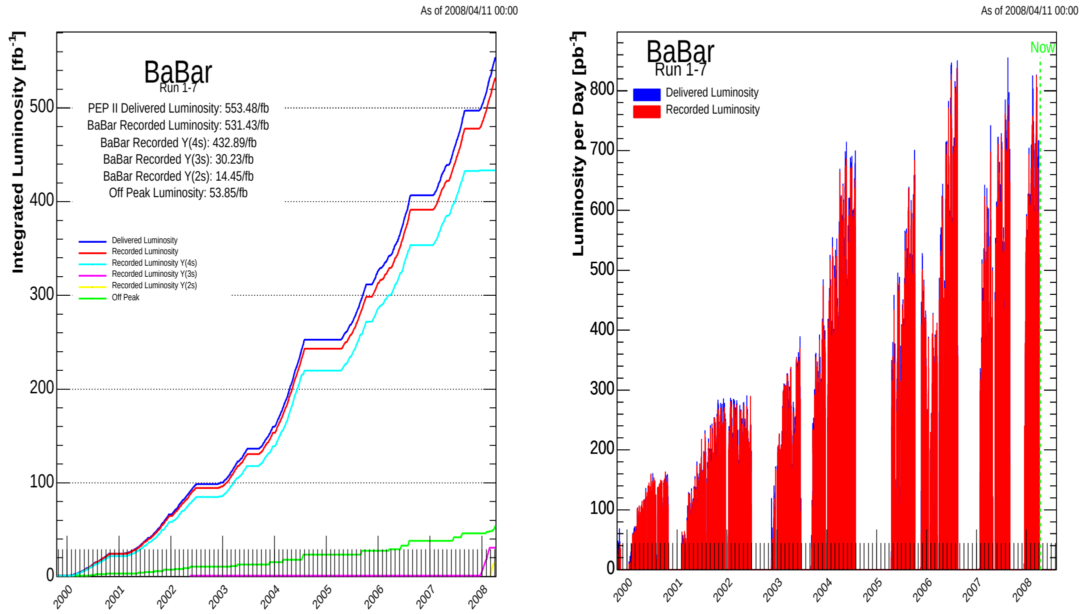

Figure 3.5: Left: PEP-II -*BABAR* integrated luminosity since startup. Right: PEP-II -*BABAR* integrated luminosity per day.

3.4 The *BABAR* detector

The *BABAR* detector resembles the other general purpose detectors used in high-energy physics, with some features that address the demandings of flavor physics analyses. Charged-particles resulting from the interaction are detected, and their momenta are measured, by a combination of five layers of double-sided silicon microstrip detectors (SVT) and a 40-layer drift chamber (DCH). Both systems operate in the 1.5 T magnetic field of a superconducting solenoid. Photons and electrons are identified in a CsI(Tl) crystal electromagnetic calorimeter (EMC). Charged-particle identification (PID) is provided by the specific energy loss ($\mathrm{d}E/\mathrm{d}x$) in the tracking devices, and by an internally reflecting, ring-imaging Čerenkov detector (DIRC). Muons and K_L^0 mesons are identified in the instrumented flux return (IFR) iron of the magnet. In the following sections we describe the several subsystems that compose the *BABAR* detector and we also discuss trigger techniques used to suppress uninteresting events. Further details may be found elsewhere [311].

3.4.1 Silicon Vertex Tracker

Together, the SVT and the DCH form the charged particle tracking system. Precise and efficient measurement of track 4-momentum is necessary for full reconstruction of many tracks final states and to provide good mass and vertex resolution. An image of fully assembled SVT is shown Fig. 3.6.

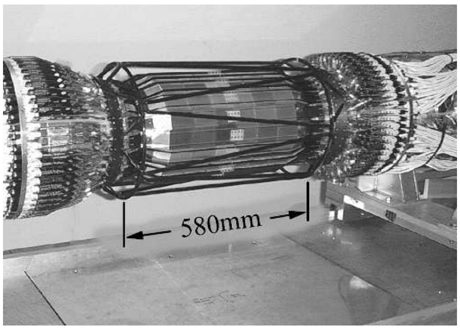

Figure 3.6: Fully assembled SVT. The silicon sensors of the outer layer are visible, as is the carbon-fiber space frame (black structure) that surrounds the silicon.

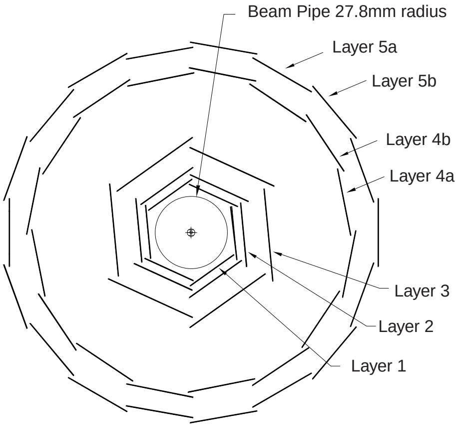

Figure 3.7: Transverse section of the SVT.

The SVT is the most important subdetector for CP-violation studies at *BABAR*, since

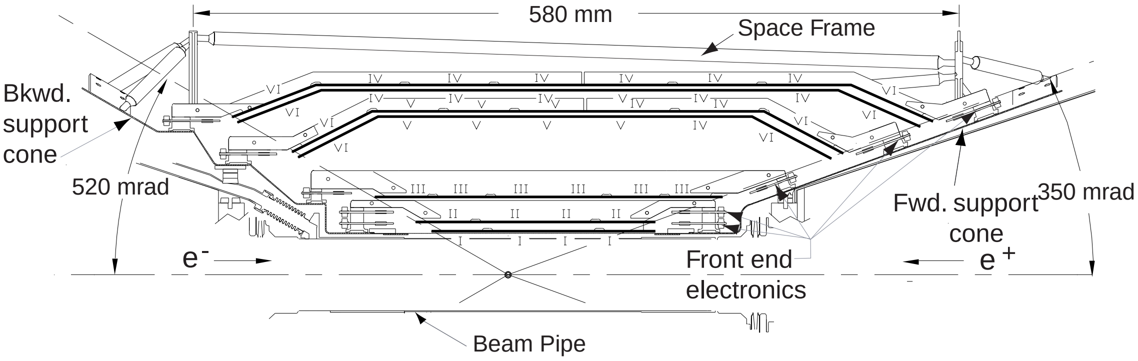

Figure 3.8: Longitudinal section of the SVT.

it provides a precise measurement of the B meson decay vertex. Furthermore, the SVT should provide standalone tracking for soft tracks with momentum less than $120\ \mathrm{MeV}/c$, which is the minimum momentum that can be reliably measured in the DCH.

The SVT is composed by five layers of double sided striplets silicon detectors (Fig. 3.7. Strips on the opposite sides of each layer are orthogonal: ϕ strips run parallel to the beam axis and z strips run transverse to the beam direction. The 5 layers and relatively long radial separation between SVT detector layers provide both standalone track pattern recognition and refinement of drift chamber tracks via addition of SVT hits.

The SVT detectors are composed of 300 μm thick n-type substrate with p^+ and n^+ strips on opposite sides. The bias voltage ranges from 25 to 35 V. The layers of the SVT are divided radially into modules, shown as line segments in Fig. 3.7. The modules in the inner 3 layers are straight along the z-axis, while those in layers 4 and 5 are arch-shaped, as shown in Fig. 3.8. The arch design was chosen to minimize the amount of silicon as well as increase the angle of incidence of tracks originating at the IP which cross the arch "*lampshades*" near the edges of acceptance. The total active silicon area is 0.96 m^2.

The strip pitch (width) varies from 50 to 210 μm depending on the layer (inner layers are more closely bonded). The strips are AC-coupled to the electronic readout. Only approximately half the strips are read out. The signal is then amplified and discriminated with respect to a signal threshold by front-end electronics. The time over threshold of the signal is related to the charge of the signal and is read out by the data acquisition system for triggered events. The resulting information on the ionization energy loss dE/dx provides a 2σ separation between kaons and pions up to a momentum of $500\,\mathrm{MeV}/c$ and between kaons and protons above $1\,\mathrm{GeV}/c$.

The offline reconstruction has the responsibility for the alignment of each SVT module. Alignment is critical for the accuracy of vertexing and of track reconstruction, and is done in two steps. The local SVT alignment uses dimuon and cosmic ray events to calibrate the relative position of each of the 340 modules. The global alignment then determines the overall position and rotation of the SVT with respect to the DCH.

The proximity of the SVT to the interaction point demands to withstand a high dose of integrated ionizing radiation, up to a lifetime-integrated dose of $2\,\mathrm{Mrad}$. To limit the exposure, the SVT includes a radiation protection system consisting of PIN diodes (doped p-type and n-type semiconductor regions separated by an intrinsic semiconducting region) and diamond diode sensors located in close proximity to the beam. These monitors can abort the colliding beams in the event of sudden high instantaneous or prolonged background levels that could damage the hardware components.

The SVT performed according to design essentially since its inception. A combined hardware and software hit-finding efficiency greater than 95% was observed, excluding the 4 (out of 208) readout sections which were defective. Single hit resolution for tracks originating from the IP averages 20 μm in both z and ϕ for hits on the inner 3 layers and 40 μm in z and 20 in ϕ for hits in the outer 2 layers.

3.4.2 Drift Chamber

The *BABAR* DCH surrounds the SVT and complete the tracking system. The DCH provides accurate momentum measurement for tracks with transverse momentum p_t larger than $100\,\mathrm{MeV}/c$. The DCH also provides particle identification information based on the measurement of the dE/dx for low momentum particles ($< 700\,\mathrm{MeV}/c$), and those in the extreme forward and backward directions that fall outside the geometric acceptance of the DIRC. Finally, reconstruction of long lived particles such as K^0_S is mainly based on DCH information.

The DCH is 3 m long, has an inner diameter of 24 cm and outer diameter of 84 cm. The final design adopted for the DCH is illustrated in Fig. 3.9. It is composed by hexagonal cells consisting of one grounded gold-coated tungsten-rhenium sense wire surrounded by six gold-coated aluminum field wires held at more than 1900 V in a 80:20 mixture of helium:isobutane gas. The choice of low-mass aluminum field-wires and of a helium-based gas mixture is aimed at reducing the material budget to limit the effect of multiple scattering on the momentum measurement. The hexagonal drift cells are arranged in 40 cylindrical layers; the layers are grouped into 10 superlayers. Two of the four layers in each superlayer are directed along the z-axis, while the other two are set at small stereo angles relative to the two axial layers, thus providing a measurement of the longitudinal (z) position of tracks with good ($\sim 1\,\mathrm{mm}$) resolution. In Fig. 3.10 we show a schematic view of the layer organization in the DCH.

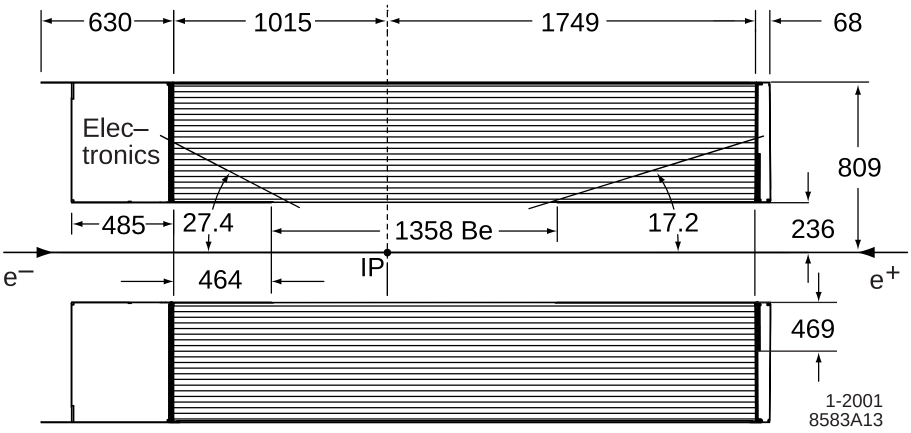

Figure 3.9: Longitudinal section of the drift chamber.

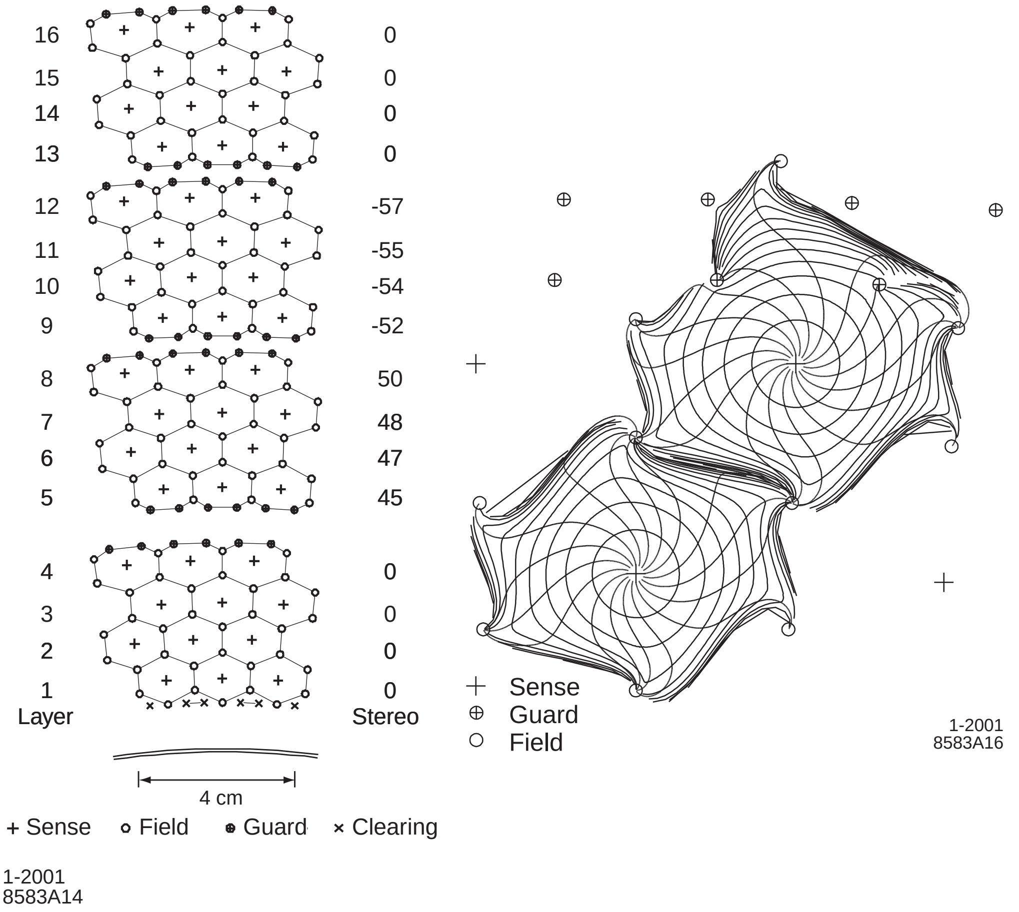

Figure 3.10: Left: schematic layout of the drift cells for the four innermost superlayers. The numbers on the right side give the stereo angles in mrad of sense wires in each layer. Right: DCH cell drift isochrones for cells in layers 3 and 4 (axial). Isochrones are at 100 ns intervals.

A charged particle coming across the DCH ionizes the gas, the electrons from the gas ionization drift trough the sense wire and are accelerated, thus producing a negative-charge shower that can be detected. The position of the primary ionization clusters is derived from timing of the leading edge of the amplified signal from the sense wire, while the total charge induced on the wire is a measure of the ionization energy loss. The DCH has a typical position resolution of $110\ \mu\mathrm{m}$, and dE/dx resolution of 7.5%, that were determined using Bhabha events. In Fig. 3.11 we show the position resolution dependence on the distance from the sense wire, as well as measured dE/dx as a function of the particle momentum

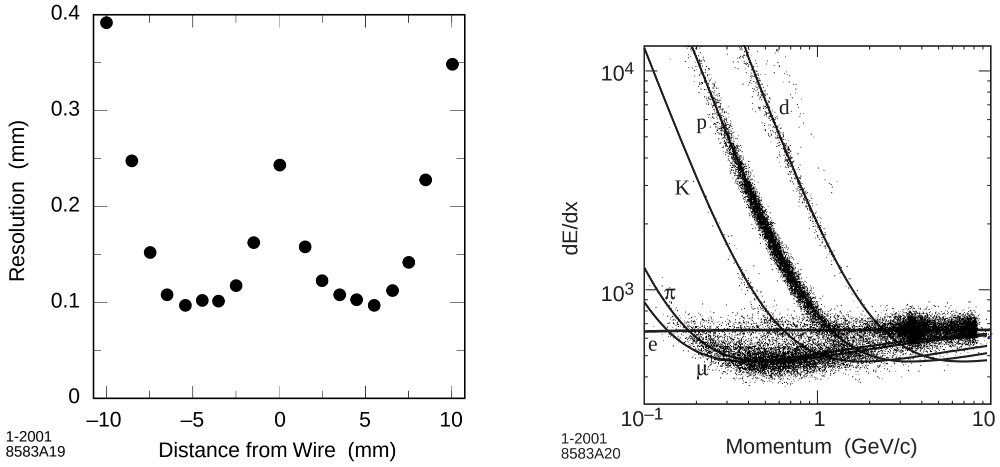

Figure 3.11: (left) DCH drift distance resolution as a function of the drift distance in the cell. (right) DCH particle identification as a function of momentum using $\mathrm{d}E/\mathrm{d}x$.

The achieved resolution on transverse momentum is

$$\sigma_{p_t}/p_t = (0.13 \pm 0.01)\% \cdot p_t + (0.45 \pm 0.03)\%, \tag{3.1}$$

where p_t is given in units of GeV/c. The first contribution comes from the curvature error due to finite spatial measurement resolution; the second contribution, dominating at the low momenta, is due to multiple Coulomb scattering.

3.4.3 Čerenkov Detector

BABAR has stringent requirements for $\pi - K$ separation over a large momentum range.

The DIRC (Detector of Internally Reflected Čerenkov light) principle uses internal reflection within quartz bars to propagate Čerenkov light to readout phototubes while preserving the Čerenkov angle. This requires extremely flat surfaces in order to avoid the dispersion of the reflected angles. The Čerenkov angle contains information on particle type via the relation $\cos\theta_c = 1/(n\beta)$, with β being the particle velocity normalized to the

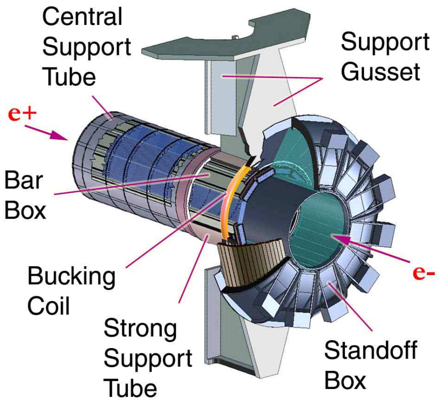

Figure 3.12: View of the DIRC mechanical structure.

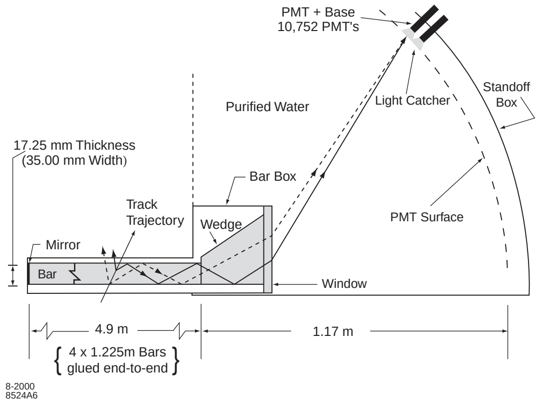

Figure 3.13: DIRC sketch showing the principle behind Particle IDentification (PID) measurements. The Čerenkov angle is preserved through specular internal reflection.

speed of light, and n being the mean refraction index ($= 1.473$ for fused silica). Fused, synthetic silica quartz bars are used as both Čerenkov radiator and light guide thanks to the excellent optical surface it allows through polishing, as well as other favorable properties such as long attenuation length, low chromatic dispersion, small radiation length, and radiation hardness. Furthermore, silica bars minimize the material to be put in front of the calorimeter. At the backward end of the bars, the photons pass through a standoff box filled with purified water that has refractive index ($n = 1.346$) similar to the silica one, so that refraction at the silica-water boundary is minimized. A mirror is placed at the opposite end the standoff box to collect light internally reflected toward the opposite end of the detector. The rear surface of the standoff box is instrumented with photomultiplier tubes (PMTs), which collect the photons, convert them to electrons with photocathodes, and amplify the signal using the gas-avalanche principle. As the standoff box is located outside the solenoid magnet, it is possible to limit the magnetic field in its volume to about 1 Gauss with a bucking coil that counteracts the field of the solenoid, so that conventional PMTs, which do not tolerate high magnetic fields, can be used. A schematic view of the DIRC and its functioning are shown in Figs. 3.12– 3.13.

The emission angle of the Čerenkov photons are reconstructed from the spacial coordinates and the timing of the PMT signals. The Čerenkov coordinates (θ_C, ϕ_C and δ_t) are then obtained via a maximum likelihood fit. The measured time resolution, *i.e.* the time interval between the t_0 of the event and the time at which an hit in the PMTs occurs, is 1.7 ns. Timing gives information on the photon propagation angles, providing an independent measurement of the Čerenkov angle, and is critical for background hit rejection, resolving ambiguities, and separation of hits from differing tracks within an event. In Fig. 3.14 we show the effect of applying PMTs timing requirements to the DIRC output in a dimuon event.

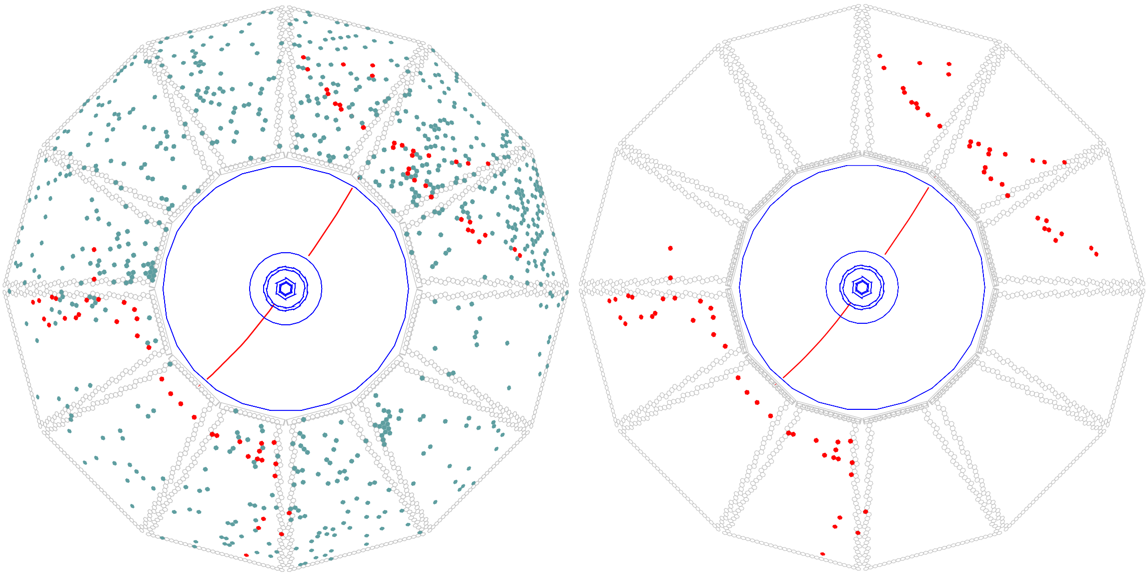

Figure 3.14: Display of an $e^+e^- \to \mu^+\mu^-$ event reconstructed in *BABAR* with two different time cuts. On the left, all DIRC PMTs with signals within the ±300 ns trigger window are shown. On the right, only those PMTs with signals within 8 ns of the expected Čerenkov photon arrival time are displayed.

The DIRC performed well throughout *BABAR*'s operational lifetime: The Čerenkov angle resolution for dimuon events was 2.5 mrad, close to the design goal of 2.2 mrad. This resulted in $\pi - K$ separation of 4.2σ at a momentum of $3\ \mathrm{GeV}$. The distributions of the Čerenkov angle, as function of the momentum, for a control sample of π and K are shown in Fig. 3.15.

3.4.4 Electromagnetic Calorimeter

The design parameters for the *BABAR* EMC are driven by the requirements of precisely measuring energies over a spectrum from 20 MeV up to 9 GeV, in a 1.5 T magnetic field and a high radiation environment. At the high end of the energy spectrum, measurements of QED processes such as Bhabha and two-photon scattering, as well as (at slightly lower energies) photons from the critical physics processes $B^0 \to \pi^0\pi^0$ and $B^0 \to K^*\gamma$ decays, present the motivating incentive. The need for efficient detection of photons from high multiplicity B decays containing π^0's determines the requirement for the low end of the energy spectrum.

BABAR uses a thallium-doped cesium iodide (CsI(Tl)) crystal calorimeter in order to achieve the necessary energy and angular resolution to meet these physics requirements.

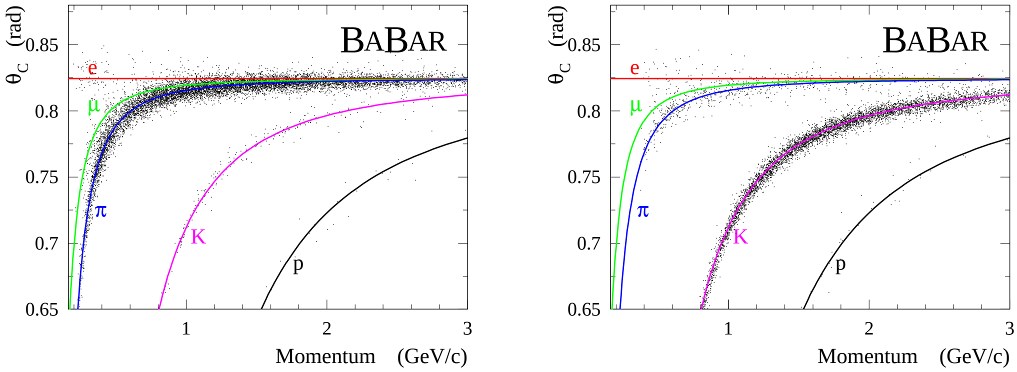

Figure 3.15: Čerenkov angle distributions, as a function of the momentum, for (left) π and (right) K events from control sample. The control sample used is $D^{*+} \rightarrow D^0\,(\rightarrow K^-\pi^+)\,\pi^+$.

The EMC is formed by a cylindrical barrel and a conical endcap. The longitudinal section of the EMC is shown in Fig. 3.16. The crystals have nearly square front and rear faces, with a trapezoidal longitudinal cross-section. Two silicon PIN diodes mounted on the rear face of each crystal are used to readout the scintillation light. The section of a typical EMC crystal is shown in Fig. 3.16

Several calibrations of the EMC were performed, by the use of a neutron source, a xenon flash light pulser system, high energy photons from Bhabha process, and low energy photons from a π^0 control sample. The clustering pattern recognition uses a seed crystal algorithm to recognize energy clusters. Local energy maxima within a cluster are used (if there are more than 1) to separate the cluster into bumps. Charged particle tracks are associated with bumps using a χ^2 consistency requirement.

Energy resolution, using $\chi_{c1}\rightarrow J/\psi\,\gamma$ and Bhabha scattering events, was found to be

$$\frac{\sigma_E}{E} = \frac{(2.32 \pm 0.30)\%}{\sqrt[4]{E(\mathrm{GeV})}} \oplus (1.85 \pm 0.12)\% \qquad (3.2)$$

and angular resolution, using π^0 and η decays, was found to be

$$\left(\frac{3.87 \pm 0.07}{\sqrt{E(\mathrm{GeV})}} + 0.00 \pm 0.04\right) \mathrm{mrad}. \qquad (3.3)$$

In both cases, the first term is due to fluctuations in the number of photons and to electronic noise of the photon detector and electronics, while the second term arises from the non-uniformity of light collection, leakage and absorption due to materials between and in front of the crystals, and calibration uncertainties.

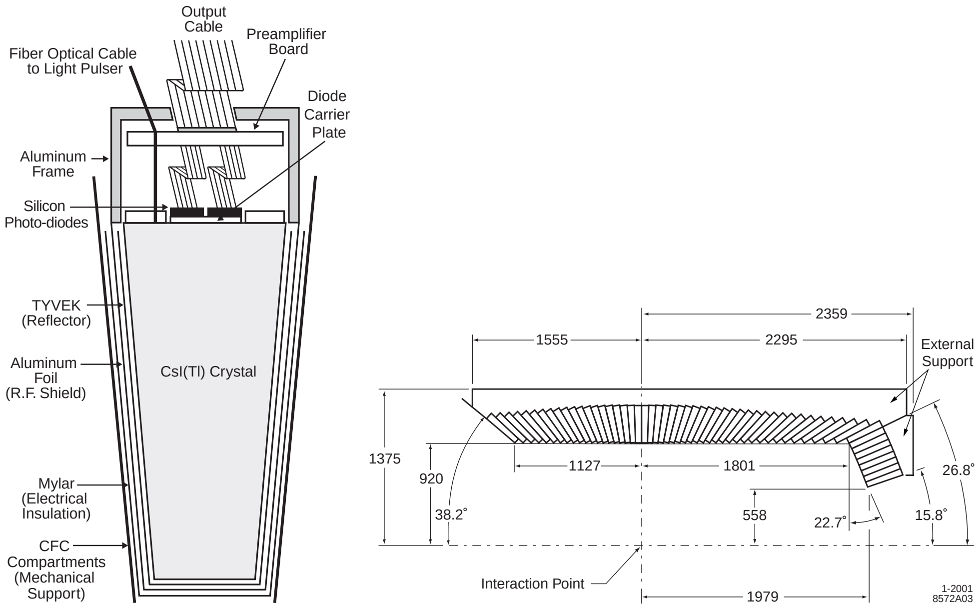

Figure 3.16: (left) Schematic of a wrapped CsI(Tl) crystal and read out package. (right) Longitudinal cross-section of the EMC; dimensions are in mm.

3.4.5 Instrumented Flux Return

Detection of neutral hadrons (primarily K_L^0's) and muons is necessary for several *BABAR* analyses: muons are important for J/ψ reconstruction, semileptonic B decays studies, and B flavor tag; K_L^0 reconstruction is critical for the $B^0 \to J/\psi K_L^0$ and $B^0 \to \eta' K_L^0$ channels. The main requirements of the *BABAR* IFR is a large coverage angle and a good discrimination efficiency for muons with momentum as low as 1 GeV/c.

The IFR is composed of one barrel region and two endcaps. Its layout is illustrated in Fig. 3.17. The IFR uses the steel flux return of the magnet as a muon filter and hadron absorber. It was originally equipped with layers of resistive plate chambers (RPCs) In addition, two layers of cylindrical RPCs were installed between the EMC and the cryostat of the magnet to improve the matching between IFR and EMC showers. Resistive plate chambers consist of two highly-resistive bakelite planes closely separated by a gap filled with a gas mixture, held at a large potential voltage. The inside surface of the bakelite is smoothed with a linseed-oil coating, so that the electric field is uniform, thus preventing discharges in the gas and large dark currents. The RPCs operate in "*streamer*" mode: particles passing through the chamber ionize the gas, and the applied high voltage accelerates the resulting electrons into a controlled gas-discharge avalanche. The streamer signal is collected by inducing a charge in capacitatively-coupled read-out strips outside the RPC. The gas gain in streamer mode is sufficient to produce a large signal independent of initial ionization, greatly simplifying the electronics read-out. A cross-sectional diagram of

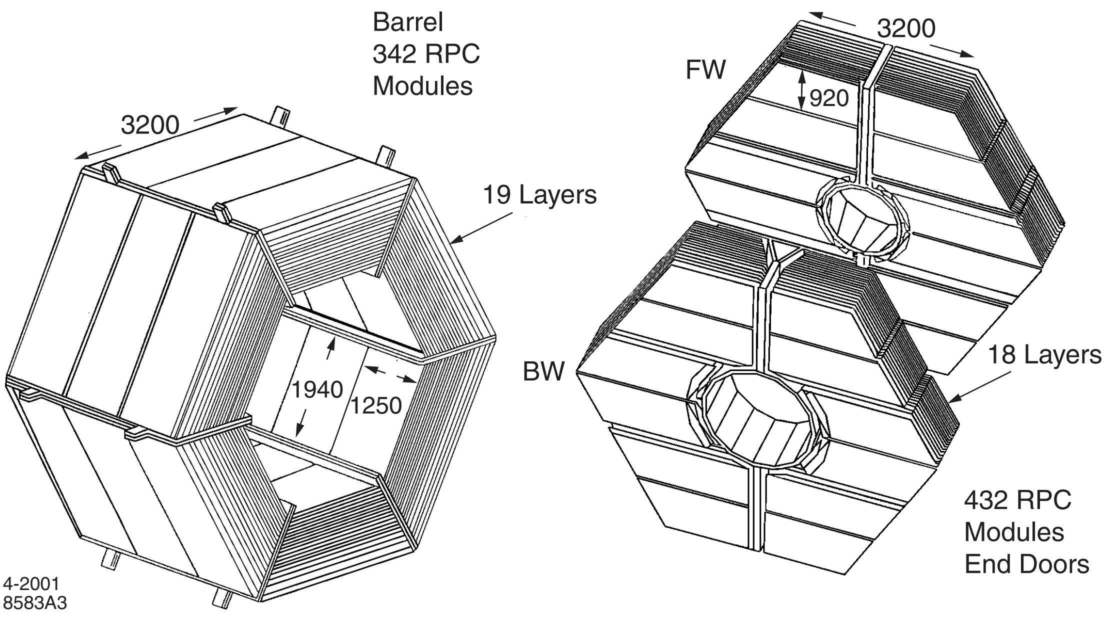

Figure 3.17: Overview of the barrel sectors and forward and backward end doors of the IFR. The shape of the RPC modules and their dimensions in mm are indicated.

a planar RPC is shown in Fig. 3.18.

During the first year of operation, a large fraction of the RPC modules suffered significant losses in efficiency. It was found that linseed-oil droplets had formed on the inner surface of the bakelite plates, probably because of high operating temperatures ($> 37^\circ$ C). These accumulating droplets, under the high electric field, could “*bridge the gap*” between the plates, leading to discharge and large detector dead areas. In 2002, new RPCs constructed under much stricter tolerances were installed into the forward endcap. The backward endcap was not retrofitted, as its acceptance in the CM frame is small. In the barrel, the RPCs were replaced with limited streamer tubes (LST) during two installation phases, in 2004 and 2006.

The LSTs consist of a PVC gas-filled cells with grounded graphite-coated walls and a central gold-plated beryllium-copper anode wire held at high voltage (Fig. 3.19 and Fig. 3.20). Similar to RPCs, the gas operates in streamer mode when ionized, with the charge collected on the high voltage sense wire while simultaneously inducing a charge on a plane, which is mounted below the tube. The LSTs are mounted with the wire directed along the beam, thus providing information about the azimuthal angle of the hit. The induced charge on the plane is detected using copper strips perpendicular to the wire direction and conveys the z coordinate.

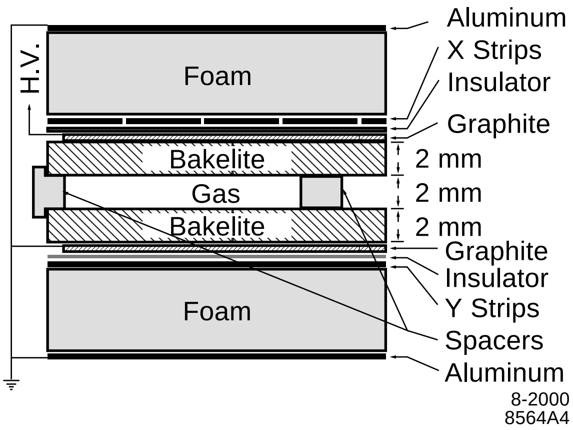

Figure 3.18: Cross-section of a *BABAR* RPC.

Figure 3.19: Sketch of an 8-cell module (top), and photo of an LST partially inserted in the sleeves (shown at the bottom of the picture).

3.4.6 Trigger

The *BABAR* trigger needs to select interesting events with high efficiency, while rejecting most of the background arising from physical processes such as Bhabha events. The total output rate should not be higher than 120 Hz, to satisfy computing limitations of the

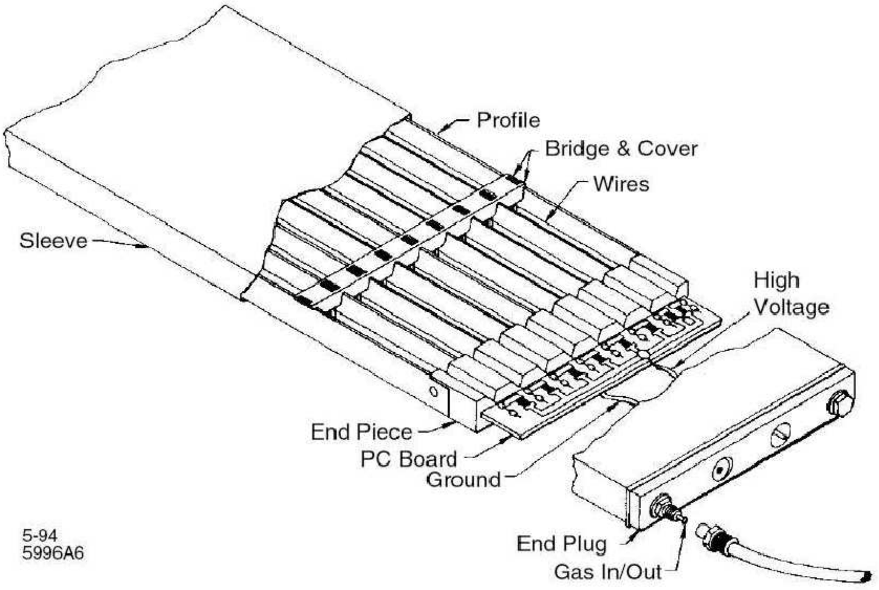

Figure 3.20: Diagram of a prototypical limited streamer tube.

offline processing farm. Events with either a DCH track or a $> 100\ \mathrm{MeV}$ EMC cluster occur at 20 kHz, thus the trigger is responsible for scaling this rate down by a factor of more than 150 while accepting over 99% of B events, 95% of hadronic continuum, and 90% of $\tau^+\tau^-$ events. The trigger should also be flexible enough to deal with changing background conditions.

The *BABAR* trigger is implemented in two levels, a Level 1 hardware trigger (called L1), and a Level 3 software trigger (called L3); a Level 2 trigger is used in some other high energy particle physics experiments, but was not needed for *BABAR*.

The L1 trigger uses information from basic tracks reconstruction from the DCH and presence of energy deposit in the EMC to trigger interesting events. It may also trigger independently on DCH and EMC by using IFR information to trigger events with muons or cosmic rays. The combined L1 Trigger efficiency is larger than 99.9% for generic $B\overline{B}$ events, 99% for continuum, and 94.5% for $\tau^+\tau^-$ events.

The L3 trigger refines the selection from L1 trigger, to further reduce background events. The L3 DCH algorithm fits L1 tracks to helices and is able to determine the impact parameter of the tracks. The impact parameter information allows to efficiently reject machine backgrounds such as beam-gas interactions. Events that passes the L3 trigger are then stored to be reprocessed offline and used in analyses.

Chapter 4

Analysis of $\gamma\gamma \to \mathrm{K^0_S K^\pm}\pi^\mp$ and $\gamma\gamma \to \mathrm{K^+K^-}\pi^+\pi^-\pi^0$

4.1 Introduction

This thesis is aimed at studying the $\gamma\gamma \to K^0_S K^\pm \pi^\mp$ and $\gamma\gamma \to K^+ K^- \pi^+ \pi^- \pi^0$ process[1].

The $\gamma\gamma \to K^0_S K^\pm \pi^\mp$ process is known to show clear $\eta_c(1S)$ [158, 196, 314] and $\eta_c(2S)$ [196, 315] signals. The $\eta_c(2S)$ parameters are measured with poor experimental precision [49]. To date, the most precise single measurement of $\eta_c(2S)$ width was obtained by *BABAR* in this process with a dataset corresponding to 88 fb^{-1} [315]. Belle recently reported a measurement [157] with a better precision with respect to that of the *BABAR* one [315]. We update the *BABAR* measurement by using the final *BABAR* dataset corresponding to 519.2 fb^{-1} of data to provide a precise measurement of the $\eta_c(2S)$ mass and width. The $\chi_{c0}(1P)$ cannot decay to $K^0_S K^\pm \pi^\mp$, due to spin-parity conservation that forbids the decay of a $J^P = 0^+$ resonance to this final state [2].

The $\gamma\gamma \to K^+ K^- \pi^+ \pi^- \pi^0$ process has never been studied before. A search for the $\eta_c(2S)$ decay to $K^+ K^- \pi^+ \pi^- \pi^0$ in the $\psi(2S) \to \gamma \eta_c(2S)$ process was performed by CLEO [162], but no significant signal was found, probably due to the small production rate [155]. The decay of the $\chi_{c2}(1P)$ to $K^+ K^- \pi^+ \pi^- \pi^0$ was studied by CLEO [316, 317] resulting in a preliminary unpublished result. The only $\eta_c(2S)$ exclusive decay mode observed so far is $K\bar{K}\pi$ [49]. Belle presented a preliminary observation of $\eta_c(2S)$ decay

---

[1] According to the convention commonly used in the spectroscopy field, we use the notation $\gamma\gamma \to X$ to refer to the $e^+e^- \to \gamma\gamma e^+e^- \to X e^+e^-$ process.

[2] The decay proceeds via strong interaction, so both J and P are conserved. In the $K^0_S K^\pm \pi^\mp$ system, let l_1 be the angular momentum between K^0_S and $K^\pm$, and l_2 the angular momentum between $\pi^\mp$ and the $K^0_S K^\pm$ system. The final state has $P = (-1)^{1+l_1+l_2}$. Since the final state spin S is equal to 0, $J = l_1 + l_2$. Thus, $J = 0$ implies $l_1 = l_2$ and $P = -1$.

to six prong final states [201]. We study the $K^+K^-\pi^+\pi^-\pi^0$ decay mode to investigate possible decays of $\eta_c(1S)$, $\chi_{c0}(1P)$, $\chi_{c2}(1P)$, and $\eta_c(2S)$ to this final state.

The $\chi_{c2}(2P)$ resonance was observed in two-photon production decaying to $D\overline{D}$ by Belle [204], and subsequently confirmed by *BABAR* [205]. We search for its possible decay into the $K^0_S K^\pm\pi^\mp$ and $K^+K^-\pi^+\pi^-\pi^0$ final states.

We restrict our study to *no-tag* events.

4.2 Data and Monte Carlo samples

The analysis presented in this thesis is based on the final dataset accumulated by *BABAR* in the period 1999-2008. Data were collected at energies corresponding to the mass of the $\Upsilon(nS)$ (nS = 2, 3, 4) resonances (on-peak). About 10% of data were collected at an energy tens of MeV lower than the $\Upsilon(nS)$ (nS = 2, 3, 4) resonances mass (off-peak). The total integrated luminosity used in this analysis is equal to 519.2 fb^{-1}. The breakdown of this total luminosity in different samples is: 429.0 fb^{-1} $\Upsilon(4S)$ on-peak, 44.8 fb^{-1} $\Upsilon(4S)$ off-peak, 28.0 fb^{-1} $\Upsilon(3S)$ on-peak, 2.4 fb^{-1} $\Upsilon(3S)$ off-peak, 13.6 fb^{-1} $\Upsilon(2S)$ on-peak, and 1.4 fb^{-1} $\Upsilon(2S)$ off-peak.

The production of Monte Carlo (MC) events is centralized and uses tools shared among the *BABAR* Collaboration. The production and decay of $B\overline{B}$ meson pairs and of the unstable particles is simulated by using the `EvtGen` generator [318]. The hadronization of quarks is modeled by using the JETSET generator [319]. The detector response is modeled by using a GEANT4-based Monte Carlo simulation [320], taking into account the varying accelerator and detector conditions. Large samples of simulated events are used to study the background arising from random combinations of particles in non-$\gamma\gamma$ events. The simulated dataset samples correspond to 786.3 fb^{-1} for $q\bar{q}$ $(q = u, d, s)$ events, 868.1 fb^{-1} for $c\bar{c}$ events, 726.1 fb^{-1} for $\tau^+\tau^-$ events, and 1.3 ab^{-1} for both $B^0\overline{B}^0$ and B^+B^- events.

The simulation of two-photon events is performed by using the `GamGam` two-photon event generator [205]. The `GamGam` generator uses the BGMS formalism [321], and was originally developed for the CLEO experiment and later adapted to *BABAR* and used in previous two-photon analyses [205, 315]. In the process involving quasi-real photons, the differential cross-section for the $e^+e^-\to\gamma\gamma\to X, X\to f$ process is given by

$$\sigma(e^+e^-\to\gamma\gamma\to X\to f) = L \times F \times \sigma(\gamma\gamma\to X) \times \mathcal{B}(X\to f), \tag{4.1}$$

where L is the two-photon flux, F is a form factor, $\mathcal{B}(X\to f)$ is the branching fraction of the X decay to the final state f, and

$$\sigma(\gamma\gamma\to X) = \int 4\pi(2J+1)(\hbar c)^2 m_X^3 \frac{\Gamma_{\gamma\gamma}}{\sqrt{K}m} \frac{\Gamma_{tot}}{(m^2 - m_X^2)^2 + m_X^2\Gamma_{tot}^2} \mathrm{dm}^2, \qquad (4.2)$$

holds for a resonance of mass m_X, width Γ_{tot} and spin J. Here $K = (q_1 q_2)^2 - q_1^2 q_2^2$, where q_i is the four-momentum of the interacting photon. The form factor F accounts for the extrapolation of the process to virtual photons and is not known *a priori*. We use the model proposed in Ref. [322]

$$F = \left(\frac{1}{1 - q_1^2/m_v^2}\right)^2 \times \left(\frac{1}{1 - q_2^2/m_v^2}\right)^2, \qquad (4.3)$$

with m_v being the mass of an appropriate vector boson (ρ, J/ψ, Z^0). Since we are interested in studying charmonium states, we use $m_v = m(J/\psi)$. The size of MC samples used to characterize the different signals is reported in Table 4.1.

$\gamma\gamma\to\eta_c(1S)\to K_S^0 K\pi$ 4.2M	$\gamma\gamma\to\chi_{c2}\to K_S^0 K\pi$ 427K	$\gamma\gamma\to\eta_c(2S)\to K_S^0 K\pi$ 417K
$\gamma\gamma\to\eta_c(1S)\to K^+K^-\pi^+\pi^-\pi^0$ 4.2M	$\gamma\gamma\to\chi_{c0}\to K^+K^-\pi^+\pi^-\pi^0$ 427K	$\gamma\gamma\to\chi_{c2}\to K^+K^-\pi^+\pi^-\pi^0$ 427K
$\gamma\gamma\to\eta_c(2S)\to K^+K^-\pi^+\pi^-\pi^0$ 427K	$\gamma\gamma\to Z(3930)\to K_S^0 K^\pm\pi^\mp$ 427K	$\gamma\gamma\to Z(3930)\to K^+K^-\pi^+\pi^-\pi^0$ 427K

Table 4.1: Monte Carlo signal events dataset sizes.

4.3 Reconstruction of the decay chain

We reconstruct the decays $\gamma\gamma\to K_S^0 K\pi$ and $\gamma\gamma\to K^+K^-\pi^+\pi^-\pi^0$. Furthermore we reconstruct the decay $\gamma\gamma\to K^+K^-\pi^+\pi^-$ that is used as control sample. The K_S^0 and π^0 mesons are reconstructed in their dominant decays $K_S^0\to\pi^+\pi^-$ and $\pi^0\to\gamma\gamma$.

4.3.1 Charged tracks reconstruction

Charged particle tracks are reconstructed from the spatial hits in the SVT and the DCH. Charged particles trajectory in *BABAR* solenoidal magnetic field is expected to be an helix. Multiple scattering, energy loss in material and inhomogeneities of the magnetic field can distort the trajectory. An iterative Kalman filter technique [323] is used to perform the pattern recognition of the piecewise-helix trajectory and to determine for each track the five parameters of the helix. The full map of the solenoidal magnetic field, the detailed distribution of the material in the detector, and the expected energy loss of the particle as it traverses the detector are taken into account in the algorithm. Dedicated algorithms are used to improve the determination of the trajectory and vertex, identify tracks coming from interaction in the material and decay-in-flight, and to reject *ghosts*, *i.e.* non-physical tracks that arise as reconstruction artifacts.

With the exception of the pions from the K^0_S decay, charged tracks produced in two-photon collisions are expected to originate from the interaction points. For such tracks, the distance of the point of closest approach of the track to the interaction point is required to be less than $1.5\ \mathrm{cm}$ in the XY plane (transverse to the magnetic field) and less than $2.5\ \mathrm{cm}$ along the Z direction (parallel to the magnetic field). We further require the maximum momentum of the track to be less than $|\mathbf{p}| < 10\,\mathrm{GeV}/c$, in order to remove tracks that are badly reconstructed.

In order to suppress both low-tracks-multiplicity background from QED and $\tau^+ \tau^-$ events, and high-tracks-multiplicity background from $e^+e^- \to q\bar{q}$ $(q = u, d, s, c)$ production or $B\overline{B}$ events, we require to have exactly four charged tracks in the event.

4.3.2 Charged tracks identification

Prompt charged tracks coming from the interaction point are required to be positively identified as either pions of kaons.

The π/K separation is achieved by classifiers based on boosted or bagged decision trees that use both global, such as total track momentum, and local information from detectors subsystems, such as the tracking system, the DIRC and the EMC. The most important PID information comes from the specific ionization energy loss dE/dx measured in the SVT and in the DCH, the ratio between the track energy as measured in the EMC and its momentum, the Čerenkov angle θ_C, and the number N_γ of Čerenkov photons reconstructed in the DIRC. In order to improve the discrimination power, some of these variables are combined using a likelihood ratio technique, whose output is then used as an input for the boosted decision tree classifier.

Several PID classifiers are available in the *BABAR* analysis framework for pions, kaons, protons, electrons and muons. Also, each classifier can be used requiring a higher or smaller purity (thus resulting in a smaller or higher detection efficiency) of the selected sample.

Auxiliary studies performed by using high-purity control samples, show that PID classifiers used in this analysis have a selection efficiency of 98% and 87%–95%, for pions and kaons, respectively. The probability of a pion to be misidentified as a kaon is smaller than 2%. The probability of a kaon to be misidentified as a pion may be as large as about 10%. The probability of an electron to be misidentified as a pion is 1.5%, and the probability to be misidentified as a kaon is as large as 20%.

4.3.3 π^0 reconstruction

A photon candidate is obtained as a single EMC cluster that cannot be associated to any track in the SVT or DCH. We require the photon energy E_γ to be larger than $30\ \mathrm{MeV}$. A π^0 candidate is obtained by combining two photons. We constrain the π^0 mass to be equal to its nominal value [49]. We reject π^0 candidates with a $\gamma\gamma$ invariant mass not in the range [0.100,0.160] GeV/c^2, or with an energy in the laboratory frame smaller than 0.200 GeV.

We use signal MC events to optimize π^0 selection criteria in the $K^+K^-\pi^+\pi^-\pi^0$ decay mode. Spurious π^0 signals arise from random photon combinations and constitute a large source of background in this decay mode. To discriminate well-reconstructed π^0 from fakes, we check if the reconstructed particle is associated to a MC π^0 at generation level. If this is the case, we classify the reconstructed π^0 as "*Well-Reconstructed*" (WR) π^0, otherwise we classify it as "*Mis-Reconstructed*" (MR) π^0. In Fig. 4.1, we show the distributions, for WR π^0, MR π^0, and different background samples, of the following variables:

– $E_\gamma^{(1)}$: the momentum of the most energetic photon from π^0 decay.

– $E_\gamma^{(2)}$: the momentum of the least energetic photon from π^0 decay.

– $\mathcal{H}_{\pi^0}$: defined as the absolute value of the cosine between the direction of one of the π^0's daughters and of π^0 mother recoil, in π^0 rest frame.

In Fig. 4.2 we show the low-energy region of the $E_\gamma^{(1)}$ and $E_\gamma^{(2)}$ distributions. The shape of $E_\gamma^{(1)}$ is similar for WR and MR signal events, so we do not apply any further requirement on this variable. We optimize a requirement on $E_\gamma^{(2)}$ and $\mathcal{H}_{\pi^0}$. Such variables are correlated at 50% level in both signal and backgrounds. Thus, we decide to perform a two-dimensional optimization on both variables at the same time, to take correlations into account. The optimization is performed by using 60×10^3 WR signal events as signal sample and 30×10^3 MR signal as background sample. We maximize the figure of merit $n_s/\sqrt{n_s + n_b}$, where n_s and n_b are the number of WR and MR signal events surviving the requirements, respectively. We use 15×10^2 independent WR signal events and 8×10^3 independent MR signal events as testing sample, in order to validate our optimization procedure. We find the optimal requirements to be $E_\gamma^{(2)} > 50\ \mathrm{MeV}$, and $\mathcal{H}_{\pi^0} < 0.95$.

4.3.4 K^0_S reconstruction

The $K^0_S \to \pi^+\pi^-$ decay is reconstructed by combining two charged tracks with pion mass hypothesis. We constrain the K^0_S mass to be equal to its nominal value [49]. We do not

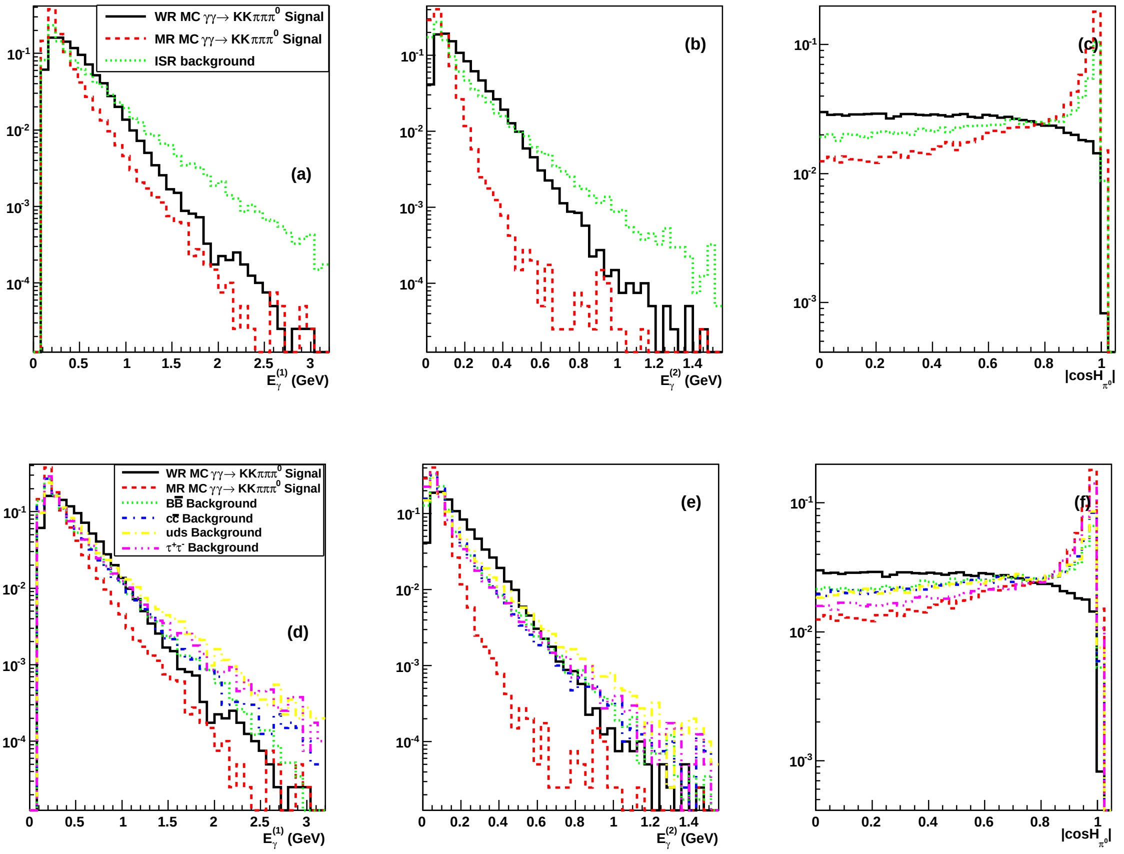

Figure 4.1: Distributions of (a) $E_\gamma^{(1)}$, (b) $E_\gamma^{(2)}$, and (c) $\mathcal{H}_{\pi^0}$ for $\gamma\gamma\to K^+K^-\pi^+\pi^-\pi^0$ MC WR signal (solid black), MR signal (red dashed), and ISR $K^+K^-\pi^+\pi^-\pi^0$ MC background (green dotted); (d) $E_\gamma^{(1)}$, (e) $E_\gamma^{(2)}$, and (f) $\mathcal{H}_{\pi^0}$ for $\gamma\gamma\to K^+K^-\pi^+\pi^-\pi^0$ MC WR signal (solid black), MR signal (red dashed), generic $B\overline{B}$ MC background (green dotted), generic $c\overline{c}$ MC background (blue line-dashed), generic uds MC background (yellow line-dotted), and generic $\tau^+\tau^-$ MC background (magenta dot-three points).

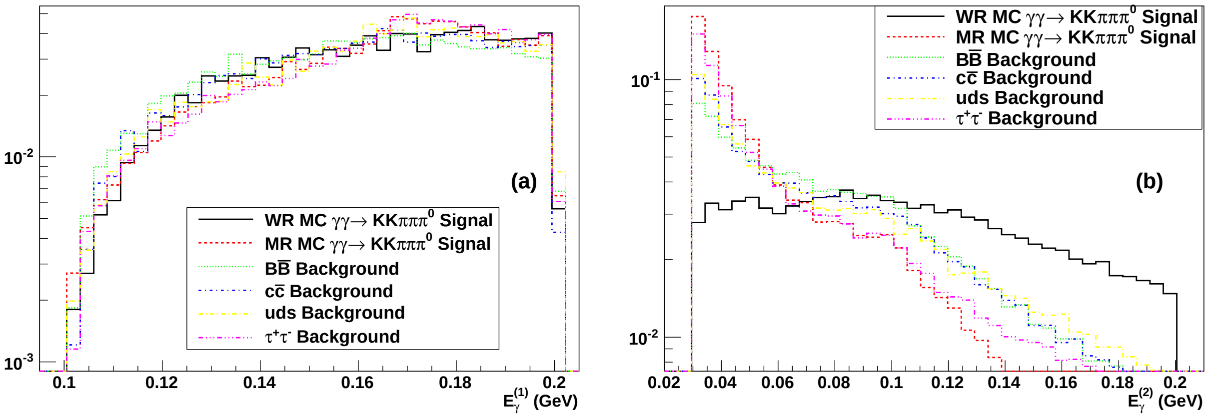

Figure 4.2: Distributions of (a) $E_\gamma^{(1)}$ and (b) $E_\gamma^{(2)}$, in the low-energy region for $\gamma\gamma \to K^+K^-\pi^+\pi^-\pi^0$ MC WR signal (solid black), MR signal (red dashed), generic $B\overline{B}$ MC background (green dotted), generic $c\bar{c}$ MC background (blue line-dashed), generic uds MC background (yellow line-dotted), and generic $\tau^+\tau^-$ MC background (magenta dot-three points).

apply any PID requirement or any condition on the origin point of the tracks. We require the reconstructed dipion mass to be in the range [0.470,0.520] GeV/c^2.

4.3.5 Resonance candidate reconstruction

A resonance candidate is obtained by fitting the relevant number of tracks and one K_S^0 or π^0 candidate to a common vertex. We require the vertex fit to have a probability larger than 0.1%. We require the total charge of the tracks to be equal to zero.

4.4 Two-photon events identification

In this section we describe criteria used to select two-photon events with high efficiency, while rejecting most of the $q\bar{q}$ annihilation and ISR background. As outlined in sec. 2.2.3, the amount of activity in the EMC, and the shape of the kinematical variables M^2_{miss} and p_T can be used to achieve such a discrimination.

4.4.1 Rejection of EMC noise background

Two-photon events are characterized by a low activity in the EMC. To exploit this feature we study the following variables:

– *Number of extra photons (N_γ)*: the number of reconstructed photons excluding the photons expected in signal.

- *Number of extra* π^0 *(*N_{π^0}*)*, the number of reconstructed π^0 excluding the π^0 expected in signal.

In Fig. 4.3 we show N_γ and N_{π^0} distributions for different kind of signal and background events. We require $N_{\pi^0} \leq 3$ and $N_\gamma \leq 6$ for $K^+K^-\pi^+\pi^-\pi^0$, and $N_{\pi^0} \leq 1$ and $N_\gamma \leq 5$

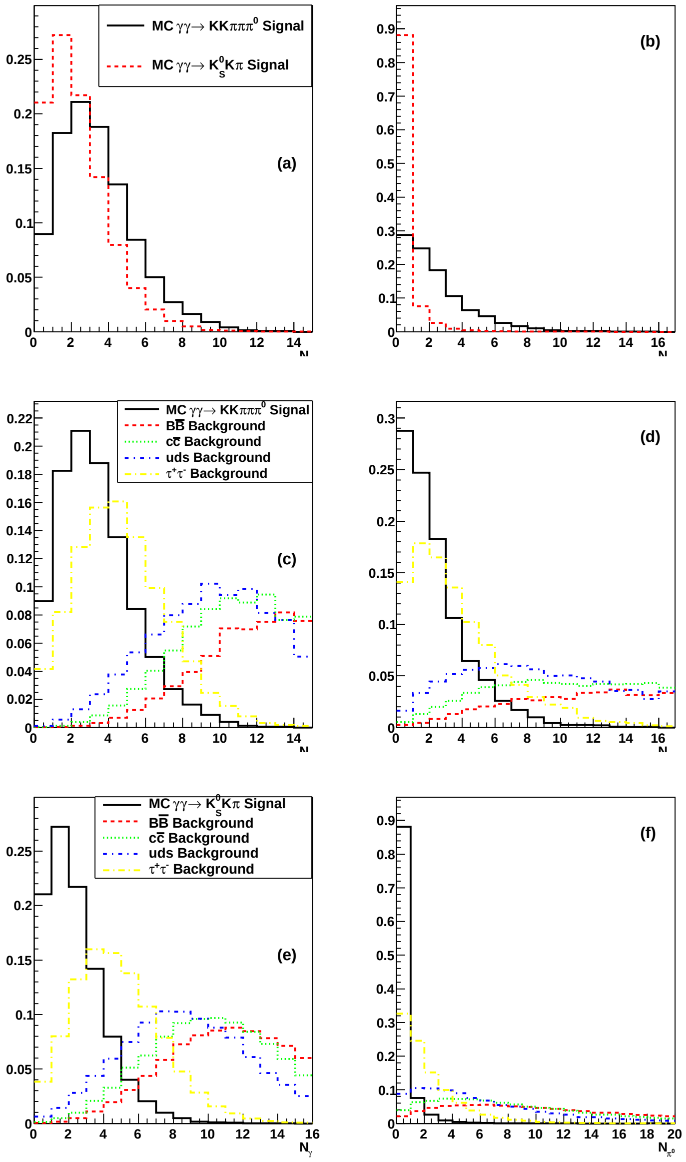

Figure 4.3: Distributions of N_γ and N_{π^0} for (a-b) $\gamma\gamma\to K^+K^-\pi^+\pi^-\pi^0$ (solid black) and $\gamma\gamma\to K^0_S K^\pm\pi^\mp$ MC signal (red dashed). Distributions of N_γ and N_{π^0} for (c-d) $\gamma\gamma\to K^+K^-\pi^+\pi^-\pi^0$ (e-f) and $\gamma\gamma\to K^0_S K^\pm\pi^\mp$ MC signal (solid black), compared to several backgrounds: generic $B\overline{B}$ MC background (red dashed), generic $c\overline{c}$ MC background (green dotted), generic uds MC background (blue line-dashed), and generic $\tau^+\tau^-$ MC background (yellow line-dotted).

for $K_S^0K^\pm\pi^\mp$. In Fig. 4.4 we show the p_T distribution for $K^+K^-\pi^+\pi^-\pi^0$ and $K_S^0K^\pm\pi^\mp$ data samples, and the effect of applying the N_γ and N_{π^0} requirements. We observe a clear peaking structure at $p_T \sim 0\mathrm{GeV}/c$ in both decay modes, characteristic of two-photon events. No peak is observed in the distribution of events rejected by the requirements. This indicates that two-photon events survive the selection with high efficiency.

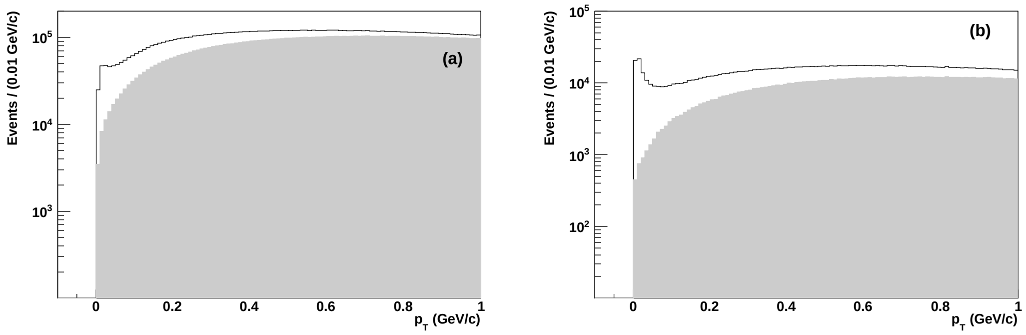

Figure 4.4: Distributions of p_T for (a) $K^+K^-\pi^+\pi^-\pi^0$ and (b) $K_S^0K^\pm\pi^\mp$ data sample before (no filling) applying requirements on N_{π^0} and N_γ, and the events rejected by these requirements (gray filled).

As an independent check of the effect of such requirements, we use the $K^+K^-\pi^+\pi^-$ control sample, where prominent $\eta_c(1S)$, $\chi_{c0}(1P)$, and $\chi_{c2}(1P)$ peaks have been observed [199]. In Fig. 4.5 we show N_γ and N_{π^0} distributions for the control sample data. The the effect of requiring $N_{\pi^0} \leq 1$ and $N_\gamma \leq 5$ on the control sample p_T and invariant mass distribution is shown in Fig. 4.6. We observe that a small amount of events belonging to the two-photon peak at ~ 0 GeV$/c$ is rejected by this requirement. The invariant mass distribution shows that most of the $\eta_c(1S)$, $\chi_{c0}(1P)$, and $\chi_{c2}(1P)$ signal events are

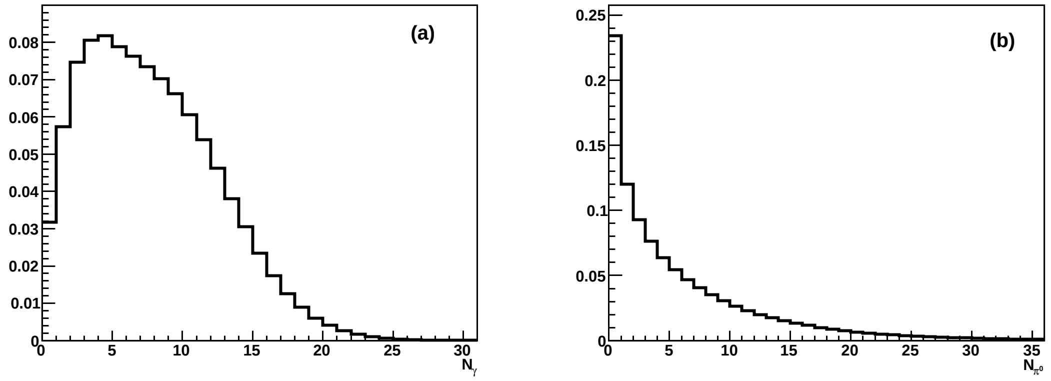

Figure 4.5: Distributions of (a) N_γ and (b) N_{π^0} for $K^+K^-\pi^+\pi^-$ control sample data.

retained. The presence of a prominent J/ψ peak, whose production is forbidden in two-photon production, in the $K^+K^-\pi^+\pi^-$ invariant mass distribution is due to the fact that, at this stage of the selection, the ISR background is not rejected, yet.

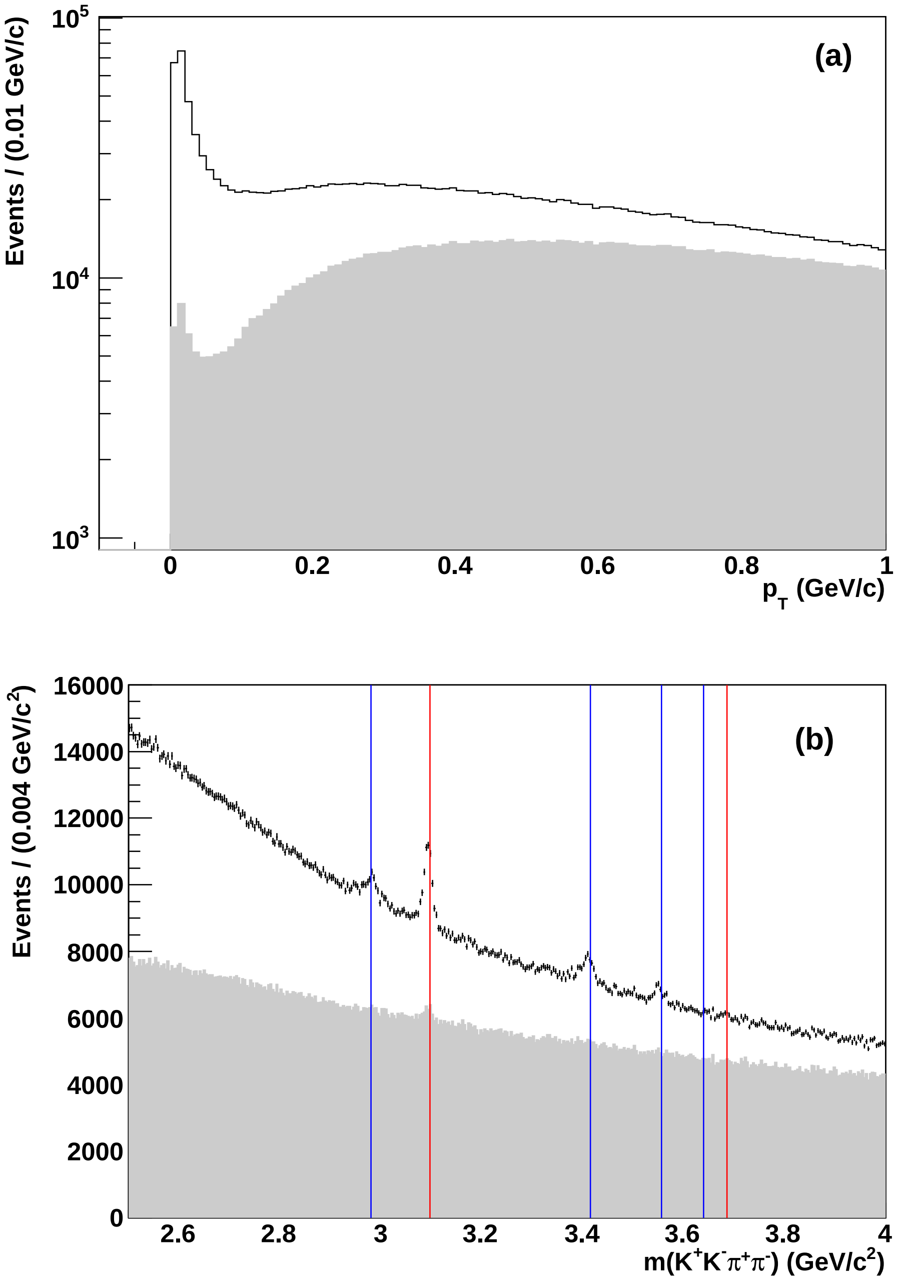

Figure 4.6: Distributions of (a) p_T and (b) $K^+K^-\pi^+\pi^-$ invariant mass for control sample data before (no filling) applying requirements on N_{π^0} and N_γ, and the events rejected by these requirements (gray filled). In (b), the blue lines are placed at the nominal [49] masses of (left to right) $\eta_c(1S)$, $\chi_{c0}(1P)$, $\chi_{c2}(1P)$, and $\eta_c(2S)$. The red lines are placed at the nominal [49] masses of (left to right) J/ψ and $\psi(2S)$.

4.4.2 Rejection of ISR background

The M^2_{miss} variable is very effective to suppress background from ISR production, which is expected to show a narrow peak in this variable at $\sim 0\ (\text{GeV}/c^2)^2$ (Fig. 2.4).

We optimize a requirement to reject ISR background contribution by using the $K^+K^-\pi^+\pi^-$ control sample. In Fig. 4.7(a) we show the M^2_{miss} distribution for the data control sample. A clear peak at $M^2_{\text{miss}} \sim 0\ (\text{GeV}/c^2)^2$ indicates the presence of a large ISR production. We fit the $K^+K^-\pi^+\pi^-$ invariant mass spectrum in intervals of M^2_{miss}, thus obtaining the J/ψ yield distribution as a function of M^2_{miss}, which is shown in Fig. 4.7(b). The peak at $M^2_{\text{miss}} \sim 0\ (\text{GeV}/c^2)^2$ in the J/ψ signal yield distribution proves that most of the large J/ψ signal observed in Fig. 4.6 originates from ISR background. In order to suppress such kind of background we require $M^2_{\text{miss}} > 2\ (\text{GeV}/c^2)^2$. In Fig. 4.8 we show the effect of applying such a requirement to control sample data. The J/ψ signal is almost completely removed.

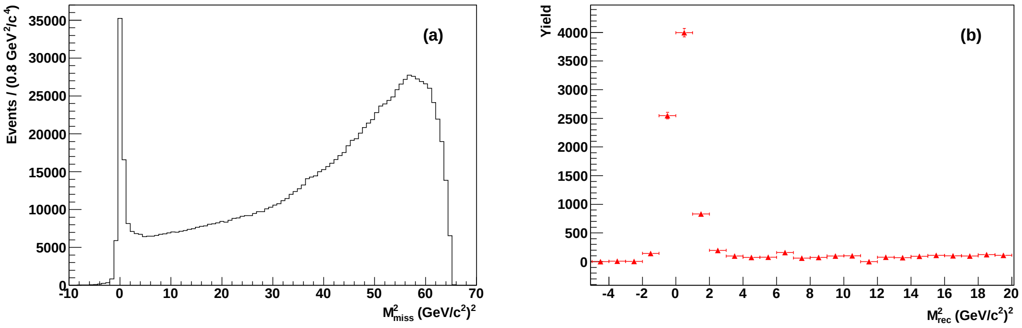

Figure 4.7: Distributions of (a) events and (b) J/ψ signal yields as a function of M^2_{miss} in $K^+K^-\pi^+\pi^-$ control sample data.

Two photon process enhancement

A small value of the transverse momentum p_T is peculiar of the two-photon production due to the collinearity of the interacting photons in *two-photon* events. Background from $e^+e^-\to q\bar{q}\ (q = u, d, s, c)$ annihilation and $B\overline{B}$ events is expected to have a higher value of p_T, since it usually originates from high-multiplicity events where some particle is lost in the reconstruction. In Fig. 4.9 we show the p_T distribution for different types of signal and background events. In Fig. 4.10, we show the p_T distribution for candidates selected with the above mentioned requirements. The distribution is fitted with a signal p_T shape obtained from MC simulation plus a combinatorial background component, modeled using a sixth-order polynomial function. A clear signature for two-photon production is observed.

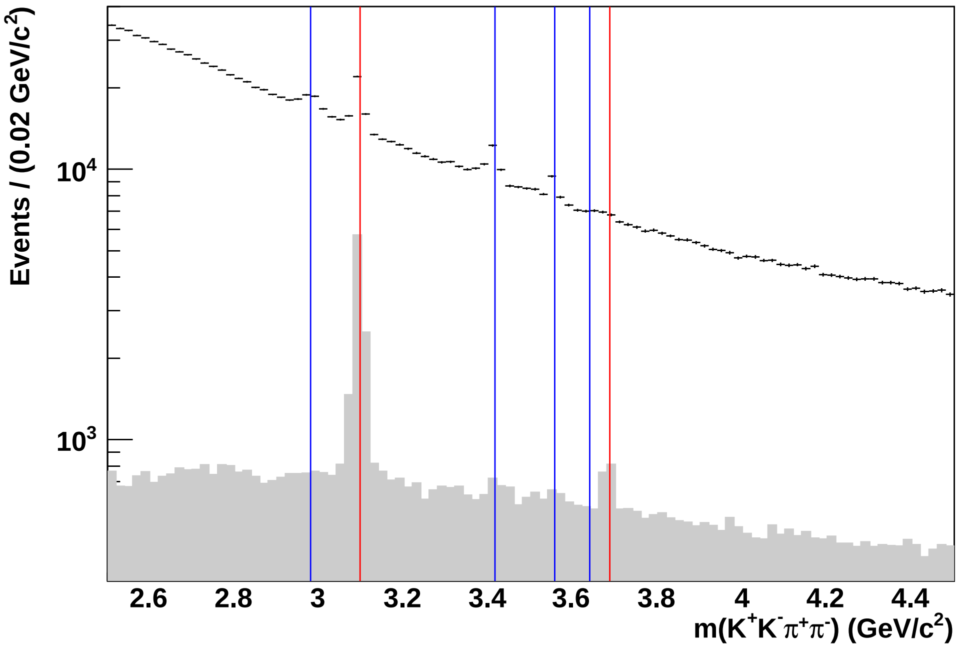

Figure 4.8: Mass spectrum of the $K^+K^-\pi^+\pi^-$ control sample before (no filling) requiring $M^2_{\rm miss} > 2({\rm GeV}/c^2)^2$, and the events rejected by this requirement (gray filled). The blue lines are placed at the nominal [49] masses of (left to right) $\eta_c(1S)$, $\chi_{c0}(1P)$, $\chi_{c2}(1P)$, and $\eta_c(2S)$. The red lines are placed at the nominal [49] masses of (left to right) J/ψ and $\psi(2S)$.

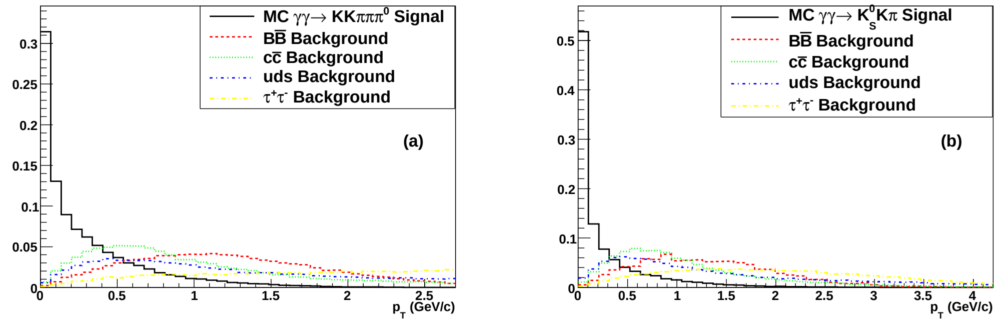

Figure 4.9: Distribution of p_T for (a) $\gamma\gamma\to K^+K^-\pi^+\pi^-\pi^0$ and (b) $\gamma\gamma\to K^0_S K^\pm\pi^\mp$ MC signal (solid black), generic $B\overline{B}$ MC background (red dashed), generic $c\bar{c}$ MC background (green dotted), generic uds MC background (blue line-dashed), and generic $\tau^+\tau^-$ MC background (yellow line-dotted).

The choice on the requirement to be applied on p_T is particularly important since a tighter p_T cut allows the rejection of more background in the $\eta_c(2S)$ mass region, but has the effect of cutting away more $\eta_c(1S)$ signal. The effect of applying different p_T

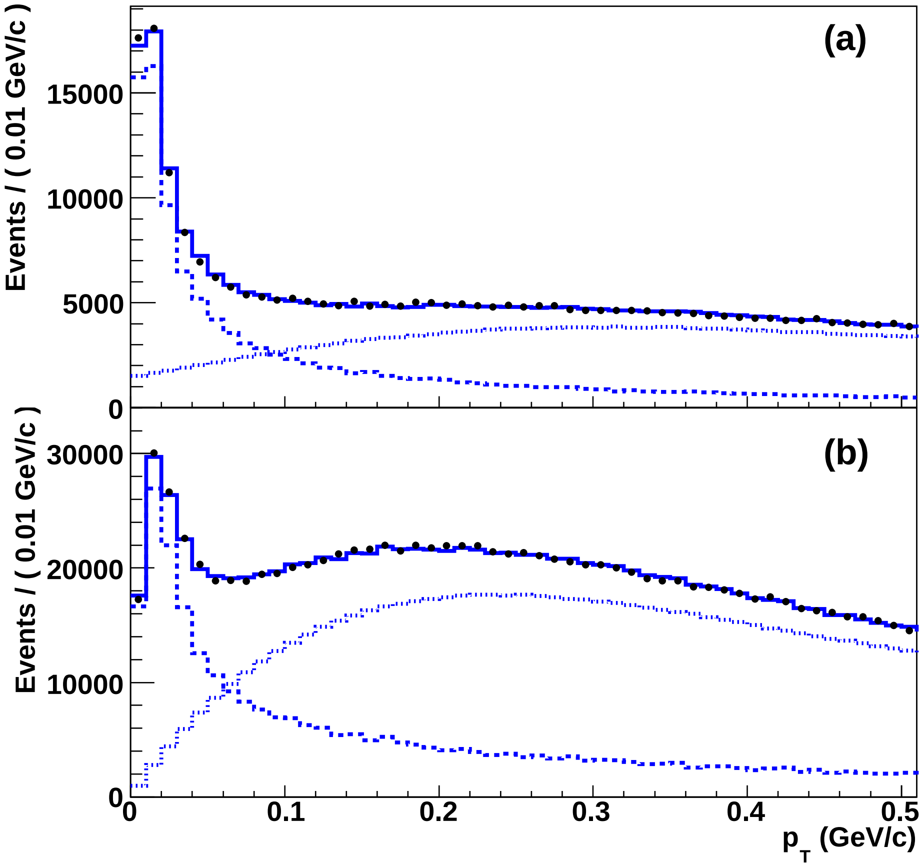

Figure 4.10: The p_T distributions for selected (a) $K_S^0 K^\pm \pi^\mp$ and (b) $K^+K^-\pi^+\pi^-\pi^0$ candidates (data points). The solid histogram represents the result of a fit to the sum of the simulated signal (dashed) and background (dotted) contributions. Figure published in Ref. [324]

requirements on the $K^+K^-\pi^+\pi^-\pi^0$ and $K_S^0 K^\pm \pi^\mp$ mass spectrum is shown in Fig. 4.11. A further insight in this issue is obtained by using the $K^+K^-\pi^+\pi^-$ control sample. We fit the $K^+K^-\pi^+\pi^-$ invariant mass distribution in intervals of p_T in order to extract the $\eta_c(1S)$ and J/ψ yield distribution as a function of p_T (Fig. 4.12). We decide to require $p_T < 0.15$ GeV$/c$. In Fig. 4.13, we show the effect of requiring $p_T < 0.15$ GeV$/c$ on the control sample mass spectrum; a small amount of $\eta_c(1S)$ and $\chi_{c0,2}(1P)$ signal is lost, but the requirement allows for a strong reduction of the combinatorial background.

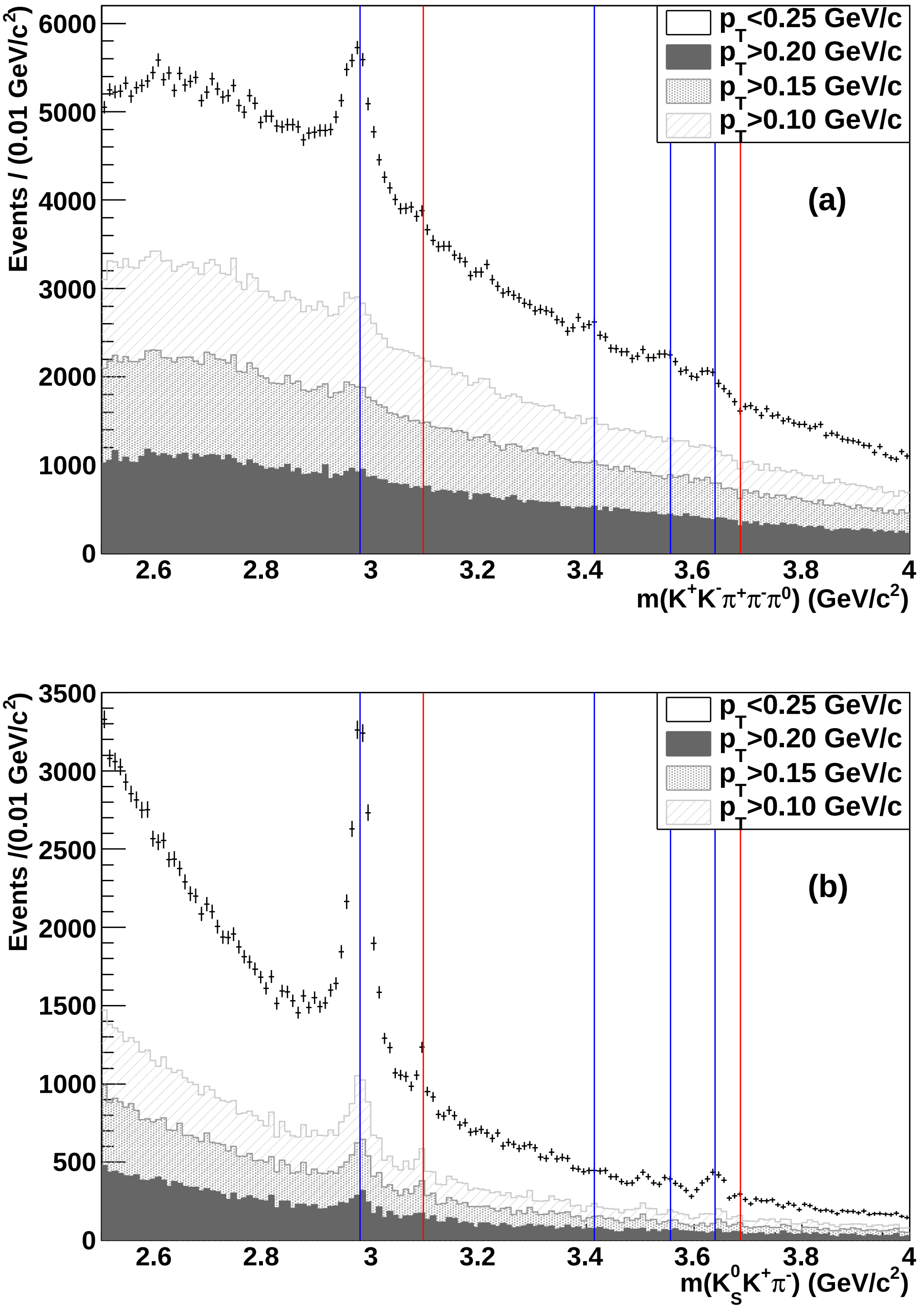

Figure 4.11: Mass distributions for (a) $K^+K^-\pi^+\pi^-\pi^0$ and (b) $K_S^0K^\pm\pi^\mp$ decay modes. For all plots we require $p_T < 0.25$ GeV$/c$. No filling plot have no additional requirements. Filled plots show the events rejected by further requiring $p_T > 0.20$ GeV$/c$ (solid black), $p_T > 0.15$ GeV$/c$ (points dark grey), $p_T > 0.10$ GeV$/c$ (lines light grey).

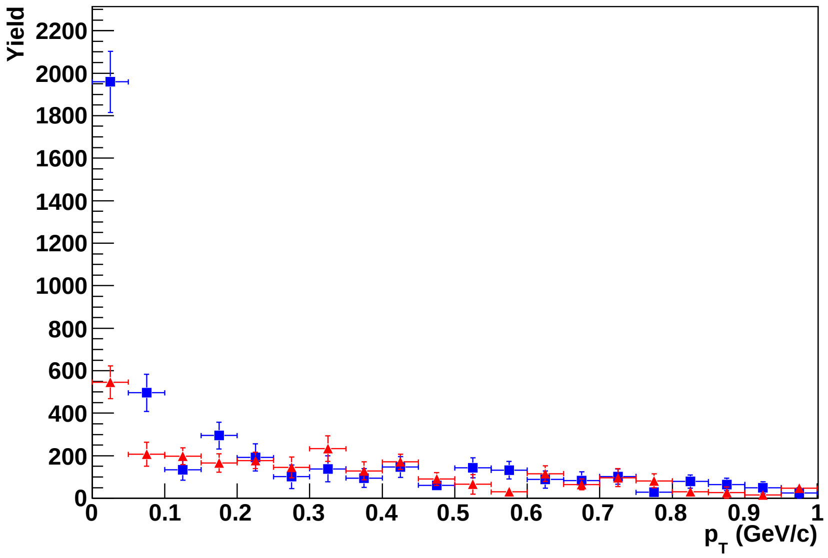

Figure 4.12: Distribution of the $\eta_c(1S)$ (blue squares) and J/ψ (red triangles) yield extracted from a fit to the $K^+K^-\pi^+\pi^-$ invariant mass spectrum. Results are reported in different p_T intervals.

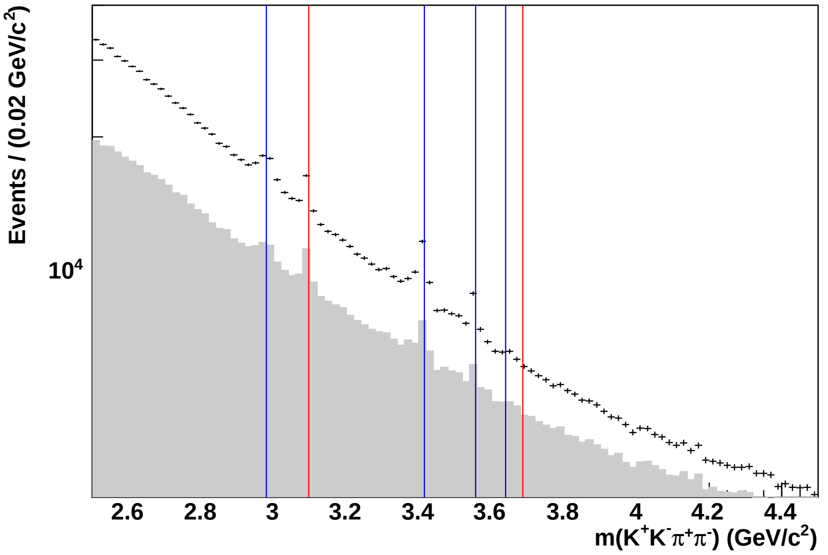

Figure 4.13: Invariant $K^+K^-\pi^+\pi^-$ mass spectrum before (no filling) requiring $p_T < 0.15~\mathrm{GeV}/c$, and the events rejected by this requirement (gray filled). The blue lines are placed at the nominal [49] masses of (left to right) $\eta_c(1S)$, $\chi_{c0}(1P)$, $\chi_{c2}(1P)$, and $\eta_c(2S)$. The red lines are placed at the nominal [49] masses of (left to right) J/ψ and $\psi(2S)$.

4.4.3 Summary of selection requirements

We summarize here all the requirements, described in the previous sections, used to select the events in this analysis:

- Number of tracks equal to 4;
- Resonance vertex fit probability greater than 0.1%;
- Prompt tracks satisfy PID requirements for pion or kaon;
- $N_{\pi^0} \leq 3$ for $K^+K^-\pi^+\pi^-\pi^0$, and $N_{\pi^0} \leq 1$ for $K^0_S K^\pm\pi^\mp$ decay mode;
- $N_\gamma \leq 6$ for $K^+K^-\pi^+\pi^-\pi^0$, and $N_\gamma \leq 5$ for $K^0_S K^\pm\pi^\mp$ decay mode;
- $E^{(1)}_\gamma > 30$ MeV and $E^{(2)}_\gamma > 50$ MeV;
- $\mathcal{H}_{\pi^0} < 0.95$;
- $M^2_{\text{miss}} > 2\ (\text{GeV}/c^2)^2$;
- $p_T < 0.15\ \text{GeV}/c$.

4.4.4 Multiple candidates

We have studied the problem of the presence of multiple candidates in the same event. After applying the selection requirements summarized in sec. 4.4.3, the number of candidates per event is equal to 1.09 and 1.003 in $K^+K^-\pi^+\pi^-\pi^0$ and $K^0_S K^\pm\pi^\mp$ signal MC events.

In order to select the best candidate, we have tested two different algorithms: pick the candidate with the lowest p_T, and pick the candidate with the highest resonance vertex fit probability. We checked that correlations between p_T, the resonance vertex probability, and the reconstructed mass is negligible.

We define a MC candidate as *MC Truth* (MCT) candidate, if all the reconstructed particles are associated to the corresponding generated MC particle at generator level. For each of the selection algorithms, we define the "*algorithm efficiency*" for selecting the best candidate as the ratio of the number of MCT candidate selected by the algorithm to the number of MCT candidates that are present before the selection. We show in Table 4.2 the algorithm efficiency for $K^0_S K^\pm\pi^\mp$ and $K^+K^-\pi^+\pi^-\pi^0$ decay modes.

We checked that candidates rejected by the "*best candidate*" selection algorithm don't create fake peaks in the resonances mass regions, as shown in Fig. 4.14. Due to this reason, there is no strong benefit by applying this best candidate selection, while one risks to distort p_T spectrum. So our final choice is *not* to apply any best candidate selection.

Algorithm	$K^+K^-\pi^+\pi^-\pi^0$ Efficiency (%)	$K^0_S K^\pm\pi^\mp$ Efficiency (%)
Lowest p_T	98.7	99.9
Best Vertex probability	94.8	99.9

Table 4.2: Efficiency of "*best candidate*" selection algorithms (see text for details).

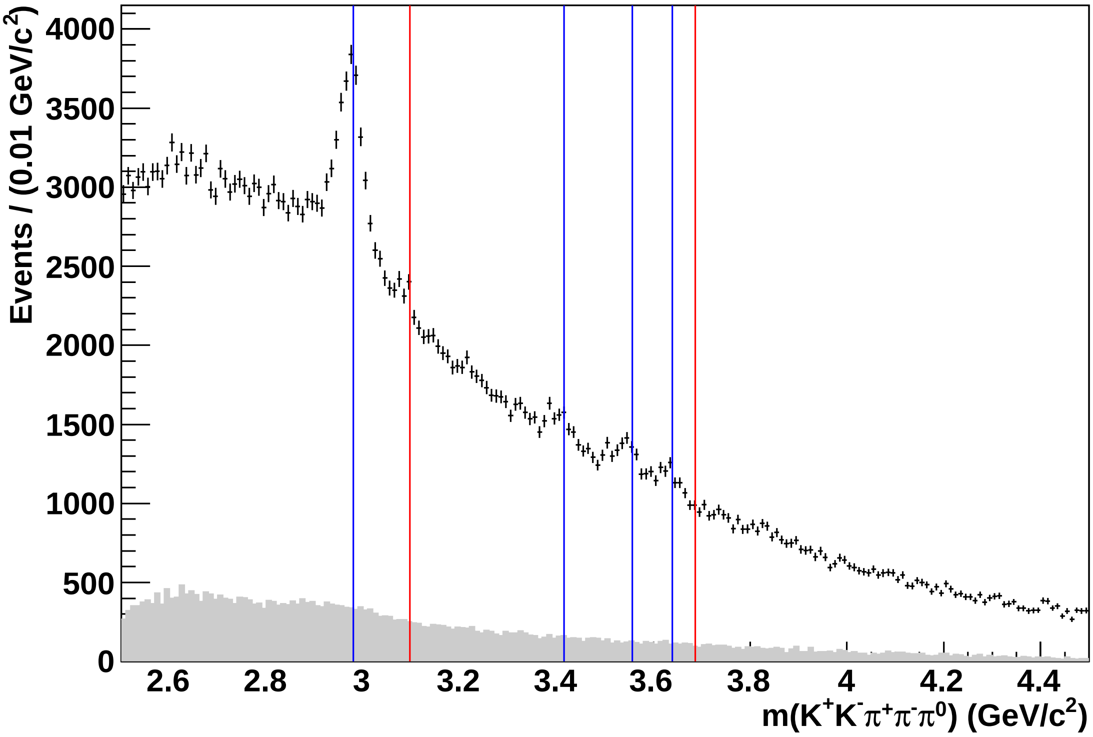

Figure 4.14: The $K^+K^-\pi^+\pi^-\pi^0$ mass spectrum (dots with error bars). The grey histogram represents the events rejected by the best candidate selection.

4.4.5 Misreconstruction background

In this section we discuss possible sources of background arising from particle misreconstruction. The treatment of combinatorial background from $q\bar{q}$ events and of physical irreducible peaking-background is discussed in sec. 4.5.

Reflections

A reflection is a fake peak created by the shift in mass of one resonance originating from particle misidentification. We study if such reflections may create fake peaks in the $\eta_c(1S)$, $\chi_{c0}(1P)$, $\chi_{c2}(1P)$, or $\eta_c(2S)$ mass region.

The misidentification probability of PID selectors used in this analysis is 2% for a real pion to be misidentified as a kaon and 10% for a real kaon to be misidentified as a pion (sec. 4.3.2). Thus, reflections arising from double misidentification have a misidentification probability in the range [0.2,1.0]%, and are not considered.

Taking into account only known resonances decay modes [49], the only decay that can mimic final states studied in this thesis, as a consequence of a single PID misidentification, is the $X \to K^{*0}K^+\pi^-$ decay, where $X = \chi_{c0}(1P)$ or $\chi_{c2}(1P)$ and $K^{*0} \to K^0_S\pi^0$, with $K^0_S \to \pi^+\pi^-$. Such decays have been observed [49] with a non-negligible branching fraction and produce the $K^+\pi^+\pi^-\pi^-\pi^0$ final state, that can mimic the $K^+K^-\pi^+\pi^-\pi^0$ signal in case of pion misidentification. To study possible reflections of these backgrounds, we generate the $\chi_{c0,2} \to K^{*0}K^+\pi^- \to K^0_S\pi^0K^+\pi^- \to K^+\pi^+\pi^-\pi^-\pi^0$ decay using a phase space generator. We study the reflection of the $\chi_{c0,2}$ mass, in case of prompt pion or K^0_S pion daughters misidentification. X is generated with a mass equal to the nominal $\chi_{c0,2}$ mass [49] and a width of 10 MeV. In Fig. 4.15 we show the results of such simulations. Such plots show that, in case of prompt pion misidentification, $\chi_{c0}(1P)$ and $\chi_{c2}(1P)$ reflections may create a broad structure in the $\chi_{c2}(1P)$ and $\eta_c(2S)$ mass region.

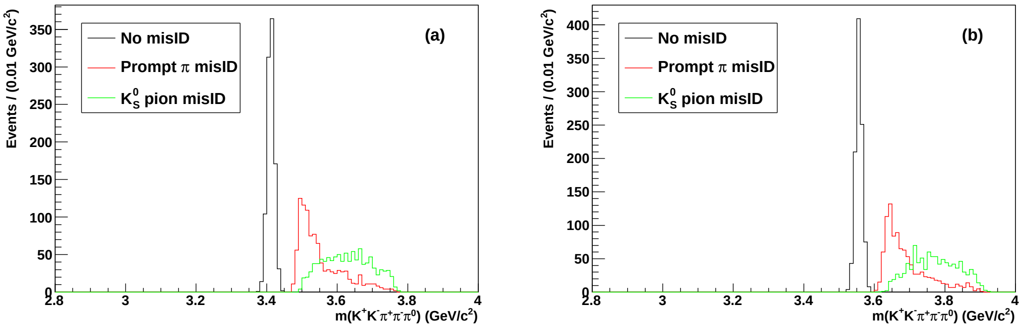

Figure 4.15: Expected $K^+K^-\pi^+\pi^-\pi^0$ mass distribution for reflection from (a) $\chi_{c0}(1P)$ and (b) $\chi_{c2}(1P)$ decays to $K^{*0}K^+\pi^- \to K^0_S\pi^0K\pi \to K\pi^+\pi^-\pi\pi^0$.

In order to investigate the possible presence of this background in data, we study the mass distribution of the $\pi^+\pi^-$ system in $K^+K^-\pi^+\pi^-\pi^0$ events. This distribution is expected to show a peak in K^0_S region if misreconstructed $K^{*0}K^+\pi^-$ events are present. In Fig. 4.16 we show the $\pi^+\pi^-$ mass distributions for real data. No peak is observed in correspondence of the K^0_S mass. In Fig. 4.17, we show the effect of removing from the $K^+K^-\pi^+\pi^-\pi^0$ mass spectrum events whose $\pi^+\pi^-$ mass is in the range [0.48,0.52] GeV/c^2. Since no relevant effect is observed, we conclude that possible background contribution from such reflections is negligible.

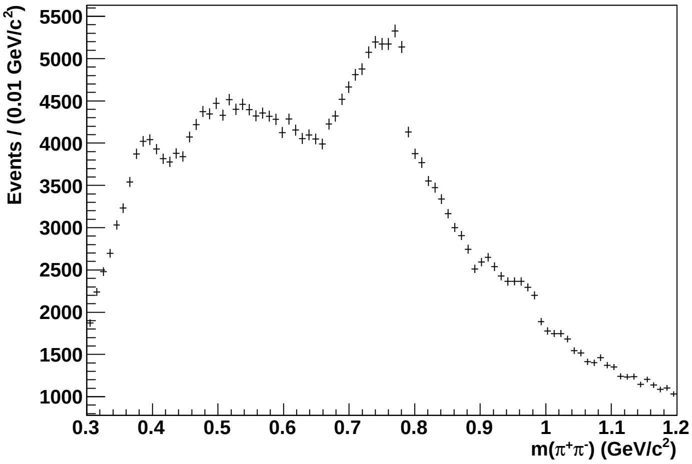

Figure 4.16: Invariant $\pi^+\pi^-$ mass distribution in the $K^+K^-\pi^+\pi^-\pi^0$ data sample.

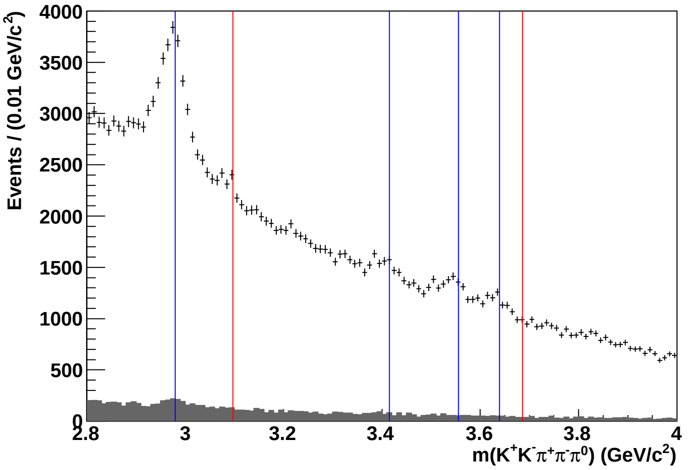

Figure 4.17: Mass distribution for the $K^+K^-\pi^+\pi^-\pi^0$ decay mode. No filling plot has no additional requirements with respect to selection described in sec. 4.4.3. Filled plots show the events rejected by requiring the $\pi^+\pi^-$ mass to be in range [0.48,0.52] GeV/c^2.

Electron contamination

In Fig. 4.16, we observe that a large number of events have a $\pi^+\pi^-$ invariant mass in proximity of of the $\pi^+\pi^-$ production threshold. This may be caused by a contamination of our sample from conversion e^+e^- pairs, misidentified as pions. In order to check if such contamination is actually present, we show in Fig. 4.18 the e^+e^- invariant mass distribution, computed by assigning the electron mass hypothesis to the tracks associated to the pions.

If the misidentified e^+e^- contamination had been present, an excess of events would have shown in proximity of $\sim 0\ \mathrm{GeV}/c^2$. The absence of any excess excludes the hypothesis of a significant contamination from e^+e^- conversions.

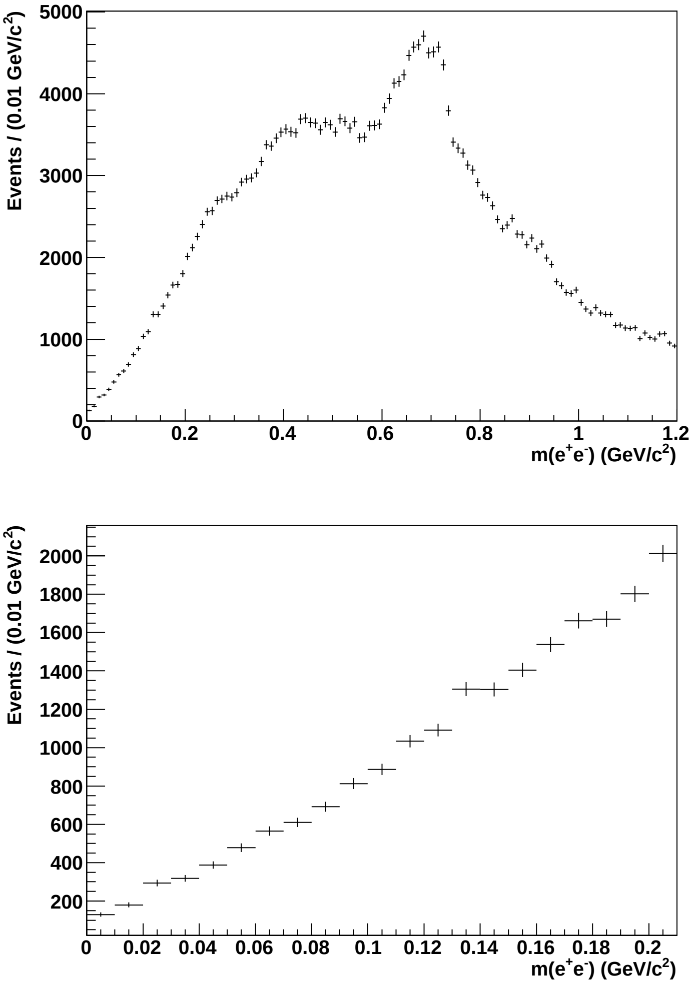

Figure 4.18: Mass distribution for $\pi^+\pi^-$, when assigning electron mass hypothesis to the pion. Bottom plot is a zoom of the region 0–200 MeV/c^2.

ϕ contamination

The presence of an excess of events near 0.3 GeV/c^2 in the $\pi^+\pi^-$ invariant mass (Fig. 4.16) may be an indication of contamination from $\phi K^+K^-\pi^0$, with the ϕ kaon daughters misidentified as pions. The ϕ reflection would manifest in a precise *locus* in the $(m_{\pi^+\pi^-}, cos\theta^H_{\pi^+})$ plane, where $m_{\pi^+\pi^-}$ is the invariant mass of the dipion system and $cos\theta^H_{\pi^+}$ is the cosine of the helicity angle of the π^+. This angle is defined as the angle between the dipion system direction in the laboratory frame and the π^+ direction in the dipion frame. Kaons coming from ϕ, misidentified as pions should create a bump of events in the ($m_{\pi^+\pi^-} \sim 0.35\mathrm{GeV}/c^2$, $-0.5 < cos\theta^H_{\pi^+} < 0.5$) region, as indicated by MC simulation shown in Fig. 4.19. In Fig. 4.20 we show the distribution of

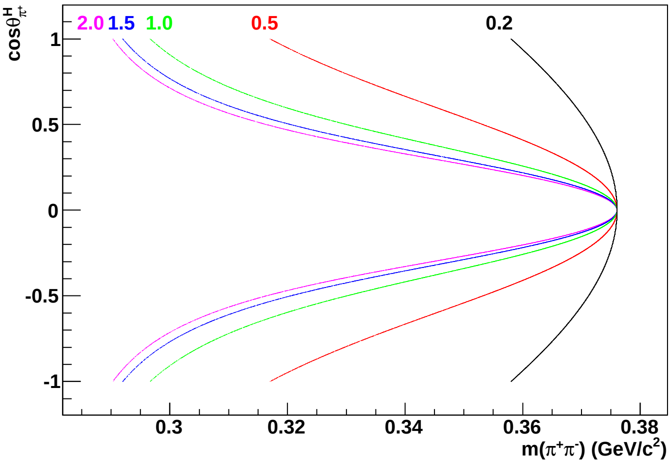

Figure 4.19: *Loci* in the $(m_{\pi^+\pi^-}, cos\theta^H_{\pi^+})$ plane where a ϕ reflection would manifest in case of double $K\rightarrow\pi$ misidentification. Each line corresponds to a different value of the ϕ momentum, which is reported as a label nearby the line.

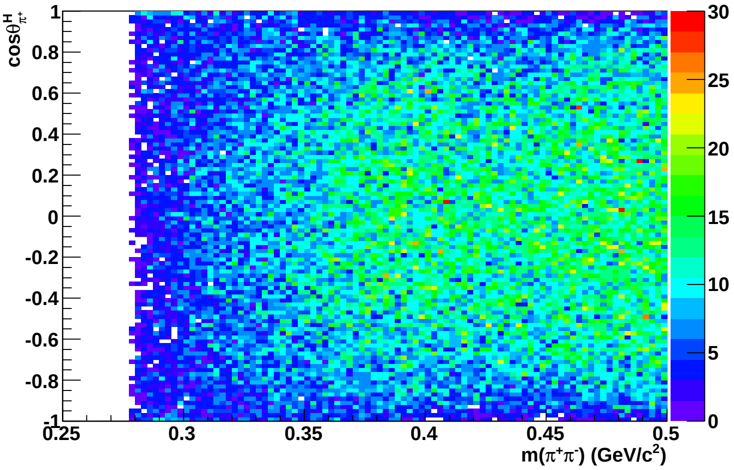

Figure 4.20: Real $K^+K^-\pi^+\pi^-\pi^0$ data events distribution on the $(m_{\pi^+\pi^-}, cos\theta^H_{\pi^+})$ plane.

$K^+K^-\pi^+\pi^-\pi^0$ data events on the $(m_{\pi^+\pi^-}, cos\theta^H_{\pi^+})$ plane. No clear enhancement in seen in the $(m_{\pi^+\pi^-} \sim 0.35\mathrm{GeV}/c^2$, $-0.5 < cos\theta^H_{\pi^+} < 0.5)$ region. The broad enhancement observed in the [0.35,0.50] GeV/c^2 region is due to the tail of the ρ meson. In order to try to enhance any possible ϕ contamination contribution, we show in Fig. 4.21 the

$m^{mis}_{K^+K^-}$ distribution after requiring $-0.5 < cos\theta^H_{\pi^+} < 0.5$. The $m^{mis}_{K^+K^-}$ distribution is obtained by assigning the kaon mass hypothesis to the tracks identified as pions. In the case of presence of a ϕ contamination, an enhanced ϕ signal is expected in the K^+K^- mass distribution, after applying such a requirement. The absence of any enhanced ϕ signal is then considered as a proof that such ϕ contamination is negligible in our sample.

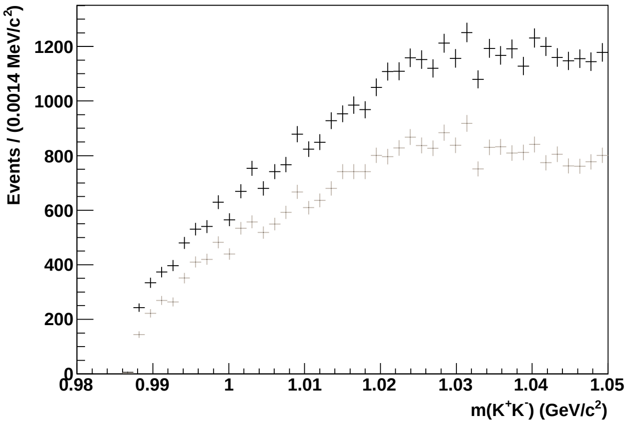

Figure 4.21: Mass distribution for $\pi^+\pi^-$, when assigning kaon mass hypothesis to the pion. In the black only requirements described in sec. 4.4.3 are applied. In the grey plot we further require $-0.5 < cos\theta^H_{\pi^+} < 0.5$.

4.5 Resonance parameters measurement

The primary goal of the analysis presented in this thesis is to measure the $\eta_c(1S)$ and $\eta_c(2S)$ parameters and to search for their decays into the previously unobserved $K^+K^-\pi^+\pi^-\pi^0$ decay mode. The $K^0_S K^{\pm}\pi^{\mp}$ and $K^+K^-\pi^+\pi^-\pi^0$ invariant mass distributions are reported in Fig. 4.22. A prominent peak in correspondence of the $\eta_c(1S)$ mass value is observed in both spectra. Signals for $\chi_{c0}(1P)$, $\chi_{c2}(1P)$, and $\eta_c(2S)$ are also present. The $\chi_{c0}(1P)$ signal is not present in the $K^0_S K^{\pm}\pi^{\mp}$ final state, since this decay is forbidden due to spin-parity conservation. A small J/ψ peak is also visible, due to residual ISR background that survives the selection criteria.

4.5.1 Fit strategy

Signal yields and resonance parameters are measured by using an extended binned maximum likelihood (ML) fit to the $K^0_S K^{\pm}\pi^{\mp}$ and $K^+K^-\pi^+\pi^-\pi^0$ invariant mass spectra. The bin width is 4 MeV/c^2. The components used in the likelihood are: $\eta_c(1S)$, $\chi_{c0}(1P)$,

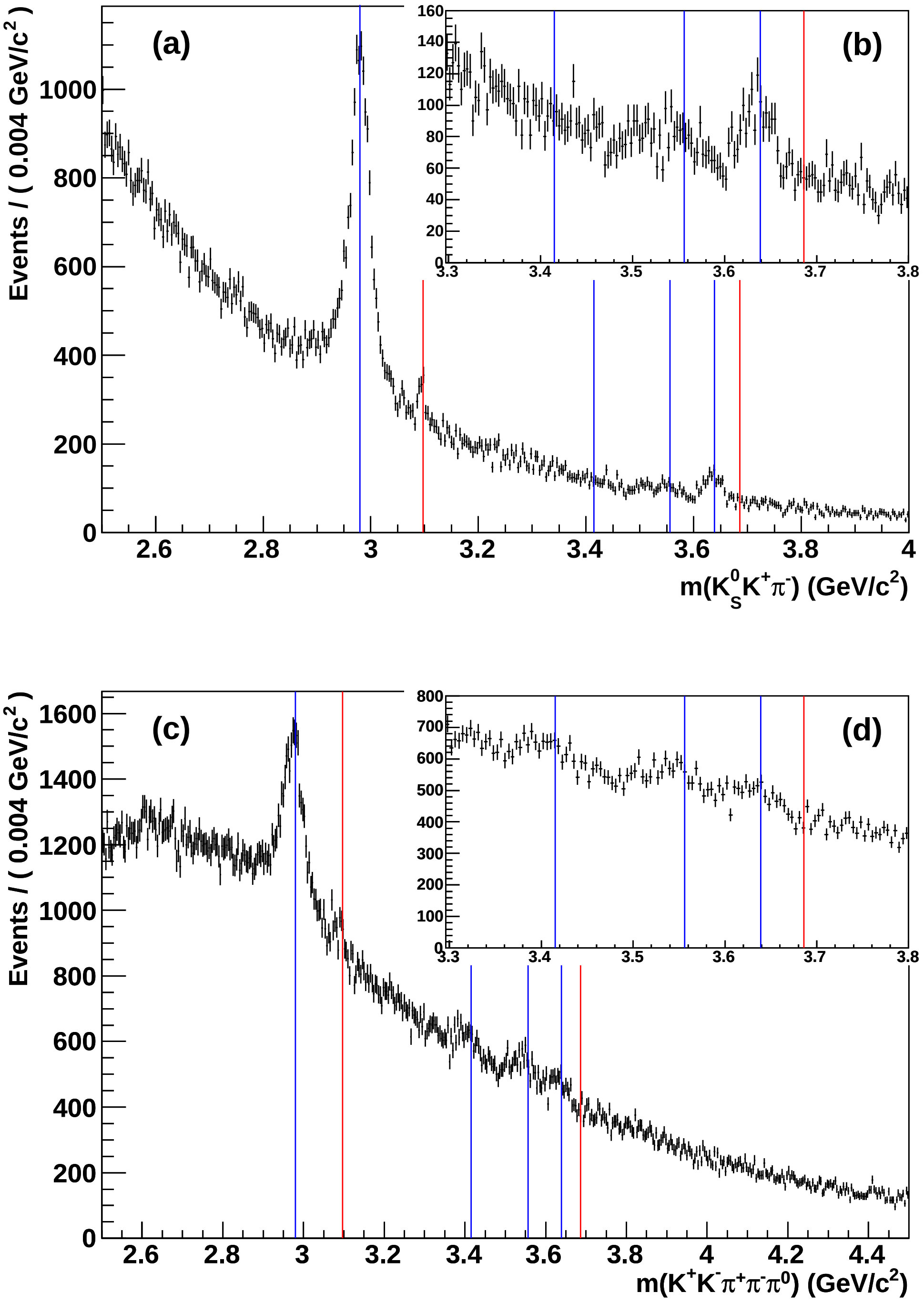

Figure 4.22: Invariant mass distribution for (a) $K_S^0 K^\pm \pi^\mp$ and (b) $K^+K^-\pi^+\pi^-\pi^0$ decay modes. The insets (b) and (d) show a the zoom in the region [3.3,3.8] GeV/c^2. The blue lines are placed at the nominal [49] masses of (left to right) $\eta_c(1S)$, $\chi_{c0}(1P)$, $\chi_{c2}(1P)$, and $\eta_c(2S)$. The red lines are placed at the nominal [49] masses of (left to right) J/ψ and $\psi(2S)$. Lines corresponding to the $\eta_c(1S)$ and J/ψ are not shown in the insets.

$\chi_{c2}(1P)$, and $\eta_c(2S)$ signal, J/ψ ISR background, and combinatorial background. The $\chi_{c0}(1P)$ component is not present in the fit to the $K^0_S K^\pm \pi^\mp$ invariant mass distribution.

Each resonance PDF is modeled as the convolution between a non-relativistic Breit-Wigner function and the detector resolution function. Details on the detector resolution function are given in sec. 4.5.2. The continuum background PDF is a fourth-order polynomial, while the residual J/ψ ISR background is parameterized with a Gaussian shape.

Signals and backgrounds yields, the $\eta_c(1S)$ and $\eta_c(2S)$ mass and width, the mass and width of the Gaussian function describing the J/ψ ISR background component, and the combinatorial background shape parameters are free parameters in the fit. Mass and width of the $\chi_{c0}(1P)$ and $\chi_{c2}(1P)$ components are fixed to their nominal values [49]. In the $K^0_S K^\pm \pi^\mp$ decay mode, the J/ψ mass is fixed to its nominal value [49], too. In the $K^+ K^- \pi^+ \pi^- \pi^0$ decay mode the width of the $\eta_c(2S)$ signal component is fixed to the value found in the $K^0_S K^\pm \pi^\mp$ decay.

The $\chi_{c2}(2P)$ resonance is searched by adding a signal component to the fit, with the mass and width fixed to the values found in Ref. [205].

4.5.2 Mass resolution

In order to obtain an accurate measurement of the $\eta_c(1S)$ and $\eta_c(2S)$ parameters, a precise description of the detector mass resolution is needed. We rely on MC simulation in order to obtain the resolution function. For each signal MCT event, we compute the mass resolution $\delta m = m^{res}_{reco} - m^{res}_{true}$, where m^{res}_{reco} is the reconstructed resonance mass, and m^{res}_{true} is the MC-generated resonance mass.

In Figs. 4.23 and 4.24 we show the δm distributions obtained using MC events that simulate different resonances production, followed by the decay in the $K^0_S K^\pm \pi^\mp$ and $K^+ K^- \pi^+ \pi^- \pi^0$ final state, respectively.

The distributions are fitted using the following shape [158]

$$F(x) = A\left(\sin^2\xi\, G(x) + \cos^2\xi\, B(x)\right), \tag{4.4}$$

where

$$G(x) = \exp\left(-\frac{(x-\mu)^2}{2\sigma^2}\right), \tag{4.5}$$

and

$$B(x) = \frac{(\Gamma_{(1,2)}/2)^{\beta_{(1,2)}}}{|x_0 - x|^{\beta_{(1,2)}} + (\Gamma_{(1,2)}/2)^{\beta_{(1,2)}}}, \tag{4.6}$$

Γ_1 (Γ_2) and β_1 (β_2) are used if $x < x_0$ ($x \geq x_0$). We checked that modifying the resolution function for $\eta_c(1S) \to K^0_S K^\pm \pi^\mp$ by adding another Gaussian component to (4.4) improves the description of the δm shape, but does not change the analysis results. Therefore, we decide to keep the $F(x)$ parameterization as in Eq. 4.4.

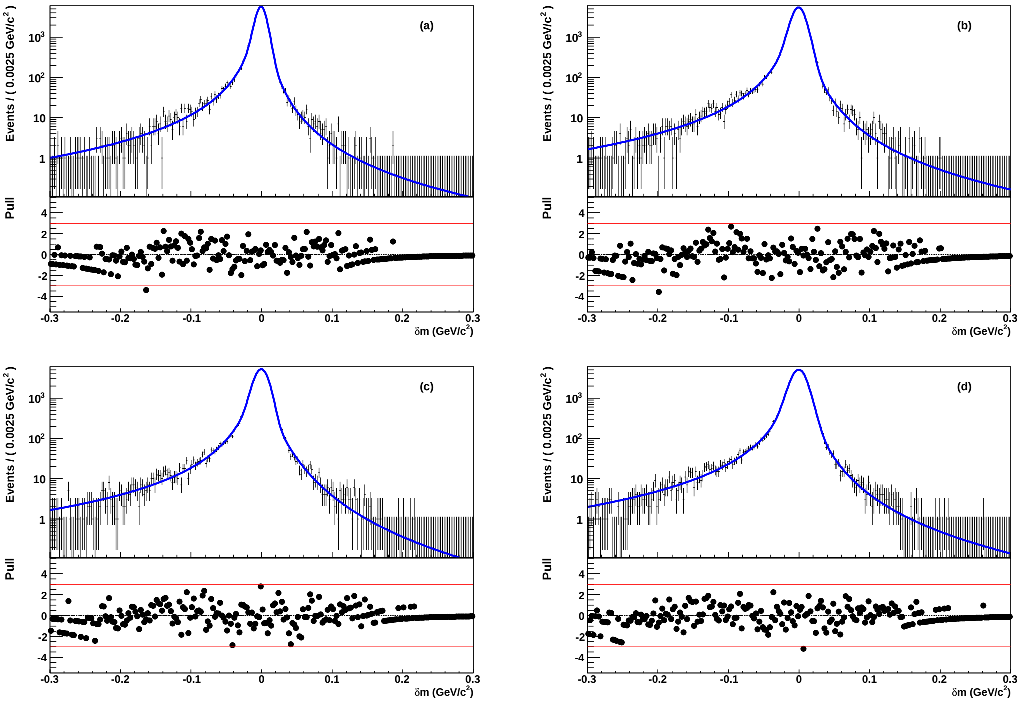

Figure 4.23: Distribution of δm (a) $\eta_c(1S)$, (b) $\chi_{c2}(1P)$, (c) $\eta_c(2S)$, and (d) $\chi_{c2}(2P)$ MCT events, in $K^0_S K^\pm \pi^\mp$ decay mode. The blue solid curve is the fit function (see text for details). In each figure we also show the distribution of the error-normalized difference (pull) between the fit function and the data points.

4.5.3 Absolute mass scale

The determination of the absolute mass scale is crucial in order to aim at a precise measurement of the $\eta_c(1S)$ and $\eta_c(2S)$ masses. We select a high-statistics J/ψ control sample by reverting the $M^2_{\rm miss}$ requirement described in sec. 4.4.2. We thus select the $e^+e^- \to \gamma_{ISR} K^0_S K^\pm \pi^\mp$ and $e^+e^- \to \gamma_{ISR} K^+K^-\pi^+\pi^-\pi^0$ ISR process.

The $K^0_S K^\pm \pi^\mp$ and $K^+K^-\pi^+\pi^-\pi^0$ invariant mass spectra of the ISR-enriched control sample is fitted to obtain the difference between the fitted $m^{meas}_{J/\psi}$ and the nominal $m^{PDG}_{J/\psi}$ [49] J/ψ mass value. We then correct the measured $\eta_c(1S)$ and $\eta_c(2S)$ mass value for the observed difference. Thus, the resulting corrected mass for the $\eta_c(nS)$ resonance is $m^{corr}_{\eta_c(nS)} = m^{meas}_{\eta_c(nS)} - (m^{meas}_{J/\psi)} - m^{PDG}_{J/\psi})$. This is equivalent to measure the mass difference between the $\eta_c(nS)$ and the well-known J/ψ mass. The mass parameters that are fixed to their nominal values in the fit described in sec. 4.5.1 are also corrected by the measured shift.

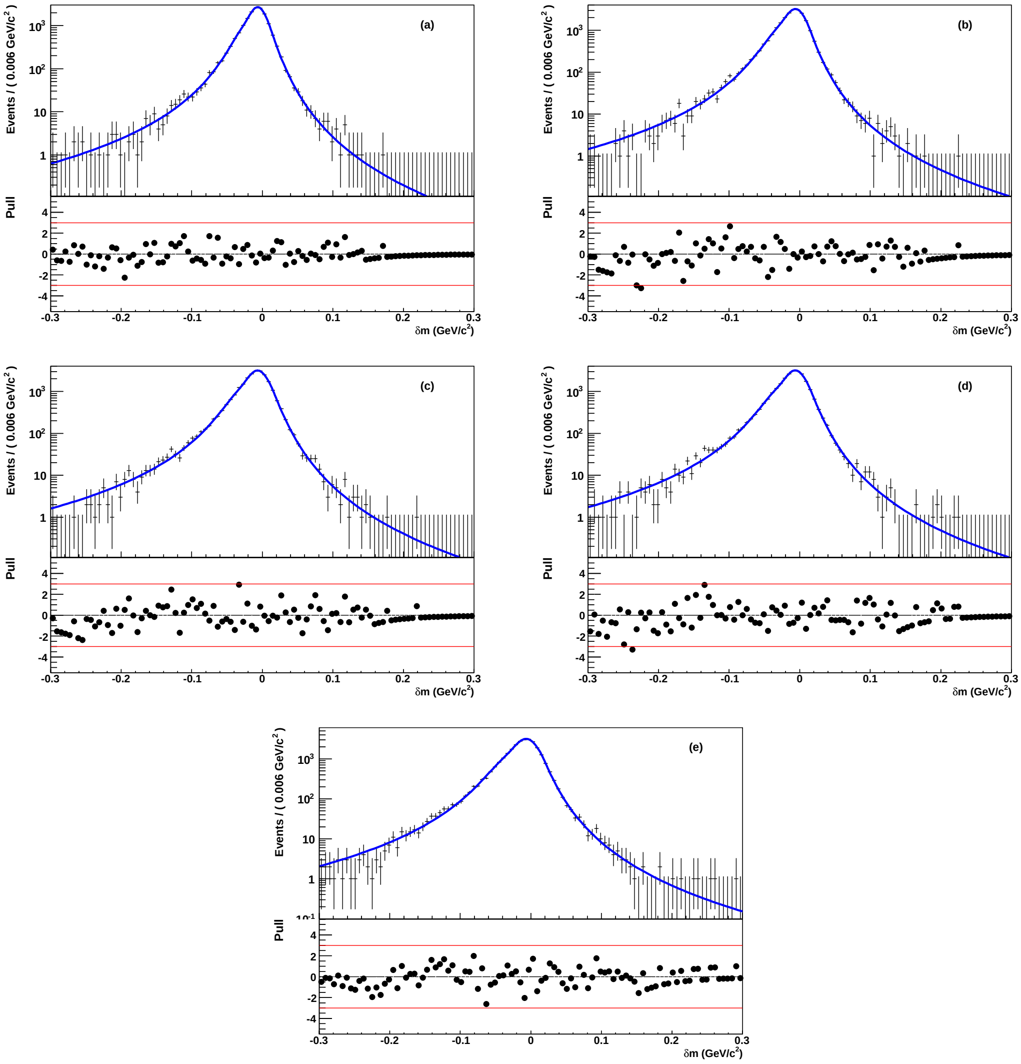

Figure 4.24: Distribution of δm (a) $\eta_c(1S)$, (b) $\chi_{c0}(1P)$, (c) $\chi_{c2}(1P)$, (d) $\eta_c(2S)$, and (e) $\chi_{c2}(2P)$ MCT events, in $K^+K^-\pi^+\pi^-\pi^0$ decay mode. The blue solid curve is the fit function (see text for details). In each figure we also show the distribution of the error-normalized difference (pull) between the fit function and the data points.

The J/ψ and $\psi(2S)$ signals are parameterized with the convolution between the detector resolution function described below and a non-resonant Breit-Wigner function. Background is parameterized with a second order polynomial function. In the $K^0_S K^\pm \pi^\mp$ decay mode, the wide structure present in the $\eta_c(1S)$ region is described by the convolution of a non-relativistic Breit-Wigner with the $\eta_c(1S)$ resolution function. The $\eta_c(1S)$ parameters are fixed to the value obtained in the fit to the nominal data sample. In order to describe the J/ψ resolution function, we use the function defined in Eq. (4.4). In the $K^+K^-\pi^+\pi^-\pi^0$ decay, the $\psi(2S)$ resolution function is parameterized using an asymmetric Gaussian with exponential tails defined as

$$C(x) = Nexp\left(\frac{-(x-\mu)^2}{2\sigma_{L,R}^2 + \alpha_{L,R}(x-\mu)^2}\right), \tag{4.7}$$

where N is a normalization factor, σ_L and α_L are used when $x \leq \mu$, and σ_R and α_R when $x > \mu$. The δm distributions for J/ψ and $\psi(2S)$ ISR MC events, and the corresponding resolution functions are shown in Fig. 4.25, for both $K_S^0 K^\pm \pi^\mp$ and $K^+K^-\pi^+\pi^-\pi^0$ decay mode.

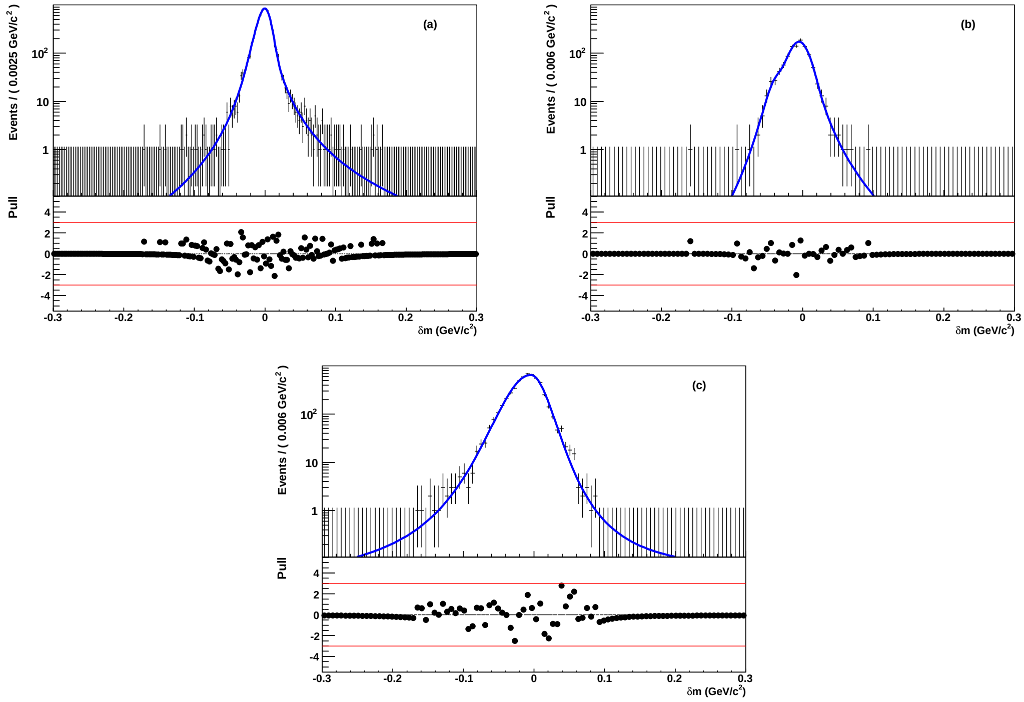

Figure 4.25: Distribution of δm for (a) $J/\psi \rightarrow K_S^0 K^\pm \pi^\mp$, (b) $J/\psi \rightarrow K^+K^-\pi^+\pi^-\pi^0$, and (c) $\psi(2S) \rightarrow K^+K^-\pi^+\pi^-\pi^0$ MCT events. The blue solid curve is the fit function (see text for details). In each plot we also show the distribution of the error-normalized difference (pull) between the fit function and the data points.

The $\eta_c(1S)$, J/ψ, and $\psi(2S)$ yields, and the J/ψ and $\psi(2S)$ masses are free parameters in the fit. For the J/ψ peak, the parameter σ of the resolution function defined in Eq. (4.5) is modified to account for possible MC/data differences. We define $\sigma^2 = \sigma_{MC}^2 + \text{sign}(\Delta\sigma) \cdot \Delta\sigma^2$, where σ^{MC} is the value obtained in the fit to the MC samples, reported in Fig. 4.25.

The results of the fits are shown in Figs. 4.26. The fitted J/ψ mass is (3096.4 ± 0.2) MeV$/c^2$ and (3095.8 ± 0.8) MeV$/c^2$, giving a mass shift of (-0.5 ± 0.2) MeV$/c^2$ and (-1.1 ± 0.8) MeV$/c^2$, for the $K_S^0 K^\pm \pi^\mp$ and $K^+K^-\pi^+\pi^-\pi^0$ decay mode, respectively.

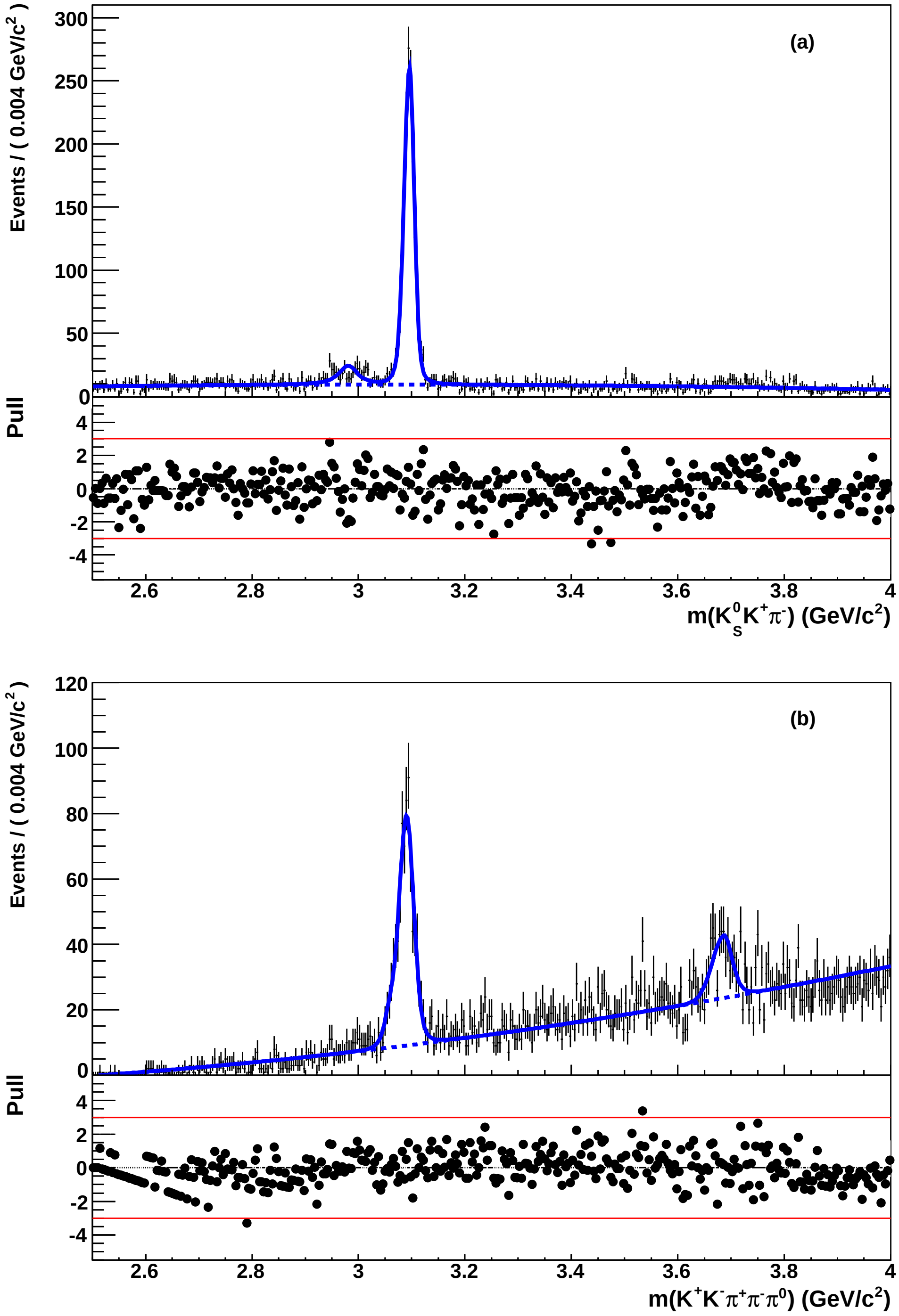

Figure 4.26: Fit to (a) $K_S^0K^\pm\pi^\mp$ and (b) $K^+K^-\pi^+\pi^-\pi^0$ mass spectrum for real data satisfying the reversed $M^2_{\rm miss}$ requirement (see text). The solid line is the total fit function, the dashed line is the background component. In each plot we also show the distribution of the error-normalized difference (pull) between the fit function and the data points.

The shifts observed by fitting ISR MC samples are consistent with these results, inside the statistical uncertainties. The fitted value of $\Delta\sigma$ is $(5.0 \pm 1.0)\ \mathrm{MeV}/c^2$, and $(4.8 \pm$

$2.5)\ \mathrm{MeV}/c^2$ for the $K_S^0K^\pm\pi^\mp$ and $K^+K^-\pi^+\pi^-\pi^0$ mode, respectively. These values are used in sec. 4.8.1 to estimate a systematic uncertainty.

4.5.4 Fit results

Results of the fit to the $K_S^0K^\pm\pi^\mp$ and $K^+K^-\pi^+\pi^-\pi^0$ mass spectra, described in sec. 4.5.1, are reported in Tab. 4.3 and shown in Fig. 4.27. The χ^2/ndf of the fit is 1.07 and 1.03, where ndf is the number of degrees of freedom which is 361 and 360, for the $K_S^0K^\pm\pi^\mp$ and $K^+K^-\pi^+\pi^-\pi^0$ final state, respectively. No significant change in fit results is obtained when a $\chi_{c2}(2P)$ component is added in the fit. The fitted $\chi_{c2}(2P)$ signal yield is -1 ± 45 and -185 ± 146, for $K_S^0K^\pm\pi^\mp$ and $K^+K^-\pi^+\pi^-\pi^0$ final state, respectively.

Decay	Signal Yield (Evts.)	Corrected Mass (MeV/c^2)	Fitted Width (MeV)
$\eta_c(1S)\to K_S^0K^\pm\pi^\mp$	12310 ± 235	2982.5 ± 0.4	32.1 ± 1.1
$\chi_{c2}(1P)\to K_S^0K^\pm\pi^\mp$	126 ± 37	3556.2 (fixed)	2 (fixed)
$\eta_c(2S)\to K_S^0K^\pm\pi^\mp$	624 ± 72	3638.5 ± 1.5	13.4 ± 4.6
$\eta_c(1S)\to K^+K^-\pi^+\pi^-\pi^0$	11158 ± 430	2984.5 ± 0.8	36.2 ± 2.8
$\chi_{c0}(1P)\to K^+K^-\pi^+\pi^-\pi^0$	1094 ± 143	3415.8 (fixed)	10.2 (fixed)
$\chi_{c2}(1P)\to K^+K^-\pi^+\pi^-\pi^0$	1250 ± 118	3556.2 (fixed)	2 (fixed)
$\eta_c(2S)\to K^+K^-\pi^+\pi^-\pi^0$	1201 ± 133	3640.5 ± 3.2	13.4 (fixed)

Table 4.3: Extraction of event yields and mass and width of the $\eta_c(1S)$ and $\eta_c(2S)$ resonances: fitted signal yield with statistical uncertainty, corrected mass, and fitted width for each decay mode.

4.6 Peaking-background subtraction

There are two different processes that can produce real resonances, thus producing physical irreducible peaking-background events. Such processes are the J/ψ and $\psi(2S)$ radiative decays, and two-photon production with higher multiplicity, such as $\gamma\gamma\to\eta_c(1S)\pi^0\to K_S^0K^\pm\pi^\mp\pi^0$. We give an estimate of such backgrounds using data-driven techniques. The number of peaking-background events originating from the $J/\psi\to\gamma\eta_c(1S)$ radiative decay is subtracted from the $\eta_c(1S)$ signal yield. The number of peaking-background events from higher multiplicity two-photon processes, like $\gamma\gamma\to\eta_c(1S)\pi^0$, is used to assign a systematic uncertainty. The number of peaking-background events for $\chi_{c0}(1P)$, $\chi_{c2}(1P)$, $\eta_c(2S)$, originating from both $\psi(2S)$ decays and two-photon processes, is used to assign a systematic uncertainty as described in sec. 4.8.

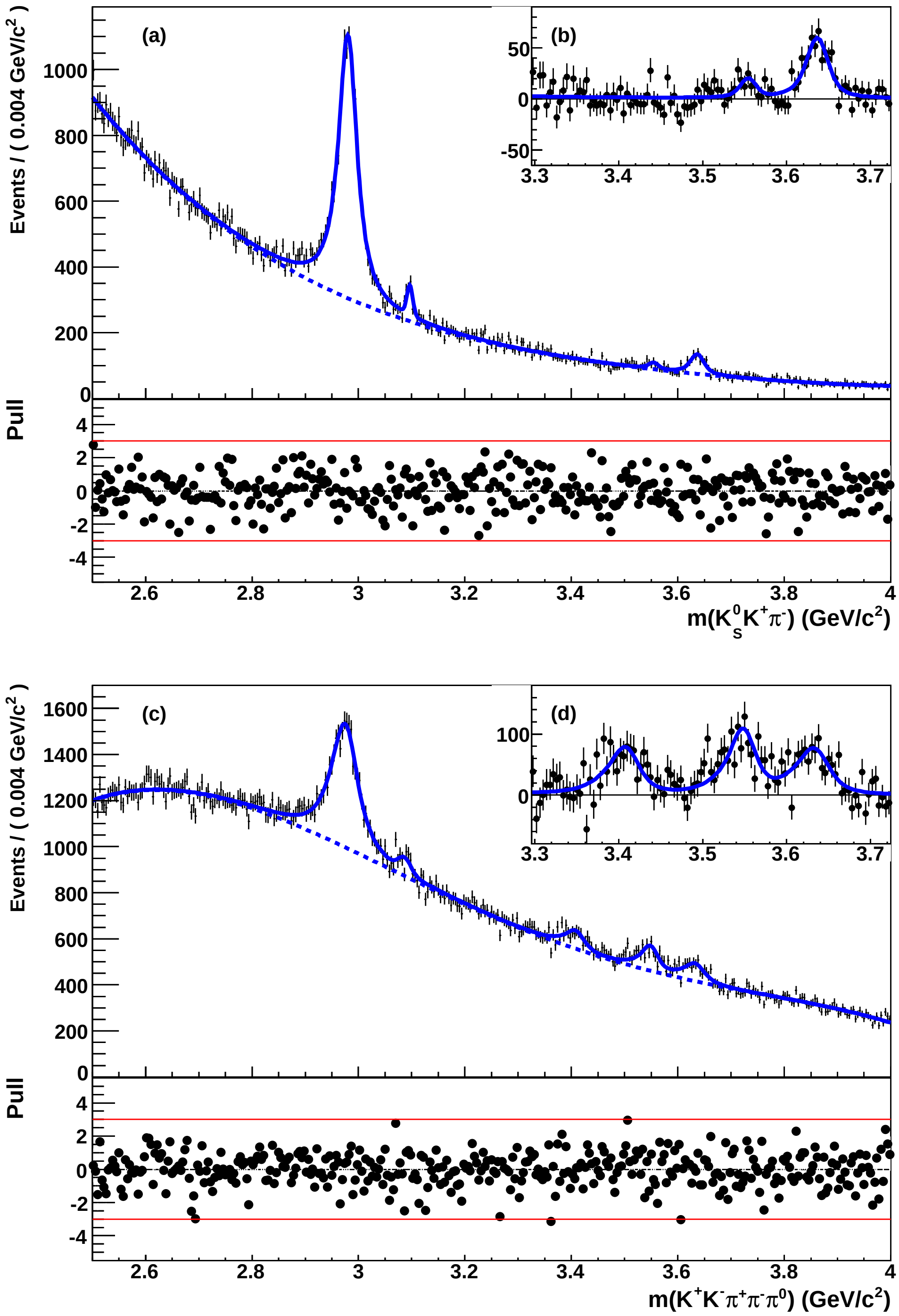

Figure 4.27: Fit to (a) the $K^0_S K^\pm\pi^\mp$ and (c) the $K^+K^-\pi^+\pi^-\pi^0$ mass spectrum. The solid curves represent the total fit functions and the dashed curves show the combinatorial background contributions. The background-subtracted distributions are shown in (b) and (d), where the solid curves indicate the signal components. In each plot we also show the distribution of the error-normalized difference (pull) between the fit function and the data points.

4.6.1 ψ's radiative decays background

J/ψ background

Background arising from J/ψ radiative decays are estimated using the fitted number of J/ψ events $N^{J/\psi}_{fitted}$ in the nominal fit. The number of background events from J/ψ radiative decays is equal to

$$N_f^{J/\psi\to\eta_c(1S)} = \frac{\epsilon(e^+e^-\to J/\psi\gamma_{ISR},\ J/\psi\to\gamma\eta_c(1S),\ \eta_c(1S)\to f)}{\epsilon(e^+e^-\to J/\psi\gamma_{ISR},\ J/\psi\to f)}\times \frac{\mathcal{B}(J/\psi\to\gamma\eta_c(1S))\mathcal{B}(\eta_c(1S)\to f)}{\mathcal{B}(J/\psi\to f)}\times N^{J/\psi}_{fitted}, \tag{4.8}$$

where $\epsilon(Y)$ and $\mathcal{B}(Y)$ represent the efficiency and branching fraction for the relevant Y process. Efficiencies are estimated using MC simulation and are equal to:

$$\frac{\epsilon(e^+e^-\to J/\psi\gamma_{ISR},\ J/\psi\to\gamma\eta_c(1S),\ \eta_c(1S)\to K^0_S K^\pm\pi^\mp)}{\epsilon(e^+e^-\to J/\psi\gamma_{ISR},\ J/\psi\to K^0_S K^\pm\pi^\mp)} = 3.31\pm 0.05, \tag{4.9}$$

$$\frac{\epsilon(e^+e^-\to J/\psi\gamma_{ISR},\ J/\psi\to\gamma\eta_c(1S),\ \eta_c(1S)\to K^+K^-\pi^+\pi^-\pi^0)}{\epsilon(e^+e^-\to J/\psi\gamma_{ISR},\ J/\psi\to K^+K^-\pi^+\pi^-\pi^0)} = 1.96\pm 0.08. \tag{4.10}$$

We use world average values for branching fractions [49], except for $\mathcal{B}(\eta_c(1S)\to K^+K^-\pi^+\pi^-\pi^0)$ which is taken from the results of this thesis. The relevant branching fraction ratios are equal to:

$$\frac{\mathcal{B}(J/\psi\to\gamma\eta_c(1S))\mathcal{B}(\eta_c(1S)\to K^0_S K^\pm\pi^\mp)}{\mathcal{B}(J/\psi\to K^0_S K^\pm\pi^\mp)} = 0.20\pm 0.07, \tag{4.11}$$

$$\frac{\mathcal{B}(J/\psi\to\gamma\eta_c(1S))\mathcal{B}(\eta_c(1S)\to K^+K^-\pi^+\pi^-\pi^0)}{\mathcal{B}(J/\psi\to K^+K^-\pi^+\pi^-\pi^0)} = 0.03\pm 0.01. \tag{4.12}$$

The fitted number of events in the the J/ψ peak is 324 ± 49 and 442 ± 11, in $K^0_S K^\pm\pi^\mp$ and $K^+K^-\pi^+\pi^-\pi^0$ sample, respectively. Using Eq. (4.8) and values from Eqs. (4.9)–(4.12), the number of expected $\eta_c(1S)$ peaking-background events, originating from J/ψ decays, is 214 ± 82 and 26 ± 9, in $K^0_S K^\pm\pi^\mp$ and $K^+K^-\pi^+\pi^-\pi^0$ final state, respectively.

$\psi(2S)$ background

The $\psi(2S)$ decays radiatively to $\chi_{c0}(1P)$ and $\chi_{c2}(1P)$, with a branching fraction of (9.6 ± 0.3)% and (8.7 ± 0.4)%, respectively [49]. The branching fraction of $\psi(2S)$ radiative decay to $\eta_c(2S)$ has been recently measured and is equal to 8×10^{-4} [155]. In principle the background contamination from $\psi(2S)$ decays may be estimated using Eq. (4.8) by changing J/ψ with $\psi(2S)$. Since the $\psi(2S)$ peak is not observed in the mass spectra (Fig. 4.22), this component is not included in the fit. The number $N^{\psi(2S)}_{fitted}$ to be used in

Eq. (4.8) is then obtained as

$$N^{\psi(2S)}_{fitted} = \frac{\epsilon^{standard}(\psi(2S)\to f)}{\epsilon^{reverted}(\psi(2S)\to f)} N^{\psi(2S)}_{reverted}, \tag{4.13}$$

where the number $N^{\psi(2S)}_{reverted}$ of $\psi(2S)$ events is obtained by fitting the ISR-enriched sample selected by reverting the M^2_{miss} requirement, as described in sec. 4.5.3. The efficiencies $\epsilon^{standard}(\psi(2S)\to f)$ and $\epsilon^{reverted}(\psi(2S)\to f)$ for the $\psi(2S)\to f$ process selected with nominal and reverted M^2_{miss} requirements, respectively, are obtained from MC. In the $K^0_S K^\pm\pi^\mp$ decay mode, the $\psi(2S)$ peak is not even observed in the enriched dataset (Fig. 4.26). We thus conclude that background from $\psi(2S)$ radiative decays is negligible for this channel. In the $K^+K^-\pi^+\pi^-\pi^0$ decay mode, 231 ± 28 $\psi(2S)$ events are observed. The ratio between the efficiencies obtained with standard and reverted selection criteria is

$$\frac{\epsilon^{standard}(\psi(2S)\to K^+K^-\pi^+\pi^-\pi^0)}{\epsilon^{reverted}(\psi(2S)\to K^+K^-\pi^+\pi^-\pi^0)} = 0.51\pm0.01. \tag{4.14}$$

Efficiencies needed in Eq. (4.8) are estimated using MC events and are equal to:

$$\frac{\epsilon(e^+e^-\to\psi(2S)\gamma_{ISR},\,\psi(2S)\to\gamma\chi_{c0}(1P),\,\chi_{c0}(1P)\to K^+K^-\pi^+\pi^-\pi^0)}{\epsilon(e^+e^-\to\psi(2S)\gamma_{ISR},\,\psi(2S)\to K^+K^-\pi^+\pi^-\pi^0)} = 0.73\pm0.02, \tag{4.15}$$

$$\frac{\epsilon(e^+e^-\to\psi(2S)\gamma_{ISR},\,\psi(2S)\to\gamma\chi_{c2}(1P),\,\chi_{c2}(1P)\to K^+K^-\pi^+\pi^-\pi^0)}{\epsilon(e^+e^-\to\psi(2S)\gamma_{ISR},\,\psi(2S)\to K^+K^-\pi^+\pi^-\pi^0)} = 2.19\pm0.05. \tag{4.16}$$

The quite large difference in efficiency between the two modes is related to the different energy of the radiative photon in the $\psi(2S)$ decay to $\chi_{c0}(1P)$ and $\chi_{c2}(1P)$. The larger energy of the photon from $\psi(2S)\to\gamma\chi_{c0}(1P)$ decay leads to an average p_T value for these events that is larger than that for $\psi(2S)\to\gamma\chi_{c2}(1P)$. Thus, $\psi(2S)\to\gamma\chi_{c0}(1P)$ events are more efficiently rejected by the p_T requirement. In order to estimate $\frac{\mathcal{B}(\psi(2S)\to\gamma\chi_{c0,2}(1P))\mathcal{B}(\chi_{c0,2}(1P)\to K^+K^-\pi^+\pi^-\pi^0)}{\mathcal{B}(\psi(2S)\to K^+K^-\pi^+\pi^-\pi^0)}$, needed in Eq. (4.8), one should know the value of the $\mathcal{B}(\chi_{cJ}(1P)\to K^+K^-\pi^+\pi^-\pi^0)$ branching ratios. To date, such decays have not been observed, yet. The $\chi_{cJ}(1P)\to K^+K^-\pi^+\pi^-\pi^0$ branching fraction can be obtained by the measurement of $\Gamma_{\gamma\gamma}\times\mathcal{B}(\chi_{c0,2}(1P)\to K^+K^-\pi^+\pi^-\pi^0)$ reported in this thesis (sec. 4.9) and the world-average $\Gamma_{\gamma\gamma}(\chi_{c0,2}(1P))$ values [49]. We obtain $\mathcal{B}(\chi_{c0}(1P)\to K^+K^-\pi^+\pi^-\pi^0) = (1.14\pm0.27)\%$ and $\mathcal{B}(\chi_{c2}(1P)\to K^+K^-\pi^+\pi^-\pi^0) = (1.30\pm0.36)\%$. The value of $\mathcal{B}(\chi_{c2}(1P)\to K^+K^-\pi^+\pi^-\pi^0)$ is consistent with a preliminary CLEO measurement [316, 317]. We find:

$$\frac{\mathcal{B}(\psi(2S)\to\gamma\chi_{c0}(1P))\mathcal{B}(\chi_{c0}(1P)\to K^+K^-\pi^+\pi^-\pi^0)}{\mathcal{B}(\psi(2S)\to K^+K^-\pi^+\pi^-\pi^0)} = 0.87\pm0.22, \tag{4.17}$$

$$\frac{\mathcal{B}(\psi(2S)\to\gamma\chi_{c2}(1P))\mathcal{B}(\chi_{c2}(1P)\to K^+K^-\pi^+\pi^-\pi^0)}{\mathcal{B}(\psi(2S)\to K^+K^-\pi^+\pi^-\pi^0)} = 0.90\pm0.25. \tag{4.18}$$

Using the number of $\psi(2S)$ fitted events and values in Eqs. (4.14)–(4.18), we estimate 75 ± 21 and 233 ± 73 peaking-background events from $\psi(2S)$ radiative decay to $\chi_{c0}(1P)$ and $\chi_{c2}(1P)$, respectively. The number of peaking-background events for $\eta_c(2S)$ is found to be negligible.

4.6.2 Two-photon backgrounds

The amount of irreducible peaking background originating from two-photon events with high multiplicity and other processes that produce real resonances is estimated by comparing the p_T distribution of resonance signal events with those expected for two-photon MC signals.

The combinatorial-background-subtracted p_T distribution for each resonance is obtained by fitting the $K^0_S K^\pm \pi^\mp$ and $K^+ K^- \pi^+ \pi^- \pi^0$ invariant mass spectrum in intervals of p_T, with a width of 0.05 GeV/c. For each interval, we repeat the fit procedure described in sec. 4.5.1, with the resonances parameters fixed to the values reported in Tab. 4.3. These fits are performed in the three intervals corresponding to the nominal p_T range [0,0.15] GeV/c, and in a sideband region, used to better parameterize the background p_T shape. The sideband range is [0.15,0.50] GeV/c and [0.15,0.90] GeV/c, for $K^+ K^- \pi^+ \pi^- \pi^0$ and $K^0_S K^\pm \pi^\mp$ decay modes, respectively. For $\chi_{c0,2}(1P)$ decays, we observe some upwards fluctuations in the high-p_T region, that originate from background fluctuations. These fluctuations were found to bias the estimate of the number of expected peaking-background events. We then decide to use [0.15,0.30] GeV/c and [0.15,0.20] GeV/c as sidebands for $\chi_{c0,2}(1P)$ decays, in $K^+ K^- \pi^+ \pi^- \pi^0$ and $K^0_S K^\pm \pi^\mp$ decay modes, respectively.

The yield distribution as a function of p_T is fitted to the sum of the MC-expected signal p_T distribution plus a flat background. Peaking-background events from $J/\psi \to \gamma \eta_c(1S)$ radiative decays are expected to have a p_T distribution similar to the signal one. Adding an explicit ISR-background component in the fit to the p_T distribution introduces negligible effects in the results. In Figs. 4.28–4.29 we show the results of the fits to the resonance yield distribution as a function of p_T. The expected number of peaking-background events are reported in Tab. 4.4. This method to estimate background was already proven to be effective for the $\gamma\gamma \to \eta_c(1S)\pi^0 \to K^0_S K^\pm \pi^\mp \pi^0$ background [158]. We cross-check the validity of this method for the $K^+ K^- \pi^+ \pi^- \pi^0$ final state with an exclusive study of the $\gamma\gamma \to K^+ K^- \pi^+ \pi^- \pi^0 \pi^0$ background process. Background contribution from such process is found to be negligible. Details about this study are reported in App. A. The two-photon background estimate given in the present section is more conservative with respect to the one obtained by studying the exclusive final state.

	$K^0_S K^\pm\pi^\mp$ Decay			$K^+K^-\pi^+\pi^-\pi^0$ Decay			
	$\eta_c(1S)$	$\chi_{c2}(1P)$	$\eta_c(2S)$	$\eta_c(1S)$	$\chi_{c0}(1P)$	$\chi_{c2}(1P)$	$\eta_c(2S)$
N_{peak} (p_T fit)	189 ± 18	-45 ± 11	25 ± 5	118 ± 32	-39 ± 19	14 ± 24	-46 ± 17
N_ψ (ψ's Decays)	214 ± 82	–	–	26 ± 9	75 ± 21	233 ± 73	–

Table 4.4: Summary of expected irreducible peaking-background events for each resonance: N_{peak} is the number of peaking-background events estimated with the p_T fit, and N_ψ the number of peaking-background events from ψ's radiative decays.

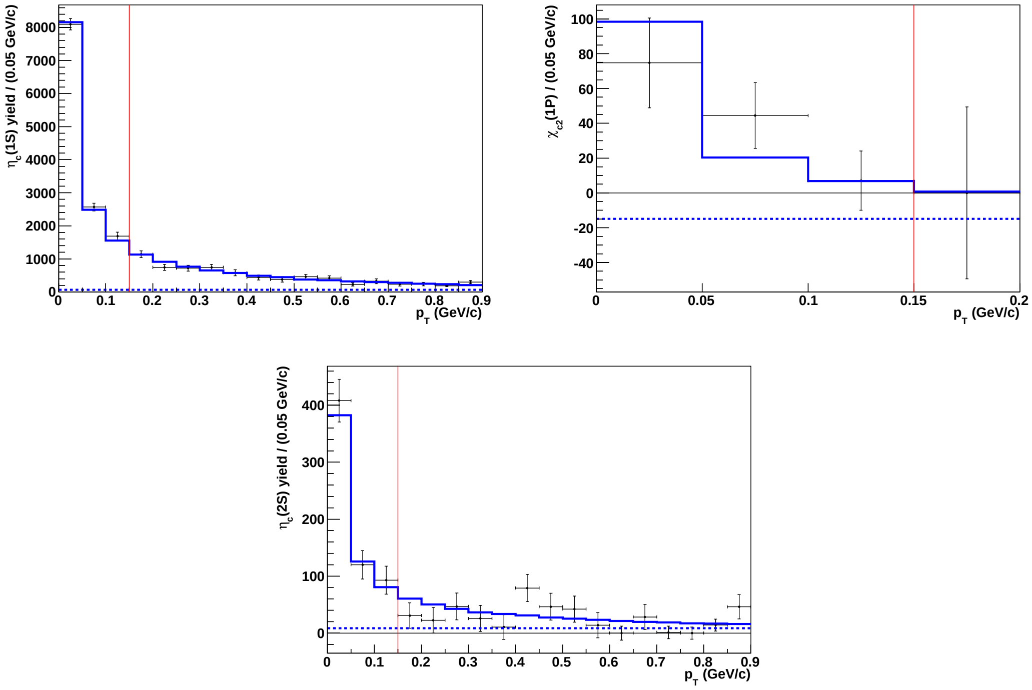

Figure 4.28: The (a) $\eta_c(1S)$, (b) $\chi_{c2}(1P)$, and (c) $\eta_c(2S)$ signal yield distribution as a function of p_T, in the $K^0_S K^\pm\pi^\mp$ decay mode. Points with error bars are the fitted resonance yield in each p_T interval, the blue solid line is the MC signal shape plus flat background fit function, the blue dashed line is the flat background contribution. The red line denotes the separation between signal ($p_T < 0.15$) and sideband ($p_T > 0.15$) region.

4.7 Two-photon couplings measurement

The measurement of the two-photon coupling $\Gamma_{\gamma\gamma}$ of the charmonium resonances is of a particular interest since this quantity carries information about the charmonium structure [1, 2].

The cross-section for the two-photon production of a X resonance decaying to the f final state is equal to

$$\sigma\left(e^+e^-\to e^+e^-\gamma\gamma\to e^+e^-X\to e^+e^-f\right) = \frac{N_f^X}{\varepsilon_f \int \mathcal{L}\Delta t} \tag{4.19}$$

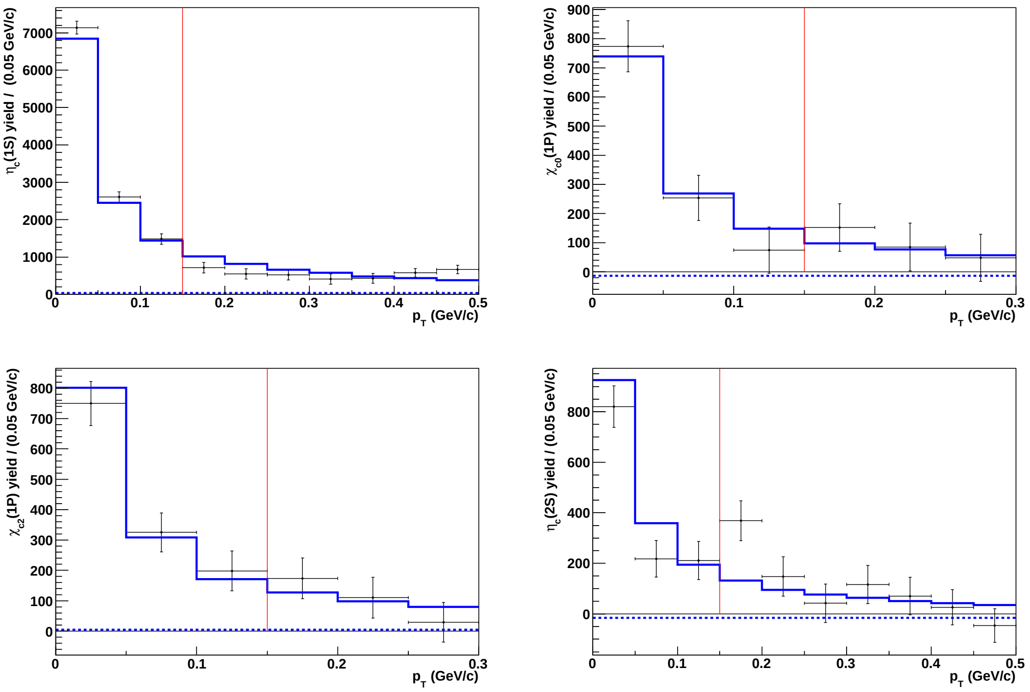

Figure 4.29: The (a) $\eta_c(1S)$, (b) $\chi_{c0}(1P)$, (c) $\chi_{c2}(1P)$, and (d) $\eta_c(2S)$ signal yield distribution as a function of p_T, in the $K^0_S K^\pm \pi^\mp$ decay mode. Points with error bars are the fitted resonance yield in each p_T interval, the blue solid line is the MC signal shape plus flat background fit function, the blue dashed line is the flat background contribution. The red line denotes the separation between signal ($p_T < 0.15$) and sideband ($p_T > 0.15$) region.

where ε_f is the average detection efficiency and $\int \mathcal{L}\Delta t$ is the total integrated luminosity. According to Eqs. (4.1)–(4.2), such a cross-section is proportional to the product between $\Gamma_{\gamma\gamma}(X)$ and the final state branching fraction $\mathcal{B}(X \to f)$. The flux term L and the form-factor F in Eq. (4.1), and the integral in Eq. (4.2) may be computed by using the `GamGam` generator [205]. Thus, the `GamGam` generator allows to relate the product $\Gamma_{\gamma\gamma}(X) \times \mathcal{B}(X \to f)$ to the measured cross-section values.

We also measure the ratio between the branching fractions of the $K^0_S K^\pm \pi^\mp$ and $K^+K^-\pi^+\pi^-\pi^0$ decay mode for the $\eta_c(1S)$ and $\eta_c(2S)$. This ratio is equal to

$$\frac{\mathcal{B}(\eta_c(nS) \to K^+K^-\pi^+\pi^-\pi^0)}{\mathcal{B}(\eta_c(nS) \to K^0_S K^\pm \pi^\mp)} = \frac{N^{\eta_c(nS)}_{KK3\pi}}{N^{\eta_c(nS)}_{K^0_S K\pi}} \cdot \frac{\epsilon^{\eta_c(nS)}_{K^0_S K\pi}}{\epsilon^{\eta_c(nS)}_{KK3\pi}}, \tag{4.20}$$

where $\eta_c(nS)$ denotes $\eta_c(1S)$ or $\eta_c(2S)$, $N^{\eta_c(nS)}_f$ represents the peaking-background-subtracted $\eta_c(nS)$ yield, and $\epsilon^{\eta_c(nS)}_f$ the average detection efficiency, for the f final state.

4.7.1 Fit strategy

The cross-section and the branching fraction ratio, according to Eqs. (4.19)–(4.20) are proportional to the N_f^X/ε_f ratio. Since the detection efficiency is not uniform over the phase space available to the decay, the average efficiency should depend on the sub-resonant decay structure. Such sub-resonant structure was never studied in detail for the $K^0_S K^\pm\pi^\mp$ final state [158], and is unknown for the $K^+K^-\pi^+\pi^-\pi^0$ final state. The ignorance about the decay dynamic may then lead to a large systematic uncertainty.

In order to reduce such uncertainty, we extract N_f^X/ε_f with an unbinned maximum likelihood fit, where each event is given a weight w, proportional to ε_f^{-1}, that takes into account the efficiency dependence on the decay kinematics. A detailed description of the efficiency parameterization is given in sec. 4.7.2. The weight w is equal to $\epsilon_f^{*-1} = \overline{\epsilon}_f/\varepsilon_f \sim 1$, where $\overline{\epsilon}_f$ is the average value of the efficiency over the available phase space for the decay. This procedure is needed in order to have fit weights of $\mathcal{O}(1)$, since weights far from one may lead to an underestimation of the statistical uncertainty of the fit [325]. With this convention, the ratio N_f^X/ε_f becomes

$$\frac{N_f^X}{\epsilon_f} = \frac{N_f^X}{\epsilon_f^* \times \overline{\epsilon}_f} \tag{4.21}$$

The fit to the weighted dataset is performed independently in two separate mass regions, near the $\eta_c(1S)$ ([2.5,3.3] GeV/c^2) and $\eta_c(2S)$ ([3.2,3.9] GeV/c^2) masses, in order to take into account the dependence of the reconstruction efficiency on the invariant mass. We use the same PDFs parameterization used in the fit to the unweighted dataset, described in sec. 4.5.1. The resonance parameters are fixed to the values reported in Tab. 4.3. The free parameters of the fit are the yields of the background and signal resonances, the mean and width of the Gaussian function describing the ISR J/ψ background, and the background shape parameters. Since the cross-section in Eq. (4.19) depends on the CM energy, the measurement of $\Gamma_{\gamma\gamma} \times \mathcal{B}$ is performed by using 473.8 fb^{-1} collected near the $\Upsilon(4S)$ mass energy. The whole 519.2 fb^{-1} dataset is used to measure the branching fraction ratio of Eq. (4.20).

The kinematics of peaking-background events is similar to those of the signal, so we assume the signal to peaking-background ratio to be unaffected by the weighting technique. The $\eta_c(1S)$ weighted yield is corrected by subtracting the number of expected background events originating from $J/\psi\to\gamma\eta_c(1S)$, while we assign a systematic uncertainty (see sec. 4.8.1) to account for the presence of peaking-background for $\chi_{c0}(1P)$, $\chi_{c2}(1P)$, and $\eta_c(2S)$.

4.7.2 Efficiency parameterization

The reconstruction efficiency is expected to depend on the kinematics variables describing the $K_S^0 K^\pm \pi^\mp$ and $K^+K^-\pi^+\pi^-\pi^0$ decay. In the following sections we describe the efficiency parameterization that is used to compute efficiencies, and thus weights, that enter in the fit described in sec. 4.7.1.

$K_S^0 K^\pm \pi^\mp$ **decay mode**

We describe the $K_S^0 K^\pm \pi^\mp$ decay kinematics by using the “*Squared Dalitz Plot*” formalism. The decay is described by the invariant $K\pi$ mass versus the angle between the direction of the K^+ in the $K\pi$ rest frame and that of the $K\pi$ system in the $K_S^0 K^\pm \pi^\mp$ reference frame. The “*Squared Dalitz Plot*” is a standard technique used to study three-body decays. Its main advantages with respect to the “*standard*” Dalitz Plot are the fact that the angular structure of the decay is made explicit, the presence of a rectangular boundary, and the fact that reflections originating from mis-PID manifest in precise *loci*.

The efficiency dependence on these variables is parameterized by using a two-dimensional histogram. The efficiency in each bin is computed as the ratio of the number of MCT signal events surviving the selection to the number of MC generated signal events. While computing efficiency, we set the efficiency to zero in bins with less than 10 events. The number of real data events falling in these bins is smaller than 0.5%. In Figs. 4.30–4.31 we show the efficiency and the efficiency uncertainty distribution over the “*Squared Dalitz Plot*”, for the $\eta_c(1S)$ and $\eta_c(2S)$ mass regions. We also show such distributions over the “*standard*” Dalitz Plot as a function of the $K_S^0\pi$ versus the $K\pi$ mass.

$K^+K^-\pi^+\pi^-\pi^0$ **Decay Mode**

In order to describe a five body decay, 8 independent variables are needed. We generalize the Cabibbo-Maksymowicz variables [326] used to describe a four-body decay, by grouping the decay products in two sub-systems that we identify with the two kaons and the three pions system, respectively. The 5 body decay kinematics can be parameterized by using the following variables, as sketched in Fig. 4.32:

1. m_{KK}: the invariant mass of the K^+K^- system;
2. $m_{3\pi}$: the invariant mass of the $\pi^+\pi^-\pi^0$ system;
3. $m_{\pi\pi}$: the invariant mass of the $\pi^+\pi^-$ system;

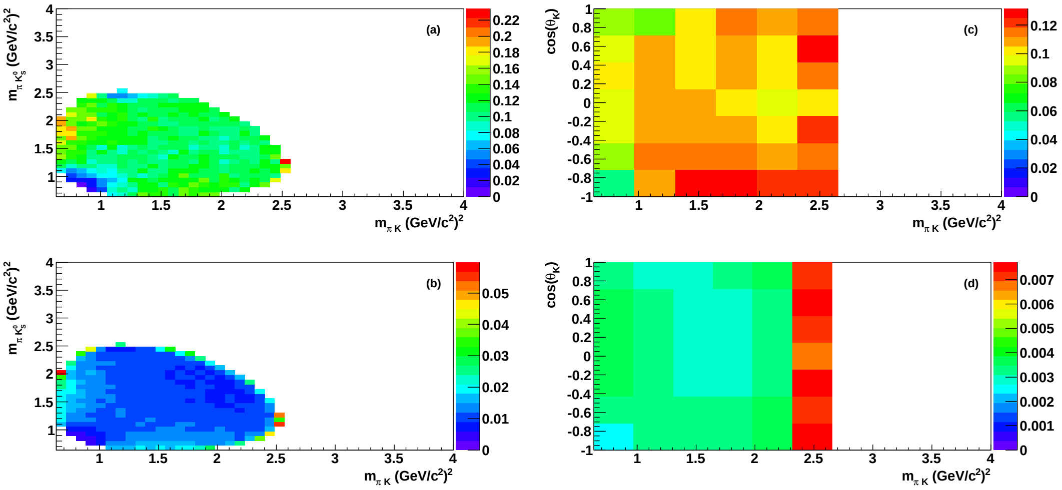

Figure 4.30: Signal efficiency ((a) and (c)), and its uncertainty ((b) and (d)) distributions over the "*standard*" and (c-d) "*squared*" Dalitz Plot, for $\eta_c(1S)$ mass region.

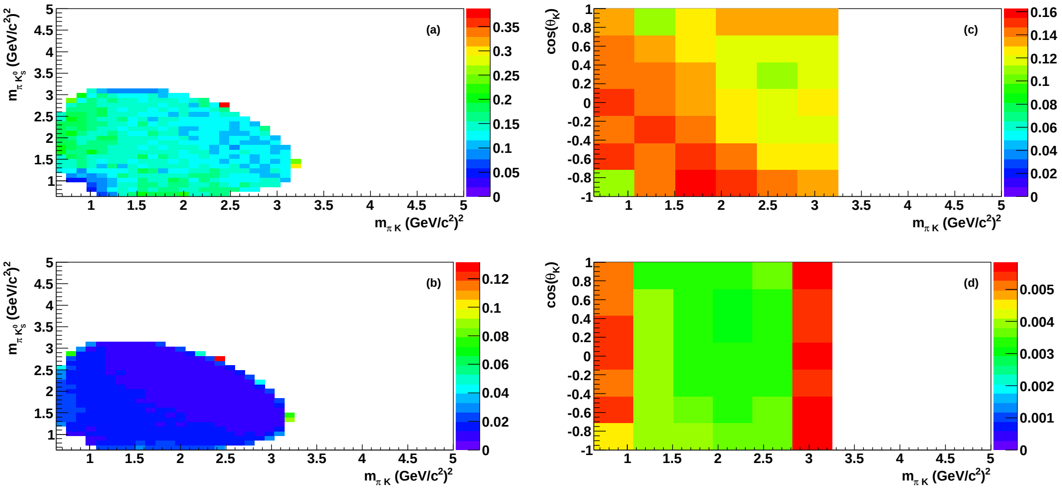

Figure 4.31: Signal efficiency ((a) and (c)), and its uncertainty ((b) and (d)) distributions over the "*standard*" and (c-d) "*squared*" Dalitz Plot, for $\eta_c(2S)$ mass region.

4. $\cos\theta_K$: the cosine of the angle between the direction of K^+ and the recoil of the 3π system, in the K^+K^- frame;

5. $\cos\Theta$: the cosine of the angle between the normal $\widehat{n}$ to the 3π decay plane and the recoil direction of the K^+K^- system, in the 3π frame. This angle describes the polar orientation of $\widehat{n}$ with respect to the recoil direction of the K^+K^- system;

6. Φ: the angle that describes an azimuthal rotation of $\widehat{n}$ with respect to the recoil direction of the K^+K^- system;

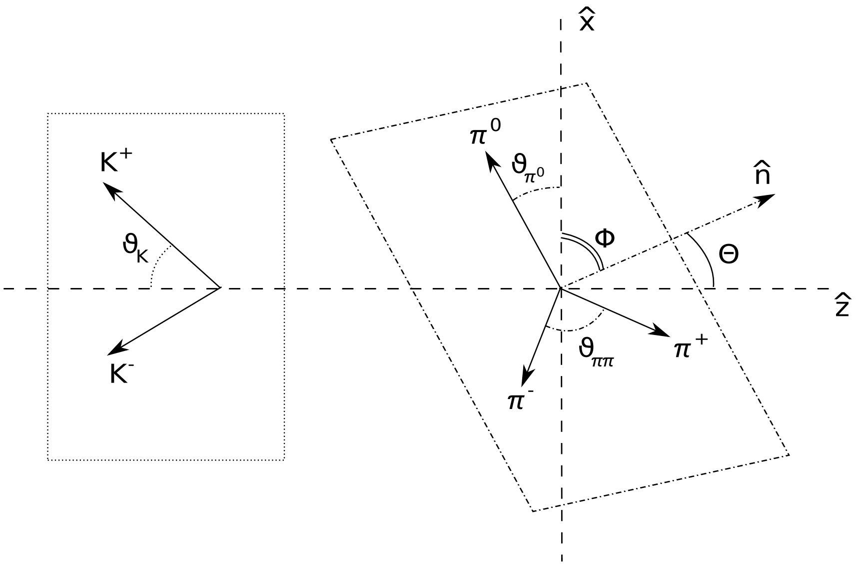

Figure 4.32: Representation of the 5 body decay system split in the K^+K^- and 3π systems, and of angles used to describe the decay (see text for further details).

7. θ_π: the angle that describes a rotation of the whole 3π system on its decay plane;
8. $\cos\theta_{\pi\pi}$: the cosine of the angle between π^+ and π^- momenta, in the 3π frame.

Correlations between m_{KK}, $m_{3\pi}$, and $m_{\pi\pi}$ are as large as 60%. Correlation between different angular variables and between angular variables and the invariant masses are usually negligible, with the exception of the correlation between $\cos\theta_{\pi\pi}$ and $m_{\pi\pi}$ which is -70%. The efficiency dependence on each of the eight variables described above is shown in Fig. 4.33–4.34, for $\eta_c(1S)$ and $\eta_c(2S)$ mass regions, respectively. The efficiency has a weak dependence on the angular variables, while has strong dependence on $m_{\pi\pi}$, m_{KK} and $m_{3\pi}$.

A full parameterization in eight dimensional space is not feasible due to limited MC statistics. A three-dimensional histogram is used to parameterize the dependence on the invariant masses. The binning of the three-dimensional efficiency histogram needs to be optimized in order to be small enough not to loose information, but also large enough to keep the statistical error, due to MC sample size, reasonably low. We choose a binning that allows to have at least half of the bins with a relative error on the efficiency lower than 10%. We assign null efficiency to bins with less than 10 events. The number of real data events falling in these bins is $3-4\%$. In Figs. 4.35–4.36, we show the projection of

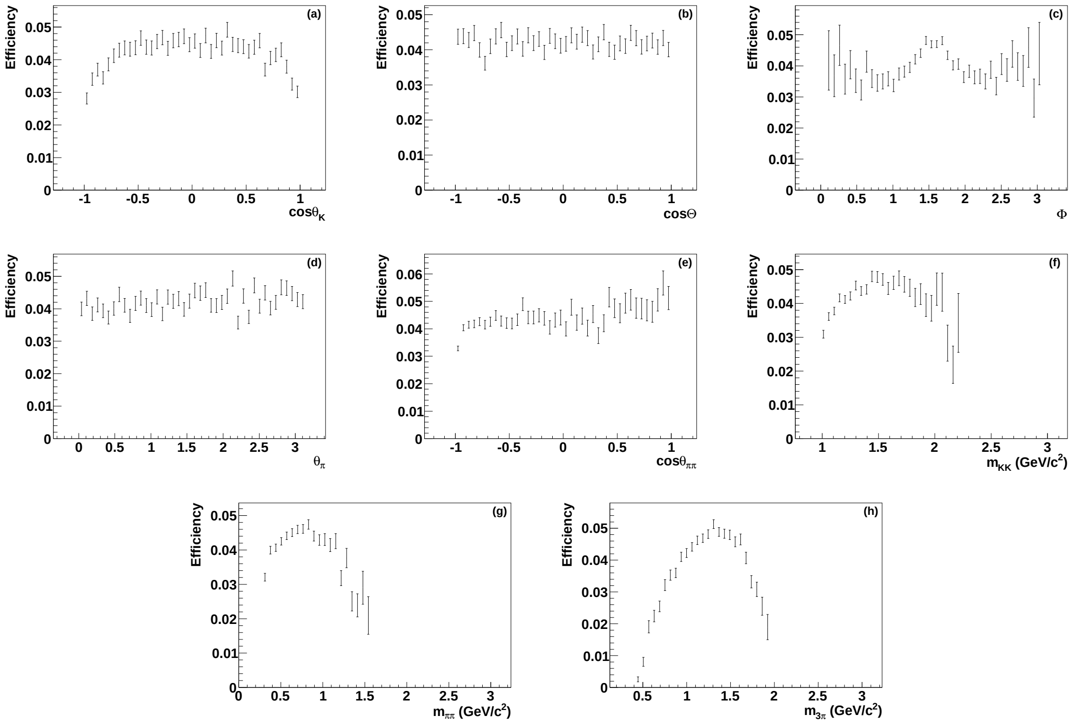

Figure 4.33: 1D projections of $\gamma\gamma\to\eta_c(1S)\to K^+K^-\pi^+\pi^-\pi^0$ efficiency on (a) $\cos\theta_K$, (b) $\cos\Theta$, (c) Φ, (d) θ_π, (e) $\cos\theta_{\pi\pi}$, (f) m_{KK}, (g) $m_{\pi\pi}$, and (h) $m_{3\pi}$.

the signal efficiency and its uncertainty on the two-dimensional planes $(m_{KK}, m_{\pi\pi})$ and $(m_{KK}, m_{3\pi})$, in the $\eta_c(1S)$ and $\eta_c(2S)$ mass regions, respectively. The signal efficiency obtained by the three-dimensional histogram is corrected taking into account its dependence on the angular variables. The correction factor distribution as a function of each angular variable is obtained by dividing the efficiency distribution as a function of the relevant variable by its mean value. The correction factor distribution is parameterized with fourth and second-order polynomial shapes as shown in Fig. 4.37.

The total efficiency ε for one event is given by

$$\begin{aligned}\varepsilon &= \varepsilon^{3D}(m_{KK}, m_{3\pi}, m_{\pi\pi}) \times c_1(\cos\theta_K) \times c_2(\cos\Theta) \times c_3(\Phi) \times \\ &\quad c_4(\theta_\pi) \times c_5(\cos\theta_{\pi\pi}),\end{aligned} \tag{4.22}$$

where ε^{3D} is the efficiency obtained from the three-dimensional histogram and c_i ($i = 1, 2, 3, 4, 5$) are the correction factors depending on the angular variables. The factorization of the correction factors in Eq. (4.22) implies the assumption that the correlations involving the angular variables are negligible The -70% correlation between $\cos\theta_{\pi\pi}$ and $m_{\pi\pi}$ results in a change of the efficiency that is taken into account as a systematic uncertainty as described in sec. 4.8.2.

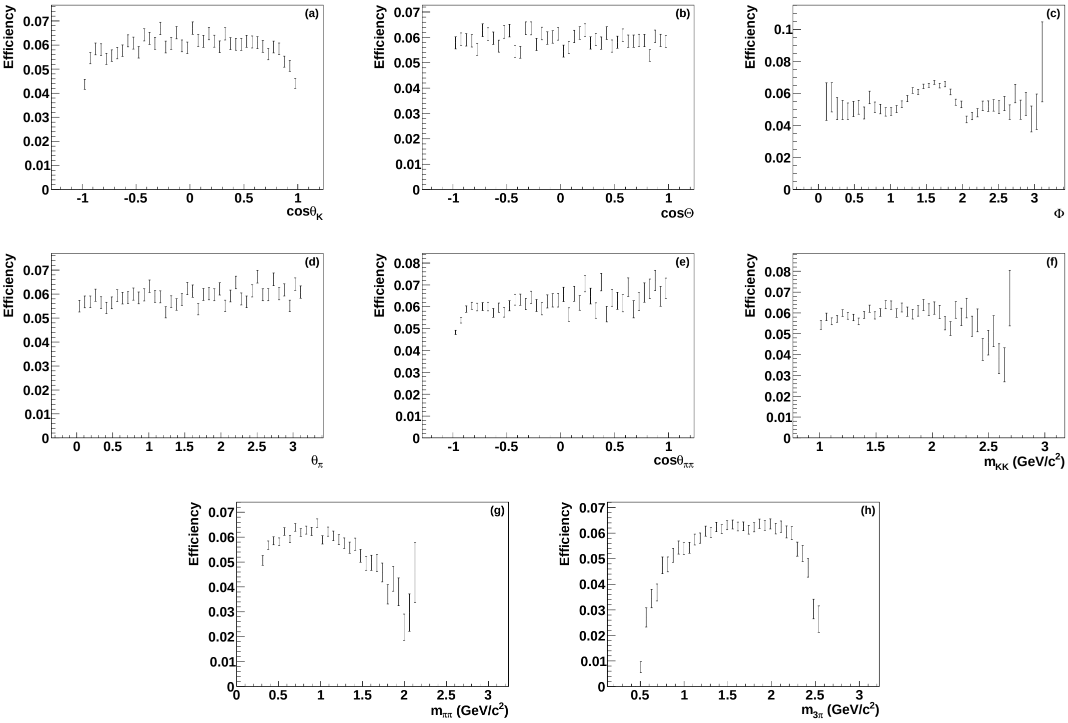

Figure 4.34: 1D projections of $\gamma\gamma{\to}\eta_c(2S){\to}K^+K^-\pi^+\pi^-\pi^0$ efficiency on (a) $\cos\theta_K$, (b) $\cos\Theta$, (c) Φ, (d) θ_π, (e) $\cos\theta_{\pi\pi}$, (f) m_{KK}, (g) $m_{\pi\pi}$, and (h) $m_{3\pi}$.

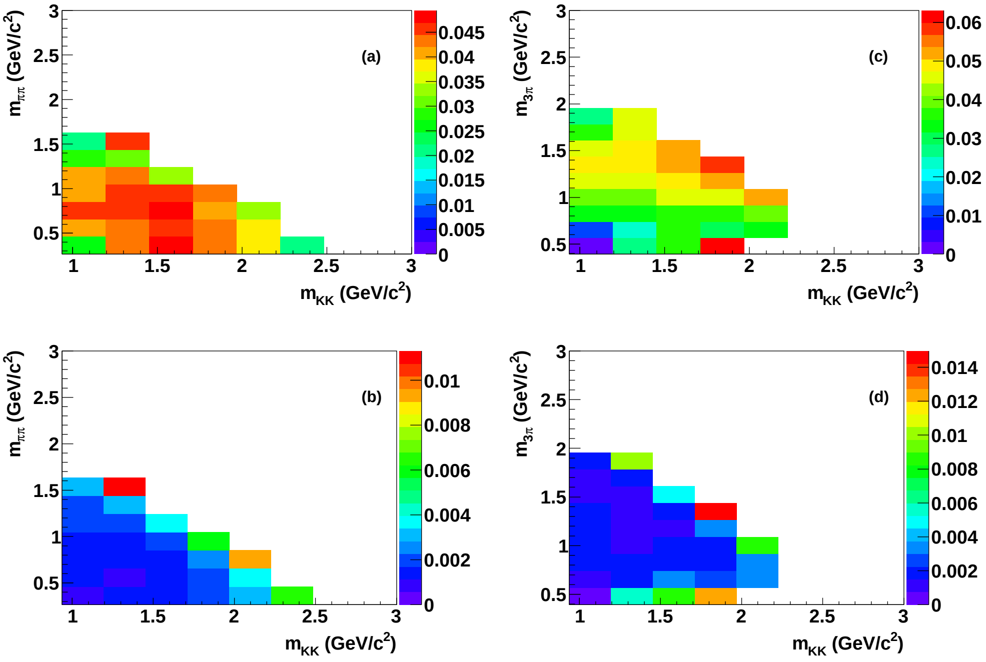

Figure 4.35: Signal efficiency ((a) and (c)), and its uncertainty ((b) and (d)) distributions over the $(m(KK), m(\pi\pi))$ and $(m(KK), m(3\pi))$ planes , for the $K^+K^-\pi^+\pi^-\pi^0$ decay mode in the $\eta_c(1S)$ mass region.

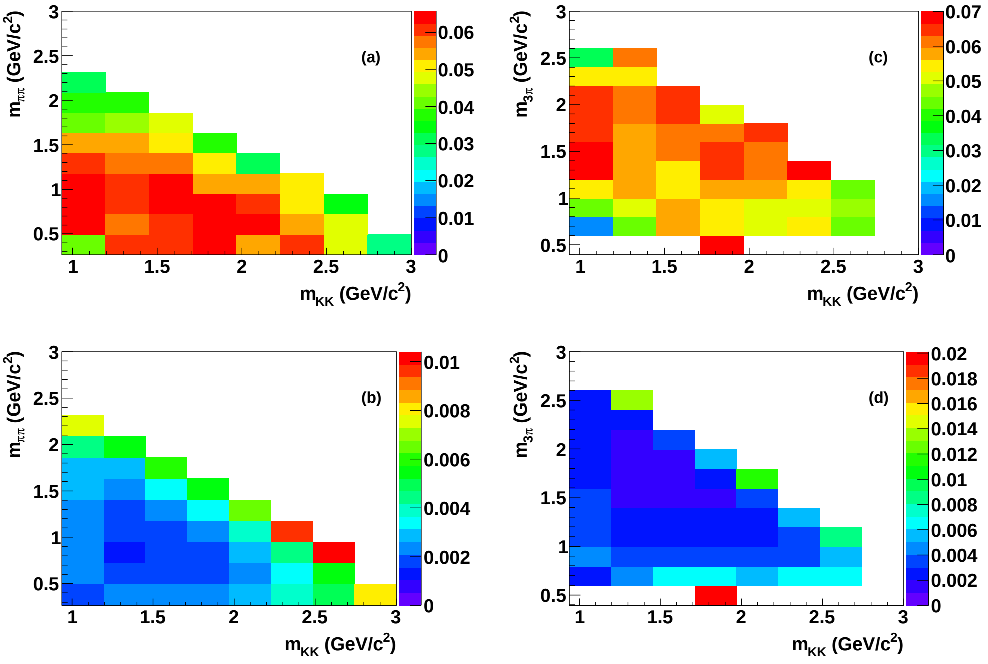

Figure 4.36: Signal efficiency ((a) and (c)), and its uncertainty ((b) and (d)) distributions over the $(m(KK), m(\pi\pi))$ and $(m(KK), m(3\pi))$ planes , for the $K^+K^-\pi^+\pi^-\pi^0$ decay mode in the $\eta_c(2S)$ mass region.

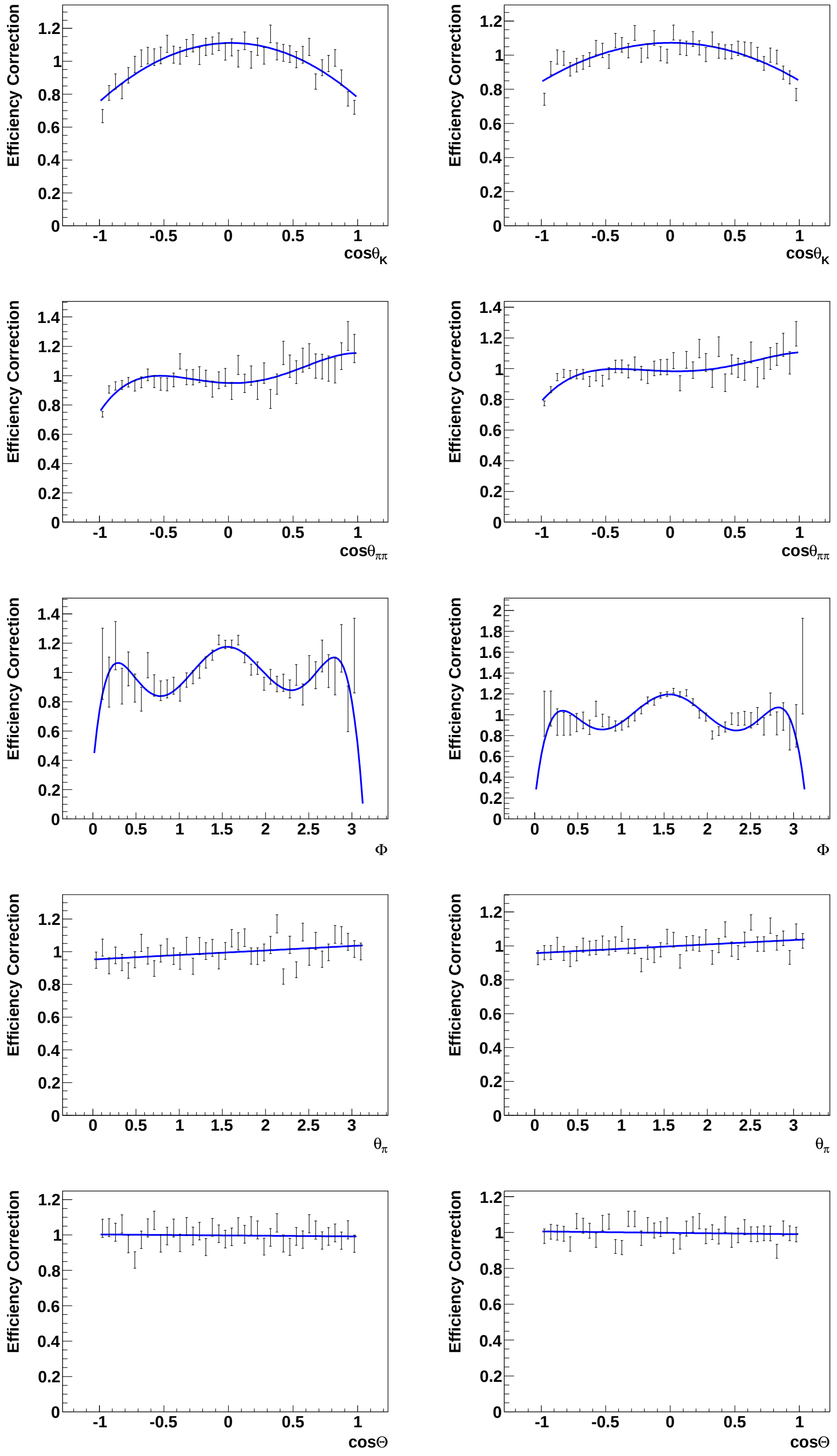

Figure 4.37: Fit to efficiency correction factors depending on the angular variables in $\eta_c(1S)\to K^+K^-\pi^+\pi^-\pi^0$ (left) and $\eta_c(2S)\to K^+K^-\pi^+\pi^-\pi^0$ (right) decay. Top to bottom: $\cos\theta_K$, $\cos\theta_{\pi\pi}$, Φ, θ_π, and $\cos\Theta$.

4.7.3 Fit results

In Tab. 4.5 we show the cross-section results for each resonance, obtained with data collected near the $\Upsilon(4S)$ energy. The cross-section for the $K^0_SK^\pm\pi^\mp$ decay mode is corrected to take into account $\mathcal{B}(K^0_S\to\pi^+\pi^-) = (69.20\pm0.05)\%$ [49]. The weighted signal yield to be used for the branching fraction ratio measurement, obtained by using the whole dataset, is 109550 ± 2038 and 223496 ± 7160 for $\eta_c(1S)$, and 4483 ± 447 and 14375 ± 2542 for $\eta_c(2S)$, in the $K^0_SK^\pm\pi^\mp$ and $K^+K^-\pi^+\pi^-\pi^0$ decay mode, respectively. In Figs. 4.38 and 4.39 we show the fitted spectra in the $\eta_c(2S)$ and $\eta_c(2S)$ mass regions. We compute a χ^2 using the total fit function and the binned relevant mass distribution obtained after weighting. The values of χ^2/ndf are 1.16 and 1.15 for $\eta_c(1S)$, and 1.20 and 1.00 for $\eta_c(2S)$ mass regions, in the $K^0_SK^\pm\pi^\mp$ and $K^+K^-\pi^+\pi^-\pi^0$ channel, respectively.

	cross-section (fb)			
	$\eta_c(1S)$	$\chi_{c0}(1P)$	$\chi_{c2}(1P)$	$\eta_c(2S)$
$K^0_SK^\pm\pi^\mp$	299.0 ± 5.9	$-$	2.6 ± 0.9	12.3 ± 1.3
$K^+K^-\pi^+\pi^-\pi^0$	431.7 ± 14.5	30.3 ± 5.3	29.8 ± 4.6	26.8 ± 5.1

Table 4.5: Cross-section results for data collected near the $\Upsilon(4S)$ energy.

4.8 Systematic uncertainties

In the following section we discuss the sources of systematic uncertainty in our measurements. We discuss separately the sources that affect yield and resonance parameters measurement and those that are involved in the cross-section and relative branching fraction measurement.

4.8.1 Yields and resonances parameters systematics

Here below we list the sources of systematic uncertainties affecting the yield and resonance parameters measurement and the method used for their estimate. A summary of all the contributions may be found in Tab. 4.7.

PDFs shape

A systematic uncertainty is assigned to account for the uncertainty related to parameters that are fixed in the fit described in sec. 4.5.1. We assign as systematic the sum in quadrature of the changes in results observed when performing the nominal fit by varying the

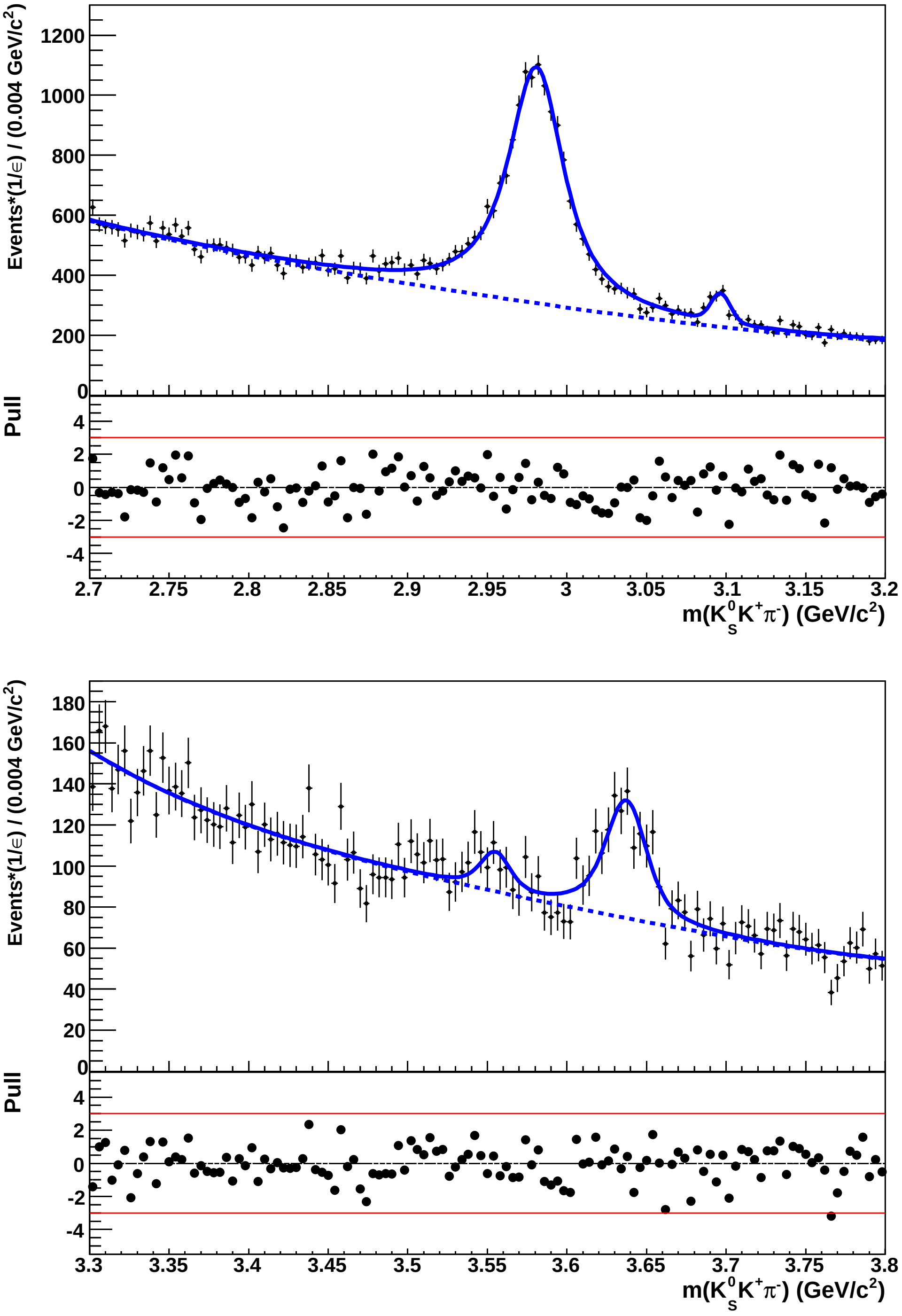

Figure 4.38: Fit to the $K^0_S K^{\pm}\pi^{\mp}$ efficiency-weighted mass spectrum in the (a) $\eta_c(1S)$ region and (b) $\eta_c(2S)$region. The solid line is the total fit function, the dashed line is the background component. In each plot we also show the distribution of the error-normalized difference (pull) between the fit function and the data points.

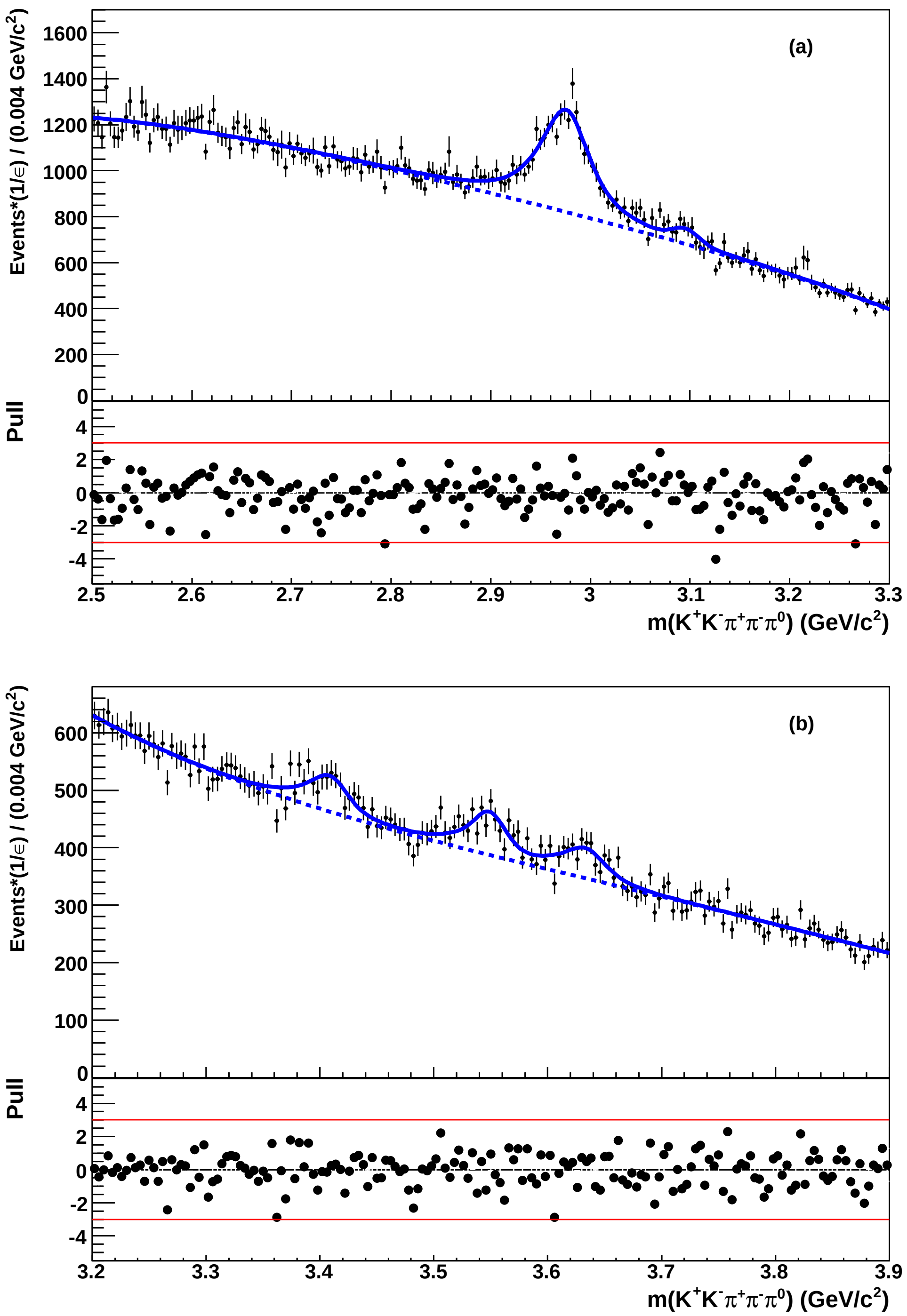

Figure 4.39: Fit to the $K^+K^-\pi^+\pi^-\pi^0$ efficiency-weighted mass spectrum in the (a) $\eta_c(1S)$ region and (b) $\eta_c(2S)$region. The solid line is the total fit function, the dashed line is the background component. In each plot we also show the distribution of the error-normalized difference (pull) between the fit function and the data points.

fixed parameters of $\pm 1\sigma$ with respect to their central value. In this systematic we include the uncertainty related to fixing $\chi_{c0}(1P)$, $\chi_{c2}(1P)$ and some of the J/ψ and $\eta_c(2S)$ parameters in the fit.

Background shape

Possible background mismodeling is evaluated by changing the background shape from fourth to sixth order polynomial. Changes in the fit results are taken as systematic on the background shape.

Absolute mass scale

The absolute mass scale is determined by fitting the ISR-enriched sample as described in sec. 4.5.3. The observed mass shift with respect to the nominal J/ψ mass value is $(-0.5\pm 0.2)\ \mathrm{MeV}/c^2$ and $(-1.1\pm 0.8)\ \mathrm{MeV}/c^2$, for $K^0_S K^\pm\pi^\mp$ and $K^+K^-\pi^+\pi^-\pi^0$ decay modes, respectively. We assign the statistical error on the shift as systematic uncertainty on the absolute mass scale.

$\eta_c(1S)$-J/ψ momentum distribution

The shift in the absolute mass scale determined by using the ISR-enriched sample may be biased due to the fact that two-photon and ISR events have quite different distribution of the longitudinal momentum p_z. Possible mismodeling of the detector response may lead to a systematic shift in the value of the corrected mass [158]. The distribution of p_z for signal two-photon and J/ψ ISR MC events is shown in Fig. 4.40.

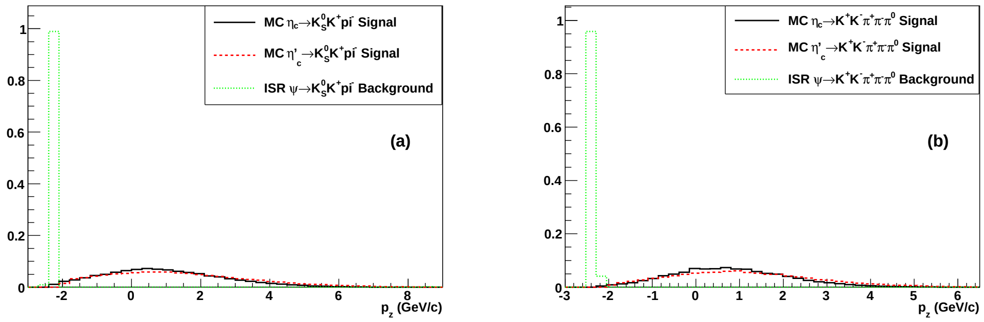

Figure 4.40: Distribution of p_Z for (a) $K^0_S K^\pm\pi^\mp$ and (b) $K^+K^-\pi^+\pi^-\pi^0$. The black solid line is the $\eta_c(1S)$ signal MC, the red dashed line is the $\eta_c(2S)$ signal MC, and the green dotted line is the J/ψ ISR background MC.

We divide data into three subsamples, with approximatively the same statistics, but with a different average value of p_z. The average value of p_z in the three $K^0_S K^\pm\pi^\mp$

subsamples is -0.9 GeV/c, 0.7 GeV/c, and 2.6 GeV/c, respectively. The average value of p_z in the three $K^+K^-\pi^+\pi^-\pi^0$ subsamples is -0.7 GeV/c, 0.7 GeV/c, and 2.4 GeV/c, respectively. For comparison, p_z is peaked around -2.3 GeV/c for ISR J/ψ events in both $K^0_S K^\pm\pi^\mp$ and $K^+K^-\pi^+\pi^-\pi^0$ decays, as shown in Fig. 4.40 Each subsample is then fitted with the procedure described in sec. 4.5.1. In these fits, the $\eta_c(2S)$ width is fixed to the value reported in Tab. 4.3.

The differences between the nominal fitted mass, reported in Tab. 4.3, and the values obtained when fitting the three subsamples are:

- $(+0.2 \pm 0.6)$ GeV/c^2, $(+0.1 \pm 0.6)$ GeV/c^2, (-0.4 ± 0.6) $\mathrm{GeV}/c^2$for $\eta_c(1S)$ in $K^0_S K^\pm\pi^\mp$ decay;
- (-0.6 ± 2.7) GeV/c^2, $(+0.2 \pm 4.0)$ GeV/c^2, $(+0.3 \pm 2.1)$ $\mathrm{GeV}/c^2$for $\eta_c(2S)$ in $K^0_S K^\pm\pi^\mp$ decay;
- $(+0.3 \pm 1.3)$ GeV/c, (-0.1 ± 1.3) GeV/c, (-0.0 ± 1.6) GeVfor $\eta_c(1S)$ in $K^+K^-\pi^+\pi^-\pi^0$ decay;
- (-3.1 ± 5.1) GeV, $(+7.2 \pm 6.5)$ GeV/c, (-1.1 ± 4.8) GeV/c for $\eta_c(2S)$ in $K^+K^-\pi^+\pi^-\pi^0$ decay;

No significant shift is observed. The value of the shift observed in the subsample where the average p_z value is maximum is taken as an estimate of the systematic uncertainty on the resonance mass.

MC/data resolution

The systematic uncertainty due to the different mass resolution in data and MC is estimated by repeating the nominal fit described in sec. 4.5.1 with a modified value of σ in Eq. (4.5). We define $\sigma^2 = \sigma^2_{MC} + \text{sign}(\Delta\sigma)\cdot\Delta\sigma^2$, where σ_{MC} is the value obtained from MC simulation, and $\Delta\sigma$ is determined in the fit to the ISR-enriched sample described in sec. 4.5.3. The fitted value of $\Delta\sigma$ is equal to (5.0 ± 1.0) MeV/c^2, and (4.8 ± 2.5) MeV/c^2 for $K^0_S K^\pm\pi^\mp$ and $K^+K^-\pi^+\pi^-\pi^0$ mode, respectively. The changes in results with respect to the values reported in Tab. 4.3, observed when using the modified value of σ in the fit, are taken as systematic uncertainties.

Background subtraction

We subtract the number of $J/\psi\to\gamma\eta_c(1S)$ peaking-background events from the $\eta_c(1S)$ signal yield. A systematic uncertainty equal to the uncertainty on the number of $J/\psi\to\gamma\eta_c(1S)$ peaking-background events is assigned.

Peaking background

We assign as systematic uncertainty due to the presence of two-photon irreducible peaking-background the number of peaking-background events obtained with the fit to the yield distribution as a function of p_T, summed in quadrature with its uncertainty. For the $\chi_{c0,2}(1P)$, we also add to this systematic the estimated number of $\psi(2S) \to \gamma\chi_{c0,2}(1P)$ peaking-background events summed in quadrature with its uncertainty.

Resolution function distortion

The fact that the subresonant structure of the decay is different between data and MC (that is simulated with phase-space assumption) may lead to distortion of the resolution function.

Distributions for data over the Dalitz Plot in signal and background region for the $K^0_S K^\pm \pi^\mp$ decay mode are shown in App. B. The Dalitz Plot is divided in different regions as illustrated in Fig. 4.41. The 23 (4) regions labeled with "*A*" and "*B*" are used to study the systematic effect on the $\eta_c(1S)$ and $\eta_c(2S)$ parameters, respectively. The $\eta_c(1S)$ and $\eta_c(2S)$ yield is fitted in each region to obtain the experimental Dalitz Plot distribution. The signal MC samples are reweighted in order to reproduce such a distribution. The $\eta_c(1S)$ and $\eta_c(2S)$ resolution functions are then fitted by using events from the reweighted MC samples, and the fit described in sec. 4.5.1 is repeated by using these "*reweighted*" resolution functions. The changes observed in the fitted resonances parameters with respect to the results reported in Tab. 4.3 are taken as systematic uncertainties.

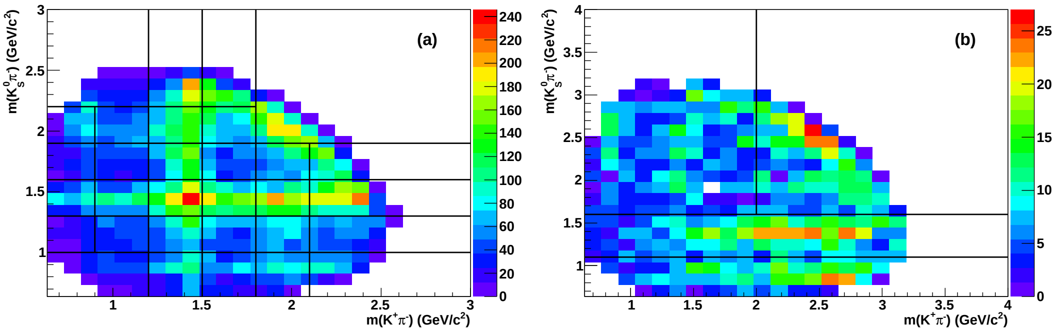

Figure 4.41: Division of the Dalitz plot into regions: (a) the 23 "*A*" regions used to evaluate systematics for the $\eta_c(1S) \to K^0_S K^\pm \pi^\mp$ decay; (b) the 4 "*B*" regions used to evaluate systematics for the $\eta_c(2S) \to K^0_S K^\pm \pi^\mp$ decay. Plotted data are taken from Fig. B.1 (a) and (b), respectively.

In the $K^+K^-\pi^+\pi^-\pi^0$ decay mode, due to the limited statistics, the weighting technique is applied to projections of the data over one or two invariant masses combination per time. Invariant masses distributions for data in signal and background regions for the $K^+K^-\pi^+\pi^-\pi^0$ decay mode are shown in App. B. In Figs. 4.42–4.43 we show the "*A*" and "*B*" regions used to fit the $\eta_c(1S)$ and $\eta_c(2S)$ yields, respectively. For each projection, we reweight the MC events in order to reproduce the distribution obtained by fitting the data. The reweighted MC events are used to fit a resolution function that is used in the fit described in sec. 4.5.1. We perform a fit to the data using each of the "*reweighted*" resolution functions. We take as systematic the largest among the differences between the nominal fit results reported in Tab. 4.3 and the values obtained with the "*reweighted*" resolution functions.

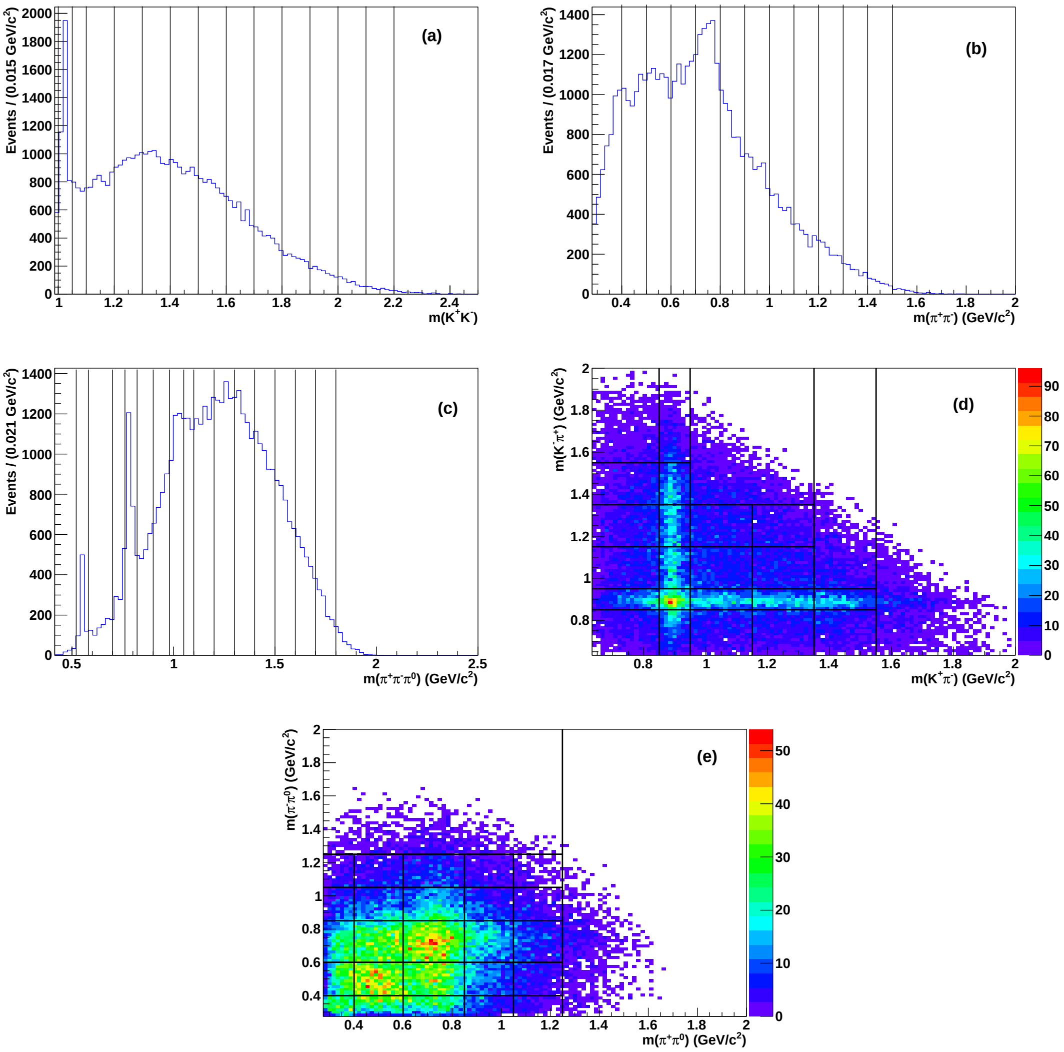

Figure 4.42: Division of the invariant mass projections into "*A*" regions used to compute the systematic for the $\eta_c(1S)\to K^+K^-\pi^+\pi^-\pi^0$ deacy; (a) $m(KK)$, (b) $m(\pi^+\pi^-)$, (c) $m(\pi^+\pi^-\pi^0)$, (d) $(m(K^+\pi^-), m(K^-\pi^+))$, (e) $(m(\pi^+\pi^0), m(\pi^-\pi^0))$. Plotted data are taken from Figs. B.2–B.6(a).

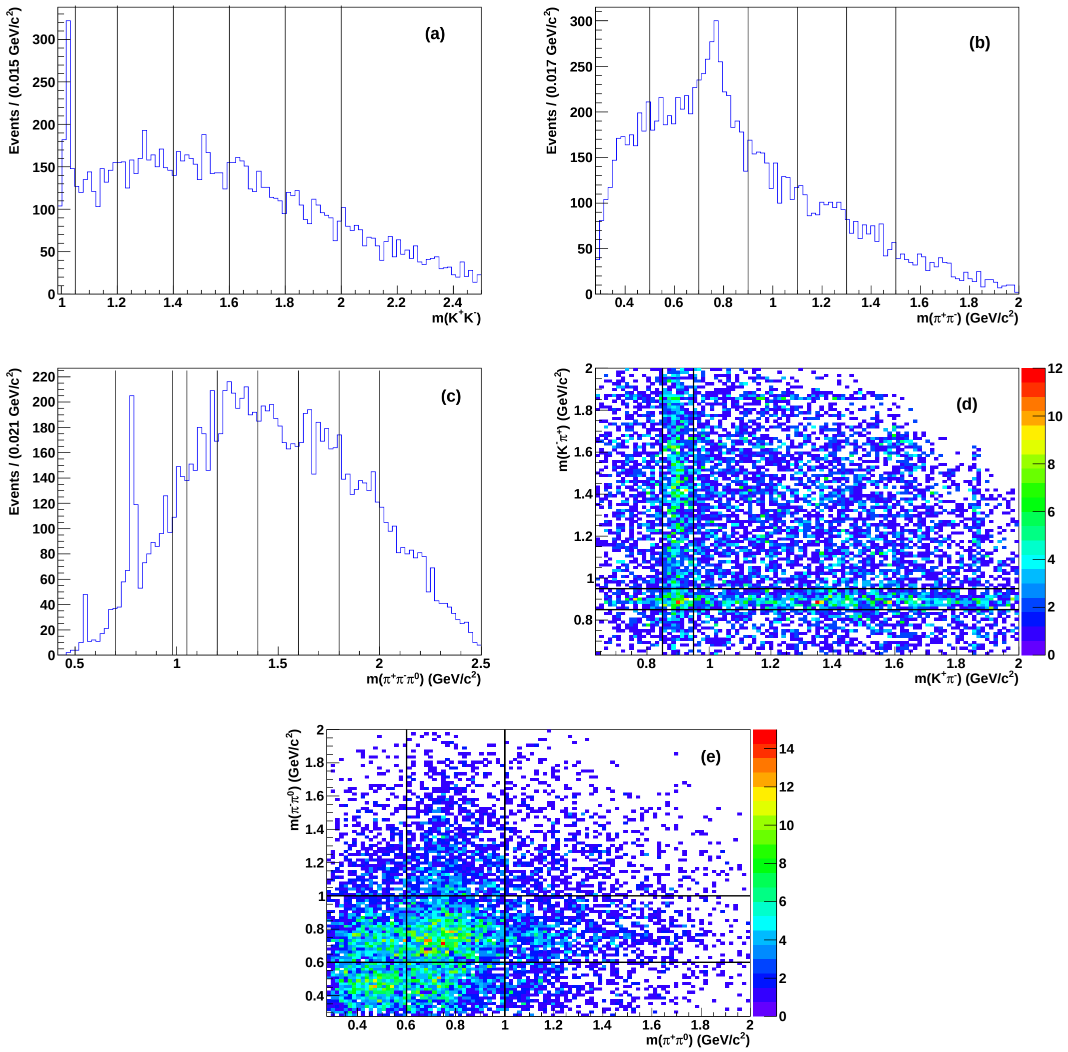

Figure 4.43: Division of the invariant mass projections into “*B*” regions used to compute the systematic for the $\eta_c(2S)\to K^+K^-\pi^+\pi^-\pi^0$ deacy; (a) $m(KK)$, (b) $m(\pi^+\pi^-)$, (c) $m(\pi^+\pi^-\pi^0)$, (d) $(m(K^+\pi^-), m(K^-\pi^+))$, (e) $(m(\pi^+\pi^0), m(\pi^-\pi^0))$. Plotted data are taken from Figs. B.2–B.6(a).

Efficiency distortion

The resonance lineshape may be distorted due to the change of the efficiency as a function of the $K^0_S K^\pm\pi^\mp$ and $K^+K^-\pi^+\pi^-\pi^0$ invariant mass. This dependence is fitted with a first order polynomial. The invariant mass spectrum is then corrected taking into account this efficiency dependence, and the nominal fit is performed. We take as systematic uncertainty the differences between the results of this fit and the nominal results reported in Tab. 4.3. All the observed changes are small compared to the statistical uncertainty of the measurement.

The change of the average reconstruction efficiency due to the subresonant decay dynamics can lead to distortion of the resonance lineshape, too. We take as systematic uncertainty due to this effect the difference between the nominal results reported in Tab. 4.3 and the ones obtained by leaving the mass and width of the resonances floating in the efficiency-weighted fit described in sec. 4.7.1. All the observed changes are small compared to the statistical uncertainty of the measurement.

The systematic contribution originating from these two efficiency-related effects are listed separately in Tab. 4.7. The first effect is named "*Mass Efficiency*" and the latter "*DP Efficiency*".

Interference

Interference between the signal and the non-resonant background may lead to a distortion of resonance lineshape as discussed in sec. 2.3.1. In order to estimate this possible contribution to the systematic uncertainty, we include an interference term in the signal PDF. The $\eta_c(1S)$ signal Breit-Wigner is substituted by the function

$$\left|\frac{\Gamma/2}{M-M_0-i\Gamma/2}+Ae^{i\phi}\sqrt{\frac{P_4(M)}{P_4(M_0)}}\right|^2, \tag{4.23}$$

where the first term is the resonance signal PDF and the second is the PDF of the interfering non-resonant background. M_0 and Γ are the mass and width of the signal resonance, A and ϕ are real parameters. $P_4(x)$ has the same functional form used to describe the non-interfering background shape. We use the same $P_4(x)$ shape parameters for both interfering and non-interfering background PDFs.

When including interference effects, the fitted "*signal yield*" N_{sg}^{fitted} receives contributions from signal, interference and interfering background terms. We define

$$\alpha = \int\left|\frac{\Gamma/2}{M-M_0-i\Gamma/2}\right|^2 \mathrm{d}m \tag{4.24}$$

$$\beta = \int\left|Ae^{i\phi}\sqrt{\frac{P_4(M)}{P_4(M_0)}}\right|^2 \mathrm{d}m \tag{4.25}$$

$$f = \frac{\alpha}{\alpha+\beta} \tag{4.26}$$

where the integral is performed on the fitting range and the PDFs parameters are obtained from the fit. Thus, we define the resonance signal yield as $N_{sg}^{res} = f\cdot N_{sg}^{fitted}$.

In Tab. 4.6 we summarize the changes in fit results with respect to the ones reported in Tab. 4.3, observed when introducing the interference term in the signal PDF. These changes are taken as a systematic uncertainty.

Decay	A	ϕ (deg)	Difference with respect to nominal fit Resonance Yield (Events)	Mass MeV/c^2	Width MeV
$\eta_c(1S) \to K_S^0 K^\pm \pi^\mp$	0.03 ± 0.02	182.2 ± 190.1	$+10 \pm 287$	$+1.2 \pm 0.5$	$+0.2 \pm 1.1$
$\eta_c(1S) \to K^+ K^- \pi^+ \pi^- \pi^0$	0.08 ± 0.04	135^*	-26 ± 762	$+2.9 \pm 1.5$	$+0.6 \pm 2.9$

Table 4.6: Results of fits with interference term added. * value that minimizes fit-data χ^2 obtained with a scan.

The interference between signal and non-resonant background produces a change in the tails of the signal distribution, thus making this effect difficult to be estimated in presence of a small signal size and a poor signal to background ratio. We therefore do not consider any systematic effect due to interference for the $\eta_c(2S)$.

	$\eta_c(1S)$			$\chi_{c0}(1P)$	$\chi_{c2}(1P)$	$\eta_c(2S)$		
	Yield (Evts.)	Mass MeV/c^2	Width MeV	Yield (Evts.)	Yield (Evts.)	Yield (Evts.)	Mass MeV/c^2	Width MeV
	$K^0_S K^\pm\pi^\mp$ Decay Mode							
PDFs shape	19	0.3	0.4	–	2	4	0.2	0.7
Background shape	144	0.0	0.5	–	5	10	0.1	0.2
Absolute mass scale	–	0.2	–	–	–	–	0.2	–
Momentum distribution	–	0.4	–	–	–	–	0.3	–
MC/data resolution	105	0.09	0.9	–	7	20	0.07	2.9
Background subtraction	82	–	–	–	–	–	–	–
Peaking background	190	–	–	–	11	25	–	–
Res. function distortion	0	0.1	0.0	–	–	3	0.1	0.1
Mass Efficiency	–	0.1	0.2	–	–	–	0.0	0.7
DP Efficiency	–	0.3	0.8	–	–	–	0.7	0.7
Interference	10	1.2	0.2	–	–	–	–	–
Total	274	1.4	1.3	0	14	34	0.8	3.2
	$K^+K^-\pi^+\pi^-\pi^0$ Decay Mode							
PDFs shape	$^{+44}_{-55}$	0.8	1.0	$^{+57}_{-54}$	$^{+67}_{-60}$	99	$^{+1.8}_{-1.6}$	–
Background Shape	417	0.1	2.0	104	137	154	0.2	–
Absolute mass scale	–	0.8	–	–	–	–	0.8	–
Momentum distribution	–	0.0	–	–	–	–	1.1	–
MC/data resolution	9	0.2	0.1	10	11	0	0.2	–
Background subtraction	9	–	–	–	–	–	–	–
Peaking background	122	–	–	80	246	17	–	–
Res. function distortion	52	0.3	0.8	–	–	17	0.2	–
Mass Efficiency	–	0.1	1.3	–	–	–	0.1	–
DP Efficiency	–	0.2	1.2	–	–	–	0.9	–
Interference	26	2.9	0.6	–	–	–	–	–
Total	442	3.1	3.0	143	290	185	2.5	–

Table 4.7: Summary of systematic uncertainties for yield and resonance parameters measurements. The uncertainty on yield measurement is expressed in number of events. The uncertainty on mass and width measurement is expressed in MeV/c^2 and MeV, respectively.

4.8.2 Cross-section systematics

Here below we list the sources of systematic uncertainties on the measured value of N_f^X/ε_f. As described in sec. 4.7.1, N_f^X/ε_f is used to compute both the cross-section for the $e^+e^-\to\gamma\gamma\to X\to f$ process, with $X=\eta_c(1S),\chi_{c0}(1P),\chi_{c2}(1P),\eta_c(2S)$, and the ratio of the branching fraction of the $\eta_c(nS)$ to the $K_S^0K^\pm\pi^\mp$ and $K^+K^-\pi^+\pi^-\pi^0$ decay mode. The systematic uncertainties affecting the cross-section measurement are estimated using data collected near the $\Upsilon(4S)$ energy and are summarized in Tab. 4.8. The systematic uncertainties affecting the ratio of branching fraction measurement are estimated using the whole dataset and are summarized in Tab. 4.9. Systematic uncertainties are divided into additive systematic, that affect the measured N_f^X/ε_f by causing a bias, and multiplicative systematics that are related to uncertainties in term, like the efficiency and the integrated luminosity, that enter multiplicatively in the cross-section and branching fraction ratio measurements.

PDFs shape

The uncertainty due to fixing parameters in the fit is estimated as described in sec. 4.8.1.

Peaking background

The scaled number of irreducible-peaking-background events are computed by scaling the number of expected peaking-background events from two-photon processes and ψ radiative decays reported in Tab. 4.4, by the ratio between N_f^X/ε_f and the resonance yield reported in Tab. 4.3. The systematic uncertainty due to the presence of peaking-background events is estimated as described in secs. 4.8.

Weights uncertainty

The weighting procedure used to extract N_f^X/ε_f relies on the efficiency parameterization obtained from MC simulation. Due to finite MC sample size effect, this parameterization has a statistical uncertainty that enters in the N_f^X/ε_f determination.

In order to quantify the uncertainty on N_f^X/ε_f originating from the uncertainty on the efficiency parameterization, we perform 500 simulated (toy) experiments. In each experiment the value of the efficiency in each histogram bin and the coefficients of the functions describing the dependence on $\cos\theta_K$, $\cos\theta_{\pi\pi}$, $\cos\Theta$, θ_π and Φ are varied within their statistical uncertainties. We then use this "*toy*"-efficiency to weight data and we perform the weighted fit described in sec. 4.7.1.

The resulting distribution of the fitted N_f^X/ε_f value is usually a Gaussian. In the $K^+K^-\pi^+\pi^-\pi^0$ decay mode a tail at higher values of N_f^X/ε_f, with respect to the Gaussian core, is observed. This is caused by the fact that the efficiency weights, which are usually Gaussian distributed, may present a tail when the uncertainty on the efficiency is large. This reflects the fact that the inverse of a Gaussian distribution shows a tail when the Gaussian width is large. We fit the N_f^X/ε_f distribution with a Gaussian shape or a Crystal Ball [327–329] function. In Figs. 4.44–4.45 we show the distributions of the fitted $N_f^{\eta_c(nS)}/\varepsilon_f$ values in the $K^0_S K^\pm\pi^\mp$ and $K^+K^-\pi^+\pi^-\pi^0$ decay modes, respectively. No significant bias is observed with respect to the values reported in sec. 4.7.3. The width of the Gaussian (Crystal Ball) function is taken as systematic related to the efficiency parameterization.

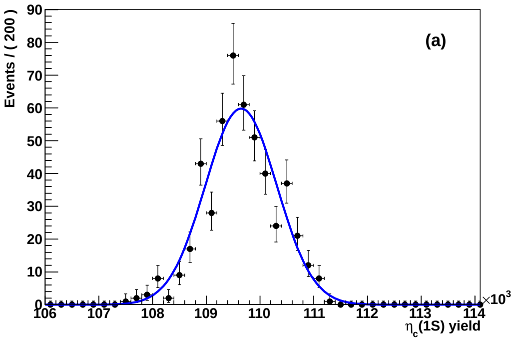

Figure 4.44: Distribution of the fitted values of (left) $N^{\eta_c(1S)}_{K^0_S K^\pm\pi^\mp}$ and (right) $N^{\eta_c(2S)}_{K^0_S K^\pm\pi^\mp}$ in 500 toy experiment. In each toy experiment the efficiency-related weights are varied according to their uncertainty. The distribution is fitted with a Gaussian shape.

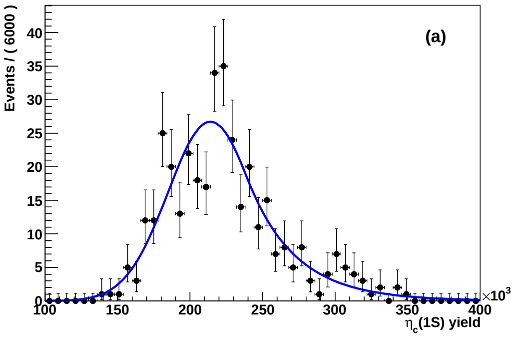

Figure 4.45: Distribution of the fitted values of (left) $N^{\eta_c(1S)}_{K^+K^-\pi^+\pi^-\pi^0}$ and (right) $N^{\eta_c(2S)}_{K^+K^-\pi^+\pi^-\pi^0}$ in 500 toy experiment. In each toy experiment the efficiency-related weights are varied according to their uncertainty. The distribution is fitted with a Gaussian shape.

Events falling in null-efficiency bins are accounted for in this systematic calculation.

As described in sec. 4.7.2, a bin is given null efficiency if the number of reconstructed MC events falling in it is less than 10. We divide null-efficiency bins in two categories:

I : High-efficiency bins, where the number of generated MC events n_{gen} is ~ 10

II : Low-efficiency bins, where $n_{gen} \gg 10$. Such bins are located in proximity of mass thresholds.

The "*toy*"-efficiency used to weight events falling in high-efficiency bins is computed using $N = max[n_{reco}, 3]$, where N is the number of reconstructed events entering in the efficiency determination, and n_{reco} is the number of reconstructed events actually observed in the bin. The "*toy*"-efficiency used to weight events falling in low-efficiency bins is 0.05% for $\eta_c(1S)$ and 0.5% for $\eta_c(2S)$. For comparison, the minimum efficiency observed in the two(three)-dimensional histogram is 0.16% and 1.6%, for $\eta_c(1S)$ and $\eta_c(2S)$, respectively.

Correlation between $\theta_{\pi\pi}$ and $m_{\pi\pi}$

In the $K^+K^-\pi^+\pi^-\pi^0$ decay mode, the efficiency corrections as a function of the angular variables that describe the decay kinematics are computed neglecting their correlations with the invariant masses $m_{\pi\pi}$, $m_{3\pi}$, and m_{KK}. Actually, $\theta_{\pi\pi}$ and $m_{\pi\pi}$ are correlated at -70% level. We take as systematic the changes in results observed when removing the correction factor depending on the $\theta_{\pi\pi}$ value.

Tracking efficiency

A systematic is assigned to take into account the difference between data and MC efficiency for correctly reconstructing a track originating from the interaction region. This uncertainty is estimated by auxiliary studies based on a $\tau^+\tau^-$ control sample with one τ lepton decaying to $e\overline{\nu}_e\nu_\tau$ or $\mu\overline{\nu}_\mu\nu_\tau$, and the other one to $\pi\pi\pi\nu_\tau$. The systematic uncertainty for tracks selected with the requirements described in sec. 4.3 is 0.216% per track.

K^0_S finding efficiency

A systematic is assigned to take into account the difference between data and MC efficiency for correctly reconstructing a track originating from a vertex that is displaced from the interaction region. This uncertainty is estimated by auxiliary studies based on a K^0_S control sample. The systematic uncertainty is computed for K^0_S selected with the requirements described in sec. 4.3, taking into account the relevant kinematic signatures, such as the transverse momentum and the polar angle of the K^0_S momentum observed in our dataset. The systematic contribution is 1.7% per K^0_S.

π^0 efficiency

A systematic is assigned to take into account the difference between data and MC efficiency for correctly reconstructing a π^0. This uncertainty is estimated by auxiliary studies based on a $\tau^+\tau^-$ control sample with one τ lepton decaying to $e\overline{\nu}_e\nu_\tau$, and the other one to $\rho^+\nu_\tau$ The systematic uncertainty for π^0 selected with the requirements described in sec. 4.3 is 3% per π^0.

PID requirements

A systematic is assigned to take into account the difference between data and MC efficiency for assigning the correct PID to a charged track. This uncertainty is estimated by auxiliary studies based on high purity control samples. Electrons and muons are selected by using Bhabha events; pions are selected in K^0_S decays or in $\tau^+\tau^-$ events with one τ lepton decaying to $e\overline{\nu}_e\nu_\tau$ or $\mu\overline{\nu}_\mu\nu_\tau$, and the other one to $\pi\pi\pi\nu_\tau$; kaons are selected in the $D^{*0}\to D^0\pi^+$ decay, with $D^0\to K^-\pi^+$; protons are selected in the $\Lambda\to p\pi$ decay. The systematic uncertainty is computed for tracks selected with the requirements described in sec. 4.3, taking into account the relevant kinematic signatures, such as the transverse momentum and the polar angle of the tracks observed in our dataset. This systematic uncertainty is 0.5% per track for both pion and kaon PID.

Luminosity

The value of the integrated luminosity is taken from auxiliary studies performed by using Bhabha $\mu^+\mu^-$ events. The total uncertainty on the luminosity measurement is 1.1%.

4.9 Results

4.9.1 Yield and resonance parameters

The results of the fit to the whole unweighted $K^0_S K^\pm\pi^\mp$ and $K^+K^-\pi^+\pi^-\pi^0$ spectrum can be found in Tab. 4.3. The $\eta_c(1S)$ yields are corrected by subtracting the number of expected peaking-background events from the $J/\psi\to\eta_c(1S)$ decay reported in Tab. 4.4, as described in sec. 4.5.1. The mass values are corrected to account for the mass shift of the J/ψ mass observed in the fit on the ISR-enriched dataset, described in sec. 4.8.1. The systematic uncertainties are summarized in Tab. 4.7. The statistical significance of the

	$K^0_S K^\pm \pi^\mp$ Decay			$K^+K^-\pi^+\pi^-\pi^0$ Decay			
	$\eta_c(1S)$	$\chi_{c2}(1P)$	$\eta_c(2S)$	$\eta_c(1S)$	$\chi_{c0}(1P)$	$\chi_{c2}(1P)$	$\eta_c(2S)$
PDFs shape (A)	3224	80	561	8151	914	1064	1402
Background Subtraction (A)	666	–	–	165	–	–	–
Peaking Background (A)	1541	74	168	2246	1051	2769	180
Efficiency Weight (A)	683	12	25	27575	1951	1716	1488
$\theta_{\pi\pi}$-$m_{\pi\pi}$ Correlation (M)	–	–	–	1.4	1.0	2.4	1.1
Tracking (M)	0.4	0.4	0.4	0.8	0.8	0.8	0.8
K^0_S (M)	1.7	1.7	1.7	–	–	–	–
π^0 (M)	–	–	–	3.0	3.0	3.0	3.0
PID (M)	1.0	1.0	1.0	2.0	2.0	2.0	2.0
Luminosity (M)	1.1	1.1	1.1	1.1	1.1	1.1	1.1
Sub-Total (A)	3698	110	586	28843	2397	3427	2052
Sub-Total (M)	2.3	2.3	2.3	4.1	4.0	4.5	4.0
Sub-Total A (fb)	11.3	0.3	1.7	88.0	7.4	10.4	6.2
Sub-Total M (fb)	6.8	0.0	0.3	25.6	1.7	2.0	1.6
Total (fb)	13.2	0.3	1.7	91.6	7.5	10.7	6.5

Table 4.8: Systematic uncertainty on cross-section measurement for data collected near the $\Upsilon(4S)$ energy. The additive (A) contributions are given in number of weighted events, the multiplicative (M) contributions are given in percentage. The total contribution is converted in fb, taking into account $\mathcal{B}(K^0_S \to \pi^+\pi^-) = (69.20 \pm 0.05)\%$ [49].

	Weighted Yield Uncertainty			
	$K^0_S K^\pm \pi^\mp$ Decay		$K^+K^-\pi^+\pi^-\pi^0$ Decay	
	$\eta_c(1S)$	$\eta_c(2S)$	$\eta_c(1S)$	$\eta_c(2S)$
PDFs shape (A)	$^{+3480}_{-3522}$	$^{+601}_{-632}$	$^{+8952}_{-8766}$	$^{+1362}_{-1414}$
Background Subtraction (A)	730	–	180	–
Peaking Background (A)	1690	184	2448	203
Efficiency Weight (A)	667	28	29198	1617
$\theta_{\pi\pi}$-$m_{\pi\pi}$ Correlation (M)	–	–	1.4	1.1
Tracking (M)	0.4	0.4	0.8	0.8
K^0_S (M)	1.7	1.7	–	–
π^0 (M)	–	–	3.0	3.0
PID (M)	1.0	1.0	2.0	2.0
Sub-Total (A)	$^{+3993}_{-4030}$	$^{+629}_{-659}$	$^{+30638}_{-30584}$	$^{+2124}_{-2158}$
Sub-Total (M)	2.0	2.0	3.9	3.9
Total (Events)	$^{+4555}_{-4587}$	$^{+636}_{-665}$	$^{+31853}_{-31802}$	$^{+2196}_{-2229}$

Table 4.9: Systematic uncertainty on weighted yield measurement for $\eta_c(1S)$ and $\eta_c(2S)$, using the whole dataset. The additive (A) contributions are given in number of events, the multiplicative (M) contributions are given in percentage. The total contribution is given in number of weighted events.

signal is computed as the ratio of the number of observed events to the sum in quadrature of the its statistical and systematic uncertainties. Results are summarized in Tab. 4.10.

The mass and width of the $\eta_c(2S)$ resonance in the $K^0_S K^\pm \pi^\mp$ decay are measured

Decay Mode	Corrected Yield (Evts.)	N_{peak} (Evts.)	N_ψ (Evts.)	Significance (σ)	Corrected Mass (MeV/c^2)	Fitted Width (MeV)
$\eta_c(1S)\to K^0_S K^\pm\pi^\mp$	$12096 \pm 235 \pm 274$	189 ± 18	214 ± 82	33.5	$2982.5 \pm 0.4 \pm 1.4$	$32.1 \pm 1.1 \pm 1.3$
$\chi_{c2}(1P)\to K^0_S K^\pm\pi^\mp$	$126 \pm 37 \pm 14$	-45 ± 11	–	3.2	3556.2 (fixed)	2 (fixed)
$\eta_c(2S)\to K^0_S K^\pm\pi^\mp$	$624 \pm 72 \pm 34$	25 ± 5	–	7.8	$3638.5 \pm 1.5 \pm 0.8$	$13.4 \pm 4.6 \pm 3.2$
$\eta_c(1S)\to K^+K^-\pi^+\pi^-\pi^0$	$11132 \pm 430 \pm 442$	118 ± 32	26 ± 9	18.1	$2984.5 \pm 0.8 \pm 3.1$	$36.2 \pm 2.8 \pm 3.0$
$\chi_{c0}(1P)\to K^+K^-\pi^+\pi^-\pi^0$	$1094 \pm 143 \pm 143$	-39 ± 19	75 ± 21	5.4	3415.8 (fixed)	10.2 (fixed)
$\chi_{c2}(1P)\to K^+K^-\pi^+\pi^-\pi^0$	$1250 \pm 118 \pm 290$	14 ± 24	233 ± 73	4.0	3556.2 (fixed)	2 (fixed)
$\eta_c(2S)\to K^+K^-\pi^+\pi^-\pi^0$	$1201 \pm 133 \pm 185$	-46 ± 17	–	5.3	$3640.5 \pm 3.2 \pm 2.5$	13.4 (fixed)

Table 4.10: Analysis results: corrected signal yield with statistical and systematic uncertainties, number of peaking-background events estimated with the p_T fit (N_{peak}), number of peaking-background events from J/ψ and $\psi(2S)$ radiative decays (N_ψ), significance (including systematic uncertainty), corrected mass, and fitted width for each decay mode. We do not report N_ψ for modes where it is negligible.

with a better precision with respect to the current world-average value [49]. This result supersede the previous *BABAR* measurement [315]. We report the first observation of the $\eta_c(1S)$ $\chi_{c0}(1P)$, and $\eta_c(2S)$, and evidence of the $\chi_{c2}(1P)$ decay into the $K^+K^-\pi^+\pi^-\pi^0$ final state. No significant signal for the $\chi_{c2}(2P)$ has been observed in both $K^0_S K^\pm\pi^\mp$ and $K^+K^-\pi^+\pi^-\pi^0$ decay mode. This result, together with Belle's preliminary observation of $\eta_c(2S)$ decay to six-particle final state [201], is the first observation of an exclusive hadronic decay of $\eta_c(2S)$ other than $K\overline{K}\pi$.

4.9.2 $\Gamma_{\gamma\gamma} \times \mathcal{B}$ measurement

The measured value of the two-photon production cross-section for each resonance and final state, obtained with data collected near the $\Upsilon(4S)$ energy, is reported in Tab. 4.5. The relevant systematic uncertainties are reported in Tab. 4.8. From the $K^0_S K^\pm\pi^\mp$ cross-section, we obtain the $K\overline{K}\pi$ cross-section by taking into account the isospin relation $3\mathcal{B}(K^0_S K^\pm\pi^\mp) = \mathcal{B}(K\overline{K}\pi)$.

Since no significant $\chi_{c2}(2P)$ signal is observed, we determine a Bayesian upper limit at 90% Confidence Level (CL) on its cross-section, assuming a uniform prior probability distribution. We obtain the likelihood function shape with a scan over the relevant $\chi_{c2}(2P)$ cross-section. The likelihood function is then convolved with a Gaussian with mean equal to zero and width equal to the systematic uncertainty, in order to take systematic effect into account in the upper limit calculation. Systematic uncertainties for the $\chi_{c2}(2P)$ cross-section are estimated with the procedures described in sec. 4.8.2. We compute the upper limit by finding the value of the cross-section below which lies 90% of the convolved likelihood integral in the positive cross-section region.

As described in sec. 4.7, we use the `GamGam` generator to obtain the value of $\Gamma_{\gamma\gamma} \times \mathcal{B}$ that corresponds to the measured production cross-section for each resonance. The systematic uncertainty associated to the cross-section calculation performed by `GamGam` generator is estimated by comparing its output to that of the `TRESP` generator [330], that is used by Belle. This uncertainty is 3 % [205] and is summed in quadrature with the cross-section uncertainty for the $\Gamma_{\gamma\gamma} \times \mathcal{B}$ measurement.

In Tab. 4.11 we report the measured cross-section and the corresponding $\Gamma_{\gamma\gamma} \times \mathcal{B}$ for each resonance, in both $K^0_S K^\pm\pi^\mp$ and $K^+K^-\pi^+\pi^-\pi^0$ decay mode. The $\eta_c(1S) \to K\overline{K}\pi$ measurement is consistent with, but slightly more precise than, the current world-average value [49]. The other entries are first measurements.

Process	Cross-section (fb)	$\Gamma_{\gamma\gamma}\times\mathcal{B}$ (keV)
$\eta_c(1S)\to K\overline{K}\pi$	$896.9\pm17.8\pm39.6$	$0.386\pm0.008\pm0.021$
$\chi_{c2}(1P)\to K\overline{K}\pi$	$7.7\pm2.7\pm0.9$	$(1.8\pm0.5\pm0.2)\times10^{-3}$
$\eta_c(2S)\to K\overline{K}\pi$	$37.0\pm3.9\pm5.1$	$0.041\pm0.004\pm0.006$
$\chi_{c2}(2P)\to K\overline{K}\pi$	<6.5	$<2.1\times10^{-3}$
$\eta_c(1S)\to K^+K^-\pi^+\pi^-\pi^0$	$431.7\pm14.5\pm64.7$	$0.190\pm0.006\pm0.028$
$\chi_{c0}(1P)\to K^+K^-\pi^+\pi^-\pi^0$	$30.3\pm5.3\pm5.3$	$0.026\pm0.004\pm0.004$
$\chi_{c2}(1P)\to K^+K^-\pi^+\pi^-\pi^0$	$29.8\pm4.6\pm7.4$	$(6.5\pm0.9\pm1.5)\times10^{-3}$
$\eta_c(2S)\to K^+K^-\pi^+\pi^-\pi^0$	$26.8\pm5.1\pm4.5$	$0.030\pm0.006\pm0.005$
$\chi_{c2}(2P)\to K^+K^-\pi^+\pi^-\pi^0$	<10.0	$<3.4\times10^{-3}$

Table 4.11: Results for $\Gamma_{\gamma\gamma}\times\mathcal{B}$ for each resonance in $K\overline{K}\pi$ and $K^+K^-\pi^+\pi^-\pi^0$ final states. The first uncertainty is statistical, the second systematic. Upper limits are computed at 90% confidence level.

4.9.3 Relative branching fraction

The ratio of the branching fractions to the $K^0_S K^\pm\pi^\mp$ and $K^+K^-\pi^+\pi^-\pi^0$ final state, for both $\eta_c(1S)$ and $\eta_c(2S)$ is computed using the values of $N_f^{\eta_c(nS)}/\varepsilon_f$ obtained from the fit to the whole dataset and reported in sec. 4.7.3. The $\eta_c(1S)$ yields are corrected by subtracting the number of expected peaking-background events from $J/\psi\to\gamma\eta_c(1S)$ decay, scaled taking into account the reconstruction efficiency. The systematic uncertainties are reported in Tab. 4.9. Taking into account $\mathcal{B}(K^0_S\to\pi^+\pi^-) = (69.20\pm0.05)\%$ [49], we find

$$\frac{\mathcal{B}(\eta_c(1S)\to K^+K^-\pi^+\pi^-\pi^0)}{\mathcal{B}(\eta_c(1S)\to K^0_S K^\pm\pi^\mp)} = 1.43\pm0.05\pm0.21 \tag{4.27}$$

$$\frac{\mathcal{B}(\eta_c(2S)\to K^+K^-\pi^+\pi^-\pi^0)}{\mathcal{B}(\eta_c(2S)\to K^0_S K^\pm\pi^\mp)} = 2.2\pm0.5\pm0.5 \tag{4.28}$$

where the first error is statistical and the second systematic. The uncertainty in the efficiency parameterization is the main contribution to the systematic uncertainties and is equal to 0.17 and 0.3, in Eqs. (4.27) and (4.28), respectively. Using Eqs. (4.27)–(4.28), $\mathcal{B}(\eta_c(1S)\to K\overline{K}\pi) = (7.0\pm1.2)\%$ and $\mathcal{B}(\eta_c(2S)\to K\overline{K}\pi) = (1.9\pm1.2)\%$ [49] , and isospin relations, we obtain

$$\mathcal{B}(\eta_c(1S)\to K^+K^-\pi^+\pi^-\pi^0) = (3.3\pm0.8)\%, \tag{4.29}$$

$$\mathcal{B}(\eta_c(2S)\to K^+K^-\pi^+\pi^-\pi^0) = (1.4\pm1.0)\%, \tag{4.30}$$

where we have summed in quadrature the statistical and systematic uncertainties.

Conclusions

In this thesis we have reported the analysis of the $\gamma\gamma\to K^0_S K^\pm\pi^\mp$ and $\gamma\gamma\to K^+K^-\pi^+\pi^-\pi^0$ two-photon processes using the final *BABAR* experiment dataset. The analysis of $\gamma\gamma\to K^0_S K^\pm\pi^\mp$ is an update of a previous measurement [197], using a dataset six times larger. The dataset used in the present analysis has a large overlap with that used in another recent analysis by *BABAR* [158]. The $\gamma\gamma\to K^+K^-\pi^+\pi^-\pi^0$ is first studied in this thesis. Results are summarized in sec. 4.9.

We report a precise measurement of the $\eta_c(1S)$ and $\eta_c(2S)$ parameters in the $K^0_S K^\pm\pi^\mp$ decay mode. Such results are consistent with the world-average values [49] and other results recently obtained by other experiments [155, 157]. The measurement of the $\eta_c(2S)$ parameters supersedes that reported in the previous *BABAR* analysis [315], and is the most accurate single measurement available [49, 155, 157]. We observe for the first time $\eta_c(1S)$, $\chi_{c0}(1P)$, and $\eta_c(2S)$ decay into $K^+K^-\pi^+\pi^-\pi^0$, and report first evidence of $\chi_{c2}(1P)\to K^+K^-\pi^+\pi^-\pi^0$. The values of the $\eta_c(1S)$ and $\eta_c(2S)$ parameters measured in $K^+K^-\pi^+\pi^-\pi^0$ are consistent with, but less precise than those obtained in the $K^0_S K^\pm\pi^\mp$ decay mode. We search for the $\chi_{c2}(2P)$ in both final states, but no significant signal is found.

We measure the product of the two-photon width and the final state branching fraction for all the resonances observed, in both decay modes. The measured value for the $\gamma\gamma\to\eta_c(1S)\to K^0_S K^\pm\pi^\mp$ process is consistent with, and slightly more precise than the world-average value [49]. The others are first measurements. For the $\chi_{c2}(2P)$ state, we put a Bayesian upper limit at 90% confidence level on this product. We measure the ratio of the $K^+K^-\pi^+\pi^-\pi^0$ and $K^0_S K^\pm\pi^\mp$ branching fractions for the $\eta_c(1S)$ and the $\eta_c(2S)$. From earlier measurements of the $K\overline{K}pi$ branching fractions [49], we derive $\mathcal{B}(\eta_c(2S)\to K^+K^-\pi^+\pi^-\pi^0) = (1.4\pm1.0)\%$. We have applied an event-by-event weighting procedure that allows to greatly reduce the systematic uncertainty in the two-photon width and branching fractions ratio measurements.

The results reported in this thesis have been published in *Physics Review D* [324]. The candidate has presented these results at following conferences or workshops: "8^{th} *International Workshop on Heavy Quarkonium*", held on October 4-7, 2011, in GSI, Darmstadt, Germany [331]; “*Incontri di Fisica delle Alte Energie 2011*” [332], held on April 27-29, 2011, in Perugia, Italy; “*XCVI Congresso della Società Italiana di Fisica*”, held on September 20-24, 2011, in Bologna Italy.

Appendix A

$K^+K^-\pi^+\pi^-\pi^0\pi^0$ background

A.1 Introduction

The number of peaking-background events originating from two-photon processes with a higher multiplicity with respect to the signal is estimated in sec. 4.6.2, by comparing the p_T shape distribution of the fitted resonances yield with MC expectation for signal events. This procedure has been proven to be effective for the $K^0_S K^\pm\pi^\mp$ final state, by studying the $\gamma\gamma\to\eta_c(1S)\pi^0\to K^0_S K^\pm\pi^\mp\pi^0$ background process exclusively [158]. In this section we study the background process $\gamma\gamma\to X\pi^0\to K^+K^-\pi^+\pi^-\pi^0\pi^0$, where $X = \eta_c(1S), \chi_{c0}(1P), \chi_{c2}(1P)$ or $\eta_c(2S)$, in order to check that the p_T-shape-based method works also for the $K^+K^-\pi^+\pi^-\pi^0$ final state.

A.2 Event selection

We select events by applying the following requirements:

- exactly four charged tracks in the event with zero net charge;
- fit vertex probability greater than 0.1%;
- tracks should satisfy pion or kaon PID. The net charge of the dipion and two-kaon system should be zero;
- $N_{\pi^0} \leq 3$ and $N_\gamma \leq 6$;
- π^0 photons energy larger than 100 MeV;
- the two π^0 in the final state should not have overlapping photons;
- M^2_{miss} of the $K^+K^-\pi^+\pi^-\pi^0\pi^0$ system larger than $2\ (\text{GeV}/c^2)^2$.

In Fig. A.1 we show the p_T distribution of the $K^+K^-\pi^+\pi^-\pi^0\pi^0$ events in data. The presence of a peak at $p_T \sim 0$ GeV$/c$ indicates the presence of the two-photon signal. For each event there are two possible combinations to obtain the $X\pi^0$ ($X = \eta_c(1S),\ \chi_{c0}(1P)$, $\chi_{c2}(1P),\ \eta_c(2S)$) final state. In fact, due to the fact that the two π^0 are indistinguishable, the system $K^+K^-\pi^+\pi^-\pi^0_1\pi^0_2$ may be combined as $(K^+K^-\pi^+\pi^-\pi^0_1)\pi^0_2$ or $(K^+K^-\pi^+\pi^-\pi^0_2)\pi^0_1$. We thus create two resonance candidates for each event.

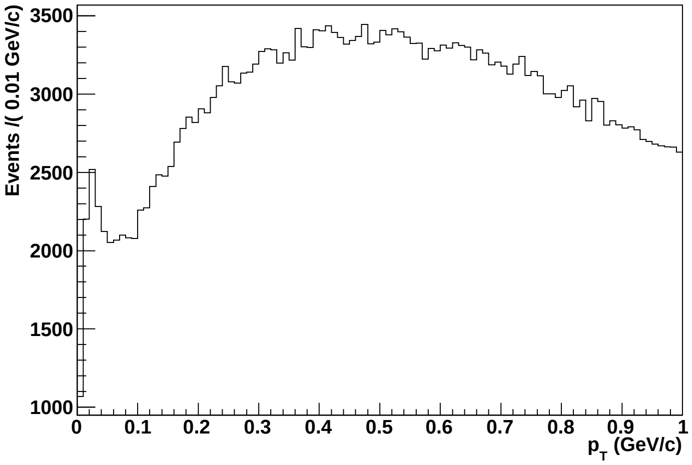

Figure A.1: Distribution of p_T for selected $K^+K^-\pi^+\pi^-\pi^0\pi^0$ events.

A.3 Mass spectrum and fit

In Fig. A.2 we show the invariant mass distribution for the $K^+K^-\pi^+\pi^-\pi^0$ system after applying a p_T cut to enhance the two-photon contribution. No peaking structure is observed in correspondence of the $\eta_c(1S)$, $\chi_{c,}$ $\chi_{c2}(1P)$, and $\eta_c(2S)$ mass.

We fit the $K^+K^-\pi^+\pi^-\pi^0\pi^0$ mass distribution with a fourth order polynomial shape that model the background distribution. Results of the fit are shown in Fig. A.3. For each point of the mass spectrum, the pull is defined as $(N^{obs} - N^{fit})/\sigma$, where N^{obs} is the number of events observed in data, N^{fit} the number of events expected by the fit, and σ is the statistical uncertainty associated to each point. The pull distribution is shown in Fig. A.3. No significant excess is observed at the position of the studied resonances. We thus conclude that the $K^+K^-\pi^+\pi^-\pi^0\pi^0$ process does not give substantial contribution to the peaking-background. The estimate of the number of peaking-background events originating by two-photon processes obtained in sec. 4.6.2 is then considered to be conservative.

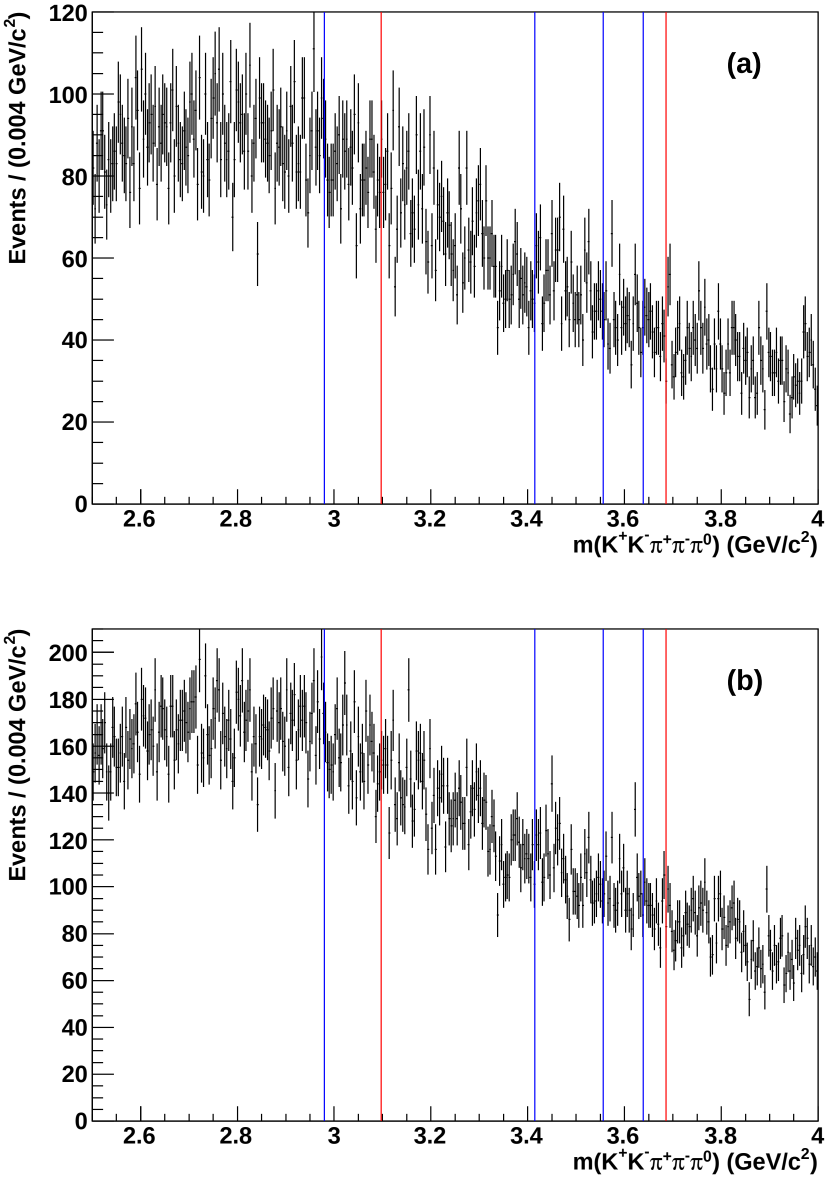

Figure A.2: Invariant mass of the $K^+K^-\pi^+\pi^-\pi^0$ system for the $K^+K^-\pi^+\pi^-\pi^0\pi^0$ final state after applying a (a) $p_T < 0.1$ GeV$/c$ and (b) $p_T < 0.2$ GeV$/c$ requirement.

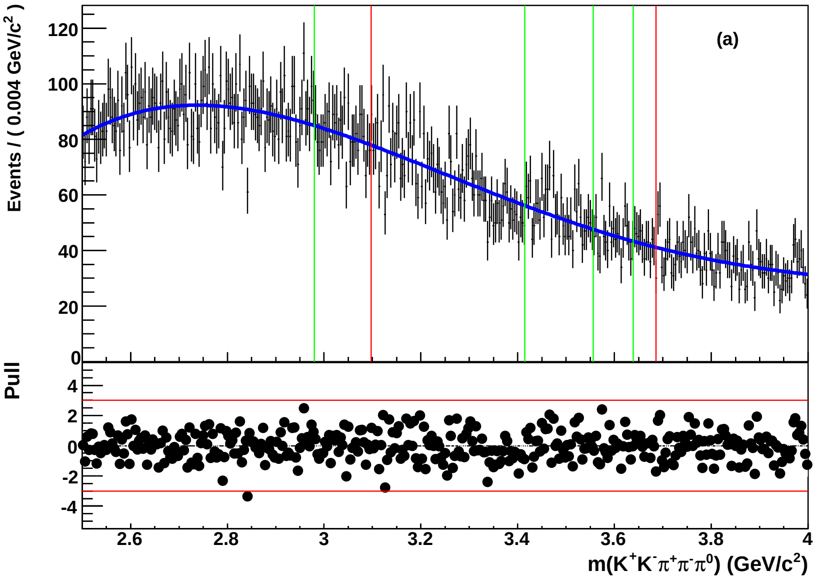

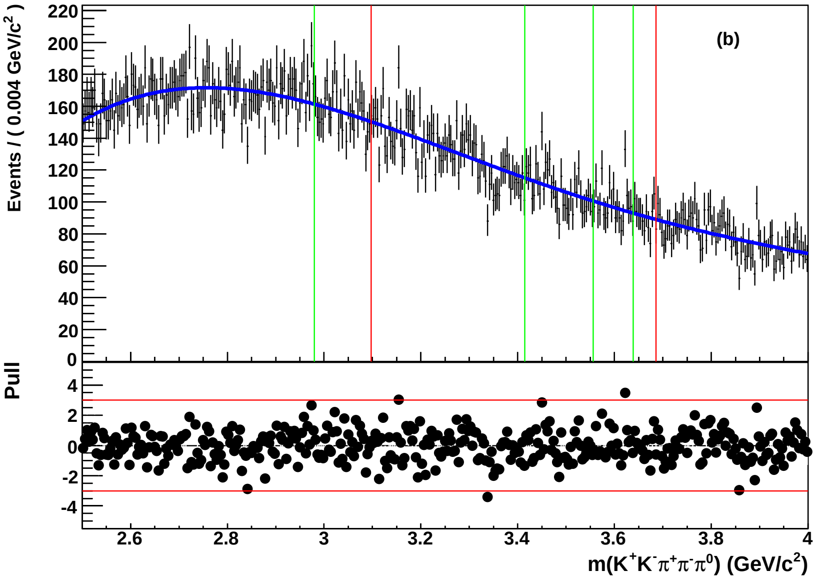

Figure A.3: Fit to the $K^+K^-\pi^+\pi^-\pi^0$ invariant mass for the $K^+K^-\pi^+\pi^-\pi^0\pi^0$ final state after applying a (a) $p_T < 0.1$ GeV$/c$ and (b) $p_T < 0.2$ GeV$/c$ requirement. The green lines are placed at the nominal [49] masses of (left to right) $\eta_c(1S)$, $\chi_{c0}(1P)$, $\chi_{c2}(1P)$, and $\eta_c(2S)$. The red lines are placed at the nominal [49] masses of (left to right) J/ψ and $\psi(2S)$.

Appendix B

Invariant mass projections

In Fig. B.1 we show the Dalitz Plot distribution for events in the $K_S^0 K^\pm \pi^\mp$ decay mode. In each figure, we show a plot for signal $\eta_c(nS)$ and background region.

In Figs. B.2– B.6 we show the one-dimensional projections of $K^+K^-\pi^+\pi^-\pi^0$ data over the K^+K^-, $\pi^+\pi^-$, and $\pi^+\pi^-\pi^0$ invariant mass, and the two-dimensional projections in the $(m(K^+\pi^-), m(K^-\pi^+))$ and $(m(\pi^+\pi^0), m(\pi^-\pi^0))$ plane. In each figure, we show a plot for signal $\eta_c(nS)$ and background region.

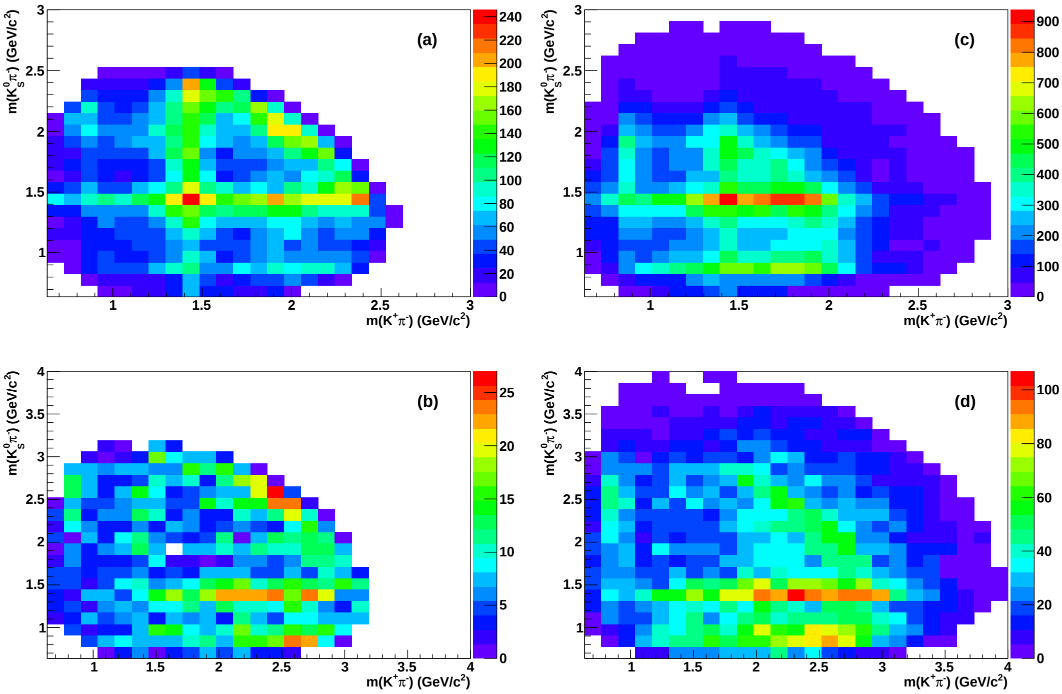

Figure B.1: Dalitz plot distributions for $K^0_S K^\pm \pi^\mp$ events in (a) $\eta_c(1S)$ region ($2.9 < m_{K^0_S K^\pm \pi^\mp} < 3.05\ \mathrm{GeV}/c^2$), (b) $\eta_c(2S)$ region ($3.6 < m_{K^0_S K^\pm \pi^\mp} < 3.7\ \mathrm{GeV}/c^2$), (c) $\eta_c(1S)$ sideband region ($m_{K^0_S K^\pm \pi^\mp} < 2.9\ \mathrm{GeV}/c^2$ or $3.05 < m_{K^0_S K^\pm \pi^\mp} < 3.4\ \mathrm{GeV}/c^2$), and (d) $\eta_c(2S)$ sideband region ($3.4 < m_{K^0_S K^\pm \pi^\mp} < 3.5\ \mathrm{GeV}/c^2$ or $m_{K^0_S K^\pm \pi^\mp} > 3.7\ \mathrm{GeV}/c^2$).

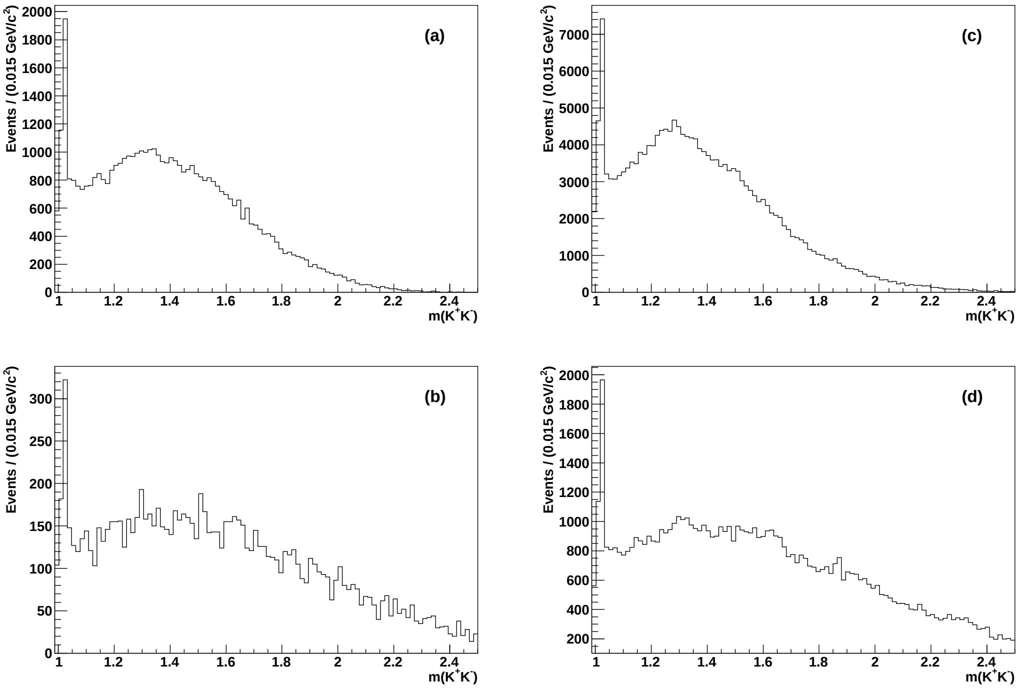

Figure B.2: Invariant K^+K^- mass distributions for $K^+K^-\pi^+\pi^-\pi^0$ events in (a) $\eta_c(1S)$ region ($2.9 < m_{K^0_S K^\pm \pi^\mp} < 3.05\ \mathrm{GeV}/c^2$), (b) $\eta_c(2S)$ region ($3.6 < m_{K^0_S K^\pm \pi^\mp} < 3.7\ \mathrm{GeV}/c^2$), (c) $\eta_c(1S)$ sideband region ($m_{K^0_S K^\pm \pi^\mp} < 2.9\ \mathrm{GeV}/c^2$ or $3.05 < m_{K^0_S K^\pm \pi^\mp} < 3.4\ \mathrm{GeV}/c^2$), and (d) $\eta_c(2S)$ sideband region ($3.4 < m_{K^0_S K^\pm \pi^\mp} < 3.5\ \mathrm{GeV}/c^2$ or $m_{K^0_S K^\pm \pi^\mp} > 3.7\ \mathrm{GeV}/c^2$).

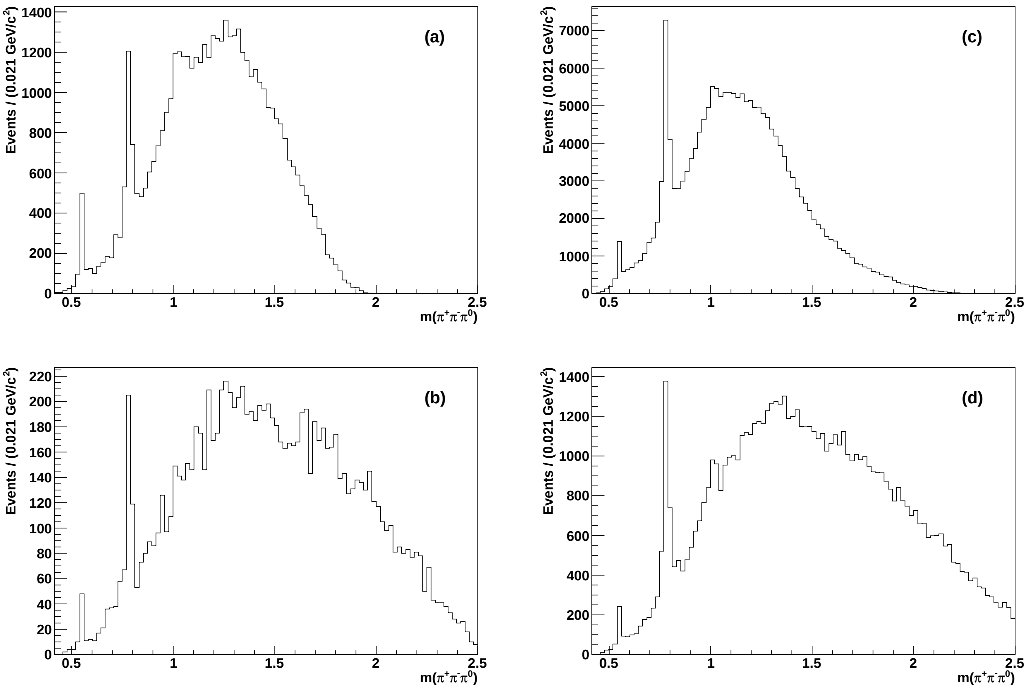

Figure B.3: Invariant $\pi^+\pi^-\pi^0$ mass distributions for $K^+K^-\pi^+\pi^-\pi^0$ events in (a) $\eta_c(1S)$ region ($2.9 < m_{K^0_S K^\pm \pi^\mp} < 3.05$ GeV$/c^2$), (b) $\eta_c(2S)$ region ($3.6 < m_{K^0_S K^\pm \pi^\mp} < 3.7$ GeV$/c^2$), (c) $\eta_c(1S)$ sideband region ($m_{K^0_S K^\pm \pi^\mp} < 2.9$ GeV$/c^2$ or $3.05 < m_{K^0_S K^\pm \pi^\mp} < 3.4$ GeV$/c^2$), and (d) $\eta_c(2S)$ sideband region ($3.4 < m_{K^0_S K^\pm \pi^\mp} < 3.5$ GeV$/c^2$ or $m_{K^0_S K^\pm \pi^\mp} > 3.7$ GeV$/c^2$).

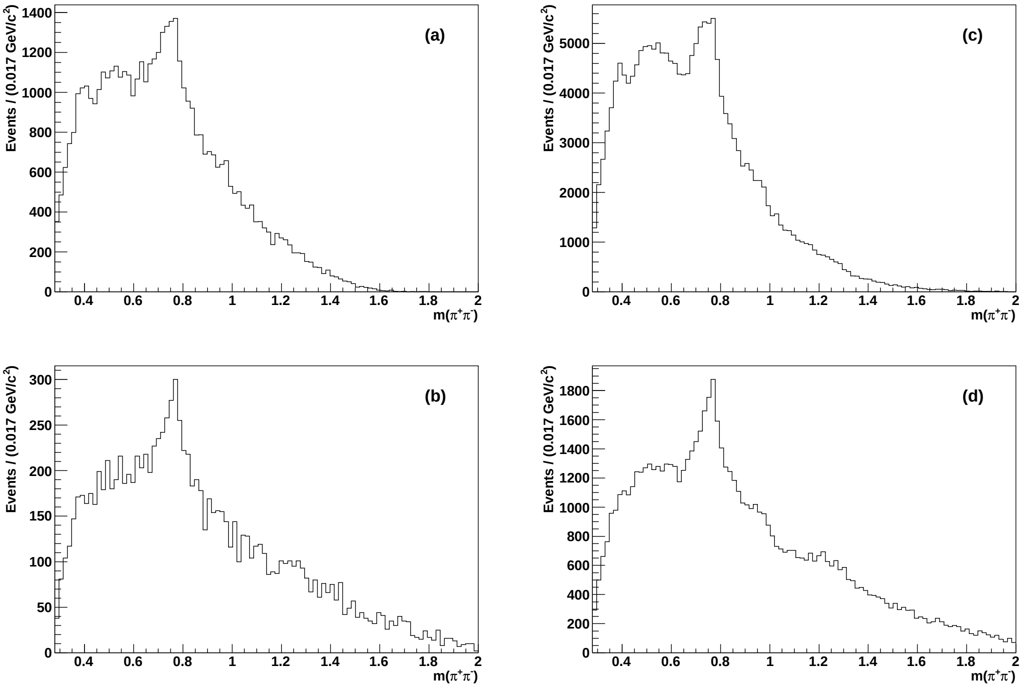

Figure B.4: Invariant $\pi^+\pi^-$ mass distributions for $K^+K^-\pi^+\pi^-\pi^0$ events in (a) $\eta_c(1S)$ region ($2.9 < m_{K^0_S K^\pm \pi^\mp} < 3.05$ GeV$/c^2$), (b) $\eta_c(2S)$ region ($3.6 < m_{K^0_S K^\pm \pi^\mp} < 3.7$ GeV$/c^2$), (c) $\eta_c(1S)$ sideband region ($m_{K^0_S K^\pm \pi^\mp} < 2.9$ GeV$/c^2$ or $3.05 < m_{K^0_S K^\pm \pi^\mp} < 3.4$ GeV$/c^2$), and (d) $\eta_c(2S)$ sideband region ($3.4 < m_{K^0_S K^\pm \pi^\mp} < 3.5$ GeV$/c^2$ or $m_{K^0_S K^\pm \pi^\mp} > 3.7$ GeV$/c^2$).

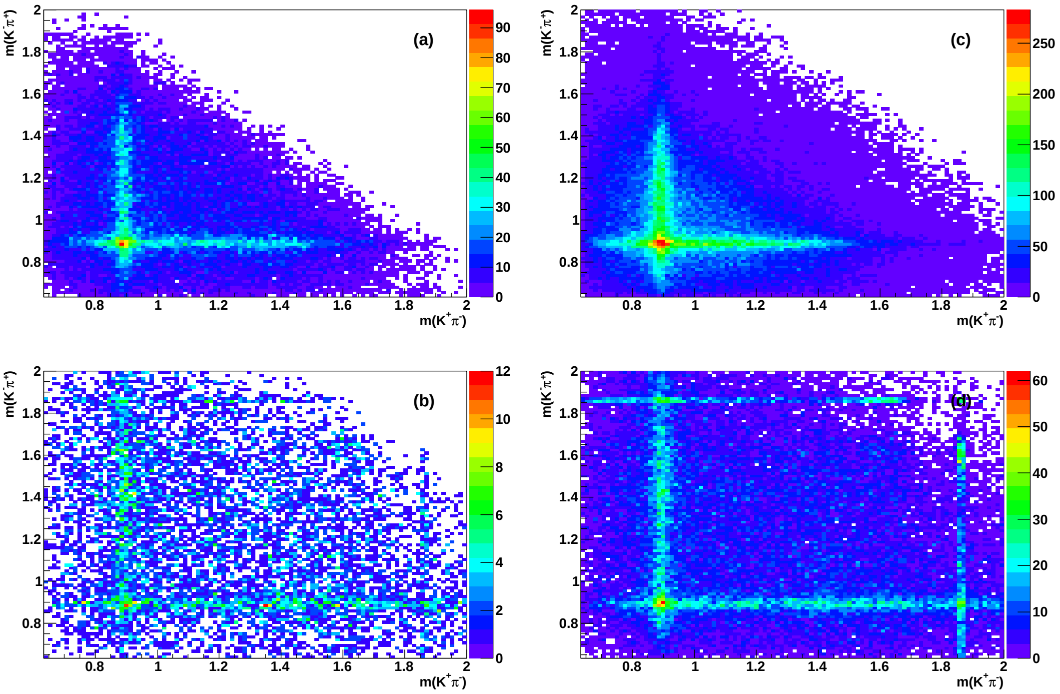

Figure B.5: Invariant $(m(K^+\pi^-), m(K^-\pi^+))$ mass distributions for $K^+K^-\pi^+\pi^-\pi^0$ events in (a) $\eta_c(1S)$ region ($2.9 < m_{K^0_S K^\pm \pi^\mp} < 3.05$ GeV/c^2), (b) $\eta_c(2S)$ region ($3.6 < m_{K^0_S K^\pm \pi^\mp} < 3.7$ GeV/c^2), (c) $\eta_c(1S)$ sideband region ($m_{K^0_S K^\pm \pi^\mp} < 2.9$ GeV/c^2 or $3.05 < m_{K^0_S K^\pm \pi^\mp} < 3.4$ GeV/c^2), and (d) $\eta_c(2S)$ sideband region ($3.4 < m_{K^0_S K^\pm \pi^\mp} < 3.5$ GeV/c^2 or $m_{K^0_S K^\pm \pi^\mp} > 3.7$ GeV/c^2).

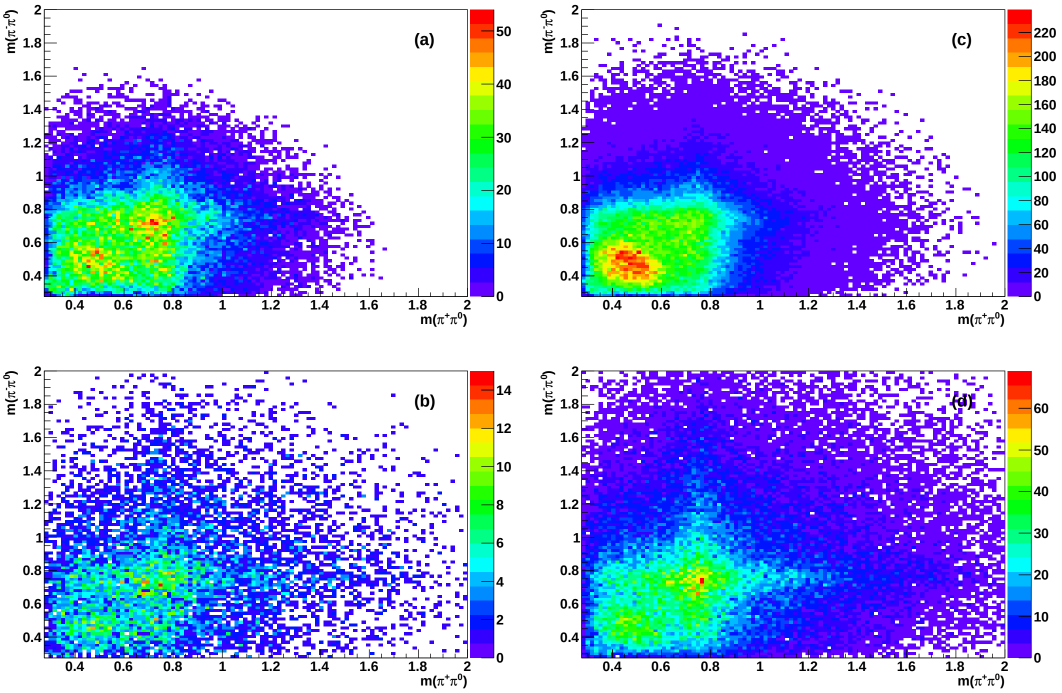

Figure B.6: Invariant $(m(\pi^+\pi^0), m(\pi^-\pi^0))$ mass distribution for (a) $\eta_c(1S)$ region $2.9 < m_{K^0_S K^\pm \pi^\mp} < 3.05$ GeV$/c^2$, (b) $\eta_c(2S)$ region $3.6 < m_{K^0_S K^\pm \pi^\mp} < 3.7$ GeV$/c^2$, (c) $\eta_c(1S)$ sideband region $m_{K^0_S K^\pm \pi^\mp} < 2.9$ GeV$/c^2$ or $3.05 < m_{K^0_S K^\pm \pi^\mp} < 3.4$ GeV$/c^2$ (c), and (d) $\eta_c(2S)$ sideband region $3.4 < m_{K^0_S K^\pm \pi^\mp} < 3.5$ GeV$/c^2$ or $m_{K^0_S K^\pm \pi^\mp} > 3.7$ GeV$/c^2$.

Acknowledgments

Everything I did during my Ph.D. years would have not been possible without the support of many people. First of all I want to express my deep gratitude to my advisor Prof. Fernando Palombo, for motivating me in working hard to excel in what I was doing, for giving me the opportunity of presenting my results, for supporting me through successes and failures, and for fairly accepting my decision to leave. In my thesis work the guidance of Prof. Antimo Palano was fundamental, he put me on the right trails and looked at me walking. I felt his appreciation when I started running and his support when I occasionally fell. I really want to express him all my gratitude. I would also like to thank Prof. Gautier Hamel de Monchenault for the useful suggestions he gave me.

In my work and everyday life I enjoyed the presence of the several Milan *BABAR* group fellows, in particular I want to thank Alfio “codefather” Lazzaro, Vincenzo “BDP” Lombardo, Nicola “R5” Neri, Ale Berra, Paolo “Oxford” Gandini, Chiara Piacentini, Ale “Brenda” Colnago and Ricky Pellegrini. Me and Simone Stracka shared the same offices for almost three years, becoming good colleagues and good friends. I will miss our discussions about physics, science, economics, politics, life. My days would not have been so happy without the presence of my lunch and coffee mates Alessandra Re and Davide “Dr.” Trezzi, I hope that our friendship will last long in the future.

I am grate to the *BABAR* members that reviewed this work: Abi Soffer, Bill Dunwoodie, Torsten Schroeder, and Vladimir Druzhinin. I would also like to thank Prof. M. Shepherd and Dr. C. P. Shen for useful discussions. I express my gratitude to the referee of this thesis, Claudia Patrigniani, for providing me interesting suggestions to improve it. The Swedish version of the sentence used in this thesis as aphorism was kindly provided by Prof. Björne Larsson. I would like to thank those that in *BABAR* followed my work, and in particular present and former conveners of the Quarkonium, Quasi-Two-Body and Three-Body analysis working groups: Bryan Fulsom, Arafat Gabareen Mokhtar, Claudia Patrigniani, Veronique Ziegler, Adrian Bevan, Alessandro Gaz, Jim Smith, Pablo del Amo Sanchez, and Eli Ben-Haim. I also extend my appreciation to the people that reviewed other works I did in *BABAR*: Gerard Bonneaud, John Fry, Bill Gary, Wolfgang Gradl, Zijin Guo, Jelena Ilic, Livio Lanceri, David Lange, Xinchou Lou, Brian

Meadows, Claudia Patrigniani, Ida Peruzzi, Elisabetta Prencipe, and Christophe Yeche. My stays at SLAC and at many conferences and schools would not have been that good without the presence of many fellows: Fabio Anulli, Ilaria Besana, Tina Cartaro, Antonio Caseracciu, Riccardo Cenci, Enrico Feltresi, Nicola Gagliardi, Isabella Garzia, Elisa “Drive” Guido, Elisa “Big Hands” Manoni, Maurizio Martinelli, David Lopes Pegna, Enrico “NinoBoy” Rinaldi, Marcello Rotondo, and Valentina Santoro. I cannot forget some university fellows that spent some time with me: Alice, Andrea F., Andrea I., Daniele, Fede, Michele, Rosa, and Ruggero.

There are many people outside the university whose support has been fundamental during these years. I would like to thank my friends Chiara, Angelo, Simona, Nando, Rosanna, Teo, and Yuri, for helping me to stop thinking at physics during the week-ends. My good friend Elena was always at my side when I needed her help, even when she went to Zambia for one year. Her support is priceless. Me and Gigi meet rarely, but I never forget about him. My basketball-mates Lorenzo, Raffa, Andrea, Filippo, Alice and Valeria shared with me amazing and annoying moments. During our “lightly” meetings I really had a lot of fun.

I am really grate to my parents Piera and Carlo and to my brother Enrico. They gave me every kind of support during these years and accepted all my choices, especially those that they did not like.

The last words of this period of my life are dedicated to the person that followed me day by day, sharing happiness, sadness, dreams, frustrations, disillusions, projects, and everything else. I hope we will realize our projects and dreams together. I love you.

Bibliography

[1] E. Eichten *et al.*, Rev. Mod. Phys. **80**, 1161 (2008).

[2] N. Brambilla *et al.*, Eur. Phys. Jour. C **71**, 1534 (2011).

[3] J. J. Aubert *et al.* (E698 Collaboration), Phys. Rev. Lett. **33**, 1404 (1974).

[4] J. E. Augustin *et al.*, Phys. Rev. Lett. **33**, 1406 (1974).

[5] C. Quigg and J. L. Rosner, Phys. Lett. B **71**, 153 (1977).

[6] E. Eichten *et al.*, Phys. Rev. D **17**, 3090 (1978) [Erratum Phys. Rev. D **21**, 313 (1980)].

[7] E. Eichten *et al.*, Phys. Rev. D **21**, 203 (1980).

[8] S. Godfrey and N. Isgur, Phys. Rev. D **32**, 189 (1985).

[9] L. P. Fulcher, Phys. Rev. D **44**, 2079 (1991).

[10] J. Zeng *et al.*, Phys. Rev. D **52**, 5229 (1995).

[11] S. N. Gupta and J. M. Johnson, Phys. Rev. D **53**, 312 (1996).

[12] D. Ebert *et al.*, Phys. Rev. D **67**, 014027 (2003).

[13] E. Eichten *et al.*, Phys. Rev. D **69**, 094019 (2004).

[14] T. Barnes *et al.*, Phys. Rev. D **72**, 054026 (2005).

[15] Y. B. Ding *et al.*, Phys. Lett. **10**, 460 (1993).

[16] K. T. Chao and J. H. Liu, Proceedings of the Workshop on Weak Interactions and CP Violation, Beijin, August 22-26, 1989. World Scientific (Singapore 1990), 109, (1990).

[17] B.-Q. Li *et al.*, Phys. Rev. D **80**, 014012 (2009).

[18] E. Braaten, OHSTPY-HEP-T-97-004 (1997).

[19] W. E. Caswell and G. P. Lepage, Phys. Lett. B **167**, 437 (1986).

[20] G. T. Bodwin *et al.*, Phys. Rev. D **51**, 1125 (1995) [Erratum Phys. Rev. D **55**, 5853 (1997)].

[21] A. Pineda and J. Soto, Nucl. Phys. **B** (Proc. Suppl) **64**, 428 (1998).

[22] N. Brambilla *et al.*, Nucl. Phys. B **566**, 275 (2000).

[23] N. Brambilla *et al.*, Rev. Mod. Phys. **77**, 1423 (2005).

[24] B. A. Kniehl and A. A. Penin, Nucl. Phys. B **563**, 200 (1999).

[25] W. E. Caswell and G. P. Lepage, Phys. Lett. B **167**, 437 (1986).

[26] C. T. H. Davies *et al.*, Phys. Rev. D **52**, 6519 (1995).

[27] A. A. Khan *et al.* (CP-PACS Collaboration), Nucl. Phys. Proc. Suppl. **94**, 325 (2001).

[28] S. Aoki *et al.* (CP-PACS Collaboration), Nucl. Phys. Proc. Suppl. **106**, 364 (2002).

[29] M. Okamoto *et al.* (CP-PACS Collaboration), Phys. Rev. D **65**, 094508 (2002).

[30] X. Liao and T. Manke, Report N. CU-PT-1063 (2002).

[31] D. Q. Liu, Chin. Phys. Lett. **21**, 2136 (2004).

[32] J. J. Dudek *et al.*, Phys. Rev. D **77**, 034501 (2008).

[33] J. J. Dudek and E. Rrapaj, Phys. Rev. D **78**, 094504 (2008).

[34] C. DeTar, “*Charmonium Spectroscopy from Lattice QCD*”, Proceedings of the CHARM2010 Conference, Beijing, October 21-24, 2010. arXiv:1101.0212 [hep-lat].

[35] R. E. Mitchell *et al.* (CLEO Collaboration), Phys. Rev. Lett. **102**, 011801 (2009).

[36] S. Okuba, Phys. Lett. **5**, 165 (1963).

[37] G. Zweig, CERN Report TH-401 and TH-412 (1964).

[38] J. Iizuka, Prog. Theor. Phys, Suppl. **37 & 38**, 21 (1966).

[39] S.-K. Choi *et al.* (Belle Collaboration), Phys. Rev. Lett. **91**, 262001 (2003).

[40] B. Aubert *et al.* (*BABAR* Collaboration), Phys. Rev. Lett. **95**, 142001 (2005).

[41] T. E. Coan *et al.* (CLEO Collaboration), Phys. Rev. Lett. **96**, 162003 (2006).

[42] C. Z. Yuan *et al.* (Belle Collaboration), Phys. Rev. Lett. **99**, 182004 (2007).

[43] B. Aubert *et al.* (*BABAR* Collaboration), Phys. Rev. Lett. **98**, 212001 (2007).

[44] X. L. Wang *et al.* (Belle Collaboration), Phys. Rev. Lett. **99**, 142002 (2007).

[45] B. Aubert *et al.* (*BABAR* Collaboration), Phys. Rev. Lett. **98**, 212001 (2007).

[46] X. L. Wang *et al.* (Belle Collaboration), Phys. Rev. Lett. **99**, 142002 (2007).

[47] S.-K. Choi *et al.* (Belle Collaboration), Phys. Rev. Lett. **94**, 182002 (2005).

[48] B. Aubert *et al.* (*BABAR* Collaboration), Phys. Rev. Lett. **101**, 082001 (2008).

[49] Particle Data Group, K. Nakamura *et al.*, J. Phys. G **37**, 075021 (2010).

[50] W. Kwong and P. B. MacKenzie, Phys. Rev. D **37**, 3210 (1988).

[51] A. Petrelli *et al.*, Nucl. Phys. B **514**, 245 (1998).

[52] E. Eichten *et al.*, Phys. Rev. Lett. **34**,369 (1975) [Erratum Phys. Rev. Lett. **36**, 1276 (1976)].

[53] E. Eichten *et al.*, Phys. Rev. Lett. **36**, 500 (1976).

[54] V. Zambetakis and N. Byers, Phys. Rev. D **28**, 2908 (1983).

[55] H. D. A. Grotch *et al.*, Phys. Rev. D **30**, 1924 (1984).

[56] X. Zhang *et al.*, Phys. Rev. D **44**, 1606 (1991).

[57] S. Godfrey and J. L. Rosner, Phys. Rev. D **64**, 074011 (2001) [Erratum Phys. Rev. D **65**, 039901 (2002)].

[58] T. A. Lahde, Nucl. Phys. **A 714**, 183 (2003).

[59] N. Brambilla *et al.*, Phys. Rev. D **73**, 054005 (2006).

[60] W. Kwong and J. L. Rosner, Phys. Rev. D **38**, 279 (1988).

[61] P. Hasenfratz *et al.* Phys. Lett. B **95**, 299 (1980).

[62] S. Perantonis and C. Michael, *Nucl. Phys. B* **347**, 854 (1990).

[63] S. Ishida *et al.*, Phys. Rev. D **47**, 179 (1993) and references therein.

[64] T. Barnes *et al.* Phys. Rev. D **52** 5242 (1995).

[65] F. E. Close and P. R. Page, *Nucl. Phys. B* **443**, 233 (1995).

[66] Y. S. Kalashnikova and D. S. Kuzmenko, *Phys. Atom. Nucl.***66**, 955 (2003).

[67] G. Chiladze *et al.*, Phys. Rev. D **58**, 034013 (1998).

[68] F. E. Close and P. R. Page, Phys. Lett. B **628**, 215 (2005).

[69] E. Kou and O. Pene, Phys. Lett. B **631**, 164 (2005).

[70] N. A. Tornqvist, Phys. Rev. Lett. **67**, 556 (1991).

[71] N. A. Tornqvist, *Z. Phys. C*, **61**, 525 (1994).

[72] N. A. Tornqvist, Phys. Lett. B **590** 209 (2004).

[73] E. Braaten and M. Kusunoki, Phys. Rev. D **69**, 074005 (2004).

[74] F. Close and P. R. Page, Phys. Lett. B **578**, 199 (2004).

[75] E. S. Swanson, Phys. Lett. B **588**, 189 (2004).

[76] E. Braaten and M. Kusunoki, *Phys. Rep.*, **429**, 243 (2006).

[77] F. Close and C. E. Thomas, Phys. Rev. D **78**, 034007 (2008).

[78] F. Close *et al.* Phys. Rev. D **81**, 074033 (2010).

[79] T. J. Burns *et al.*, Phys. Rev. D **82**, 074003 (2010).

[80] M. T. AlFiky *et al.*, Phys. Lett. B **640**, 238 (2006).

[81] S. Weinberg, Phys. Rev. **130**, 776 (1963).

[82] S. Weinberg Phys. Rev. **131**, 440 (1963).

[83] S. Weinberg, Phys. Rev. **137**, 627 (1965).

[84] V. Baru *et al.*, Phys. Lett. B **586**, 53 (2004).

[85] V. Baru *et al.*, Eur. Phys. Jour. A **23**, 523 (2005).

[86] D. Gamermann *et al.*, Phys. Rev. D **81**, 014029 (2010).

[87] L. Maiani *et al.*, Phys. Rev. D **71**, 014028 (2005).

[88] N. Drenska *et al.*, [hep-ph/1006.2741] and references threin.

[89] D. Ebert *et al.*, Phys. Lett. B **634**, 214 (2006).

[90] D. Ebert *et al.*, Phys. Rev. D **76**, 114015 (2007).

[91] T. W Chiu and T. H. Hsieh, Phys. Lett. B **646**, 95 (2007) and references therein.

[92] L. Liu, PoS(LAT2009), 99 (2009).

[93] Z.-G Wang *et al.*, [hep-ph/1004.0484] and referneces therein.

[94] L. Maiani *et al.* Phys. Rev. D **72**, 031502 (2005).

[95] R. Jaffe and F. Wilczek, Phys. Rev. Lett. **91**, 232003 (2003).

[96] M. Abud *et al.* Adv. Stud. Theor. Phys. **2**, 929 (2008).

[97] M. Abud *et al.* Phys. Rev. D **81**, 074018 (2010).

[98] M. B. Voloshin, Prog. Part. Nucl. Phys. **61**, 455 (2008).

[99] S. Dubynskiy and M. B. Voloshin, Phys. Lett. B **666**, 344 (2008).

[100] S. Dubynskiy *et al.*, Phys. Lett. B **671**, 82 (2009).

[101] R. Mizuk *et al.* (Belle Collaboration), Phys. Rev. D **78**, 072004 (2008).

[102] S.-K. Choi *et al.* (Belle Collaboration), Phys. Rev. Lett. **100**, 142001 (2008).

[103] E. van Beveren and George Rupp, hep-ph/0605317 (2006).

[104] J. L. Rosner, Phys. Rev. D **76**, 114002 (2007).

[105] D. V. Bugg, J. Phys. **G35**, 075005 (2008).

[106] D. V. Bugg, *Int. J. Mod. Phys.A* **24**, 394 (2009) and references therein.

[107] G.-Z. Meng *et al.*, Phys. Rev. D **80**, 034503 (2009).

[108] I. V. Danilkin and P. Yu. Kulikov, JTEP Lett. **89**, 390 (2009).

[109] B.-Q. Liu and K.-T. Chao, Phys. Rev. D **79**, 094004 (2009).

[110] Yu. S. Kalashnikova, Phys. Rev. D **72**, 034010 (2005).

[111] Yu. S. Kalashnikova and A. V. Nefediev, Phys. Rev. D **80**, 074004 (2009).

[112] I. V. Danilkin and Yu. A. Simonov, Phys. Rev. D **81**, 074027 (2010).

[113] I. V. Danilkin and Yu. A. Simonov, Phys. Rev. Lett. **105**, 102002 (2010).

[114] S.Coito *et al.*, Eur. Phys. Jour. C **71**, 10, 1762 (2010).

[115] M. K. Gaillard and B. W. Lee, Phys. Rev. Lett. **33**, 108 (1974).

[116] G. Altarelli and L. Maiani, Phys. Lett. B **52**, 351 (1974).

[117] J. H. Kühn *et al.*, Z. Phys. C **5**, 117 (1980).

[118] M. Diehl and G. Hiller, JHEP**06**, 067 (2001).

[119] G. T. Bodwin *et al.*, Phys. Rev. D **46**, 3703 (1992).

[120] M. Beneke *et al.*, Phys. Rev. D **59**, 054003 (1999)

[121] P. Colangelo *et al.*, Phys. Lett. B **542**, 71 (2002)

[122] Z.-G. Wang, Eur. Phys. Jour. C **58**, 245 (2008)

[123] H. Albrecht *et al.* (ARGUS Colalboration), Phys. Lett. B **241**, 278 (1990).

[124] M. Ablikim *et al.* (BESIII Collaboration), Nucl. Instrum. Methods Phys. Res., Sect. A **614**, 345 (2010).

[125] R. A. Briere *et al.* (CLEO-c/CESR-c Taskforces and CLEO-c Collaboration), Cornell University, LEPP Report No. CLNS 01/1742 (2001), unpublished.

[126] M. Benayoun *et al.*, Mod. Phys. Lett. A Vol.**14**, No.37, 2605 (1999).

[127] S. J. Brodsky *et al.*, Phys. Rev. D **4**, 1532 (1971).

[128] C. N. Yang, Phys. Rev. **77**, 242 (1950).

[129] K. Abe *et al.*, (Belle Collaboration), Phys. Rev. Lett. **89**, 142001 (2002).

[130] B. Aubert *et al.*, (*BABAR* Collaboration), Phys. Rev. D **72**, 031101 (2005).

[131] V. V. Kiselev *et al.*, Phys. Lett. B **332**, 411 (1994).

[132] P. Cho and A. K. Leibovich, Phys. Rev. D **53**, 150 (1996).

[133] P. Cho and A. K. Leibovich, Phys. Rev. D **53**, 6203 (1996).

[134] F. Yuan *et al.*, Phys. Rev. D **56**, 321 (1997).

[135] S. Baek *et al.*, J. Korean Phys. Soc. **33**, 97 (1998).

[136] E. Braaten and J. Lee, Phys. Rev. D **67**, 054007 (2003) [Erratun Phys. Rev. D **72**, 099901 (2005)].

[137] K.-Y. Liu *et al.*, Phys. Lett. B **557**, 45 (2003).

[138] K. Hagiwara *et al.*, Phys. Lett. B **570**, 39 (2003).

[139] G. T. Bodwin *et al.*, Phys. Rev. D **74**, 014014 (2006).

[140] Z. G. He *et al.*, Phys. Rev. D **75**, 074011 (2007).

[141] G. T. Bodwin *et al.*, Phys. Rev. D **77**, 094018 (2008).

[142] Y. J. Zhang *et al.*, Phys. Rev. Lett. **96**, 092001 (2006).

[143] B. Gong and J. X. Wang, Phys. Rev. D **78**, 054006 (2008).

[144] Y. J. Zhang *et al.*, Phys. Rev. D **78**, 054006 (2008).

[145] K. Wang *et al.*, Phys. Rev. D **034022** (2011).

[146] T. M. Himel *et al.* (MarkII Collaboration), Phys. Rev. Lett. **45**, 1146 (1980).

[147] R. Partridge *et al.* (Crystal Ball Collaboration), Phys. Rev. Lett. **45**, 1150 (1980).

[148] R. M. Baltrusaitis *et al.* (MarkIII Collaboration), Phys. Rev. Lett. **52**, 2126 (1984).

[149] R. M. Baltrusaitis *et al.* (MarkIII Collaboration), Phys. Rev. D **33**, 629 (1986).

[150] G. Gaiser *et al.* (Crystall Ball Collaboration), Phys. Rev. D **24**, 711 (1986).

[151] Z. Bai *et al.* (MarkIII Collaboration), Phys. Rev. Lett. **65**, 1309 (1990).

[152] J. Z. Bai *et al.* (BES Collaboration), Phys. Rev. D **60**, 072002 (2000).

[153] J. Z. Bai *et al.* (BES Collaboration), Phys. Lett. B **555**, 174 (2000).

[154] R. E. Mitchel *et al.* (CLEO Collaboration), Phys. Rev. Lett.102, 011801 (2009).

[155] H.-B. Li *“Highlights from BESIII experiment”*, Proceedings of the *“XIV International Conference on Hadron Spectroscopy (HADRON2011)”*, 13-17 June 2011, Münich; arXiv:1108.5789 [hep-ex].

[156] V. V. Anashin *et al.* (KEDR Collaboration), *Measurement of* $B(J/\psi- > \eta_c\gamma)$ *at KEDR*, to appear in the proceedings of the 4th International Workshop on Charm Physics (CHARM2010), October 21-24 2010, Beijing, China; arXiv:1012.1694 [hep-ex].

[157] A. Vinokurova *et al.* (Belle Collaboration), Phys. Lett. B **706**, 139 (2011).

[158] J. P. Lees *et al.* (*BABAR* Collaboration), Phys. Rev. D **81**, 052010 (2010).

[159] H. Nakazawa, *Measurement of the* η_c *and* η_c' *Mesons in Two-Photon Process at Belle*, proceedings of the International Conference on the Structure and Interactions of the Photon (PHOTON2007), July 2007, Paris, France; Nucl. Phys. Proc. Suppl. **184**, 220 (2008).

[160] K. Abe *et al.* (Belle Collaboration), Phys. Rev. Lett. **98**, 082001 (2007).

[161] G. S. Abrams *et al.*, Phys. Rev. Lett. **33**, 1453 (1974).

[162] D. Cronin-Hennessy *et al.* (CLEO Collaboration), Phys. Rev. D **81**, 052002 (2010).

[163] T. Appelquist and H. D. Politzer, Phys. Rev. Lett. **34**, 43 (1975).

[164] A. De Rujula and S. L. Glashow, Phys. Rev. Lett. **34**, 46 (1975).

[165] M. E. B. Franklin *et al.*, Phys. Rev. Lett. **51**, 963 (1983).

[166] N. E. Adam *et al.* (CLEO Collaboration), Phys. Rev. Lett. **94**, 012005 (2005).

[167] M. Ablikim *et al.* (BES COllaboration), Phys. Lett. B **619**, 247 (2005).

[168] L. Chen and W. M. Dunwoodie (MARK-III Collaboration), SLAC-PUB-5674 (1991).

[169] W. Buchmuller and S. H. H. Tye, Phys. Rev. D **23**, 132 (1981).

[170] S. N. Gupta *et al.*, Phys. Rev. D **34**, 201 (1986).

[171] P. Moxhay and J. L. Rosner, Phys. Rev. D **28** 1132(1983)

[172] R. McClary and N. Byers, Phys. Rev. D **28**, 1692 (1983).

[173] A. Duncan and A. Mueller, Phys. Lett. B **93**, 119 (1980).

[174] H. F. Jones and J. Wyndham, Nucl. Phys. **B195**, 222 (1982).

[175] M. Anselmino and F. Murgia, Phys. Rev. D **47**, 3977 (1993).

[176] J. Bolz *et al.*, Eur. Phys. Jour. C **2**, 705 (1998).

[177] S. M. H. Wong, Eur. Phys. Jour. C **14**, 643 (2000).

[178] D. Ebert *et al.*, Mod. Phys. Lett. **A18**, 601 (2003).

[179] A. Petrelli *et al.*, Nucl. Phys. **B514**, 245 (1998).

[180] M. Ablikim *et al.* (BESIII Collaboration), Phys. Rev. Lett. **107**, 092001 (2011).

[181] M. Ablikim *et al.* (BES Collaboration), Phys. Lett. B **630**, 7 (2005).

[182] M. Ablikim *et al.* (BES Collaboration), Phys. Lett. B **642**, 197 (2006).

[183] H. G. Zhou *et al.*, Phys. Lett. B **611**, 123 (2005).

[184] S. J. Brodsky and G. P. Lepage, Phys. Rev. D **81**, 014017 (1981).

[185] Z.-H Liu and Q. Zhao, Phys. Rev. D **81**, 014017 (2010).

[186] D.-Y. Chen *et al.*, Phys. Rev. D **81**, 074006 (2010).

[187] P. Rubin *et al.* (CLEO Collaboration), Phys. Rev. D **72**, 092004 (2005).

[188] T. Manke *et al.* (CP-PACS Collaboration), Phys. Rev. D **62**, 114508 (2000).

[189] S. Dobbs *et al.* (CLEO Collaboration), Phys. Rev. Lett. **101**, 182003 (2008).

[190] M. Ablikim *et al.* (BESIII Collaboration), Phys. Rev. Lett. **104**, 132002 (2010).

[191] M. Andreotti *et al.* (E835 Collaboration), Phys. Rev. D **72**, 032001 (2005).

[192] T. K. Pedlar *et al.* (CLEO Collaboration), Phys. Rev. Lett. **107**, 041803 (2011).

[193] C. Edwards *et al.* (Crystal Ball Collaboration), Phys. Rev. Lett. **48**, 70 (1982).

[194] S.-K. Choi *et al.* (Belle Collaboration), Phys. Rev. Lett. **89**, 102001 (2002).

[195] B. Aubert *et al.* (*BABAR* Collaboration), Phys. Rev. D **78**, 012006 (2008).

[196] D. M. Asner *et al.* (CLEO Collaboration), Phys. Rev. Lett. **92**, 142001 (2004).

[197] B. Aubert *et al.* (*BABAR* Collaboration), Phys. Rev. Lett. **92**, 142002 (2004).

[198] K.-T. Chao *et al.*, Commun. Theor. Phys. **25**, 471 (1996).

[199] S. Uehara *et al.* (Belle Collaboration), Eur. Phys. Jour. C **53**, 1, (2008).

[200] M. Ambrogiani *et al.* (E835 Colalboration), Phys. Rev. D **64**, 052003 (2001).

[201] H. Nakazawa "*Particle Production in Two-Photon Collisions at Belle*", Proceedings of the XXXV International Conference of High Energy Physics (ICHEP2010), 22-28 July 2010, Paris, France; PoS(ICHEP 2010), 162 (2010).

[202] K. Abe *et al.* (Belle Collaboration), Phys. Rev. D **70**, 071102 (2004).

[203] B. Aubert *et al.* (*BABAR* Collaboration), Phys. Rev. Lett. **96**, 052002 (2006).

[204] S. Uehara *et al.* (Belle Collaboration), Phys. Rev. Lett. **96**, 082003 (2006).

[205] B. Aubert *et al.* (*BABAR* Collaboration), Phys. Rev. D **81**, 092003 (2010).

[206] C. R. Munz, *Nucl. Phys. A* **609**, 364 (1996).

[207] D. E. Acosta *et al.* (CDF Collaboration), Phys. Rev. Lett. **93**, 072001 (2004).

[208] V. M. Abazov *et al.* (D0 Collaboration), Phys. Rev. Lett. **93**, 162002 (2004).

[209] B. Aubert *et al.* (*BABAR* Collaboration), Phys. Rev. D **71**, 071103 (2005).

[210] CMS Collaboration, CMS PAS BPH-10-018 (2010).

[211] LHCb Collaboration, LHCb-CONF-2011-021 (2011).

[212] S.-K. Choi *et al.* (Belle Collaboration), Phys. Rev. D **84**, 052004 (2011).

[213] A. Abulencia *et al.* (CDF Collaboration), Phys. Rev. Lett. **96**, 102002 (2006).

[214] A. Abulencia *et al.* (CDF Collaboration), Phys. Rev. Lett. **98**, 132002 (2007).

[215] J. L. Rosner, Phys. Rev. D **70**, 094023 (2004).

[216] D. V. Bugg, Phys. Rev. D **71**, 016006 (2005).

[217] G. Gokhroo *et al.* (Belle Collaboration), Phys. Rev. Lett. **97**, 162002 (2006).

[218] B. Aubert *et al.* (*BABAR* Collaboration), Phys. Rev. D **77**, 011102(R) (2008).

[219] T. Aushev *et al.* (Belle Collaboration), Phys. Rev. D **81**, 031103 (2010).

[220] K. Abe *et al.* (Belle Collaboration), hep-ex/0505037 (2005).

[221] P. del Amo Sanchez *et al.* (*BABAR* Collaboration), Phys. Rev. D **82**, 011101(R) (2010).

[222] K. Abe *et al.* (Belle Collaboration), hep-ex/0505038 (2005).

[223] B. Aubert *et al.* (*BABAR* Collaboration), Phys. Rev. Lett. **102**, 132001 (2009).

[224] V. Bhardwaj *et al.* (Belle Collaboration), Phys. Rev. Lett. **107**, 091803 (2011).

[225] T.-H. Wang and G.-L. Wang, Phys. Lett. B **697**, 233 (2011).

[226] T. J. Burns *et al.*, Phys. Rev. D **82**, 074003 (2011).

[227] A. M. Badalian *et al.*, Phys. Atom. Nucl. **63**, 1635 (2011).

[228] Y. Jia *et al.*, hep-ph/1007.4541 (2010).

[229] Yu. S. Kalashinkova and A. V. Nefediev, Phys. Rev. D **82**, 097502 (2010).

[230] M. B. Voloshin, Phys. Lett. B **579**, 361 (2004).

[231] I. W. Lee *et al.*, Phys. Rev. D **80**, 094005 (2009).

[232] E. S. Swanson, Phys. Lett. B **598**, 197 (2004).

[233] R. D. Matheus *et al.*, Phys. Rev. D **80**, 056002 (2009).

[234] P. G. Ortega *et al.*, Phys. Rev. D **81**, 054023 (2010).

[235] M. Nielsen and C. M. Zanetti, Phys. Rev. D **82**, 116002 (2010).

[236] M. Harada and Y.-L. Ma, Prog. Theor. Phys. **126**, 91 (2011).

[237] C. M. Zanetti *et al.*, Phys. Lett. B **702**, 359 (2011).

[238] C. Bignamini *et al.* Phys. Rev. Lett. **103**, 162001 (2009).

[239] S. Narison *et al.*, Phys. Rev. D **83**, 016004 (2011).

[240] S. Dubnicka *et al.*, Phys. Rev. D **84**, 014006 (2011).

[241] B. Aubert *et al.* (*BABAR* Collaboration), Phys. Rev. D **71**, 031501(R) (2005).

[242] A. Aaltonen *et al.* (CDF Collaboration), Phys. Rev. Lett. **103**, 152001 (2009).

[243] T. Fernandez-Carames *et al.*, Phys. Rev. Lett. **103**, 222001 (2009).

[244] S. Uehara *et al.* (Belle Collaboration), Phys. Rev. Lett. **104**, 092001 (2010).

[245] X. Liu *et al.* Phys. Rev. Lett. **104**, 122001 (2010).

[246] X. Liu *et al.* Eur. Phys. Jour. C **61**, 411 (2009).

[247] T. Branz *et al.* Phys. Rev. D **80**, 054019 (2009).

[248] W. H. Liang *et al.* Eur. Phys. Jour. A **44**, 479 (2010).

[249] T. Branz *et al.*, Phys. Rev. D **83**, 114015 (2011).

[250] P. Pakhlov *et al.* (Belle Collaboration), Phys. Rev. Lett. **100**, 202001 (2008).

[251] E. J. Eichten *et al.*, Phys. Rev. D **73**, 014014 (2006) [Erratum Phys. Rev. D **73**, 079903 (2006)].

[252] T. Barnes, Int. J. Mod. Phys. **A21**, 5583 (2006).

[253] K.-T. Chao, Phys. Lett. B **661**, 348 (2008).

[254] Y.-C. Yang, Phys. Rev. D **81**, 094003 (2010).

[255] R. Molina and E. Oset, Phys. Rev. D **80**, 114013 (2009).

[256] B. Aubert *et al.* (*BABAR* Collaboration), SLAC-PUB-13360.

[257] G. Pakhlova *et al.* (Belle Colalboration), Phys. Rev. Lett. **98**, 092001 (2007).

[258] B. Aubert *et al.* (*BABAR* Collaboration), Phys. Rev. D **79**, 092001 (2009).

[259] G. Pakhlova *et al.* (Belle Colalboration), Phys. Rev. Lett. **101**, 172001 (2008).

[260] A. M. Badalian *et al.*, Phys. Atom. Nucl. **72**, 638 (2009).

[261] S.-L. Zhu, Phys. Lett. B **625**, 212 (2005).

[262] K. J. Juge *et al.*, Phys. Rev. Lett. **82**, 4400 (1999).

[263] T.-W. Chiu *et al.* (TWQCD Collaboration), Phys. Rev. D **73**, 094510 (2006).

[264] G.-J. Ding, Phys. Rev. D **79**, 014001 (2009).

[265] R. M. Albuquerque and M. Nielsen, Nucl. Phys. **A 815**, 53 (2009); [Erratum Nucl. Phys. **A 857**, 48 (2011)].

[266] F.-K. Guo *et al.*, Phys. Lett. B **665**, 26 (2008).

[267] Z.-G. Wang and X.-H. Zhang, Commun. Theor. Phys. **54**, 323 (2010).

[268] F.-K. Guo *et al.*, Phys. Rev. Lett. **102**, 242004 (2009).

[269] F.-K. Guo *et al.*, Phys. Rev. D **82**, 094008 (2010).

[270] J.-R. Zhang and M.-Q. Huang, Phys. Rev. D **83**, 036005 (2011).

[271] W. Chen and S.-L. Zhu, Phys. Rev. D **83**, 034010 (2011).

[272] D. Ebert *et al.*, Eur. Phys. J. **C 58**, 399 (2008).

[273] D.-Y. Chen *et al.*, Phys. Rev. D **83**, 054021 (2011).

[274] D.-Y. Chen *et al.*, Phys. Rev. D **83**, 074012 (2011).

[275] B. Aubert *et al.* (*BABAR* Colalboration), Phys. Rev. D **76**, 092006 (2007).

[276] N. V. Drenska *et al.* Phys. Rev. D **79**, 077502 (2009).

[277] T. Aaltonen *et al.* (CDF Collaboration), Phys. Rev. Lett. **102**, 242002 (2009).

[278] T. Aaltonen *et al.* (CDF Collaboration), hep-ex/1101.6058, submitted to Phys. Rev. Lett..

[279] C.-Z. Yuan, *XXIX Physics in Collision*, Proceedings of the International Symposium, August 30 - September 2 2009, Kobe, Japan.

[280] LHCb Collaboration, LHCb-CONF-2011-045 (2011).

[281] X. Liu and S. L. Zhu, Phys. Rev. D **80**, 017502 (2009).

[282] G. J. Ding, Eur. Phys. Jour. C **64** 297, (2009).

[283] X. Liu and H. W. Ke, Phys. Rev. D **80**, 034009 (2009).

[284] R. M. Albuquerque *et al.* Phys. Lett. B **678**, 186 (2009).

[285] J. R. Zhang and M. Q. Huang, Phys. Rev. D **80**, 056004 (2009).

[286] J. R. Zhang and M. Q. Huang, *J. Phys. G* **37**, 025005 (2010).

[287] N. Mahajan, Phys. Lett. B **679**, 228 (2009).

[288] X. Liu *et al.*, Phys. Lett. B **699**, 341 (2011).

[289] S. I. Finazzo, Phys. Lett. B **701**, 101 (2011).

[290] Fl. Stancu, *J. Phys. G* **37**, 075017 (2010).

[291] E. van Beveren and G. Rupp, hep-ph/0906.2278 (2009).

[292] X. Liu, Phys. Lett. B **680**, 137 (2009).

[293] Z.-G. Wang, Eur. Phys. Jour. C **63**, 115 (2009).

[294] Z.-G. Wang *et al.* Eur. Phys. Jour. C **64**, 373 (2009).

[295] C. P. Shen *et al.* (Belle Collaboration), Phys. Rev. Lett. **104**, 112004 (2010).

[296] A. Albuquerque *et al.* Phys. Lett. B **690** 141 (2010).

[297] Z.-G. Wang, Phys. Lett. B **690**, 403 (2010).

[298] R. Mizuk *et al.* (Belle Collaboration), Phys. Rev. D **80**, 031104(R) (2009).

[299] S.-K. Choi *et al.* (Belle Collaboration), Phys. Rev. Lett. **100**, 142001 (2008).

[300] B. Aubert *et al.* (*BABAR* Collaboration), Phys. Rev. D **79**, 112001 (2009).

[301] R. Mizuk *et al.* (Belle Collaboration), Phys. Rev. D **78**, 072004 (2008).

[302] P. del Amo Sanchez *et al.*, BABAR-PUB-11/022, submitted to Phys. Rev. D .

[303] S. H. Lee *et al.*, Phys. Lett. B **661**, 28 (2008).

[304] X.-Liu *et al.*, Phys. Rev. D **77**, 094015 (2008).

[305] G.-J. Ding *et al.*, Phys. Rev. D **79**, 034026 (2009).

[306] T. Branz *et al.*, Phys. Rev. D **82**, 054025 (2010).

[307] M. E. Bracco *et al.*, Phys. Lett. B **671**, 240 (2009).

[308] X. Liu *et al.*, Phys. Rev. D **77**, 114021 (2008).

[309] Y. Li *et al.*, Phys. Rev. D **77**, 054001 (2008).

[310] T. Matsuki *et al.*, Phys. Lett. B **669**, 156 (2008).

[311] B. Aubert *et al.* (*BABAR* Collaboration), Nucl. Instrum. Methods Phys. Res., Sect. A **479**, 1 (2002).

[312] A. Abashian *et al.*, (Belle Colalboration), Nucl. Instrum. Methods Phys. Res., Sect. A **479**, 117 (2002).

[313] P. Oddone, in *Procedings of the UCLA Workshop: Linear Collider* $B\overline{B}$ *Factory Conceptual Design,* edited by D. Stork (World Scientific), 243 (1987).

[314] J. Abdallah *et al.* (DELPHI Collaboration), Eur. Phys. Jour. C **31**, 481 (2003).

[315] B. Aubert *et al.* (*BABAR* Collaboration), Phys. Rev. Lett. **92**, 142002 (2004).

[316] B. Heltsley, "*New CLEO Results on Charmonium Transitions*", The Sixth International Workshop on Heavy Quarkonia, Nara, Japan, 2008, `http://www-conf.kek.jp/qwg08/session1_3/heltsley.pdf`.

[317] K. Gao, Ph.D. Thesis, University of Minnesota, 2008, arXiv:0909.2812[hep-ex].

[318] D. Lange *et al.*, Nucl. Instrum. Methods Phys. Res., Sect. A **462**, 152 (2001).

[319] T. Sjostrand, Comput. Phys. Commun. **82**, 74 (1994).

[320] The *BABAR* detector Monte Carlo simulation is based on GEANT4: S. Agostinelli *et al.*, Nucl. Instrum. Methods Phys. Res., Sect. A **506**, 250 (2003).

[321] V. M. Bundev *et al.*, Phys. Rep. **15**, 181 (1975).

[322] M. Poppe, Int. J. Mod. Phys. **A1**, 545 (1986).

[323] P. Billoir and S. Qian, *"Simultaneous Pattern Recognition And Track Fitting By The Kalman Filtering Method"*, Nucl. Instrum. Methods Phys. Res., Sect. A **294**, 219 (1990).

[324] P. del Amo Sanchez *et al.* (*BABAR* Collaboration), Phys. Rev. D **84**, 012004 (2011).

[325] A. G. Frodesen *et al.*, *Probability and Statistics in Particle Physics* (Universitetsforlaget, Bergen, Norway, 1979).

[326] N. Cabibbo and A. Maksymowicz, Phys. Rev. **352**, 9 (1964).

[327] M. J. Oreglia, Ph.D Thesis, SLAC-236(1980), Appendix D.

[328] J. E. Gaiser, Ph.D Thesis, SLAC-255(1982), Appendix F.

[329] T. Skwarnicki, Ph.D Thesis, DESY F31-86-02(1986), Appendix E.

[330] S. Uehara, KEK Report 96-11 H (1996).

[331] P. Biassoni, "*Two-photon Physics at* BABAR", talk given at the "8^{th} *International Workshop on Heavy Quarkonium*", October 4-7, 2011, in GSI, Darmstadt, Germany; `https://indico.gsi.de/getFile.py/access?contribId=47t&sessionId=13&resId=0&materialId=slides&confId=1196`.

[332] P. Biassoni, "*Recent Results in Charmonium Spectroscopy at BaBar*", Proceedings of "*Incontri di Fisica delle Alte Energie 2011*", April 27-29, 2011, Perugia, Italy; to be published in Nuovo Cimento C.